




Universitat Autònoma de Barcelona

ADVERTIMENT. L'accés als continguts d'aquesta tesi queda condicionat a l'acceptació de les condicions d'ús establertes per la següent llicència Creative Commons:  http://cat.creativecommons.org/?page_id=184

ADVERTENCIA. El acceso a los contenidos de esta tesis queda condicionado a la aceptación de las condiciones de uso establecidas por la siguiente licencia Creative Commons:  <http://es.creativecommons.org/blog/licencias/>

WARNING. The access to the contents of this doctoral thesis it is limited to the acceptance of the use conditions set by the following Creative Commons license:  <https://creativecommons.org/licenses/?lang=en>

Theoretical Study of Disorder and Proximity effects in Three-dimensional Models of Topological Insulators

Thesis by

Kenan Song

Department of Physics

University of Autònoma de Barcelona (UAB)

In Fulfillment of the Requirements for the Degree of Doctor of Philosophy

(Defended on 13th, July, 2018)

Committee Members: Professor Evgueni Chulkov (Donostia International Physics Centre)

Professor Fèlix Casanova (CIC nanoGUNE)

Professor Xavier Cartoixa (University of Autònoma de Barcelona)

Abstract

This PhD manuscript mainly covers the theoretical study of the electronic properties of Bi_2Se_3 family topological insulators, in presence of different defects and proximity effects with a graphene layer. All calculations are based on density functional theory (DFT) method, tight binding (TB) and effective continuum models which allow to obtain simultaneously a realistic description of electronic properties of clean materials, but also to explore the impact of defects and disorder on such properties. Regarding the study of disorder, we have particularly scrutinized the impact of rotation mismatches inside the quintuple structure and the effect of surface hydrogenation on the properties of ultrathin TI structures. Besides that, the effect of both non-magnetic and magnetic chemical impurities have been investigated using the generic TB Fu-Kane-Mele (FKM) model of three-dimensional TI in the context of gap opening and changes of the spin textures of the surface states. By varying the density of impurities and their magnetic orientation, a series of conclusions could be made on gap features and evolving spin textures of surface states. Finally, the properties of graphene/TI heterostructures have been studied using DFT and a TB model, fitted to the first-principles calculations. The presence of a spin transport anisotropy was found to be a smoking gun of the proximity effect of the TI on the graphene states, a result which has been also discussed in the context of experimental measurements.

Acknowledgements

I would like to take this opportunity to thank Professor Stephan Roche and Professor Pablo Ordejón Rontomé for their supervision of the research work. During the whole research activities, they both provided inspiring suggestions, strong support and encouragement to me; especially, Professor Roche spent a lot time in reading and improving this thesis.

Dr. David Soriano and Dr. Roberto Robles Rodríguez provided useful technical assistances in the DFT calculations of TI with defects; while, Dr. Aron William Cummings provided essential technical support and guidance in the computational work based on TB method and continuum model. I would also like to thank Professor Sergio Osvaldo Valenzuela, Dr. Frédéric Bonell, Mr. Marc González Cuxart, Professor Saroj Prasad Dash and Dr. Dmitrii Khokhriakov for allowing me to participate in the collaboration, concerning the measurement and the interpretation of graphene/TI-based devices. Dr. Jose Hugo García Aguilar, Dr. Stephen Power and Mr. Marc Vila Tusell provided quite useful discussions on the whole PhD research works. I am really indebted to all of them for their help and suggestions.

On the other hand, I would like to thank Mr. Xavier Arandes Villalón, Mrs. Rocío Pérez, Mrs. Estefania Climent Montoya, Ms. Ainhoa Ayastuy Bermejo, Ms. Inmaculada Caño Zafra and Mr. Xavier Ros Ramentol for their technical assistances. It was really quite an enjoyable time to me during the whole research activities in Institut Català de Nanociència i Nanotecnologia (ICN2).

I would also like to thank Professor Jordi Pascual for tutoring my work during the project and Professor Evgueni Chulkov, Professor Fèlix Casanova and Professor Xavier Cartoixà for examining my PhD manuscript.

I am also indebted to my parents for their so strong support during both my studies and life. From them, I learned to become an independent and reliable person.

Contents

Chapter One: Introduction	1
References	3
Chapter Two: Theory of Topological Insulator and DFT Calculation.....	5
2.1 Introduction to Topological Insulator (TI)	5
2.1.1 2D TI	8
2.1.2 3D TI	12
2.1.3 Research and Applications of the Bi ₂ Se ₃ family TIs.....	16
2.2 Introduction to Density Functional Theory (DFT)	17
2.2.1 Many body problem	18
2.2.2 Thomas-Fermi model	21
2.2.3 Thomas-Fermi-Dirac model	22
2.2.4 Functional and Functional Derivative	23
2.2.5 Hohenberg-Kohn theorem	24
2.2.6 Kohn-Sham equation.....	26
2.2.7 Kohn-Sham equation with respect to spin	27
2.2.8 Exchange-Correlation hole	31
2.3 Approximation for Exchange-Correlation Energy (Exc)	33
2.3.1 Local density approximation (LDA)	33
2.3.2 Local spin density approximation (LSDA).....	35
2.3.3 Generalized gradient approximation (GGA)	36
2.4 Introduction to VASP Code	38
2.5 Pseudopotential.....	39
2.5.1 Introduction to Pseudopotentials	39
2.5.2 Norm-Conserving Pseudopotential.....	41
2.5.3 Ultrasoft Pseudopotential.....	42
2.6 Projector Augmented Wave Method.....	44
2.7 Spin Orbit coupling Effect.....	45
2.8 Parameters for the Computation	47
2.8.1 Cutoff Energy	48
2.8.2 <i>k</i> point sampling.....	51
2.8.3 Fourier Transform Grid	52
2.8.4 Computation Procedure in VASP Code	55

2.8.5 Density Mixing Scheme	56
References:	58
Chapter Three: Bi₂Se₃-Family Topological Insulator with Defects	61
3.1 Introduction	61
3.2 Methodology	62
3.3 Twin grain boundaries.....	63
3.4 Surface doping on Bi ₂ Se ₃ thin films	71
3.5 Combining twin grain boundaries and surface doping in Bi ₂ Se ₃ thin films	74
3.6 Conclusions	74
References	75
Chapter Four: Electronic Properties of Graphene/Topological Insulator Heterostructures	77
4.1 Introduction to Graphene/TI Heterostructures	77
4.2. Parameter settings for DFT calculations	80
4.3. Band structure of Gr/1QL Bi ₂ Se ₃ system with hollow configuration.....	81
4.4. Band structure for Gr/6QL Bi ₂ Se ₃ system with hollow configuration	86
4.5. Band structure for Gr/1QL Bi ₂ Se ₃ system with bridge configuration	88
4.6. Band structure for Gr/1QL Bi ₂ Se ₃ system with top configuration.....	92
4.7. Band structure for Gr/1QL Bi ₂ Se ₃ system with three configurations.....	94
4.8. Band structure for Gr/1QL Bi ₂ Te ₃ system with three different configurations....	96
4.9. Band structure for Gr/1QL Sb ₂ Te ₃ system with three different configurations.	101
4.10. Spin texture for graphene layer in Gr/Bi ₂ Se ₃ system with hollow configuration	104
4.11 Spin texture and anisotropy for graphene layer in Gr/Bi ₂ Se ₃ system with bridge, top and all three configurations	112
4.12. Spin texture for graphene layer in Gr/1QL Bi ₂ Te ₃ and Sb ₂ Te ₃ systems with hollow, bridge, top configurations	114
4.13. TB method for pristine graphene system.....	118
4.14. TB method for graphene band in Gr/1QL Bi ₂ Se ₃ system with hollow configuration.....	121
4.15 TB method for graphene band in Gr/1QL Bi ₂ Se ₃ system with all three configurations	129
4.16 Conclusions	133
References	136

Chapter Five: The Effects of Non-Magnetic and Magnetic Dopants on the Electronic Properties of 3D Topological Insulators	141
5.1 Introduction to Fu-Kane-Mele Model	141
5.2 Fu-Kane-Mele model with onsite non-magnetic potential	147
5.3 Fu-Kane-Mele model with random onsite exchange potential.....	149
5.4 Conclusions	173
References	174
Chapter Six: Conclusions	177
Conclusions	177

Chapter One: Introduction

Theoretically predicted in 2007, topological insulators (TI) have gradually attracted more and more attention in the field of condensed matter physics due to their promising application in spintronic devices.[1~6] TI have a bulk bandgap, but contrary to normal insulator exhibit conducting surface states, which are described by a Dirac cone, similar to the case of graphene.

In conventional metals, electron are free to move in any direction and collide with each other or with defects, resulting in the scattering of electron in different directions.[7~9] Furthermore, as electron collide with phonon degrees of freedom, part of their energy is converted into thermal vibration so that their kinetic energy is damped. All these phenomena induce non-zero electric resistance.[10, 11] Different from conventional conductors, the TI surface states exhibit a spin-momentum locking symmetry which manifests in the fact that spin and momentum vectors are always perpendicular to each other. This affects the backscattering probability for electrons since a reversal of momentum is only allowed with a spin flip (due to the time reversal symmetry), suggesting long mean free path of surface electrons in absence of magnetic disorder. As a conclusion surface states are robust against any non-magnetic disorder which suggest low scattering and small resistance.[12] Furthermore, the energy dispersion relation on TI surface state is described by $E = v \times k$ (v is the velocity of electron). This indicates that electron on TI surface can move ‘like light’; except with a different velocity ($E = c \times k$ and c is the speed of light).[13]

Another potential application of TI is Quantum Anomalous Hall effect (QAHE). It is well known that charge current with an external magnetic field applied normal to its substrate plane can experience the Lorentz force in transverse direction which results in a Hall resistance. Quantum Hall (QH) effect is a quantum version of the Hall effect, which was first

observed in 2 dimensional electronic gas with the precise conductance values that are integers or fractional numbers of e^2/h , but requiring strong external magnetic fields.[14-16] Different from QH, Quantum Anomalous Hall (QAH) does not require external magnetic field and the Hall conductivity could acquire quantized values proportional to integer multiples of the conductance quantum, only through the combination of inner magnetic polarization and spin orbit coupling (SOC).[17] This could make QAH a more convenient mechanism for some electronic applications. Since the Bi_2Se_3 -family TI exhibits a band inversion at Γ point and strong SOC, it is a potential candidate for the achievement of QAH without external magnetic field. The observation of QAH effect has been proposed and revealed in the literature.[18~20] Indeed, many efforts have been devoted to achieve the QAH through combining TI with magnetic insulating layer or through magnetic doping elements so as to generate a non trivial gap for surface states.[17~20] More details of QHE, QSHE and QAHE are discussed in chapter 2.1.

Based on all these peculiar properties, TI was investigated in this PhD project and the effect of different defects and proximity effects were examined and are hereafter described in more details.

Chapter 1 gives a general introduction to TI, including its electronic properties and applications in spintronics, and also discusses the content of each chapter of the whole thesis.

Chapter 2 summarizes some essential literature for this PhD research work. A first part is a brief introduction to topological insulators which includes the discussion of the band structure and spin texture of Bi_2Se_3 as an example and the background mechanism. Then, a thorough introduction to density functional theory follows with the concrete deduction of important formulas. Last, the DFT calculation procedure is introduced within the framework of the VASP code, including all different parameters with their setting rules and the different techniques; such as FFT grid, density mixing scheme, pseudopotential, PAW method, noncollinear calculation with SOC effect.

Chapter 3 discusses the effect of different defects on the electronic properties of Bi_2Se_3 with ultrathin thickness and scrutinizes the role of disorder on the robustness of topological surface states, which can be analysed through their spin textures. The presence of twin grain

boundaries is found to increase the band gap of the film, while preserving the spin texture of states in the gapped bands. Differently, partial hydrogenation of one surface not only results in some self-doping effect, but also provokes some alteration of the spin texture symmetry of the electronic states. The formation of a new Dirac cone at M point in the Brillouin zone of the hydrogenated surface, together with a modified spin texture characteristics is consistent with a dominant Dresselhaus spin-orbit interaction type as more usually observed in 3D materials.

Chapter 4 discusses the proximity effect in graphene/ Bi_2Se_3 heterostructure, focusing on the spin properties of the graphene layer. Through enhancing the spin-orbit interaction in graphene via proximity with topological insulators, a novel 2D system shows the combination of nontrivial spin textures with high electron mobility and an understanding of the hybrid spin-dependent properties is also provided through a tight binding model, which could determine the precise spin texture of electronic states in graphene interfaced with a Bi_2Se_3 and agree well with the DFT simulation results. In the end, a giant spin lifetime anisotropy in the graphene layer is discussed, appearing as a measurable hallmark of spin transport in Gr/TI heterostructures and suggesting novel types of spin devices.

Chapter 5 shows the theoretical work based on Fu-Kane-Mele TB model so as to discuss the properties of 3D TI including both band structure and spin textures; particularly, the effect of disorder and magnetic doping of TI was studied based on this model. It is found that magnetic dopants on the surface could result in band gap opening and also induce a spin transport anisotropy of the surface states, providing a guideline to control the spin properties of conducting carrier on TI surface in real devices.

Chapter 6 provides a summary for the whole PhD research works.

References

- [1] König, Markus; Wiedmann, Steffen; Brüne, Christoph; Roth, Andreas; Buhmann, Hartmut; Molenkamp, Laurenc W.; Qi, Xiaoliang and Zhang, Shoucheng *Science* (2007) 318, 5851, 766–770
- [2] Gu, Zhengcheng and Wen, Xiaogang *Phys. Rev. B* (2009) 80 155131
- [3] Pollmann, F.; Berg, E.; Turner, Ari M. and Oshikawa, Masaki *Phys. Rev. B* (2012) 85, 075125
- [4] Xie, Chen; Gu, Zhengcheng and Wen, Xiaogang *Phys. Rev. B* (2011) 83, 035107

- [5] Guhr, Th.; Groening, A. Müller and Weidenmüller, H. A. *Physics Reports* (1998) 299
- [6] Hasan, M. Z. and Kane, C. L. *Rev. Mod. Phys.* (2010) 82, 3045
- [7] Zhang, Wei; Yu, Rui; Zhang, Haijun; Dai, Xi and Fang, Zhong *New J of Phys.* (2010) 12, 065013
- [8] Zhang, Yi; He, Ke; Chang, Cuizu; Song, Canli; Wang, Lili; Chen, Xi; Jia, Jinfeng; Fang, Zhong; Dai, Xi; Shan, Wenyu; Shen, Shunqing; Niu, Qian; Qi, Xiaoliang; Zhang, Shoucheng; Ma, Xucun and Xue, Qikun *Nature Physics* (2010) 6, 712
- [9] Zhang, Guanhua; Qin, Huajun; Teng, Jing; Guo, Jiandong; Guo, Qinlin; Dai, Xi; Fang, Zhong and Wu, Kehui *Appl. Phys. Lett.* (2009) 95, 053114
- [10] Datta, Supriyo *Electronic transport in mesoscopic systems*, Cambridge University Press, Chapter 2 (1995)
- [11] Rammer, Jorgen *Quantum Transport theory*, CRC Press (2004)
- [12] Xu, Yishuai; Chiu, Janet; Miao, Lin; He, Haowei; Alpichshev, Zhanybek; Kapitulnik, A.; Biswas, Rudro R. and Wray, L. Andrew *Nature Comm.* (2017) 8, 14081
- [13] Tkachov, Gregory *Topological Insulators: The Physics of Spin Helicity in Quantum Transport*, Pan Stanford (2015)
- [14] Hall, E. H. *American Journal of Mathematics* (1879) 2, 3, 287-292
- [15] Klitzing, K. v.; Dorda, G. and Pepper, M. *Phys. Rev. Lett.* (1980) 45, 494-497
- [16] Klitzing, K. v. *Rev. Mod. Phys.* (1986) 58, 519
- [17] Chang, Cuizu; Zhang, Jinsong; Feng, Xiao; Shen, Jie; Zhang, Zuocheng; Guo, Minghua; Kang, Li; Ou, Yunbo and Wei, Pang *Science* (2013) 340, 167-170
- [18] Hieh, D.; Xia, Y.; Qian, D.; Wray, L.; Dil, J. H.; Meier, F.; Osterwalder, J.; Patthey, L.; Checkelsky, J.; Ong, G. N. P.; Fedorov, A. V.; Lin, H.; Bansil, A.; Grauer, D.; Hor, Y. S.; Cava, R. J. and Hasan, M. Z. *Nature* (2009) 460, 7259
- [19] Kane, C. L. and Moore, J. E. *Physics World* (2011) 24, 32
- [20] Ortman, Frank; Roche, Stephan and Valenzuela, Sergio O. *Topological Insulator: Fundamentals and Perspectives*, chapter 1 and 6 (2015)

Chapter Two: Theory of Topological Insulator and DFT Calculation

2.1 Introduction to Topological Insulator (TI)

Chapter one gives some general basic introduction to TI, including their properties. Since, in this PhD project, Bi_2Se_3 -family topological insulators (TIs) were investigated under different conditions, for instance, rotation or hydrogenation defects and combination with graphene; therefore, an introduction to it with more details is provided.

TI represents a new state of condensed matter with unique electronic structure, insulating in the bulk but conducting at their boundaries with a Dirac cone shape at low energies.[1–3] The corresponding boundary states are protected by time reversal symmetry with a spin-momentum locking character, namely the direction towards which the carriers are travelling determines univocally the direction of the spin, thus resulting in intrinsic spin currents and unprecedented opportunities for innovative spintronics[3]. Bernevig and Zhang predicted the existence of TIs in strong spin–orbit coupling materials[4, 5] and the formation of edge channels with quantized conductance was later confirmed experimentally in Cadmium Telluride/Mercury telluride/Cadmium Telluride ($\text{CdTe}/\text{HgTe}/\text{CdTe}$) quantum wells through transport measurements [6]. Three-dimensional bulk solids of binary compounds involving bismuth were then predicted to also belong to the TIs family [7]. The first experimentally realized 3D TI state was reported in bismuth antimonide [8], and shortly after observed in pure antimony, bismuth selenide (Bi_2Se_3), bismuth telluride (Bi_2Te_3) and antimony telluride (Sb_2Te_3) using ARPES (see [3]).

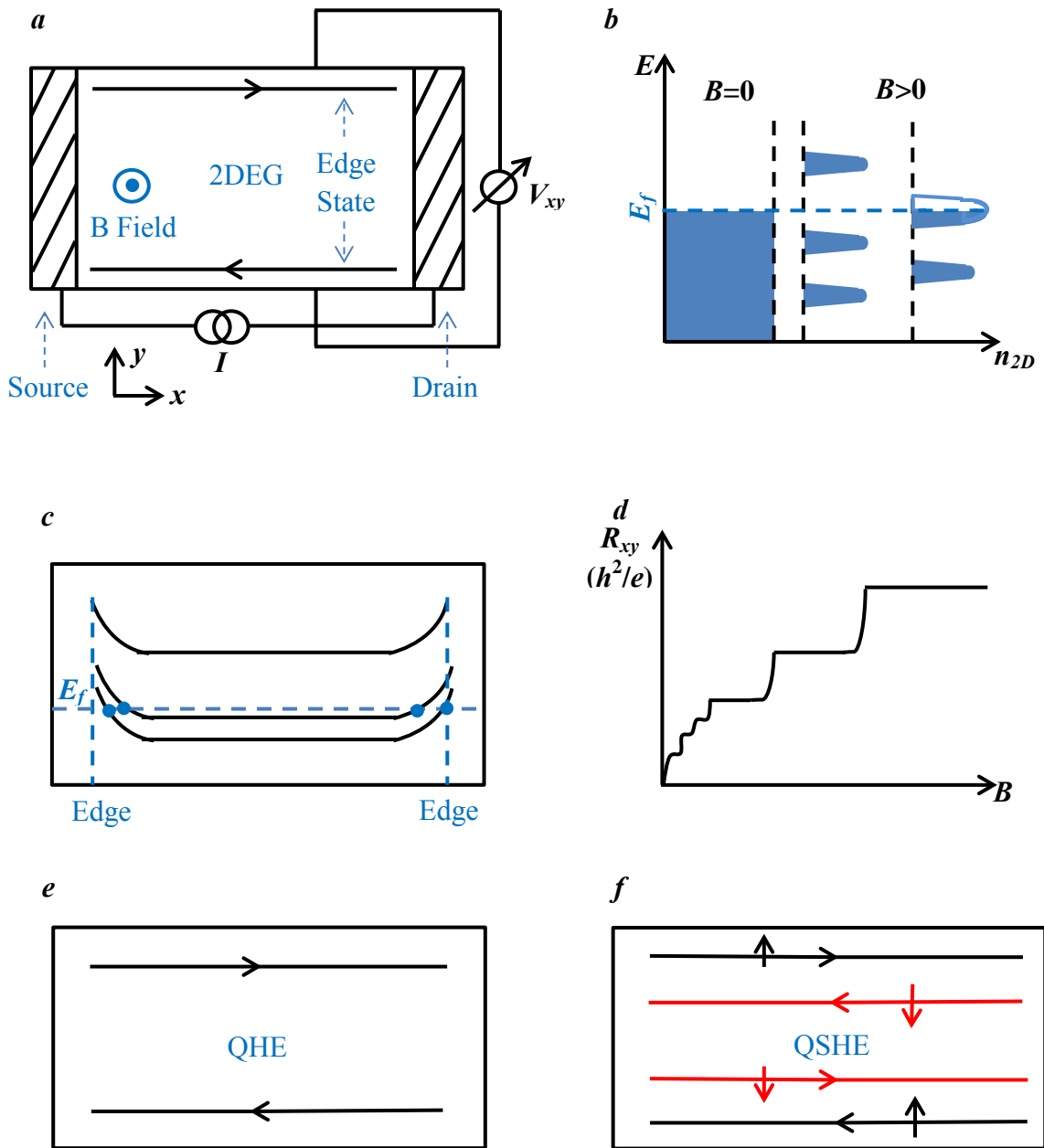


Fig. 2.1 Schematic representation of QH and QSH effects. *a* – 2D electronic gas (2DEG) patterned in Hall geometry; *b* – Landau level in density of states; *c* – Conductance mechanism for bulk and edge states; *d* – Quantum Hall conductance v.s. magnetic field strength; *e* & *f* – Quantum Hall and Quantum Spin Hall effects respectively.

Introduced in chapter one, as QHE concerned, the bulk is insulating while the edge convey propagating states which then determine quantized value for the corresponding conductance (in units of e^2/h). Fig. 2.1*a* shows a representation for the QH device, where an external magnetic (B) field is applied to the 2D electron gas (2DEG). A current (*I*) is applied to the device and a voltage drop in transverse direction (V_{xy}) can be measured. The reason why V_{xy} shows up is that electrons can precess around the B field with cyclotron frequency (eB/m), resulting

in a series of discrete energy levels, and these levels are called Landau levels (shown in Fig. 2.1*b*). These Landau Levels can be filled or depleted as a function of B field strength. When the Fermi level is located in a density of states minimum between two Landau levels (shown in Fig. 2.1*c*), the Hall resistance (R_{xy}) shows staircase-like plateaus as a function of B field (see Fig. 2.1*d*). These plateaus are quantized in steps of h/Ne^2 , where N is an integer. Based on QH effect, a spinless 1D system has both forward and backward moving carriers and these two basic degrees of freedom are spatially separated in a QH bar (see Fig 2.1*e*). The upper edge only supports a forward moving carrier; while, the lower edge only supports a backward moving carrier. Both states are robust and go around an impurity without scattering.

The QH states belong to a topological class in absence of time reversal symmetry (TRS); while, Shoucheng Zhang *et al.*[9] predicted another new class of topological quantum regime as manifested in 2D topological insulators, referred as the quantum spin Hall (QSH) state for which the spin orbit coupling (SOC) plays the main role. According to this QSH state, a spinful 1D system has four basic degrees of freedom, which are spatially separated in a QSH bar. The upper edge supports a forward moving carrier with spin up and backward moving carrier with spin down and conversely for the lower edge. In other words, this QSH state can be considered as two copies of the QH state, where states with opposite spin propagate along the edge in opposite direction as shown in Fig. 2.1*f*. These topological insulators are classified into two different classes dictated by the so-called Z_2 topological number. If the nontrivial state has a bulk gap and surface states determined by an odd number of Dirac cones with Z_2 of 1/2 modulo an integer, then the system is classified into a strong TI. Differently if the surface states are described by an even number of Dirac cones with Z_2 of 0, then, it is classified into a weak TI. As 2D topological insulators, HgTe/CdTe quantum well (QW) was first theoretically predicted when the thickness of QW becomes shorter than a critical value, the topological nontrivial state emerges, in which a pair of 1D edge states with opposite spins propagate in opposite directions. The experiment showed that the longitudinal conductance in QSH state is then quantized in units of $2e^2/h$. In 2009, a 3D version of topological insulators was predicted in Bi_2Te_3 and Sb_2Te_3 with a bulk band gap and Dirac cone describing the gapless surface states. The following sections introduce 2D and 3D TI with their Hamiltonian model and related properties respectively.

2.1.1 2D TI

Both HgTe and CdTe have the zinc blende lattice structure. They both show bands which are located near the Gamma point at the Fermi level, bands which are made from one s -orbital (Γ_6) band and two p -orbital bands split by SOC effect into a $J=3/2$ (Γ_8) band and $J=1/2$ (Γ_7) band (J and Γ denote total angular momentum and Dirac point respectively). CdTe exhibits a s -orbital (Γ_6) conduction band and p -orbital (Γ_7 & Γ_8) valence bands with a gap of about 1.6 eV. Due to Hg element with strong SOC strength, the band ordering of HgTe is inverted in the following way that Γ_8 becomes a conduction band and is shifted above Γ_6 band, thus moved below the Fermi level. Because of the degeneracy between Γ_7 and Γ_8 bands, HgTe is zero-gap semiconductor.[10]

In the structure of a quantum well, HgTe is connected with CdTe on both sides and through tuning the width of the well, different phases can be achieved. E_1 and H_1 in Fig. 2.2 denote quantum well states derived from Γ_6 and Γ_8 bands respectively. As the well width becomes shorter than a critical value, the confinement energy increases and the energy level is shifted and the well behaves like CdTe, which has the normal band ordering (Γ_6 and Γ_8 are the conduction and valence bands respectively), and becomes a normal insulator; while, as the width is larger than the critical value, the well behaves like HgTe in which the confinement is weak, Γ_6 and Γ_8 band crosses and becomes inverted. This critical width value is about 6.3 nm and the whole mechanism is illustrated in Fig. 2.2.

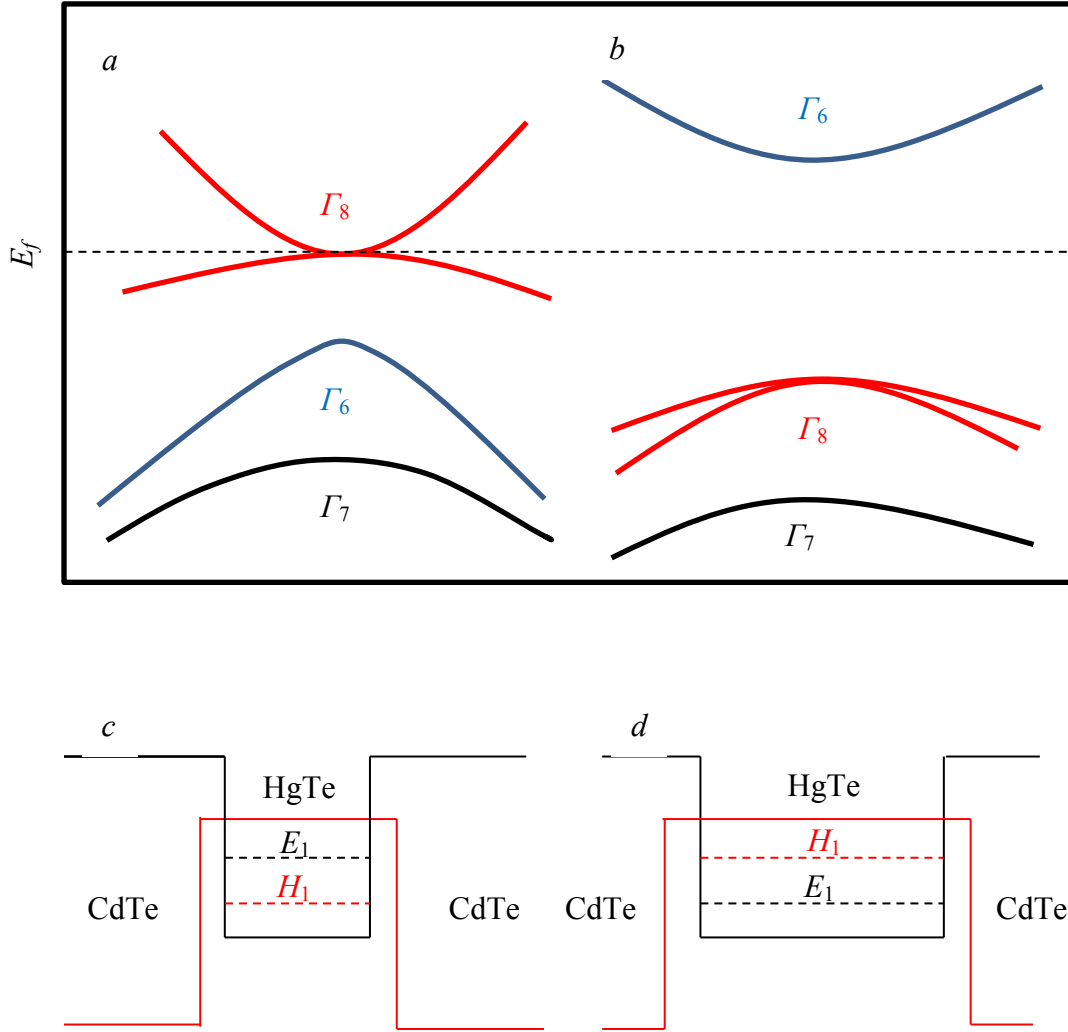


Figure 2.2 Illustration of quantum well formed by HgTe/CdTe. *a, b* – bands for HgTe and CdTe respectively. *c, d* – well width smaller and larger than the critical value. E_f indicates Fermi level

Shoucheng Zhang *et al.* built up an effective Hamiltonian model to describe this system which is written in equation 2.1.[10]

$$H = \begin{pmatrix} h_k & 0 \\ 0 & h_k^* \end{pmatrix} \quad (2.1)$$

and $h_k = \epsilon_k I_{2 \times 2} + d_k \sigma^a$; $I_{2 \times 2}$ is identity matrix;

$$\epsilon_k = C - D(k_x^2 + k_y^2); d_k = [Ak_x - Ak_y, M_k] \text{ and } M_k = M - B(k_x^2 + k_y^2)$$

where, A, B, C, D and M are quantum well dependent parameters. Taking Fermi energy level of HgTe as zero eV, and the energy spectrum of this model is written as equation 2.2.

$$E_{\pm} = \epsilon_k \pm \sqrt{A^2(k_x^2 + k_y^2) + M_k^2} \quad (2.2)$$

M_k is the Dirac mass and it controls the energy gap between Γ_6 and Γ_8 bands. When the well width is larger than the critical value, M_k becomes negative which indicates that Γ_8 band is above Γ_6 band and band inversion happens.

Furthermore, HgTe does not have inversion symmetry, but brings an additional term (shown in equation 2.3) that strongly affects the spin texture of the edge state. Such additional Hamiltonian writes

$$H_{additional} = \begin{pmatrix} 0 & 0 & 0 & -\Delta_z \\ 0 & 0 & \Delta_z & 0 \\ 0 & \Delta_z & 0 & 0 \\ -\Delta_z & 0 & 0 & 0 \end{pmatrix} \quad (2.3)$$

To simplify such Hamiltonian, a lattice regularization is applied and the eigenvalue, well width and Dirac mass are described in equations 2.4 ~ 2.6.

$$\epsilon_k = C - 2Da^{-2}(2 - \cos k_x a - \cos k_y a) \quad (2.4)$$

$$d_k = [Aa^{-1} \sin k_x a, -Aa^{-1} \sin k_y a, M_k] \quad (2.5)$$

$$M_k = M - 2Ba^{-2}(2 - \cos k_x a - \cos k_y a) \quad (2.6)$$

Here, replacing k_x by $-\partial_x$ and rewriting the eigenstate of the edge state as the following form (equation 2.7)

$$\Psi_{\uparrow} = \begin{pmatrix} \Psi_0 \\ 0 \end{pmatrix}; \Psi_{\downarrow} = \begin{pmatrix} 0 \\ \Psi_0 \end{pmatrix} \quad (2.7)$$

Then, the wave function of edge state at Γ point is given in equation 2.8

$$\Psi_0 = \begin{cases} a(e^{\lambda_1 x} - e^{\lambda_2 x})\phi_-, & A/B < 0 \\ c(e^{-\lambda_1 x} - e^{-\lambda_2 x})\phi_+, & A/B > 0 \end{cases} \quad (2.8)$$

where, $\lambda_{1,2} = \frac{1}{2B}(A \pm \sqrt{A^2 - 4MB})$ and ϕ_{\pm} satisfy $\Psi_0 = \phi e^{\lambda x}$ and \pm sign indicates solutions corresponding to $\pm\lambda$. It is obvious that the relative strength between A and B determines the spin polarization of the edge state, which indicates the helicity of Hamiltonian for the spin texture. Projection of bulk Hamiltonian onto the edge state, shown in equation 2.9, generates the model for edge state.

$$H_{edge} = \langle \Psi_{\alpha} | H | \Psi_{\beta} \rangle \quad (2.9)$$

and to leading order of k_y , the Hamiltonian is expressed in equation 2.10.

$$H_{edge} = Ak_y \sigma^z \quad (2.10)$$

According to König *et al.*[11], the A is about $3.6 \text{ eV}\text{\AA}$ and the Dirac velocity of the edge state is $5.5 \times 10^5 \text{ m/s}$.

As shown in Fig. 2.1, the QSH regime manifests the state with opposite spin which counter-propagates along a given edge. In such system, TRS prevents all backscattering paths for electrons, resulting in the fact that helical edge state is robust against disorder. The mechanism is explained below with Fig. 2.3. If a nonmagnetic impurity is present at edge and the electron is backscattered, then, the forward moving electron with one spin direction can make either a clockwise or a counterclockwise turn around the impurity. Since in the QSH regime, only electron with opposite spin can move backwards, the spin of backscattered electron has to be altered to the opposite spin with an angle of $\pm\pi$. Thus, the forward and backward paths differ by 2π of spin. On the other hand, the spin operator changes to the negative sign under 2π rotation. Therefore, two backscattering paths interfere destructively and result in full transmission. However, in the situation of a magnetic impurity located at the edge, the TRS will be broken and these two backscattering paths do not interfere destructively, so that the QSH regime is no longer insensitive to disorder.[12]

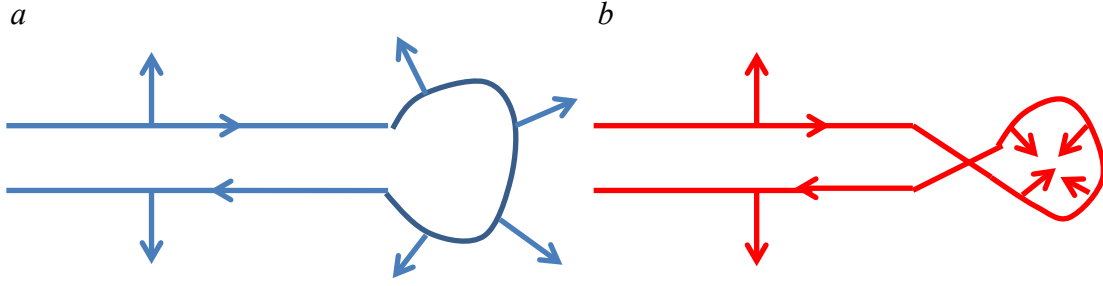


Fig. 2.3 Two backscattering paths for electron on edge and they interfere destructively, leading to the robustness against backscattering in presence of non-magnetic impurity.

2.1.2 3D TI

Similar to 2D TI, 3D TI materials can be described by Hamiltonians in which SOC effect causes the band inversion at Γ point and the structure shows a bulk band gap; while, the surface states described as Dirac fermions remain topologically protected. In 2009, H. Zhang *et al.*[13] proposed a generic model for this Bi_2Se_3 family TIs, which includes Bi_2Se_3 , Bi_2Te_3 and Sb_2Te_3 . These materials crystallize in the rhombohedral structure with space group D_{3d}^5 ($R\bar{3}m$). Taking Bi_2Se_3 as an example, it has layered crystal structure, which is composed of quintuple-layer (QL) units stacked along the trigonal axis with a threefold rotational symmetry, and the bulk crystal structure has five atoms (two Bi and three Se atoms). Covalent bonding is formed within QL and weak Van der Waals interaction exists between each QL.[14~16]

The crystal structure of Bi_2Se_3 is shown in Fig. 2.4a and the band structure for 6QLs case from DFT calculation is shown in Fig. 2.4b, from which the bulk band gap is seen to be about 0.3 eV, agreeing with experimental data. Fig. 2.4c shows the illustration for the mechanism of such electronic state at Γ point. The main contribution to the state close Fermi energy level comes from the p -shell orbital and their configurations are $6s^26p^3$ for Bi and $4s^34p^4$ for Se respectively. The chemical bonding between Bi and Se inside QL leads to some level repulsion and the inversion of the centre allows defining the eigenstate with definite parities. Crystal field effect results in the splitting between p_z orbitals from p_x and p_y , leaving Bi and Se with opposite parity near the Fermi level. Furthermore, SOC effect introduces an additional splitting of energy level and because the strength of Bi is very strong (1.25 eV for Bi $6p$ orbital), the downshifted Bi $6p_z$ orbital is large enough to bring the band inversion between Bi $6p_z$ and Se $4p_z$ levels, leaving a Dirac point (DP) at Γ point. Due to the quantum tunnelling

effect, TI film needs to be thick enough (no thinner than 6 nm) to avoid the interaction between two surface states.[17, 18]

Fig. 2.4*d* shows the spin texture, which is the most important feature of TI. Each green arrow indicates the direction of spin vector on each k point and, from the centre to each k point, it is the direction of momentum vector; therefore, it is clear to see that the spin and momentum vector are always perpendicular to each other. This direction relation is called *Rashba*-type spin texture and as long as the direction of one vector is known, that of the other one could be implied through right-hand rule. Based on this spin texture, it is known that current moving in opposite, parallel direction could have opposite spin direction on the surface edge, which makes such material very promising in the field of spintronics.[19]

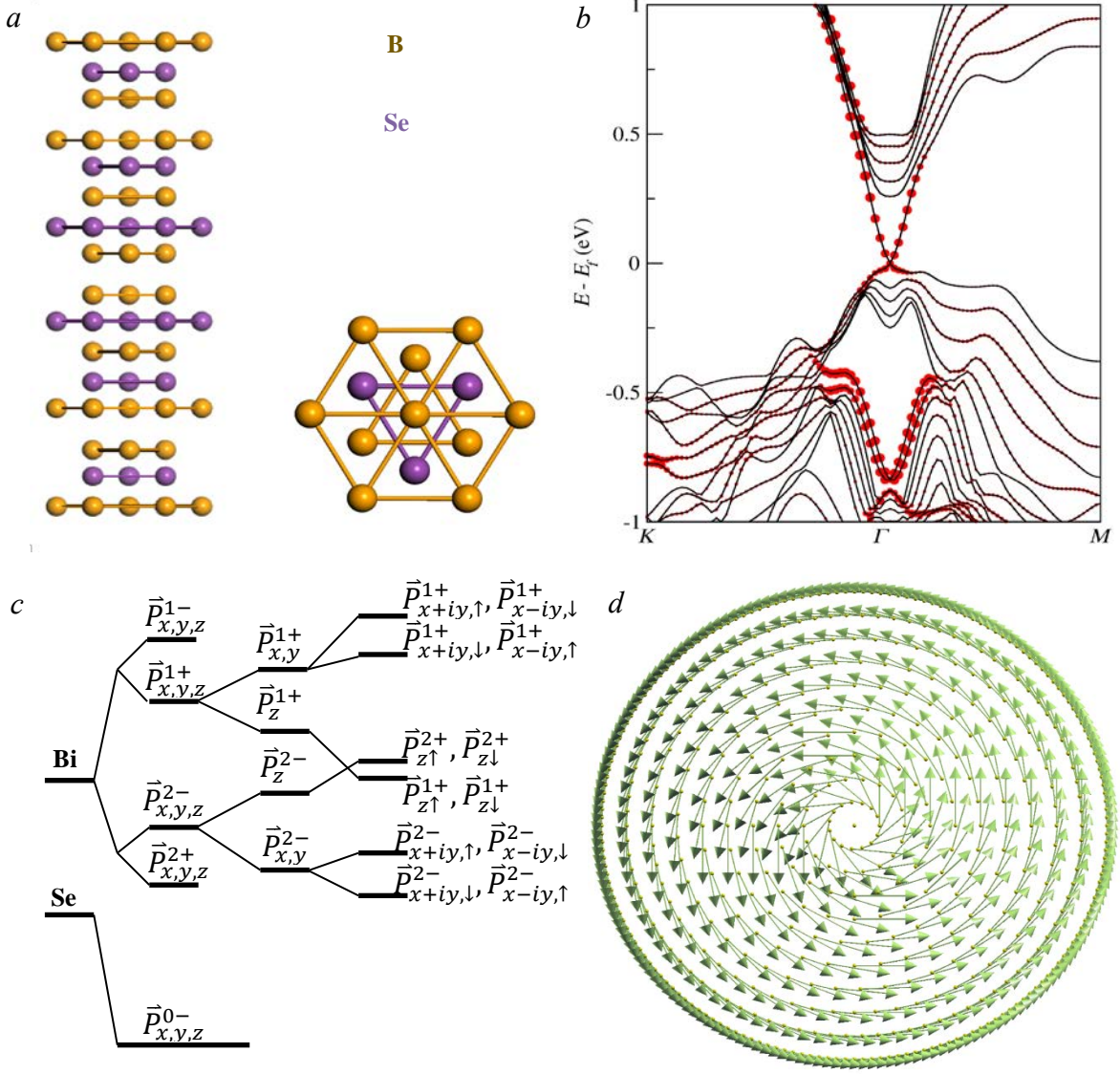


Fig. 2.4 Structure and mechanism for Bi_2Se_3 TI. *a.* - crystal structure of Bi_2Se_3 ; *b.* - band structure of 6QLs Bi_2Se_3 ; *c.* - illustration for the mechanism; *d.* - spin texture on the surface state

An effective Hamiltonian, which features the low energy property of this system, is written in formula 2.11.[20]

$$H = \epsilon_k I_{4 \times 4} + \begin{pmatrix} M_k & A_1 k_z & 0 & A_2 k_- \\ A_1 k_z & -M_k & A_2 k_- & 0 \\ 0 & A_2 k_+ & M_k & -A_1 k_z \\ A_2 k_+ & 0 & -A_1 k_z & -M_k \end{pmatrix} \quad (2.11)$$

where, $k_{\pm} = k_x \pm ik_y$, $\epsilon_k = C + D_1 k_z^2 + D_2 k_{\perp}^2$ and $M_k = M - B_1 k_z^2 + B_2 k_{\perp}^2$. This Hamiltonian has the four low lying state ($|p1_{z\uparrow}^+\rangle$, $|p1_{z\downarrow}^+\rangle$, $|p2_{z\uparrow}^-\rangle$ and $|p2_{z\downarrow}^-\rangle$) at Γ point, with the time reversal symmetry (TRS), the inversion symmetry (I) and the threefold rotation symmetry (C_3)

around z axis. In these four orbitals basis, the underlying symmetries can be represented by equation 2.12 ~ 2.14 and $I_{n \times n}$ is a $n \times n$ identity matrix, K denotes the complex conjugation operator, $\sigma^{x,y,z}$ and $\tau^{x,y,z}$ are Pauli matrices for spin and orbital respectively.

$$T = i\sigma^y K \otimes I_{2 \times 2} \quad (2.12)$$

$$I = I_{2 \times 2} \otimes \tau_3 \quad (2.13)$$

$$C_3 = \exp[i(\pi/3)\sigma^z \otimes I_{2 \times 2}] \quad (2.14)$$

All parameters in the Hamiltonian were obtained through fitting the model to *ab initio* calculations.[21] The Dirac mass (M), which denotes the bulk insulating gap (~ 0.3 eV), guarantees the formation of TI under the room temperature and according to M , B_1 and B_2 , it is obvious that the order of $|p1_{z\uparrow(\downarrow)}^+\rangle$ and $|p2_{z\uparrow(\downarrow)}^-\rangle$ is inverted at Γ point, which characterises the nontrivial nature of TI system.

Similar to that in 2D case, projecting bulk Hamiltonian onto the surface state can generate a 3D surface effective model, which is written in equation 2.15.

$$H_{surface} = C + A_2(\sigma^x k_y - \sigma^y k_x) \quad (2.15)$$

with $A_2 = 4.1$ eV \AA and the velocity on surface state is given by $v = A_2 / \hbar \approx 5.0 \times 10^5$ m/s. Through projecting the spin operators onto the subspace with the four basis states, the spin operators for this model are written in equation 2.16.

$$\left. \begin{aligned} \langle \Psi_\alpha | S_x | \Psi_\beta \rangle &= S_x \sigma_x^{\alpha\beta} \\ \langle \Psi_\alpha | S_y | \Psi_\beta \rangle &= S_y \sigma_y^{\alpha\beta} \\ \langle \Psi_\alpha | S_z | \Psi_\beta \rangle &= S_z \sigma_z^{\alpha\beta} \end{aligned} \right\} \quad (2.16)$$

where, $S_{(x,y,z)}$ are positive constants. As discussed in 2D case, the sign of the A_1/B_1 parameters, is controlled by the atomic SOC effective, and determines the direction of spin operator. In the Bi_2Se_3 family TIs, the upper Dirac cone has left hand helicity; while the lower one has the right hand helicity, shown in figure 2.4d, from the top view.

2.1.3 Research and Applications of the Bi₂Se₃ family TIs

In chapter 1 and the beginning of section 2.1, QH was discussed but a strong external magnetic field was mentioned to be essential to achieve such a quantum transport regime; while, TI has the potential to exhibit the Quantum Anomalous Hall (QAH) state without the action of any external magnetic field, which makes TI a promising candidate for spintronics. Quantum Anomalous Hall effect (QAHE) is the quantum version of Anomalous Hall (AH) and it requires the combination of magnetic polarization and spin orbit coupling to generate the Hall conductance without external magnetic field. One way to induce a QAH regime is to dope the TI system with magnetic elements and since the magnetization can break the TRS; a surface gap can be generated. Then, the Hall conductance (σ_{xy}) can be computed based on equation 2.17.

$$\sigma_{xy} = \frac{e^2}{2\pi h} \int_{BZ} \Omega_{xy} d_k^2 \quad (2.17)$$

where, e , h and Ω_{xy} are elementary charge, Planck constant, Berry curvature respectively. The integral of Berry curvature is within the whole first Brillouin zone. The Berry curvature is calculated based on equation 2.18

$$\Omega_{n,xy}(k) = -Im \sum_{v \neq n} \frac{\langle n | \nabla_x H(k) | v \rangle \langle v | \nabla_y H(k) | n \rangle}{(E_n(k) - E_v(k))^2} \quad (2.18)$$

where, $\nabla_x H$ or $\nabla_y H$ is the velocity operator along x or y axis; while, $|v\rangle$ and $|n\rangle$ are Bloch states for each k with energies $E_n(k)$ and $E_v(k)$ respectively. According to equations 2.17 and 2.18, it is clear that if the integral of Berry curvature is non-zero, the hall conductance is non-zero as well. In other words, Berry curvature can also be used to probe whether the surface gap is trivial or topological non-trivial.

Many research groups have already carried out a lot of studies in this direction. For instance, Toru Hirahara *et al.*[22] comprehensively examined Mn doped Bi₂Se₃ system and pointed out the stable composition (MnBi₂Se₄/Bi₂Se₃) for the structure with ferromagnetism, which could exhibit the QAHE feature and could have huge application in the direction of ‘topotronic devices’. M. M. Otrokov *et al.*[23] proposed a magnetic extension method, which combines the pristine TI with magnetic TI, made from Mn doping, and this method could help generate a

relatively large gap on TI and maintain the QAH signal even in the higher temperature regime.

Furthermore, Zengji Yue *et al.*[24] observed ultraviolet and visible frequency plasmons and high refractive index in nanoslit of $\text{Bi}_{1.5}\text{Sb}_{0.5}\text{Te}_{1.8}\text{Se}_{1.2}$ and Sb_2Te_3 , and pointed out the excellent electronic and optical properties of TI and their wide applications in optoelectronic devices. Jiwon Chang *et al.*[25] explored metal-oxide-semiconductor field-effect transistors (MOSFETs) based on Bi_2Se_3 and found that TI could provide reasonable performance that make it candidate in the such device; especially, with the spin polarized surface state.

Other recent research works on TI have evidenced the possibility of a truly insulating bulk on TI thin films [26, 27] and bulk crystals [28, 29]; however, the contribution of defects and bulk transport remain a critical hurdle to fully exploit the potential of those materials [30–32]. In addition, growing large area of high quality TI-films by MBE remains a true challenge, so minimizing the ‘bulk’ part of the TI is a strategy to preserve larger surface versus bulk transport channels. The symmetry breaking of opposite surfaces of TI (for instance through chemical functionalization or substrate effects [33, 34]) has been further shown to suppress the quantum tunnelling between surface states, hence offering the possibility for exploring spin transport at surface of ultrathin TI films. Juba Bouaziz *et al.*[35] investigated in the impurity doped Bi_2Te_3 and Bi_2Se_3 and found that Cr, Mn, Fe and Co dopants only altered the TI surface states but also hybridized with TI bulk states and generating many in-gap states. Lin Miao *et al.*[36] reported that disorder-rich Bi_2Se_3 showed kink-like dispersion feature and induce some renormalized surface Dirac cone.

According to all these research works on TI, it is obvious that TI has many applications with novel features and therefore, it is interesting and meaningful to study this kind of materials with focus on the electronic properties, which is the main objective of this PhD project as well.

2.2 Introduction to Density Functional Theory (DFT)

Most parts of the simulation works in this research project were based on Density Functional Theory (DFT), which is the most popular and powerful method for the calculations in many scientific fields, such as solid physics, geophysics, materials, theoretical chemistry, biology. Electronic structure, including the band structure and spin texture were all investigated by DFT method[37]; therefore, it is necessary to introduce the fundamental knowledge of this method.

2.2.1 Many body problem

To deal with the properties of the system with many particles, one needs to consider about the way to describe the systems. According to quantum mechanics, wave function is used to represent the state of the system. Take the system of N electrons under non relativistic condition as an example, wave function $\varphi_{(r_1, r_2, \dots, r_N)}$ is used to describe the state of the system and r_i denotes the position of i th electron in three dimensional space; then, one needs to solve Schrödinger equation, which is written below:

$$\left[\sum_i^N \left(-\frac{\hbar^2 \nabla_i^2}{2m} + u_i \right) + \sum_{i < j} v_{(r_i, r_j)} \right] \varphi_{(r_1, r_2, \dots, r_N)} = E \varphi_{(r_1, r_2, \dots, r_N)} \quad (2.19)$$

where $-\frac{\hbar^2 \nabla_i^2}{2m}$ denotes the kinetic energy of i th electron and u_i denotes the external potential on i th electron; while $v_{(r_i, r_j)}$ denotes the Coulomb interaction between i th and j th electrons[38].

The usual approach to solve Schrödinger equation is done in the following procedure shown in Fig. 2.5. Firstly, one needs to set up the Hamiltonian for the system by choosing u_i ; then put u_i into the equation. By solving the equation, one can get $\varphi_{(r_1, r_2, \dots, r_N)}$ and then the observables can be calculated by taking the expectation value of the operator with this wave function.

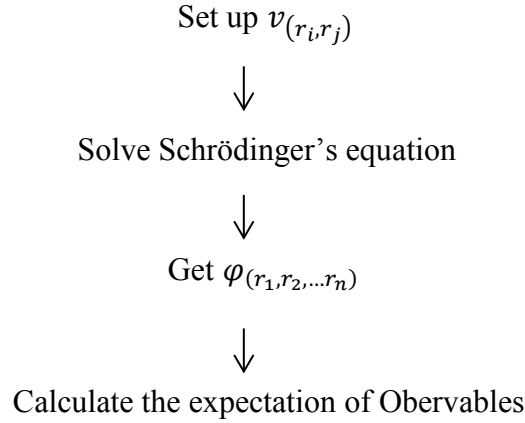


Fig. 2.5 Procedure of Solution for Schrödinger equation equa-

To calculate the properties of the interacting many-body system, such as electrons within the solid, it is important to consider about wave function and Hatree made an approximation[39], in which he wrote the many electrons wave function as a product of single particle wave functions, which is shown in equation below.

$$\varphi(r_1, r_2, \dots, r_N) = \varphi_{r_1} \varphi_{r_2} \dots \varphi_{r_N} \quad (2.20)$$

Every wave function φ_{r_i} satisfies one electron Schrödinger equation.

$$\left(-\frac{\hbar^2 \nabla^2}{2m} + u + v_i\right) \varphi_{r_i} = \varepsilon_i \varphi_{r_i} \quad (2.21)$$

where, the Coulomb potential v_i is given by Poisson equation, shown in the following equation.

$$\nabla^2 v_i = 4\pi e^2 \sum_{\substack{j=1 \\ i \neq j}}^N |\varphi_j|^2 \quad (2.22)$$

Fermi statistics can be combined through substituting the wave function by a single determinantal function. This Hatree Fock (HF) approximation[40] causes nonlocal exchange term in Schrödinger equation, while keeping the single particle framework; and the exchange effects can improve the accuracy for the calculation of total energy.

Although many powerful computational methods have been developed to solve the Schrödinger's equation, such as diagrammatic perturbation theory[41], which is based on Feynman diagrams and Green's functions, and configuration interaction (CI) methods[42], which are based on systematic expansion in Slater determinants; there exists the problem for the calcu-

lation. Each electron has three freedoms of the coordinates in space and totally the wave function has $3N$ freedoms and if spin freedom is considered as well, the total number of freedom is $4N$, which means that it is very hard to get the solution for the equation. Therefore, it is impossible to solve the problem for large and complex system through computer calculation and no one did the calculation for chemical properties of a molecule with more than hundred atoms through configuration interaction (CI) methods before.

To address this difficulty in computational work, the way of using particle density (ρ_r), instead of wave function, to describe Hamiltonian of the system was proposed[43] and the procedure for the calculation is summarised in Fig. 2.6. First step is to gain particle density and then, the wave function and the potential are implied by the density. Therefore, other observables can be gained through the wave function.

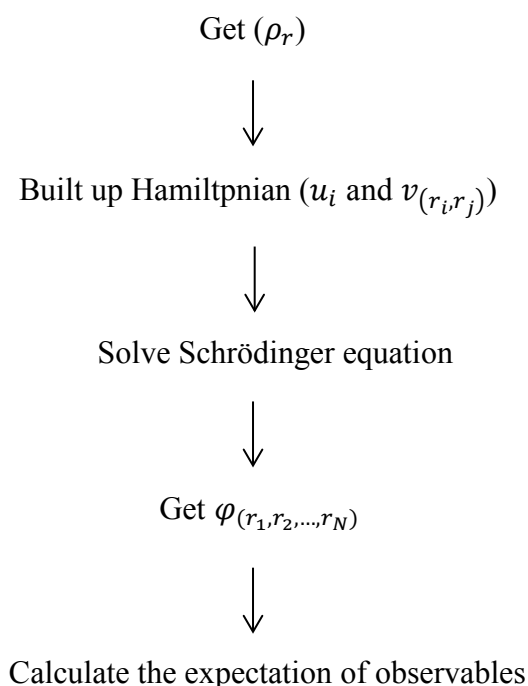


Fig. 2.6 Procedure of calculation of observables by particle density

This method provides an efficient way for the calculation of electronic structure and many properties of the system can be gained, such as band structure, magnetism, thermodynamics, dielectric and optical properties of materials. To apply particle density into practice, many physical models were built up for the calculation of the energy for the whole electronic systems.

2.2.2 Thomas-Fermi model

In 1927, Thomas and Fermi[44] used statistics to make an approximate description for the distribution of the electrons within atom. They proposed that two electrons moving at different velocities within a system with the volume of l^3 can be treated as the free electron gas moving within the six-dimensional space. The total energy of the whole system with N electrons can be expressed equation below.

$$E[\rho] = T[\rho] + \int \rho_r u_r d_r + V_{ee}[\rho] \quad (2.23)$$

where $T[\rho]$ denotes the kinetic energy and the second part denotes the potential energy between nuclei and electron while $V_{ee}[\rho]$ denotes interaction between electrons, which only indicates the Coulomb interaction within this model.

The space can be divided into several small cubics with the volume of ΔV (l^3) and different cubic has different number of electrons (ΔN). It is assumed that electrons within the cubic are treated as isolated Fermion under zero Kelvin and each small cubic is independent. With the assistance of Fermi-Dirac distribution function (equation 2.24), energy for each cubic can be expressed by the following equation.

$$f(\varepsilon) = \frac{1}{1 + e^{\beta(\varepsilon - \mu)}} = \begin{cases} 0 & \varepsilon < \varepsilon_F \\ 1 & \varepsilon \geq \varepsilon_F \end{cases} \quad (2.24)$$

where ε_F is Fermi energy level and states with energy higher than this value is unoccupied and those with energy lower than this value is occupied.

$$\Delta E = 2 \int \varepsilon f(\varepsilon) q(\varepsilon) d_\varepsilon = \frac{3}{5} \Delta N \varepsilon_F \quad (2.25)$$

where $q(\varepsilon)$ is the number of energy level within ε and $\varepsilon + \delta\varepsilon$; while 2 indicates there exist two electrons on each energy level.

With the consideration of electron density (ρ), total kinetic energy for the whole system can be described in equation below.

$$T[\rho] = C_F \int \rho^{5/3}(r) d_r \quad (2.26)$$

where $C_F = \frac{3}{10} (3\pi^2)^{2/3} = 2.871$

Therefore, the total energy for the electronic system is written in equation below.

$$E_{TF}[\rho] = C_F \int \rho^{5/3}(r) d_r - Z \int \frac{\rho_r}{r} d_r + \frac{1}{2} \iint \frac{\rho_{r1} \rho_{r2}}{|r_1 - r_2|} d_{r1} d_{r2} \quad (2.27)$$

2.2.3 Thomas-Fermi-Dirac model

On the basis of Thomas-Fermi model[45], Dirac proposed Thomas-Fermi-Dirac model, in which he adopted the same description of Kinetic energy in Thomas-Fermi model but added exchange energy into interaction between electrons. The electrons within the system are still treated as free electrons in a potential box and, with the consideration of the periodic condition ($\varphi_{(x+l)} = \varphi_x$), the orbital wave function can be written below.

$$\varphi(k_x, k_y, k_z) = \frac{1}{l^{3/2}} e^{i(k_x x + k_y y + k_z z)} = \frac{1}{V^{1/2}} e^{i k r} \quad (2.28)$$

The density matrix is expressed in the following equation.

$$\rho_1(r_1, r_2) = \frac{2}{V} \sum e^{i k(r_1 - r_2)} = \frac{1}{4\pi^3} \int_0^{k_F} k^2 d_k \iint e^{i k r_{12}} \sin \theta d_\theta d_\phi \quad (2.29)$$

where k_F is the position function and equals $[3\pi\rho_r]^{1/3}$.

Following the coordinate transformation

$$r = \frac{1}{2}(r_1 + r_2), s = r_1 - r_2 \quad (2.30)$$

$$\begin{aligned} \rho_1(r_1, r_2) &= \frac{1}{4\pi^3} \int_0^{k_F} k^2 d_k \int_0^\pi \sin \theta d_\theta \int_0^{2\pi} d_\phi = 3\rho_r \frac{\sin t - t \cos t}{t^3} \\ &= \rho_1(r, s) \end{aligned} \quad (2.31)$$

where $t = k_F(r)s$

Equation 2.31 is the description of first order density matrix for free non-polarized electron gas. Exchange energy ($K[\rho]$) is expressed below.

$$\begin{aligned} K[\rho] &= \frac{1}{4} \iint \frac{1}{r_{12}} |\rho_1(r_1, r_2)|^2 d_{r_1} d_{r_2} \\ &= \frac{1}{4} \iint \frac{|\rho_1(r, s)|^2}{s} d_r d_s = C_x \int \rho_r^{4/3} d_r \end{aligned} \quad (2.32)$$

Where $C_x = 0.7386$

The total energy for the whole electronic system can be described below.

$$E_{TFD}[\rho] = C_F \int \rho_r^{5/3} d_r + \int \rho_r v_r d_r + J_\rho - C_x \int \rho_r^{4/3} d_r \quad (2.33)$$

where J_ρ is Coulomb energy.

Thomas-Fermi and Thomas-Fermi-Dirac models can ease the calculation of the energy and other properties of the systems much more efficiently since density function is applied into

the formula. However, the accuracy of the calculation is quite difficult to be enhanced because the description for kinetic energy and interaction between electrons are approximated directly. More accurate method, Kohn-Sham equation, can be induced for the energy calculation.

2.2.4 Functional and Functional Derivative

Mathematically, Functional is defined as rule for going from a function to a number, for example the equation below describes how the particle number changes with the particle density function[46].

$$N_\rho = \int \rho_r d_r^3 \quad (2.34)$$

where N_ρ is the particle number and ρ_r is the particle density function for the coordinate (r) variable of particle.

One important point is that functional only changes with the function, not variable, thus there is no discrimination between $N_\rho(r)$ and $N_\rho(r')$. Another case is that functional also depends on a parameter, such as the formula of Hartree potential [$v_\rho(r)$] in equation below, which describes the rule that for any value of the parameter r associates a value $v_\rho(r)$ with the function ($\rho_{r'}$).

$$v_\rho(r) = q^2 \int \frac{\rho_{r'}}{|r - r'|} d_{r'}^3 \quad (2.35)$$

The functional derivative measures the first-order change in a functional upon a functional variation of its argument, shown in the following equation.

$$F[f_r + \delta f_r] = F[f_r] + \int s_r \delta f_r d_r + O(\delta f^2) \quad (2.36)$$

where, the integral arises due to the fact that the variation of functional ($F[f_r]$) depends on the variation of the function (f_r) at all points within the whole space. The first order coefficient, which could also be referred to as functional slope, is the functional derivative ($\delta F[f_r]/\delta f_r$).

Functional derivative can tell how the functional changes with the changes in the form of function from which it derives. A much more common formula for the description of the functional derivatives with respect to particle density (ρ_r) of the functional (F_ρ) is shown in equation below.

$$F_\rho = \int f(\rho' \rho'' \rho''' \dots_r) d_r \quad (2.37)$$

$$\frac{\delta F_\rho}{\delta \rho_r} = \frac{\partial f}{\partial \rho} - \frac{d}{d_r} \frac{\partial f}{\partial \rho'} + \frac{d^2}{d_{r^2}} \frac{\partial f}{\partial \rho''} - \frac{d^3}{d_{r^3}} \frac{\partial f}{\partial \rho'''} + \dots \quad (2.38)$$

where, the prime sign indicates ordinary derivatives of particle density function (ρ_r) with respect to variable (r). The above equation has many applications in description of exchange-correlation function within density functional theory.

2.2.5 Hohenberg-Kohn theorem

According to Hohenberg-Kohn theorem[47], the total energy of a system of electrons and nuclei is a unique functional of the electron density (ρ_r). To prove this theorem, consider about a system with N electrons under an external potential u_r , which leads to density (ρ_r), there is another potential u'_r , also leading to the same density. There are two different ground state wave functions φ and φ' that are related to two external potentials (u_r and u'_r), and two different Hamiltonians (\widehat{H} and \widehat{H}') of the system with ground state total energy (E_0 and E'_0). Under Rayleigh-Ritz variational principle, equation below can be built up.

$$\begin{aligned} E_0 &= \langle \varphi | \widehat{H} | \varphi \rangle < \langle \varphi' | \widehat{H} | \varphi' \rangle = \langle \varphi' | \widehat{H}' | \varphi' \rangle + \langle \varphi' | \widehat{H} - \widehat{H}' | \varphi' \rangle \\ &= E'_0 + \int \rho_r (u_r - u'_r) d_r \end{aligned} \quad (2.39)$$

Following the same principle for Hamiltonian \widehat{H}' with the function, equation below can be built up as well.

$$\begin{aligned} E'_0 &= \langle \varphi' | \widehat{H}' | \varphi' \rangle < \langle \varphi | \widehat{H}' | \varphi \rangle = \langle \varphi | \widehat{H} | \varphi \rangle + \langle \varphi | \widehat{H}' - \widehat{H} | \varphi \rangle \\ &= E_0 + \int \rho_r (u'_r - u_r) d_r \end{aligned} \quad (2.40)$$

Obviously, the above two equations contradict to each other, thus resulting in one conclusion that external potential, Hamiltonian and all the other related electronic properties of the system are the unique functional of electron density (ρ_r). The total energy of the system is written in the following format.

$$E_u[\rho] = \int \rho_r u_r d_r + F_\rho \quad (2.41)$$

Another point from Hohenberg-Kohn theorem is that the variational minimum of the energy of the system is exactly equivalent to the true ground state energy. M. Levy[48] provided a general mathematical derivation to prove it. For the system with N electrons under the exter-

nal potential (u_r), the Hamiltonian is $T[\rho] + \int \rho_r u_r d_r + V_{ee}[\rho]$ and for all N representable densities (ρ_r), those obtainable form some antisymmetric wave function $[\varphi_{r_1, r_2, r_3, \dots, r_n}]$, Levy defined the functional

$$F_\rho = \min_{\varphi \rightarrow \rho} \langle \varphi | T[\rho] + V_{ee}[\rho] | \varphi \rangle \quad (2.42)$$

where, the minimum is taken over all φ which gives the density (ρ_r).

E_{GS} , φ_{GS} and ρ_{GS} are used to represent total energy, wave function and density in ground state respectively. $\varphi_{min}^\rho(r)$ is the wave function which minimises F_ρ ; thus equation below becomes

$$F_\rho = \langle \varphi_{min}^\rho(r) | T[\rho] + V_{ee}[\rho] | \varphi_{min}^\rho(r) \rangle \quad (2.43)$$

Consider about F_ρ with external potential, inequality relation can be built up.

$$F_\rho + \int \rho_r u_r d_r = \langle \varphi_{min}^\rho(r) | T[\rho] + V_{ee}[\rho] + u | \varphi_{min}^\rho(r) \rangle \geq E_{GS} \quad (2.44)$$

Using the minimum property again, another inequality is shown in below.

$$\begin{aligned} E_{GS} &= \langle \varphi_{GS} | T[\rho] + V_{ee}[\rho] + u | \varphi_{GS} \rangle \\ &\leq \langle \varphi_{min}^{\rho_{GS}}(r) | T[\rho] + V_{ee}[\rho] + u | \varphi_{min}^{\rho_{GS}}(r) \rangle \end{aligned} \quad (2.45)$$

With the subtraction of the external potential, it is clear that

$$\langle \varphi_{GS} | T[\rho] + V_{ee}[\rho] | \varphi_{GS} \rangle \leq \langle \varphi_{min}^{\rho_{GS}}(r) | T[\rho] + V_{ee}[\rho] | \varphi_{min}^{\rho_{GS}}(r) \rangle \quad (2.46)$$

According to the definition of $\varphi_{min}^{\rho_{GS}}(r)$, it is correct that the reverse relation between two sides in equation below. Therefore, it is only possible under one condition.

$$\langle \varphi_{GS} | T[\rho] + V_{ee}[\rho] | \varphi_{GS} \rangle = \langle \varphi_{min}^{\rho_{GS}}(r) | T[\rho] + V_{ee}[\rho] | \varphi_{min}^{\rho_{GS}}(r) \rangle \quad (2.47)$$

Then equation below is built up.

$$\begin{aligned} E_{GS} &= \int \rho_{GS} u_r d_r + \langle \varphi_{GS} | T[\rho] + V_{ee}[\rho] | \varphi_{GS} \rangle \\ &= \int \rho_{GS} u_r d_r + \langle \varphi_{min}^{\rho_{GS}}(r) | T[\rho] + V_{ee}[\rho] | \varphi_{min}^{\rho_{GS}}(r) \rangle \end{aligned}$$

$$= \int \rho_{GS} u_r d_r + F[\rho_{GS}] \quad (2.48)$$

These two fundamental points are the contribution of Hohenberg-Kohn theorem and make it possible for the calculation of the properties of the system under ground state, through using the electron density.

2.2.6 Kohn-Sham equation

Different from Thomas-Fermi and Thomas-Fermi-Dirac models, Kohn and Sham did not adopt the direct approximation for kinetic energy of the system; instead, they treated the electronic system as a non-interacting electronic system, in which electrons move freely under an external potential (u_{ext}) and the Hamiltonian for the system is shown in the following equation[49].

$$\hat{H} = \sum_{i=1}^N \left(-\frac{1}{2} \nabla_i^2 \right) + \sum_{i=1}^N v(r_i) \quad (2.49)$$

Through the substitution of the non-interacting wave function ($= \frac{1}{\sqrt{N!}} \det\{\phi_1, \phi_2 \dots \phi_N\}$) into the Schrödinger's equation of non-interacting system, one electron equation below can be obtained and the density of the non-interacting system ($\rho_r = \sum_{i=1}^N |\phi_i(r)|^2$) is still equal to that of interacting system.

$$\hat{h}\phi_i = \left[-\frac{1}{2} \nabla_i^2 + v(r_i) \right] \phi_i \quad (2.50)$$

Since the exact kinetic energy functional (T) is not known, the exact kinetic energy ($T_s[\rho]$) of non-interacting system is used and the difference between them is referred as $T_c[\rho]$. F_ρ is written in equation below.

$$F_\rho = T_s[\rho] + T_c[\rho] + V_{ee}[\rho] = T_s[\rho] + J[\rho] + E_{xc}[\rho] \quad (2.51)$$

where, $J[\rho]$ is the classical Coulomb energy and $E_{xc}[\rho]$ is the exchange correlation energy.

The total energy of the interacting system can be written in equation below and through the variation, Euler equation 2.53 can be obtained.

$$E_\rho = T_s[\rho] + J[\rho] + E_{xc}[\rho] + \int \rho_r u_r d_r \quad (2.52)$$

$$\mu = \frac{\delta E_\rho}{\delta \rho} = u_r + \frac{\delta T_s[\rho]}{\delta \rho} + \frac{\delta J[\rho]}{\delta \rho} + \frac{\delta E_{xc}[\rho]}{\delta \rho} = \frac{\delta T_s[\rho]}{\delta \rho} + \beta_{KS}(r) \quad (2.53)$$

where, $\beta_{KS}(r) = u_r + v_j(r) + v_{xc}(r)$ is called Kohn-Sham potential, which is the sum of external potential (u_r), classical Coulomb potential (shown in equation 2.54) and the exchange-correlation potential (shown in equation 2.53).

$$v_j(r) = \frac{\delta J[\rho]}{\delta \rho} \quad (2.54)$$

$$v_{xc}(r) = \frac{\delta E_{xc}[\rho]}{\delta \rho} \quad (2.55)$$

Through applying the variation, the total energy can be described in equation below with the respect to one-electron orbitals (ϕ_i).

$$\begin{aligned} E_{\phi_i} = & \sum_{i=1}^N \int \langle \phi_i | -\frac{1}{2} \nabla^2 | \phi_i \rangle d_r + \frac{1}{2} \sum_{i=1}^N \sum_{j=1}^N \int \frac{|\phi_i(r)|^2 |\phi_j(r')|^2}{|r - r'|} d_r d_{r'} \\ & + \sum_{i=1}^N \int u_r |\phi_i(r)|^2 d_r + E_{xc} \end{aligned} \quad (2.56)$$

With the constraint of orthonormality of the orbital (ϕ_i), one electron equation can be expressed in the following equation.

$$\widehat{h}_{KS} \phi_i = \left[-\frac{1}{2} \nabla_i^2 + \beta_{KS}(r) \right] \phi_i = \sum_{i=1}^N \varepsilon_{ij} \phi_j \quad (2.57)$$

Since \widehat{h}_{KS} is Hermitian, the unitary transformation of the orbitals results in Kohn-Sham equations.

$$\left[-\frac{1}{2} \nabla^2 + \beta_{KS}(r) \right] \phi_i = \varepsilon_i \phi_i \quad (2.58)$$

2.2.7 Kohn-Sham equation with respect to spin[50]

Kohn-Sham equation can deal with the electronic system under scalar potential and build up the relation between the electron density and the scalar potential. In this section, a much more general situation is considered about and that is the system under vector potential, such as magnetic field. Under the magnetic field (B_r), the electron spin density, which indicates the difference between the density for the electron with spin up index (α) and that with spin down (β), was induced. Totally, there are two variables, electron density (ρ_r) and spin density (Q_r), within the three-dimensional space with

$$Q_r = \rho_r^\alpha - \rho_r^\beta \quad (2.59)$$

The Hamiltonian of the system is written in the following equation.

$$\hat{H} = -\frac{1}{2} \sum_i^N \nabla_i^2 + \sum_{i<j}^N \frac{1}{r_{ij}} + \sum_i^N u_{r_i} + 2\beta_e \sum_i^N B_r s_i \quad (2.60)$$

where $\beta_e = \frac{e\hbar}{2mc}$ is the Bohr magneton, while s_i is spin vector of i th electron.

The external potential operator, including nuclei potential (u_{r_i}) and magnetic field (B_r), can be written in equation below.

$$\hat{V} = \int u_r \hat{\rho}_r d_r - \int B_r \hat{m}_r d_r \quad (2.61)$$

where $\hat{\rho}_r = \sum_i^N \delta_{(r-r_i)}$ is the electron density operator; while $\hat{m}_r = -2\beta_e \sum_i^N s_i \delta_{(r-r_i)}$ is magnetisation density operator.

If the magnetic field is along the z axis, which is the projection of B_r on z direction and the integral is over the whole space, the expectation value of \hat{m}_r is written in equation below.

$$\begin{aligned} m_r &= -2\beta_e \langle \varphi \left| \sum_i^N s_z(i) \delta_{(r-r_i)} \right| \varphi \rangle = -2\beta_e \int s_z \delta_{(r-r')} \mathcal{Y}_1(x', x') d_{x'} \\ &= -2\beta_e \sum_{s=\alpha, \beta} s_z \mathcal{Y}(rs, rs) \end{aligned} \quad (2.62)$$

As $S = \pm \frac{1}{2}$, the expectation value of \hat{m}_r can be written in the following form.

$$m_r = -2\beta_e \left[\frac{1}{2} \gamma_1(r\alpha, r\alpha) - \frac{1}{2} \gamma_1(r\beta, r\beta) \right] = \beta_e [\rho_r^\beta - \rho_r^\alpha] \quad (2.63)$$

where, ρ_r is the expectation value for density operator and it equals $\langle \varphi | \hat{\rho}_r | \varphi \rangle$.

Then take minimum value of the total energy

$$\begin{aligned} E_0 &= \min \langle \varphi | \hat{T} + \hat{V}_{ee} + \sum_i^N u_{r_i} + 2\beta_e \sum b_{r_i} s_z(i) | \varphi \rangle \\ &= \min \left\{ \min \langle \varphi | \hat{T} + \hat{V}_{ee} | \varphi \rangle + \int [u_r \rho_r - b_r m_r] d_r \right\} \\ &= \min \left\{ F[\rho^\alpha, \rho^\beta] + \int [(u_r + \beta_e b_r) \rho_r^\alpha + (u_r - \beta_e b_r) \rho_r^\beta] d_r \right\} \end{aligned} \quad (2.64)$$

where, $F[\rho^\alpha, \rho^\beta] = \min \langle \varphi | \hat{T} + \hat{V}_{ee} | \varphi \rangle$

Equation above is the basis of the spin density functional theory[51]. However $F[\rho^\alpha, \rho^\beta]$ is still unknown and some approximations are applied to describe it.

First, $F[\rho^\alpha, \rho^\beta]$ can be expressed in equation below.

$$F[\rho^\alpha, \rho^\beta] = T_s[\rho^\alpha, \rho^\beta] + J[\rho^\alpha, \rho^\beta] + E_{xc}[\rho^\alpha, \rho^\beta] \quad (2.65)$$

where T_s and E_{xc} are the exact kinetic and exchange-correlation energy of the non-interacting electronic system respectively. They are unknown and should be approximated. The approximation for exact kinetic energy is introduced below; while that for exchange-correlation energy is introduced in section 2.3.

Perdew *et al.*[51] defined T_s through a tight binding Hamiltonian

$$T_s[\rho^\alpha, \rho^\beta] = \min \left[\sum_{i\sigma} n_{i\sigma} \int \phi_{i\sigma}^*(r) \left(-\frac{1}{2} \nabla^2 \right) \phi_{i\sigma}(r) d_r \right] \quad (2.66)$$

where, T_s is taken the minimum in the aggregate of $n_{i\sigma}$ and $\phi_{i\sigma}$. The constraint condition is written below.

$$\sum_i n_{i\alpha} |\phi_{i\alpha}(r)|^2 = \rho^\alpha(r) \text{ and } \sum_i n_{i\beta} |\phi_{i\beta}(r)|^2 = \rho^\beta(r) \quad (2.67)$$

Wave function is divided into space part and spin part separately (shown in equation 2.68). The occupation number ($n_{i\sigma}$) is zero, when the state is unoccupied, or one, when the state is occupied.

$$\varphi_i(rs) = \phi_{i\sigma}(r)\sigma(s) \quad (2.68)$$

Consider T_s reaches the minimum value so the total energy can be expressed by orbital wave function ($\phi_{i\sigma}$).

$$\begin{aligned} E[\rho^\alpha, \rho^\beta] &= \sum_{i\sigma} n_{i\sigma} \int \phi_{i\sigma}^*(r) \left(-\frac{1}{2}\nabla^2\right) \phi_{i\sigma}(r) d_r + J[\rho^\alpha, \rho^\beta] + E_{xc}[\rho^\alpha, \rho^\beta] \\ &\quad + \int [(u_r + \beta_e b_r)\rho_r^\alpha + (u_r - \beta_e b_r)\rho_r^\beta] d_r \end{aligned} \quad (2.69)$$

As the normalisation, Kohn-Sham equation can be written in the following equations.

$$\begin{aligned} \hat{h}_{eff}^\alpha \phi_{i\alpha}(r) &= \left[-\frac{1}{2}\nabla^2 + u_{eff}^\alpha(r)\right] \phi_{i\alpha}(r) = \frac{\varepsilon'_{i\alpha}}{n_{i\alpha}} \phi_{i\alpha}(r) \\ &= \varepsilon_{i\alpha} \phi_{i\alpha}(r) \quad (i = 1, 2, \dots, N^\alpha) \end{aligned} \quad (2.70)$$

$$\begin{aligned} \hat{h}_{eff}^\beta \phi_{j\beta}(r) &= \frac{\varepsilon'_{j\beta}}{n_{j\beta}} \phi_{j\beta}(r) \\ &= \varepsilon_{j\beta} \phi_{j\beta}(r) \quad (j = 1, 2, \dots, N^\beta) \end{aligned} \quad (2.71)$$

where, $\varepsilon'_{i\sigma}$ is the normalisation constraint Lagrangian multiplier for orbital wave function ($\phi_{i\sigma}$).

The potential relating to spin can be expressed 2.72.

$$u_{eff}^\alpha = u_r + \beta_e b_r + \int \frac{\rho_{r'}}{|r - r'|} d_r + \frac{\delta E_{xc}[\rho^\alpha, \rho^\beta]}{\delta \rho_r^\alpha} \quad (2.72)$$

$$u_{eff}^\beta = u_r - \beta_e b_r + \int \frac{\rho_{r'}}{|r - r'|} d_r + \frac{\delta E_{xc}[\rho^\alpha, \rho^\beta]}{\delta \rho_r^\beta} \quad (2.73)$$

$$N^\alpha = \int \rho_r^\alpha d_r \quad N^\beta = \int \rho_r^\beta d_r \quad N = N^\alpha + N^\beta \quad (2.74)$$

Exact solution for $T_s[\rho^\alpha, \rho^\beta]$ can be gained through solving equations above.

Actually, the kinetic function ($T_s[\rho^\alpha, \rho^\beta]$) consists of two spin quantities' contributions (shown in equation 2.75).

$$T_s[\rho^\alpha, \rho^\beta] = T_s[\rho^\alpha, 0] + T_s[0, \rho^\beta] \quad (2.75)$$

$$T_s[\rho^\alpha, 0] = \sum_{i\alpha} n_{i\alpha} \int \phi_{i\alpha}^*(r) \left(-\frac{1}{2} \nabla^2 \right) \phi_{i\alpha}(r) d_r \quad (2.76)$$

where, $T_s[0, \rho^\beta]$ has the similar format like $T_s[\rho^\alpha, 0]$.

2.2.8 Exchange-Correlation hole

As mentioned previously, exchange-correlation energy is the energy difference between the energy of real interacting system and that of the fictitious non-interacting system, if the external potential energy is not considered about. Scientists find many numerical approximations to evaluate this energy, which are discussed in section 2.3. Therefore, it is quite important to illustrate the physical meaning of exchange-correlation energy. This can be investigated through building up the interaction ($\frac{\lambda}{r-r'}$) within the system and λ varies from zero, which is for the non-interacting system, to one, which is for the physically interacting system. Then the Hamiltonian for the system under ground state can be expressed in equation below and it has the same electron density (ρ_r) over all λ numbers.

$$H_\lambda = -\frac{1}{2} \nabla^2 + u_{ext} + V_\lambda + \lambda V_{ee} \quad (2.77)$$

where, V_λ denotes the exchange correlation energy.

Then, the exchange-correlation energy of the real interacting system can be described in terms of the integral over the coupling constant λ .

$$E_{xc} = \frac{1}{2} \iint \frac{n_{xc}(r, r' - r)}{|r - r'|} d_r d_r \quad (2.78)$$

where, $n_{xc}(r, r' - r) \equiv \rho_{r'} \int_0^1 [g(r, r', \lambda) - 1] d\lambda$ and it is the exchange-correlation hole. $g(r, r', \lambda)$ is the pair-correlation function of the real system with electron density (ρ_r) and Coulomb interaction (λV_{ee}). $n_{xc}(r, r' - r)$ describes the effect of the inter-electronic repulsion, which indicates that one electron in position r reduces the probability of existence of another one in this same position. In other words, the exchange-correlation energy can also be regarded as the energy coming from the interaction between an electron and its exchange-correlation hole[52].

From the discussion above, it is clear that, since $g(r, r')$ tends to unity as $|r - r'|$ tends to ∞ , the separation into the electrostatic and exchange-correlation energy can be treated as the approximate separate of the consequence of long-range and short-range effects of the Coulomb interaction. This also means that the total exchange-correlation is not very sensitive to the density changes because the long-range interaction can be calculated in an exact formula.

Another point is that, with respect to the isotropic nature of the Coulomb interaction (V_{ee}) and through the variable substitution ($R \equiv r' - r$), equation below indicates that the exchange-correlation energy only depends on the spherical average part of $n_{xc}(r, R)$, thus the approximation can give a rather accurate value for this energy, even though the non-spherical part of $n_{xc}(r, R)$ is not accurate[50].

$$E_{xc} = \frac{1}{2} \int \rho_r d_r \int n_{xc}(r, R) d_\Omega \int_0^\infty \frac{R^2}{|R|} d_R \quad (2.79)$$

Last, according to the definition of the pair-correlation function, the sum rule requires that the exchange-correlation should contain one electron (shown in equation 2.80), which means that $-n_{xc}(r, r' - r)$ can be regarded as the normalised weight factor and it indicates the radius of the exchange-correlation hole (shown in equation 2.79).

$$\int n_{xc}(r, r' - r) d_{r'} = -1 \quad (2.80)$$

$$\left\langle \frac{1}{R} \right\rangle_r = - \int \frac{n_{xc}(r, R)}{|R|} d_r \quad (2.81)$$

Equation 2.81 results in the following relation.

$$E_{xc} = -\frac{1}{2} \int \left\langle \frac{1}{R} \right\rangle_r n_r d_r \quad (2.82)$$

This equation indicates that the exchange-correlation energy does not strongly rely on n_{xc} too much.

2.3 Approximation for Exchange-Correlation Energy (E_{xc})

As discussed in section 2.2, the description of Kohn-Sham scheme for the total energy of the system consists of four parts, which include exact kinetic energy for non-interacting electrons, external potential energy, Hartree potential energy and exchange-correlation energy (E_{xc}), and only E_{xc} is unknown. Approximations were made to express this value and, generally, there are three most commonly used approximations. One is local density approximation (LDA), another is generalised gradient approximation (GGA) and another one is hybrid functional. LDA and GGA are, hereby, discussed with more details.

2.3.1 Local density approximation (LDA)

The central idea of this approximation is to treat the electronic system as a number of electrons moving under a background charge distribution such that the whole ensemble is electrically neutral[53]. In 1965, Kohn and Sham used this method to calculate E_{xc} value, which is shown in equation 2.83.

$$E_{xc}^{LDA}[\rho] = \int \rho_r \varepsilon_{xc}(\rho) d_r \quad (2.83)$$

where, ε_{xc} is the exchange-correlation energy per electron within the uniform electron gas with the density ρ_r . The energy per electron is weighted with probability (ρ_r) that there is an electron at this position in space. The corresponding exchange-correlation potential is expressed in the following equation.

$$v_{xc}^{LDA}[r] = \frac{\delta E_{xc}^{LDA}}{\delta \rho_r} = \varepsilon_{xc}[\rho_r] + \rho_r \frac{\partial \varepsilon_{xc}[\rho_r]}{\partial \rho} \quad (2.84)$$

Therefore, Kohn-Sham equation can be expressed in equation 2.85 that is the famous localised density functional equation.

$$\left[-\frac{1}{2}\nabla^2 + u_r + \int \frac{\rho_{r'}}{|r-r'|} d_{r'} + v_{xc}^{LDA}(r) \right] \phi_i = \varepsilon_i \phi_i \quad (2.85)$$

$\varepsilon_{xc}[\rho_r]$ consists of two quantities.

$$\varepsilon_{xc}[\rho_r] = \varepsilon_x[\rho_r] + \varepsilon_c[\rho_r] \quad (2.86)$$

where, $\varepsilon_x[\rho_r]$ and $\varepsilon_c[\rho_r]$ denotes the exchange and correlation parts.

In late 1920's, Bloch and Dirac[54] derived the approximation for $\varepsilon_{xc}[\rho_r]$ and this exchange functional is often called Slater exchange.

$$\varepsilon_x[\rho_r] = -C_x \rho_r^{1/3} \quad (2.87)$$

where, $C_x = \frac{3}{4} \left(\frac{3}{\pi} \right)^{1/3}$

The accurate solution for correlation part ($\varepsilon_c[\rho_r]$) was found by Ceperley and Alder[55] in Quantum Monte Carlo simulation for homogeneous electron gas.

$$\varepsilon_c[\rho_r] = E_\rho - T_s(\rho) - E_x(\rho) \quad (2.88)$$

Here, $\varepsilon_{xc}[\rho_r]$ is known as long as the electron density of the system is obtained and Lee-Yang-Parr model for LDA is introduced. In 1987, Yang *et al.*[56] built up the relationship between electron density and localised Kohn-Sham potential. According to Thomas-Fermi model, equation below can be built up.

$$\rho_{TF}(r) = \left\{ \frac{3}{5C_F} [\mu - v_{eff}(r)] \right\}^{3/2} \quad (2.89)$$

Consider spin balance system, atomic or molecule closed-shell system, the electron density (ρ_r) of system under ground state is the sum of orbital density in space and can be expressed in the equation 2.90.

$$\begin{aligned} \rho(r,r') &= 2 \sum_i^{N/2} \phi_i(r) \phi_i^*(r') = 2 \sum_i^{\infty} \phi_i(r) \phi_i^*(r') \eta(\varepsilon_F - \varepsilon_i) \\ &= 2 \langle r | \eta(\varepsilon_F - \hat{h}_{eff}) | r' \rangle \end{aligned} \quad (2.90)$$

where, 2 denotes the electron occupancy number in orbits, $\eta(x)$ is Heaviside step function, ε_i is the eigenvalue of Hamiltonian (\hat{h}_{eff}) in Kohn-Sham scheme, $\phi_i(r)$ is the eigenfunction and ε_i is Fermi energy level.

Through deduction, electron density can be expressed in equation 2.91.

$$\rho_q(r, r') = 2 \int \dots \int \left(\frac{qk_q}{\hbar^2} \right)^{3q/2} J_{3q/2}(k_q l_q) \eta(k_q^2) d_{r_1} \dots d_{r_{q-1}} \quad (2.91)$$

where, $k_q^2 = \frac{2m}{\hbar^2} \left[\varepsilon_F - \frac{1}{q} \sum_{j=0}^{q-1} \mu(r_{r+1}, r_j) \right]$ and $l_q^2 = q \sum_{j=0}^{q-1} (r_{j+1} - r_j)^2$

Then, the exchange correlation can be calculated based on this electron density.

2.3.2 Local spin density approximation (LSDA)

In respect to electron spin, LDA can be extended to unrestricted case, namely spin polarisation, and as mentioned in section 2.3.1, the exchange-correlation energy can be split into two parts, which are exchange and correlation energy respectively, and can be dealt with separately.[57]

Oliver *et al.*[58] deducted the formula of exchange energy (E_x)

$$E_x(\rho^\alpha, \rho^\beta) = \frac{1}{2} E_x(\rho^\alpha, \rho^\beta) + \frac{1}{2} E_x(\rho^\alpha, \rho^\beta) = \frac{1}{2} E_x^0(2\rho^\alpha) + \frac{1}{2} E_x^0(2\rho^\beta) \quad (2.92)$$

where, ρ^α and ρ^β are spin up and spin down electron density respectively.

Combine equation below with Dirac local density approximation, local spin density approximation for E_x can be written in equation 2.93.

$$E_x^{LSDA}[\rho^\alpha, \rho^\beta] = 2^{1/3} C_x \int \left[(\rho^\alpha)^{4/3} + (\rho^\beta)^{4/3} \right] d_r \quad (2.93)$$

In 1972, Von Barth and Hedin[59] defined a spin-polarised parameter (ξ); hence, the spin up and spin down density can be expressed by ξ .

$$\xi = \frac{\rho^\alpha - \rho^\beta}{\rho} = \frac{\rho^\alpha - \rho^\beta}{\rho^\alpha + \rho^\beta}, \quad \rho^\alpha = \frac{(1 + \xi)\rho}{2}, \quad \rho^\beta = \frac{(1 - \xi)\rho}{2} \quad (2.94)$$

Substitute these two equations, E_x can be expressed equation 2.95.

$$\begin{aligned} E_x^{LSDA}[\rho^\alpha, \rho^\beta] &= \frac{1}{2} C_x \int \rho^{4/3} \left[(1 + \xi)^{4/3} + (1 - \xi)^{4/3} \right] d_r \\ &= \int \rho \varepsilon_x(\rho, \xi) d_r \end{aligned} \quad (2.95)$$

where, $\varepsilon_x(\rho, \xi) = \varepsilon_x^0(\rho) + [\varepsilon_x^1(\rho) - \varepsilon_x^0(\rho)] f_\xi$, f_ξ is the weight element and its value ranges from zero to one. $f_\xi = \frac{1}{2} (2^{1/3} - 1)^{-1} \left[(1 + \xi)^{4/3} + (1 - \xi)^{4/3} - 2 \right]$

As correlation energy (E_c) concerned, it can be written in equation 2.96.

$$E_c^{LSDA}[\rho^\alpha, \rho^\beta] = \int \rho \varepsilon_c(\rho, \xi) d_r \quad (2.96)$$

Local density approximation (LDA) or local spin density approximation (LSDA) are only accurate for simple physical model, such as homogeneous electron gas or the system with the density varying very slowly. However, most of the real systems are rather complex and their density varies rapidly.

2.3.3 Generalized gradient approximation (GGA)

Compared with LDA or LSDA, generalized gradient approximation (GGA) is more advanced, in term of consider non-uniform electron gas, which is the situation for most of the real systems[60, 61].

In 1986, Perdew and Wang[62] proposed that the exchange-correlation energy of the system not only depends on the electron density but also depends on the gradient of the density and they revised LSDA method (shown in equation 2.95). This method is also called GGA-I or PW86.

$$\varepsilon_x^{PW86} = \varepsilon_x^{LSDA} (1 + ax^2 + bx^4 + cx^6)^{1/5} \quad (2.97)$$

where, $x = \frac{|\nabla\rho|}{\rho^{4/3}}$ and a , b and c are constants.

Additionally, Perdew[63] also made revision to correlation energy in LSDA.

$$\varepsilon_c^{PW86} = \varepsilon_c^{LSDA} + \Delta\varepsilon_c^{PW86}, \quad \varepsilon_c^{PW86} = \frac{e^\phi C_\rho |\nabla\rho|^2}{f_\zeta \rho^{7/3}} \quad (2.98)$$

$$\text{where } f_\zeta = 2^{1/3} \sqrt{\left(\frac{1+\zeta}{2}\right)^{5/3} + \left(\frac{1-\zeta}{2}\right)^{5/3}} \text{ and } \phi = a \cdot \frac{c_\infty |\nabla\rho|}{C_\rho \rho^{7/6}}$$

In 1991, Perdew and Wang[64] proposed GGA-II, which is also called PW91. Exchange-correlation energy in LSDA can be written equation 2.99.

$$E_{xc}^{LSDA}[\rho_\alpha, \rho_\beta] = \int \rho \varepsilon_{xc}(r_s, \zeta) d_r^3 \quad (2.99)$$

where, $\rho_r = \rho_\alpha + \rho_\beta$ and ρ_α, ρ_β are spin-up and spin-down density respectively; $r_s = \left(\frac{3}{4\pi\rho}\right)^{1/3}$ and it is the local radius; $\zeta = (\rho_\alpha - \rho_\beta)/\rho$ is local polarization; $\varepsilon_{xc}(r_s, \zeta)$ is the exchange-correlation energy per particle in uniform electron gas.

GGA method defines local radius function (r_s). The exchange-correlation energy is expressed in equation 2.100.

$$E_{xc}^{GGA}[\rho_\alpha, \rho_\beta] = \int f(\rho_\alpha, \rho_\beta, \nabla\rho_\alpha, \nabla\rho_\beta) d_r^3 \quad (2.100)$$

Some semi-empirical parameters are induced into the exchange energy so as to enhance the accuracy.

$$E_x^{PW91}[\rho] = \int \rho \varepsilon_x(r_s, 0) F_s d_r^3 \quad (2.101)$$

where, $\varepsilon_x(r_s, 0) = -\frac{3k_F}{4\pi}$; k_F is local Fermi wave vector and equals $\frac{1.91916}{r_s}$; $F_s = 1 + 0.124s^2 + s^4$; $s = \frac{|\nabla\rho|}{2k_\rho\rho}$.

The correlation energy can be expressed in the following equation 2.102.

$$E_c^{PW91}[\rho_\alpha, \rho_\beta] = \int \rho [\varepsilon_c(r_s, \zeta) + H(t, r_s, \zeta)] d_r^3 \quad (2.102)$$

where, $t = \frac{|\nabla\rho|}{2gk_\rho}$; $g = \frac{1}{2}[(1 + \zeta)^{2/3} + (1 - \zeta)^{2/3}]$ is another probability gradient; $k_s = \left(\frac{4k_F}{\pi}\right)^{1/2}$ is local-screened wave vector and $H = H_0 + H_1$.

$$H_0 = g^3 \frac{\beta^3}{2\alpha} \cdot \ln \left[1 + \frac{2\alpha}{\beta} \cdot \frac{t^2 + At^4}{1 + At^2 + A^2t^4} \right] \quad (2.103)$$

where, $\alpha = 0.09$; $\beta = vC_c(0)$; $v = \frac{16}{\pi} \left(\frac{3}{\pi^2}\right)^{1/3}$; $C_c(0) = 0.004235$; $C_x = -0.001667$;

$$A = \frac{2\alpha}{\beta} \cdot \frac{1}{\exp\left[\frac{-2\alpha\varepsilon_c(r_s, \zeta)}{g^3\beta^2}\right] - 1}$$

$$H_1 = v \left[C_c(r_s) - C_c(0) - \frac{3}{7}C_x \right] g^3 t^2 \times \exp \left[-100g^4 \frac{k_s^2}{k_F^2} t^2 \right] \quad (2.104)$$

Correlation energy can be approximated in equation 2.105.

$$\begin{aligned} & \Delta E_c[\rho^\alpha, \rho^\beta] \\ & \approx C_c(0) \int \rho \left\{ \frac{-0.458\zeta\nabla\zeta}{[\rho(1-\zeta^2)]^{1/3}} \cdot \frac{\nabla\rho}{\rho} + \frac{(-0.037 + 0.1\zeta^2)|\nabla\zeta|^2}{\rho^{1/3}(1-\zeta^2)} \right\} d_{r^3} \end{aligned} \quad (2.105)$$

2.4 Introduction to VASP Code

All the PhD research works were carried out using VASP (Vienna Ab initio Simulation Package) code in the version of 5.4[65-67], which is a copyright-protected commercial code and the copyright belongs to University of Vienna. It is necessary to make a concrete introduction to it with more details, including its brief history, its background theory, the tasks it can do, parameters for the calculation with setting rule and how to adjust the parameters to guarantee the calculation goes well. Different pseudopotentials for the calculation in this module are also introduced.

VASP was based on code written by Mike Payne (then at MIT) and it was then brought to the University of Vienna, Austria, in July 1989 by Jürgen Hafner. The main program was written by Jürgen Furthmüller, who joined the group at the Institut für Materialphysik in January 1993, and Georg Kresse. VASP is currently being developed by Georg Kresse; recent additions include the extension of methods frequently used in molecular quantum chemistry (such

as MP2 and CCSD(T)) to periodic system. VASP is currently used by more than 1400 research groups in academia and industry worldwide on the basis of software licence agreements with the University of Vienna.[68]

VASP is a density functional code that uses plane waves and pseudopotentials to deal with the quantum calculations. It is applicable for the calculation of system with periodic structure and the formal procedure for the calculation is followed by three steps.[69]

2.5 Pseudopotential

Plane waves and pseudopotentials are used in VASP code for the expansion of the wave function so as to conduct the DFT calculation. It plays crucial role in the computation, which is based on the plane wave basis set, for the system. This section introduces its conception, its different types and its applications.

2.5.1 Introduction to Pseudopotentials

Scientists usually concern about the behaviour of valence electrons, which affects the material's chemical property, such as bonding between atoms and redox character of the compound, rather than those within the ion core, so the wave function is built up to describe the behaviour of valence electrons and used in the computation of property of material. However, the wave function of valence electrons oscillates very fast, due to the fact that it is orthogonal to that of the electrons in ion core, and, according to Fourier Transform (FT), the number of basis set used to expand the wave function can become very large so that the computational work for the computer can be exceedingly large as well, resulting in the 'out-of-RAM' problem and thus, the failure of the computation. It becomes quite necessary to solve the fast oscillation problem of the wave function and one way is to use an effective potential, which varies slowly within the ion core, to substitute the real potential to avoid the huge amount of basis set problem induced by FT method[70]. To substitute the real potential, pseudo potential must satisfy two conditions:

(1) Outside the ion core region, pseudopotential must give identical wave function that is given by genuine one.

(2) Inside the ion core region, pseudopotential must make the wave function that has no node[71].

The expression for pseudopotential is written in equation 2.106.

$$V_{PS} = V_{LOCAL} + V_{NL} \quad (2.106)$$

where, V_{LOCAL} and V_{NL} are local and non-local part of the pseudopotential respectively.

$$V_{NL} = \sum |lm\rangle V_1 \langle lm| \quad (2.107)$$

where, $|lm\rangle$ are the spherical harmonics and V_1 is the pseudopotential for angular momentum l .

When the pseudopotential uses the same potential in each angular momentum channel, it is called local pseudopotential, which has much higher computational efficiency, and the calculation for some elements can reach rather accuracy. Non-local pseudopotential does not depend on the angular momentum too much.

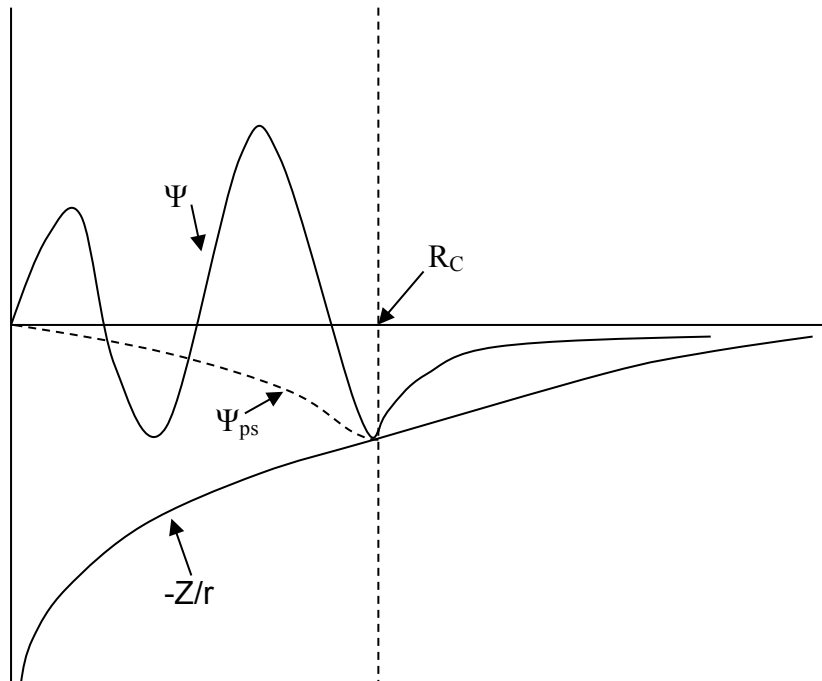


Fig. 2.7 Schematic representation of the all-electron (Ψ), pseudized (Ψ_{ps}) wave functions and potential

The hardness is an important parameter in the application of pseudopotential and when a pseudopotential can be expressed with not too many Fourier components to an accurate description, it is called soft pseudopotential and hard one otherwise. Here, two typical pseudopotentials, which relate to different hardness, are introduced.

2.5.2 Norm-Conserving Pseudopotential

Norm Conserving pseudofunctions are normalized and are solutions of a model potential chosen to reproduce the valence properties of an all electron calculation. Defining norm-conserving pseudopotential is the list of requirements for a ‘good’ *ab initio* pseudopotential given by Hamann *et al.*[72]

1. All-electron and pseudo valence eigenvalues agree for the chosen atomic reference configuration.
2. All-electron and pseudo valence wavefunctions agree beyond a chosen core radius (R_c).
3. The logarithmic derivatives of the all-electron and pseudo wavefunctions agree at R_c .
4. The integrated charge inside R_c for each wavefunction agrees norm conservation.
5. The first energy derivative of the logarithmic derivatives of the all-electron and pseudo wavefunctions agrees at R_c .

These five points show way to generate norm-conserving pseudopotential; especially, the last point is the crucial step toward the goal of constructing a ‘good’ pseudopotential. The radial equation for a spherical atom or ion can written in equation (2.108)

$$-\frac{1}{2}\phi_l''(r) + \left[\frac{l(l+1)}{2r^2} + V_{eff}(r) - \varepsilon \right] \phi_l(r) = 0 \quad (2.108)$$

where, the prime means derivative with respect to r and it can be transformed by defining the variable $x_l(\varepsilon, r)$.

$$x_l(\varepsilon, r) \equiv \frac{d}{dr} \ln \phi_l(r) = \frac{1}{r} [D_l(\varepsilon, r) + 1] \quad (2.109)$$

Through deduction, one finds at radius R

$$\frac{\partial}{\partial \varepsilon} x_l(\varepsilon, R) = -\frac{1}{\phi_l(R)^2} \int_0^R dr \phi_l(r)^2 = -\frac{Q_l(R)}{\phi_l(R)^2} \quad (2.110)$$

This points out that if ϕ_l^{PS} has the same magnitude as the all-electron function ϕ_l at R_c and obeys norm-conservation, the first energy derivative of the logarithmic derivative $x_l(\varepsilon, R)$ and $D_l(\varepsilon, R)$ is the same as for the all-electron wavefunction.

2.5.3 Ultrasoft Pseudopotential

One goal of pseudopotential is to create pseudopotentials as smooth as possible; while keep the accuracy. As discussed in section 2.5.1, the valence functions are expanded in Fourier components in plane wave calculation; thus, the definition of smoothness is to minimize the range in Fourier space required to describe the valence properties to a given accuracy. Although norm-conserving pseudopotentials achieve the goal of accuracy, it scarifies ‘smoothness’.

In 1990, Vanderbilt[71] proposed another pseudopotential that is much softer than Norm-Conserving pseudopotential. It reaches the goal of accurate calculation by a transformation that re-expresses the problem in terms of a smooth function and an auxiliary function around each ion core that represents the rapidly varying part of the density. Thus, the wavefunctions are nodeless and extended into the core region.

The non-local part in ultrasoft pseudopotential can be expressed in equation 2.111.

$$V_{NL} = \sum_{nm,I} D_{nm}^0 |\beta_n^I\rangle\langle\beta_m^I| \quad (2.111)$$

where, projector β and coefficient D^0 characterize the pseudopotential and differ for different atomic species. Index I denote the position of an atom. For each referenc atomic states (n), the smooth functions ($\widetilde{\Psi}_n$) are the solutions of the generalized eigenvalue problem.

$$[\widehat{H} - \varepsilon_s \widehat{S}] \widetilde{\Psi}_n = 0 \quad (2.112)$$

with $\widehat{H} = -\frac{1}{2}\nabla^2 + V_{LOCAL} + \delta\widehat{V}_{NL}^{US}$ and \widehat{S} an overlap operator

$$\widehat{S} = \widehat{1} + \sum_{n,m} \Delta Q_{nm} |\beta_n^I\rangle\langle\beta_m^I| \quad (2.113)$$

The eigenvalues (ε_n) agree with all-electron calculation at as many energies n as desired. The full density can be constructed from the functions $\Delta Q_{nm}(r)$ which can be replaced by a smooth version of the all-electron density.

The advantages of relaxing the norm-conservation condition ($\Delta Q_{nm} = 0$) is that each smooth pseudofunction ($\widetilde{\Psi}_n$) can be formed independently with only the constraint of matching the value of the functions $\widetilde{\Psi}_n(R_c) = \Psi_n(R_c)$ at the radius R_c . Therefore, ultrasoft technique can choose a larger R_c than norm-conserving pseudopotential; while maintain the desired accuracy by adding the auxiliary functions $\Delta Q_{nm}(r)$ and the overlap operator \hat{S} .

In the calculation that uses ultrasoft pseudopotential the solutions for the smooth functions are orthonormalized according to equation (2.114)

$$\langle \widetilde{\Psi}_n | \hat{S} | \widetilde{\Psi}_m \rangle = \delta_{ij} \quad (2.114)$$

and the valence density is defined to be

$$n(r) = \sum_{nm}^{occ} \widetilde{\Psi}_n^*(r) \widetilde{\Psi}_m(r) + \sum_{nm} \rho_{nm} \Delta Q_{nm}(r) \quad (2.115)$$

where,

$$\rho_{nm} = \sum_n^{occ} \langle \widetilde{\Psi}_n | \beta_s \rangle \langle \beta_s | \widetilde{\Psi}_n \rangle \quad (2.116)$$

The solution is found by minimizing the total energy

$$E_{total} = \sum_n^{occ} \left\langle \widetilde{\Psi}_n \left| -\frac{1}{2} \nabla^2 + V_{LOCAL}^{ion} + \sum_{nm} D_{nm}^{ion} \left| \beta_s \right\rangle \langle \beta_{s'} | \right| \widetilde{\Psi}_n \right\rangle + E_{Hartress} + E_{II} + E_{xc} \quad (2.117)$$

Finally, it leads to the generalized eigenvalue problem

$$\left[-\frac{1}{2} \nabla^2 + V_{LOCAL} + \delta \hat{V}_{NL}^{US} - \varepsilon_n \hat{S} \right] \widetilde{\Psi}_n = 0 \quad (2.118)$$

2.6 Projector Augmented Wave Method

Besides using the pseudopotential to replace real potential within the ion core region, another alternative method is to transform these rapidly oscillating wave functions into smooth wave functions, which are easy for the computation and it gives another option to compute all-electron properties from these smooth wave functions. It is called projector augmented wave (PAW) method, which can be viewed as the generalization of the pseudopotential and linear augmented plane wave method for the much more efficient computation by DFT.[74] In this PhD work, PAW method was adopted to account the behaviour of in-core electrons and provides accurate properties of materials; so it is necessary to introduce it below.

The linear transformation operator (T) transforms the fictitious pseudo wave function (Ψ) to the all electron wave function ($\tilde{\Psi}$).

$$|\Psi\rangle = T|\tilde{\Psi}\rangle \quad (2.119)$$

Here, all electron wave function is a Kohn-Sham single particle wave function; rather than the many body wave function, and to differentiate them near the in-core region, the transformation operator is written in the following format.

$$T = 1 + \sum_R \hat{T}_R \quad (2.120)$$

where, \hat{T}_R is non zero only within the spherical augmentation region (Ω_R), which encloses atom (R).

The pseudo wave function is expanded into the pseudo partial waves in the region (Ω_R) which surrounds each atom.

$$|\tilde{\Psi}\rangle = \sum_i c_i |\tilde{\phi}_i\rangle \quad (2.121)$$

Because the operator T is linear the coefficient c_i could be written as an inner product with a set of so-called projector function (p_i).

$$c_i = \langle p_i | \tilde{\Psi} \rangle \quad (2.122)$$

where, $\langle p_i | \tilde{\phi}_j \rangle = \delta_{ij}$.

The all electron partial wave ($|\phi_i\rangle = T|\hat{\phi}_i\rangle$) is the solution for the Kohn-Sham Schrödinger equation for the isolated atom. The transformation operator (T) can be expressed in the equation 2.123.

$$T = 1 + \sum_i (|\phi_i\rangle - |\tilde{\phi}_i\rangle)\langle p_i| \quad (2.123)$$

Within the spherical region, pseudo partial waves and all electron waves need to be smooth continuation; while, beyond the augmentation regions, they are identical to each other.

Furthermore, PAW method provides a way to compute the all electron observables using the pseudo-wave function from a pseudopotential calculation, which could avoid the representation of all-electron wave function in memory. Taking an operator (\hat{A}) as an example, the expectation value could be written in the following format.

$$a_i = \langle \Psi | \hat{A} | \Psi \rangle \quad (2.124)$$

where, the pseudo wavefunction could be used to replaced

$$a_i = \langle \tilde{\Psi} | T^+ \hat{A} T | \tilde{\Psi} \rangle \quad (2.125)$$

from which, the pseudo operator could be defined

$$\tilde{A} = T^+ \hat{A} T \quad (2.126)$$

If the operator is local and well-behaved, it can be expanded through the PAW operator transformation.

$$\tilde{A} = \hat{A} + \sum_{i,j} |p_i\rangle (\langle \phi_i | \hat{A} | \phi_j \rangle - \langle \tilde{\phi}_i | \hat{A} | \tilde{\phi}_j \rangle) \langle p_i| \quad (2.127)$$

where, the indices i and j run over all projectors on all atoms.

2.7 Spin Orbit coupling Effect

The band inversion in the band structure for TI mainly results from the strong spin orbit coupling (SOC) effect and it was included in all DFT calculations for the electronic properties for Bi_2Se_3 family TI; it is therefore necessary to make a brief introduction for it.

SOC effect has been implemented in many DFT codes and it is naturally incorporated in the pseudopotential approximation, since the main contribution of SOC to valence electrons comes from the in-core region.

The following procedure is the generation of angular momentum (j) dependent fully relativistic pseudopotential.

(1) Self consistent calculation without relativistic pseudopotential was performed and the Dirac equation was solved, yielding two relativistic pseudopotentials ($V_{l+1/2}$ and $V_{l-1/2}$) for $l>0$ case and one ($V_{l+1/2}$) for $l=0$ case.

(2) Pseudopotential for each l was computed again for $V_{l+1/2}$ and $V_{l-1/2}$ so that the Schrödinger equation with such pseudopotential has the same eigen value and wave function tails outside the cutoff radii as those of the original Dirac equation

Kleinman, Bachelet and Schlüter[74] showed that from fully relativistic j -dependent semilocal pseudopotential, the j -averaged, l -dependent semilocal one can be defined.

$$V_l^{SO} = \frac{2}{2l+1} [V_{l+1/2} - V_{l-1/2}] \quad (2.128)$$

Then, an additional term is added into Hamiltonian

$$\hat{H}^{SO} = \sum_{l,s} |ls\rangle V_l^{SO}(r) L \cdot S \langle ls| \quad (2.129)$$

where, $|ls\rangle\langle ls|$ is the projector on the tensor product $L \otimes S$ of function for a given angular momentum times the spin space and L/S are the orbital/spin angular momentum operator.

Kleinman and Bylander (KB)[75] proposed the scheme to transform the semilocal pseudopotential to a separable form and the total ionic pseudopotential operator including the SOC part is expressed in equation 2.130.

$$\hat{V}_{ps}^{ion}(r, r') = \sum_l |ls\rangle V_l^{SR}(r, r') \langle ls| + \sum_l |ls\rangle V_l^{SO}(r, r') \langle ls| \quad (2.130)$$

where, V_l^{SR} and V_l^{SO} are scalar relativistic (SR) and spin-orbit interaction (SO) and they are assumed to have following KB separable forms.

$$V_l^x(r, r') = f_l^x(r) E_l^{KB,x} f_l^x(r') \quad (2.131)$$

where, $E_l^{KB,x}$ is the KB energy and x is SR/SO.

For SR part, the spinor plane-wave matrix element is expressed in equation 2.132.

$$V_l^{SR}(K\sigma, K'\sigma') = \frac{4\pi}{\Omega} (2L+1) \delta_{\sigma\sigma'} E_l^{KB,SR} P_l(\cos\gamma) f_l^{SR}(K) f_l^{SR}(K') \quad (2.132)$$

where, $P_l(\cos\gamma)$ is the Legendre polynomial of the angle (γ) between different wave vectors;

$$f_l^{SR}(K) = \int_0^\infty \int_l^{SR}(r) j_l(Kr) r^2 dr$$

For the SO part, the matrix element is written in the following format.

$$V_l^{SO}(K\sigma, K'\sigma') = -i \frac{4\pi}{\Omega} (2L+1) E_l^{KB,SO} P'_l(\cos\gamma) f_l^{SO}(K) f_l^{SO}(K') \\ \times \left(\langle \sigma | S | \sigma' \rangle \cdot \frac{K \times K'}{KK'} \right) \quad (2.133)$$

where, P'_l is the first derivative of P_l .

2.8 Parameters for the Computation

Using VASP code to conduct the computation requires researcher to set up and adjust the parameters to guarantee the convergence and accuracy for the computation. These parameters also affect the computational time. Usually convergence, accuracy, time are three key objects under researcher's concern and they are closely related to each other; therefore it is quite important to understand their physical meaning and how they affect the computation. In this section, a series of parameters, which include energy cutoff value, k point, FFT grid and SCF tolerance, are introduced with more details.

2.8.1 Cutoff Energy

2.8.1.1 Bloch's theorem

Density Functional Theory (DFT) method eases the calculation but handling the system with infinite number of electrons under the static potential of an infinite number of ions still remains a difficult problem. Two issues must be solved. First, the wave function should be calculated for each of the infinite number of electrons within the system. Second, due to the fact that each electronic wave function extends throughout the whole solid material, the number of basis set that is used to expand the electronic wave function becomes infinitely large as well. These two problems exist in computation for periodic system and result in the conclusion that the computation is impossible to finish. Therefore, it is crucial solve them so as to guarantee the computation.

In 1976, Felix Bloch[73] proposed a specific function, which is named as Bloch wave, to represent the wave function for the particle so as to solve the computational difficulty and according to this theorem, the wave function for description of the electrons within the periodic solid can be re-written as the product of two parts: one is a cell periodic part and the other one is a wave-like part.

$$\Psi_i(r) = e^{ikr} u_i(r) \quad (2.134)$$

where, k is the wave vector and equation 3.135 is also called Bloch's function.

The cell periodic part of the Bloch wave can be expanded by a basis set that consists of a discrete set of plane waves whose wave vectors are reciprocal lattice vectors of the crystals.

$$u_i(r) = \sum_G C_{i,G} e^{iGr} \quad (2.135)$$

where, G is the reciprocal lattice vector and is defined in the equation 2.136.

$$G \cdot l = 2\pi m \quad (2.136)$$

where, l is a lattice vector of the crystal and m is an integer.

The wave function for electron can be expressed by the sum of plane waves.

$$\Psi_i(r) = \sum_G C_{i,k+G} e^{i(k+G)\cdot r} \quad (2.137)$$

2.8.1.2 Cutoff Energy

The reciprocal lattice represents another lattice which is obtained from Fourier transform of the crystal lattice in reality and the first Brillouin zone is a uniquely defined primitive cell in this reciprocal space. The locus of points in reciprocal space that are closer to the origin of the reciprocal lattice than they are to any other reciprocal lattice points defines the first Brillouin zone. In DFT calculation based on VASP code, all quantities; such as total energy or electron density, are obtained through computing the integral of expectation value of the observables within the first Brillouin zone. In reality, the integral calculation is replaced by the sum of expectation value on a set of discrete k points and this procedure is called k point sampling. The wave function at every k point can be expanded by a series of discrete plane wave basis set and theoretically, the number of basis set should be infinitely large, but this is not necessary. Only the coefficient ($C_{i,k+G}$) for the plane wave with small kinetic energy ($\left(\frac{\hbar^2}{2m}\right) \cdot |k + G|^2$) are much more important than those with large kinetic energy because the expectation value of observables only changes little when the plane wave with large kinetic energy has more basis set for expansion. Therefore, the series of plane basis set can be truncated to only take into account of those that have kinetic energies less than a particular value, which is cutoff energy and set up by researcher, and this makes the computation possible. In other words, the application of Bloch's theorem and cutoff energy produces the finite basis set to expand the wave function for electrons. Fig. 2.8 shows the schematic representation of cutoff used for the truncation of the basis set and the radius of the sphere is proportional to the square root of the cutoff energy ($E_{cut} = G_{max}^2 / 2$).

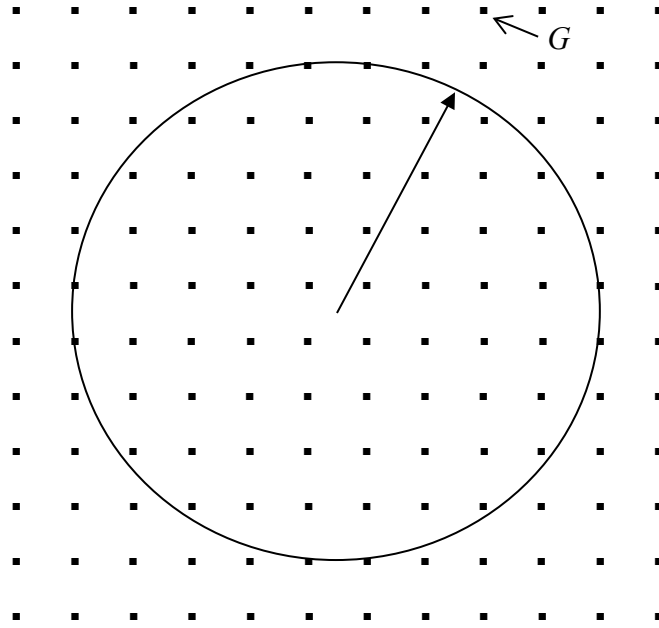


Fig. 2.8 Schematic representation of the cutoff energy

The application of cutoff energy to truncate the basis set is actually an approximate method and theoretically, more basis set used, more accurate results can be achieved. This means that error in the total energy exists and increase the number of basis set by using larger cutoff energy value can minimise this error. The cutoff energy value should be increased until the computation reach convergence but large value also means that the computational time is prolonged.

Another point regarding this technology is that the number of basis states does not change continuously with cutoff energy. The discontinuities occur at different cutoff energy for different k point. At a fixed cutoff energy, the alternation in size and shape of the computational object can result in the discontinuities in the plane wave basis set as well. Although using a denser k point sampling can reduce this discontinuity, this problem still exists even with very dense k points. To solve this problem, Francis and Payne[76] induced a correction factor to account for the difference between the number of a state in a basis set with an infinitely large number of K points and the number of basis state that is used for computation.

The finite basis set correction is quite important for the cell optimisation with a basis set that is not converged. When applied to the total energy calculation, the correction enables researcher to carry out computation with a fixed number of basis states and to interpolate the

results if more physical conditions of a fixed cutoff energy are used. The parameter for this correction is $(dE_{tot}/d \ln E_{cut})$ and E_{tot} is the total energy of the system, while E_{cut} is the cutoff energy. This parameter can give a direct reflection of the convergence of the calculation regarding the cutoff energy and k point. If this parameter for each atom is smaller than 0.01, it indicates that the computation is converged quite well.

2.8.2 k point sampling

As briefly introduced in the energy cutoff section, k point sampling is essential for the computation of the quantities of observables. The real situation is that infinite number of electrons exists on infinite number of k points; while finite number of state of electrons is occupied at every k point. Through the introduction in section 2.8.1, it can be seen that the original computation for the infinite number of wave functions for electrons is changed to the calculation of finite number of wave functions for electrons at an infinite number of k points; and every state of electron at the k point make contribution to the potential in the material, therefore, the computation for the potential is infinitely large and impossible to finish.

Fortunately, scientists found that the difference between the wave functions of electrons at the k points, which are very close to each other, is very small so that the difference can be neglected. Thus, the wave functions within a certain range of k space can be approximated by the wave function at one single k point and this means that the computation for the potential is only carried out at a finite number of k points with finite number of state of electrons, which become possible to be achieved in practice.

Many methods have been developed to gain the good results, with high accuracy, for the potential and the contribution of occupied energy band to the total energy through the computation of the finite number of state of electrons at finite number of chosen k points within the first Brillouin zone. In 1976, Monkhorst and Pack[77] developed a scheme to generate a uniform grid of k points in three axes within the reciprocal space. This grid is defined by three integers (q_i) and they determine the number of division along each axis. They also generate a series of number in equation 2.138.

$$q_i = (2r - q_i - 1) / 2q_i \quad (2.138)$$

where, r changes between 1 and q_i . The Monkhorst-Pack grid is then calculated by equation 2.139.

$$k_{prs} = u_p b_1 + u_r b_2 + u_s b_3 \quad (2.139)$$

The series of distinct points (q_1, q_2 and q_3) is further symmetrised and weights are assigned with respect to the number of symmetry images of a given point in the symmetrised set.

It is possible to put a constant shift to all of the points in the set before symmetrisation, which is shown in equation 2.140.

$$u_p = (p - 1)/q_i \quad (2.140)$$

where, p changes between 1 and q_i .

Like cutoff energy introduced in the above section, k point sampling method is also an approximation for the calculation of the potential and it can induce error in the total energy. Increasing the number of k points used in the computation can reduce this error, which can approach zero with the increased denser k points, and make the computation of the total energy reach the convergence criterion. Theoretically, the converged potential and total energy with required accuracy can always be achieved, since there is enough time to finish the computation of wave function of electrons with a series of sufficient denser k points. Certainly, the application of denser k points can also cause longer computational time. More denser k points used, more accuracy the result is and longer time the calculation would take. Therefore, it is quite important for research to make the balance between the success and accuracy of computation and the time the computation would take.

2.8.3 Fourier Transform Grid

In Bloch's theorem section, Bloch wave is introduced so as to expand the wave function of the electrons as a series of discrete plane wave basis set and make computation possible to be done.[78] Actually, it is also important to have real-space representation for the wave function of electron and this brings the technology to transform data between real and reciprocal grids. Fast Fourier Transform (FFT) is applied into the transform and makes this procedure proceed in a very efficient way.

First, the real space supercell is introduced. The direct lattice vectors along three axes are denoted by a_1 , a_2 and a_3 . The reciprocal grid vectors (b_1 , b_2 and b_3) are defined by the relation in equation 2.141.

$$a_i \cdot b_j = 2\pi\delta_{ij} \quad (2.141)$$

Using the above equation, reciprocal vectors can be built up (shown in equation 2.142, 2.143 and 2.144).

$$b_1 = \frac{a_2 \times a_3}{a_1 \cdot a_2 \times a_3} \quad (2.142)$$

$$b_2 = \frac{a_3 \times a_1}{a_1 \cdot a_2 \times a_3} \quad (2.143)$$

$$b_3 = \frac{a_1 \times a_2}{a_1 \cdot a_2 \times a_3} \quad (2.144)$$

The reciprocal grid vector (G) is expressed in equation 2.145.

$$G = n_1 b_1 + n_2 b_2 + n_3 b_3 \quad (2.145)$$

where, n_i is the integers and the wave vector are orthogonal to each other.

The plane wave e^{iGr} is commensurate with the supercell and the series of wave vector; while the real space grid is generated through dividing the lattice vectors (a_1 , a_2 and a_3) into N_1 , N_2 and N_3 points. The point in the supercell can be expressed in equation 2.146.

$$r(l_1, l_2, l_3) = \frac{l_1}{N_1} a_1 + \frac{l_2}{N_2} a_2 + \frac{l_3}{N_3} a_3 \quad (2.146)$$

where, l_i is the integer ranging from 0 to $N_i - 1$.

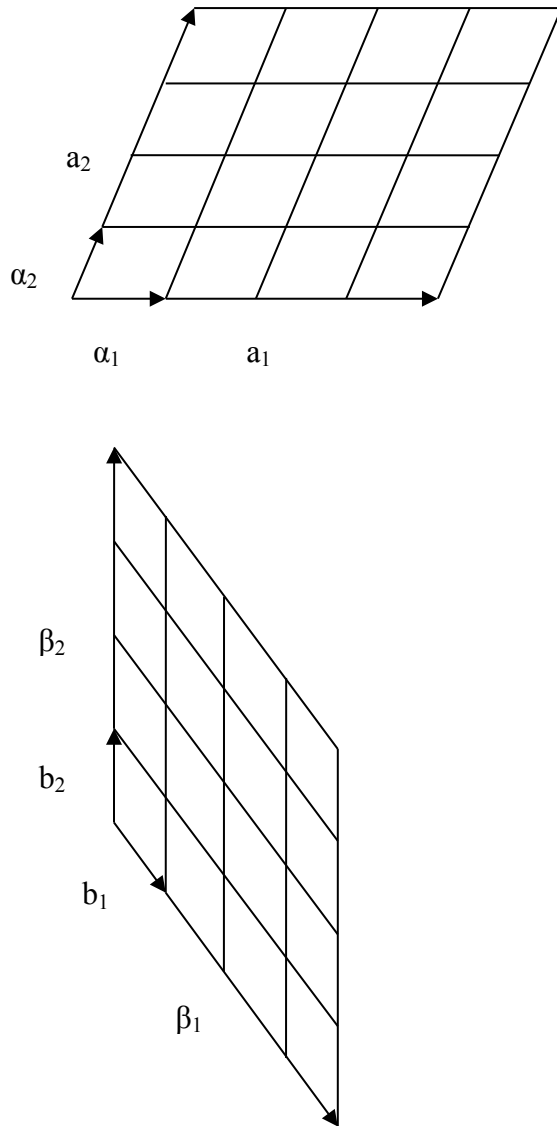


Fig. 2.9 Illustration of the real and reciprocal space grids. a is real space grid, b is reciprocal space grid, labels are the vectors

It can be seen that the real space grid is the lattice of points for the lattice vector $\alpha_i = a_i/N_i$; while, according to equation 2.141, the reciprocal lattice vector is expressed by $\beta_i = N_i b_i$. The reciprocal space grid is the lattice of points for the vector b_i and any point in this grid is determined by equation 2.145. The total number of supercell is given in equation below. Fig. 2.9 shows the relation between these two spaces.

$$N = N_1 N_2 N_3 \quad (2.147)$$

Bloch's wave described in equation 2.134 can be deemed as the discrete inverse Fourier transform of the wave function from reciprocal space to the real one with grid of N points. The forward FFT gives the wave function on the reciprocal space grid and the sum is over all N points in real space grid.

$$u_{n,k}(G) = \frac{1}{N} \sum_r \Psi_{n,k}(r) e^{-i(k+G)\cdot r} \quad (2.148)$$

2.8.4 Computation Procedure in VASP Code

As VASP code is written based on DFT method and in forgoing section 2.2, Hamiltonian of the system is expressed by the density of electron (ρ_r) but the density is not known, therefore VASP code adopts self-consistent field to proceed the computation, which is shown in Fig. 2.10. The first step is to build up an initial density (ρ_r); then use this density to generate Hamiltonian for the system and solve the Schrödinger equation so as to get the engine value of the system. Examine the computed eigen value and check it is converged. If converged, the computation is done and this density would be applied to calculation of the total energy for the system; while it not converged, a new density would be constructed though the density generation scheme, such as the density mixing method or all band electron method. Then the new density is used to replace the initial density and repeat the step discussed above. During the whole computational procedure, the sum of electronic eigenvalues is minimized in the fixed potential instead of the self-consistent minimization of the total energy.

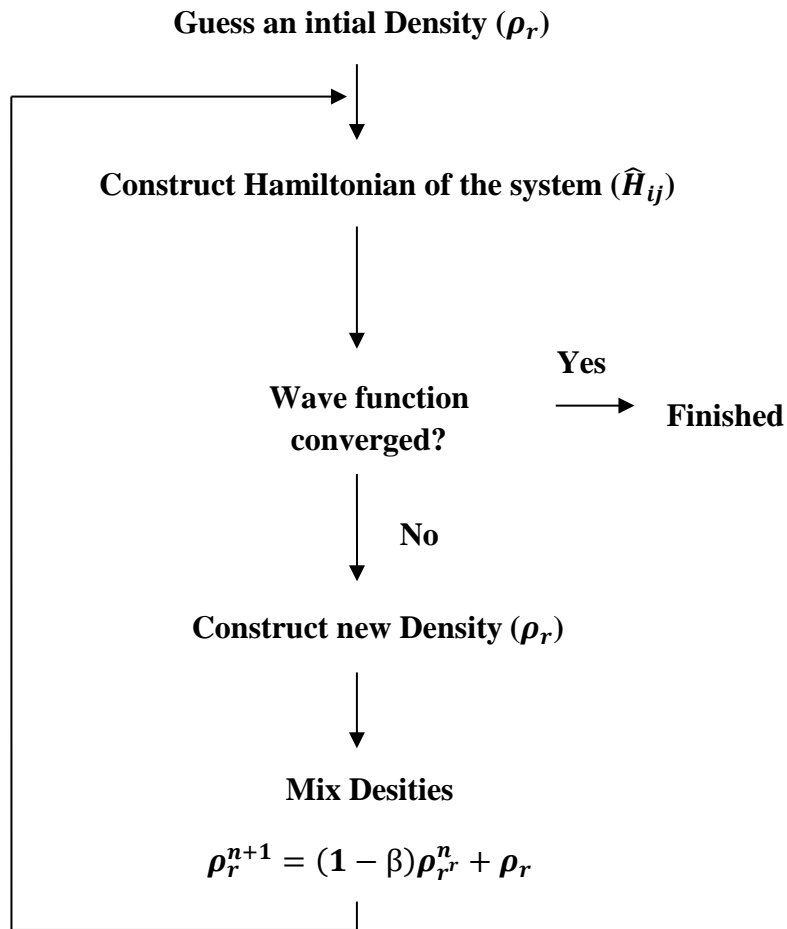


Fig. 2.10 Procedure of the Computation by VASP code

2.8.5 Density Mixing Scheme

In section 2.8.4, when the engine value is not converged, a new density would be generated through a generation scheme, such as density mixing or all band electron method. All band electron method is relatively traditional way for the electronic relaxation, which involves the minimisation of the total energy through preconditioned conjugate gradient technique. The wave function of electrons is expanded by a series of plane wave basis set and the coefficients are altered to minimise the total energy. However this method is very time-expensive for the computation, thus most of the calculations were not carried out through it. As density mixing method was chosen in this PhD research, it is introduced with more details here.

A number of schemes were developed for this method, including linear mixing, Kerker mixing, Broyden mixing and Pulay mixing. As linear mixing scheme concerned, it requires one

parameter and the output density is produced as a linear combination of the print and output densities on the last iteration; while Kerker mixing scheme considers about the fact that small- G components of the charge density should be mixed with smaller weights so as to stop charge sloshing during SCF optimisation.[79] The generation of new density is introduced in equation 2.149.

$$\rho_{new}(G) = \rho_{in}(G) + A \frac{G^2}{G^2 + G_{max}^2} [\rho_{out}(G) - \rho_{in}(G)] \quad (1.149)$$

According to the equation above, it can be seen that Kerker scheme is defined by two parameters the mixing amplitude (A) and the cutoff wave vector (G_{max}).

Pulay mixing scheme is the most efficient one and this method save the input charge density and the residual vector over a number of SCF optimisation steps. The new input density is generated in every step through the linear combination of charge densities of all previous steps. The new density is determined such that it minimises the normal of the residual vector subject to the constraint of conserving the number of electrons. Pulay's scheme starts with a Kerker type step, thus it is effectively controlled by three parameters: the mixing amplitude (A), the cutoff wave vector (G_{max}) and the depth of the optimisation history. These three parameters affect the convergence and computational time. When the convergence encounters problems, it is usually to reduce the value of mixing amplitude; increase the cutoff wave vector to three or four times the original value and increase the value of optimisation history parameter. However, this could increase the computational time as more iteration steps are needed to make the engine value converge. Therefore, it is suggested to adjust these parameter while keeping the computation efficiency. Pulay's mixing scheme was chosen to the computation in this PhD research.

The main advantage of density mixing method is its robustness for the metallic system; especially for metallic surface and it can converge equally well for insulating and metallic cases, providing a factor of three increasing in speed of moderately sized insulator systems. Most of the calculations can be converged by density mixing method and if the calculation cannot reach the convergence criterion, all band electron method can solve the problem. However, as mentioned before, it is very time consuming and should be used with care.

References:

- [1] Hasan, M. Z. and Kane, C. L. *Rev. Mod. Phys.* (2010) 82, 3045
- [2] Qi, X-L and Zhang, S-C *Rev. Mod. Phys.* (2011) 83, 1057
- [3] Ortmann, F.; Roche, S and Valenzuela, S. O. Topological Insulators, *Fundamentals and Perspectives* (New York: Wiley) (2015)
- [4] Bernevig, B. A. and Zhang, S-C *Phys. Rev. Lett.* (2006) 96, 106802
- [5] Bernevig, B. A.; Hughes, T. L. and Zhang, S-C *Science* (2006) 314, 1757
- [6] König, M.; Wiedmann, S.; Brüne, C.; Roth, A.; Buhmann, H.; Molenkamp, L. W.; Qi, X-L and Zhang, S-C *Science* (2007) 318, 766
- [7] Fu, L. and Kane, C. L. *Phys. Rev. B* (2007) 76, 045302
- [8] Hsieh, D.; Qian, D.; Wray, L.; Xia, Y.; Hor, Y.; Cava, R. J. and Hasan M. Z. *Nature* (2008) 452, 970
- [9] Bernevig, B. A.; Hughes, T. L. and S. C. Zhang *Science* (2006) 314, 1757
- [10] Qi, X. L.; Hughes, T. L. and Zhang, S. C. *Phys. Rev. B* (2008) 78, 19, 195424
- [11] König, M.; Buhmann, H.; Molenkamp, L. W.; Hughes, T. L.; Liu C.-X.; Qi X. L. and Zhang S. C. *J. Phys. Soc. Jpn.* (2008) 77, 031007
- [12] Zhang, Haijun; Liu, Chaoxing; Qi, Xiaoliang; Dai, Xi; Fang, Zhong and Zhang, ShouCheng *Nature Physics* (2009) 5, 438-442
- [13] Chen, Y. L.; Analytis, James G.; Chu, J. H.; Liu, Z. K.; Mo, S. K.; Qi, Xiaoliang; Zhang, H. J.; Lu, D. H.; Dai, Xi; Fang, Zhong; Zhang, Shoucheng; Fisher, Ian R.; Hussain, Zahid and Shen, Z. X. *Science* 325, 5937, 178-181 (2009)
- [14] Ortmann, Frank; Roche, Stephan and Valenzuela, Sergio O. *Topological Insulator: Fundamentals and Perspectives*, chapter 6
- [15] Qi, X. L.; Hughes, T. L. and Zhang, S. C. *Phys. Rev. B* (2008) 78, 19, 195424
- [16] Xu, Y.; Miotkowski, I.; Liu, C.; Tian, J.; Nam, H.; Alidoust, N.; Hu, J.; Shih, C. K.; Hasan, M. Z. and Chen, Y. P. *Nature Physics* (2014) 10, 956-963
- [17] Zhang, H.; Liu, C. X.; Qi, X. L.; Dai, X.; Fang, Z. and Zhang, S. C. *Nature Phys.* (2009) 5, 438
- [18] Chen, Y. L.; Analytis, James G.; Chu, J. H.; Liu, Z. K.; Mo, S. K.; Qi, Xiaoliang; Zhang, H. J.; Lu, D. H.; Dai, Xi; Fang, Zhong; Zhang, Shoucheng; Fisher, Ian R.; Hussain, Zahid and Shen, Z. X. *Science* (2009) 325, 5937, 178-181
- [19] Sinha, Debabrata *Europhysics Letters* (2016) 115, 3
- [20] Qi, Xiaoliang and Zhang, Shoucheng *Rev. Mod. Phys.* (2011) 83, 1057-1110
- [21] Liu, C.-X.; Qi, X.-L.; Zhang, H.; Dai, X.; Fang Z. and Zhang, S.-C. *Phys. Rev. B* (2010) 82, 045122
- [22] Hirahara, Toru; Ereameev, Sergey V.; Shirasawa, Tetsuroh; Okuyama, Yuma; Kubo, Takayuki; Nakanishi, Ryosuke; Akiyama, Ryota; Takayama, Akari; Hajiri, Tetsuya; Ideta, Shin-ichiro; Matsunami, Masaharu; Sumida, Kazuki; Miyamoto, Koji; Takagi, Yasumasa; Tanaka, Kiyohisa; Okuda, Taichi; Yokoyama, Toshihiko; Kimura, Shin-ichi; Hasegawa, Shuji and Chulkov, Evgueni V. *Nano Lett.* 17, 6, 3493-3500 (2017)
- [23] Otrokov, M. M.; Menshchikova, T. V.; Vergniory, M. G.; Rusinov, I. P.; Vyazovskaya, A. Yu; Koroteev, Yu M.; Bihlmayer, G.; Ernst, A.; Echenique, P. M. and Arnau, A. *2D Mater.* 4, 025082 (2017)
- [24] Yue, Zengji; Wang, Xiaolin and Gu, Min arXiv: 1802.07841
- [25] Chang, Jiwon; Register, Leonard F. and Banerjee, Sanjay K. *J. Appl. Phys.* (2012) 112, 3045–3067
- [26] Kim, D.; Syers, P.; Butch, N. P.; Paglione, J. and Fuhrer, M. S. *Nat. Commun.* (2013) 4, 2040
- [27] Brahlek, M.; Koirala, N.; Salehi, M.; Bansal, N and Oh, S. *Phys. Rev. Lett.* (2014) 113, 026801

- [28] Kushwaha, S. K.; Gibson, Q. D.; Xiong, J.; Pletikosic, I.; Weber, A. P.; Fedorov, A. V.; Ong, N. P.; Valla, T. and Cava, R. J. *J. Appl. Phys.* (2014) 115, 143708
- [29] Brahlek, M.; Koirala, N. and Oh, S. *Sol. Stat. Commun.* (2015) 215, 54
- [30] Brüne, C.; Liu, C. X.; Novik, E. G.; Hankiewicz, E. M.; Buhmann, H.; Chen, Y. L.; Qi, X. L.; Shen, Z. X.; Zhang, S. C. and Molenkamp, L. W. *Phys. Rev. Lett.* (2011) 106, 126803
- [31] Checkelsky, J. G.; Hor, Y. S.; Liu, M-H; Qu, D-X; Cava, R. J. and Ong, N. P. *Phys. Rev. Lett.* (2009) 103, 246601
- [32] Costache, M. V.; Neumann, I.; Sierra, J. F.; Marinova, V.; Gospodinov, M. M.; Roche, S. and Valenzuela, S. O. *Phys. Rev. Lett.* (2014) 112, 086601
- [33] Soriano, D.; Ortman, F. and Roche, S. *Phys. Rev. Lett.* (2012) 109, 266805
- [34] Zhu, X-G and Hofmann, P. *Phys. Rev. B* (2014) 89, 125402
- [35] Bouaziz, Juba; Dias, Manuel dos Santos, Azpiroz, Julen Ibañez and Lounis, Samir arXiv:1805.01002
- [36] Miao, Lin; Xu, Yishuai; Zhang, Wenhan; Older, Daniel; Breitweiser, S. Alexander; Kotta, Erica; He, Haowei; Suzuki, Takehito; Denlinger, Jonathan D.; Biswas, Rudro R.; Checkelsky, Joseph; Wu, Weida and Wray, L. Andrew arXiv:1805.00084
- [37] Scanlon, D. O.; Walsh, A.; Morgan, B. J.; Nolan, M.; Fearon, J.; Watson, G. W. *J. Phys. Chem. C* (2007) 111, 7971-7979
- [38] Perdew, J. P. and Zunger, Alex *Phys. Rev. B* (1981) 23, 10, 5048-5079
- [39] Hinchliffe and Alan *Modelling Molecular Structures* (2nd ed.), Baffins Lane, Chichester, West Sussex PO19 1UD, England: John Wiley & Sons Ltd. (2000) 186 ISBN 0-471-48993-X
- [40] Koch, Wolfram and Holthausen, Max C. *A Chemist's Guide to Density Functional Theory*, ISBN: 3-527-30372-3, (2001) 8-13
- [41] Monthoux, P. *Phys. Rev. B* (2004) 70, 144403-144419
- [42] Knowles, P. J. and Werner, H. J. *Chemical Physics Letters* (1988) 145, 514-522
- [43] Resnick, R.; Eisberg, R.; Wiley, J. and Sons, *Quantum Physics of Atoms, Molecules, Solids, Nuclei and Particles* (2nd ed.) (1985) ISBN 978-0-471-87373-0
- [44] Thomas, L. H. *Proc. Cambridge Phil. Soc.* (1927) 23 (5) 542-548
- [45] Zhou, Z. X. and Parr, R. G. *International Journal of Quantum Chemistry* (1992) 42, 6, 1759-1769
- [46] Parr, R. G. and Yang, W. *Density-Functional Theory of Atoms and Molecules*, Oxford University Press (1989)
- [47] Hohenberg, P. and Kohen, W. *Phys. Rev. B* (1964) 76, 6062
- [48] Perdew, J. P. and Levy, Mel *Phys. Rev. B* (1985) 31, 6264
- [49] Chermette, H. *Coordination Chemistry Reviews* (1998) 178-180, 1, 699-721
- [50] Kohn, W. and Sham, L. J. *Phys. Rev.* (1965) 140, 4A, 1133-1138
- [51] Perdew, John P.; Parr, Robert G.; Levy, Mel; Balduz, Jose L. and Jr., *Phys. Rev. Lett.* (1982) 49, 23, 1691-1694
- [52] Jones, R. O. *Computational Nanoscience NIC Series* (2006) 31, 45-70 ISBN 3-00-017350-1
- [53] Hohenberg, P. and Kohen, W. *Phys. Rev.* (1964) 136, 3B, 864-871
- [54] Slater, J. C. *Phys. Rev.* (1951) 81, 385
- [55] Ceperley, D. M. and Alder, B. J. *Phys. Rev. Letts.* (1980) 45, 566
- [56] Lee, C.; Yang, W. and Parr, R. G. *Phys. Rev. B: Condens. Matter Mater. Phys.* (1988) 37, 785-789
- [57] Vosko, S. H.; Wilk, L. and Nusair, M. *Can. J. Phys.* (1980) 58(8), 1200
- [58] Oliver, G. L. and Perdew, J. P. *Phys. Rev. A* (1979) 20, 397
- [59] Barth, U. von and Hedin, L. *J. Phys. C: Solid State Phys.* (1972) 5, 1629
- [60] Perdew, J. P.; Burke, K.; Ernzerhof, M. *Phys. Rev. Lett.* (1996) 77, 18, 3865-3868

- [61] Wu, Z.; Cohen, R. E. *Phys. Rev. B* (2006) 73, 235116-235122
- [62] Perdew, J. P. and Yue, Wang *Phys. Rev. B* (1986) 33, 8800(R)
- [63] Perdew, J. P.; Harbola, M. K. and Sahni, V *Condensed Matter Theories* (1988) 235-247
- [64] Perdew, J. P. in *Electronic Structure Theory of Solids*, P. Ziesche and H. Eschrig, eds. (Akademie Verlag, Berlin, 1991)
- [65] Kresse, G. and Hafner, J. *Phys. Rev. B* (1993) 47, 558
- [66] Kresse, G. and Furthmüller, J. *Phys. Rev. B* (1996) 54 , 11, 169
- [67] Kresse, G. and D. Joubert, *Phys. Rev.* (1999) 59, 1758
- [68] Marsman, Martijn *History of VASP* (2011)
- [69] *Documentation of VASP code*, <https://www.vasp.at/index.php/documentation>
- [70] Schwerdtfeger, P. *Chem. Phys. Chem.* (2011) 12, 17, 3143-3155
- [71] Vanderbilt, David *Phys. Rev. B* (1990) 41, 11, 7892-7895
- [72] Hamann, D. R.; Schlüter, M. and Chiang, C. *Phys. Rev. Lett.* (1979) 43, 1494-1497
- [73] Blöchl, P. E. *Phys. Rev. B* (1994) 50, 24, 17953–17978
- [74] Bachelet, G. B. and Schlüter, M. *Phys. Rev. B* (1982) 25, 2103
- [75] Kleinman L. and Bylander, D. M. *Phys. Rev. Lett.* (1982) 48, 1425
- [76] Francis, G. P. and Payne, M. C. *J. Phys.: Condens. Matter* (1990) 2, 4395-4404
- [77] Monkhorst, H. J. and Pack, J. D. *Phys. Rev. B* (1977) 16, 1748-1749
- [78] Cooley, J. W. and Tukey, J. W. *Math. Comput.* 19, no. 90, (1965) pp. 297–301
- [79] Pulay, *Chem. Phys. Let.* (1990) 73, 393

Chapter Three: Bi_2Se_3 -Family Topological Insulator with Defects

3.1 Introduction

As mentioned in 2.1.3, many research works have been devoted to studying the effect of defects on the properties of 3D TI, which has ultrathin thickness. The remaining important question is to quantify the impact of individual defects (twin grain boundaries, vacancies, oxygen defects, ad-atoms, substitutional impurities *etc.*) in such circumstances.[1~3] In this chapter, using first-principles calculations, we investigate the detrimental effect of twin grain boundaries and surface doping in the limit of thin TI films. We study two different types of defects which may strongly affect the electronic structure of low dimensional TIs: (i) twin grain boundaries where adjacent QLs become rotated 180° with respect to the other (Fig. 3.1*b*), and (ii) surface doping induced by hydrogen adatoms (Fig. 3.1*c*). As a limiting case, we also study how the topological surface states are modified when both defects are present in the same sample (Fig. 3.1*d*).

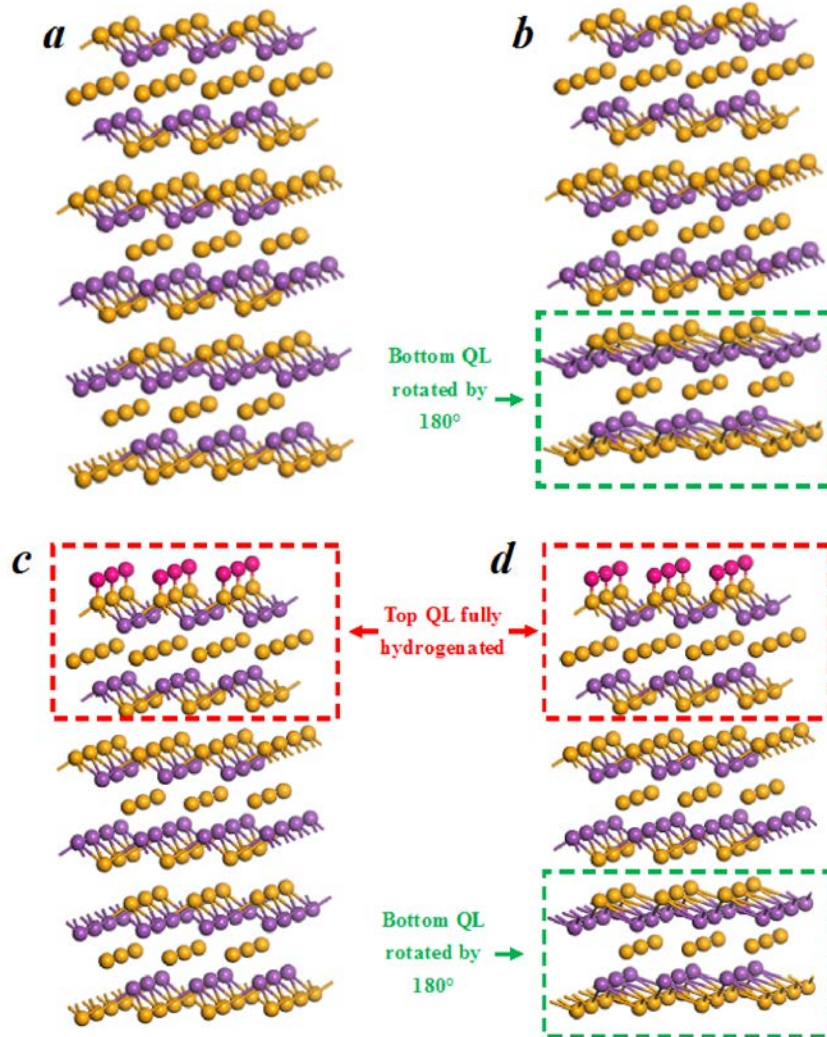


Fig. 3.1 Model of 3-QLs Bi_2Se_3 slabs used in the calculations. *a* - Pristine slab; *b* - slab with the bottom QL rotated by 180° ; *c*, *d* - same slabs as in *a*, *b* - where the top surface has been fully hydrogenated. Bi, Se and H atoms are represented in purple, orange and magenta, respectively

3.2 Methodology

First principles calculations were carried out in the framework of the density-functional theory as implemented in the Vienna ab initio simulation package [4]. Wave functions were expanded by means of plane-wave basis sets with an energy cut-off of 450 eV. The projector augmented wave method was used to describe core electrons [5, 6]. For the choice of the exchange-correlation energy, we use the generalized gradient approximation in the PBE form

[7]. A $11 \times 11 \times 1$ k-point mesh was generated to sample the Brillouin zone. Missing dispersion forces were included using the Tkatchenko–Scheffler method [8]. The lattice structure was relaxed until the forces on each atom were smaller than 10^{-3} eV \AA^{-1} . The crystal structure of Bi_2Se_3 is rhombohedral. Bismuth and selenium atoms combine forming quintuple layers that stack together along the (111)-direction by means of van der Waals interactions (see Fig. 3.1a). In this work we focus on unit cells containing only three quintuple layers (~ 3 nm), and describe the impact of fully saturated surface atoms and twin boundaries on the electronic band structure as well as on the spin texture of low-energy states. The spin texture is analysed by plotting the expectation value of the spin operators in a properly chosen set of k-points.

3.3 Twin grain boundaries

Twin grain boundaries in Bi_2Se_3 thin films Grain boundaries (GBs) are always present in polycrystalline and MBE-grown samples of TIs [9]. Here we report on the impact of twin grain boundaries on the electronic structure of thin films of Bi_2Se_3 samples containing different number of quintuple layers. We start describing the impact of twin GBs on 2QL Bi_2Se_3 films, where the absence of bulk states inhibit the formation of topological surface states, and then we extend our study to samples containing 3, 4 and 5QLs, where quasi-bulk states start to form and enable nontrivial topological phases [10, 11].

To examine the stability of the defect, the total energy difference ($|\Delta E|$) with and without GBs are computed ($|\Delta E| = 5.7$ meV \AA^{-2} (2QL); 6.5 meV \AA^{-2} (3QL); 5.1 meV \AA^{-2} (4QL 3 + 1); 5.0 meV \AA^{-2} (4QL 2 + 2); 7.8 meV \AA^{-2} (5QL 4 + 1) and 5.9 meV \AA^{-2} (5QL3 + 2)). All slabs studied show a small $|\Delta E|$, lower than 8 meV \AA^{-2} , indicating that twin GBs can be stabilized within the slab.

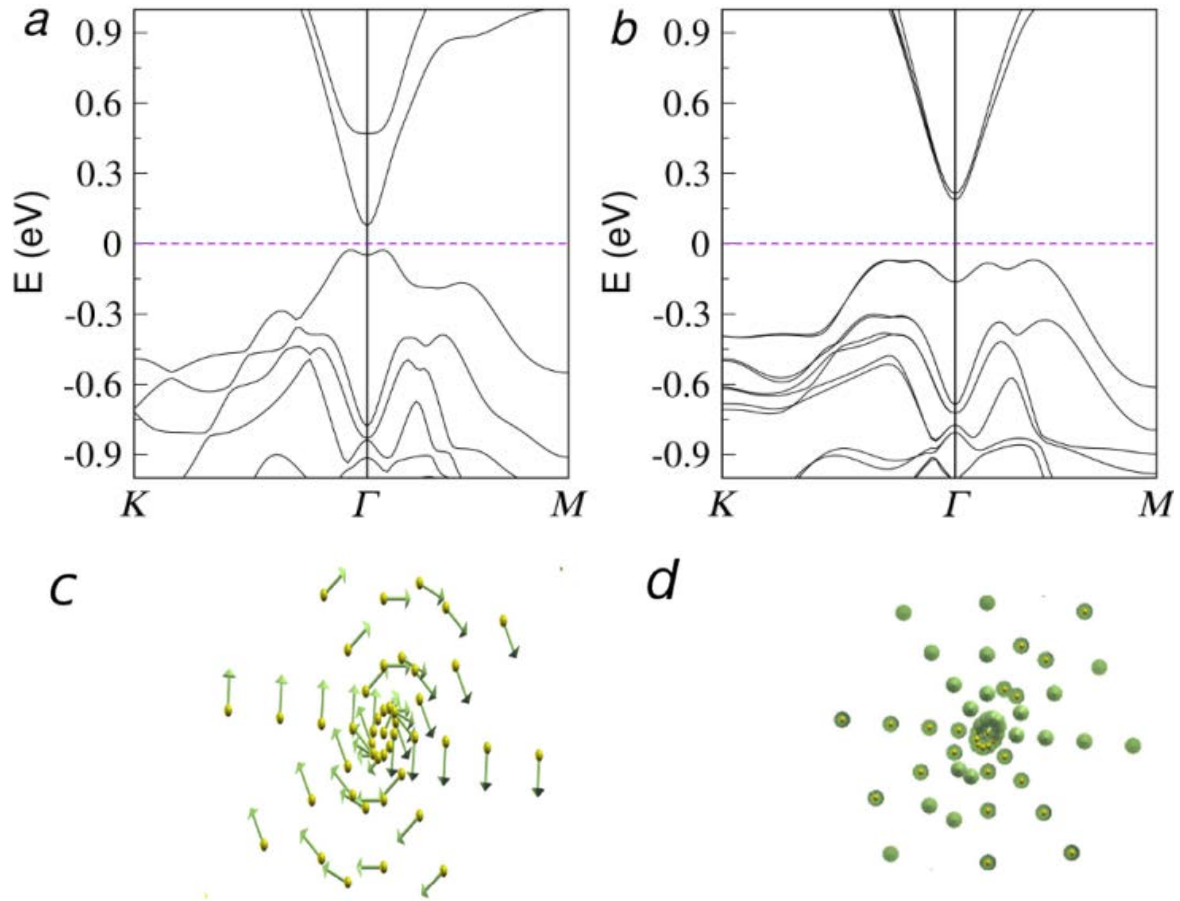


Fig. 3.2 Band structure of 2QL Bi_2Se_3 pristine. *a* - and with the bottom QL rotated by 180° *b*. *c* and *d* - spin textures of the 2QL slab in absence and in presence of a twin GB calculated around the Γ point. It is important to note the modification of the spin texture when the GB is present in the slab

2QL slab—Fig. 3.2*a* shows the band structure of a pristine 2QL Bi_2Se_3 thin film. The value of the gap at the Γ -point is around 110 meV. Fig. 3.2*b* shows the band structure of a 2QL slab with the bottom QL rotated 180° . The distance between QLs increases from 2.55 Å in the pristine case to 3.66 Å, leading to a band gap of about 240 meV, twice as large as the one reported for the pristine case. Previous first-principles calculations by Liu and coworkers [10] have shown that 1QL and 2QL Bi_2Se_3 are trivial two-dimensional insulators due to the absence of bulk states. The spin textures without and with GB are plotted in Figs. 3.2 (*c* and *d* respectively). A change of the spin texture from a helical one (pristine case) to an out-of-plane polarized texture can be clearly observed. This may have a substantial impact on the spin transport properties in this material, depending on the initial spin polarization of injected electrons.

3QL slab—Fig. 3.3*a* shows the band structure of a pristine 3QL Bi₂Se₃ slab. Despite the small thickness of the slab, the presence of a single-QL bulk region allows for the appearance of topological surface states. However, a small gap of 36 meV opens at the Fermi level owing to the interaction between surface states at opposite boundaries. The analysis of the spin texture around the Γ -point (Fig. 3.3*c*) shows a clear helical behavior in the surface state bands. After the rotation of the bottomlayer of the slab by 180° and subsequent geometry relaxation, we do not observe strong variations of the lattice constants within each QL. In contrast, the van der Waals spacing between the middle QL and the bottom one increases from 2.576 to 3.589 Å. Fig. 3.3*b* shows how the presence of the twin grain boundary yields an enhancement of the energy gap up to 194 meV.

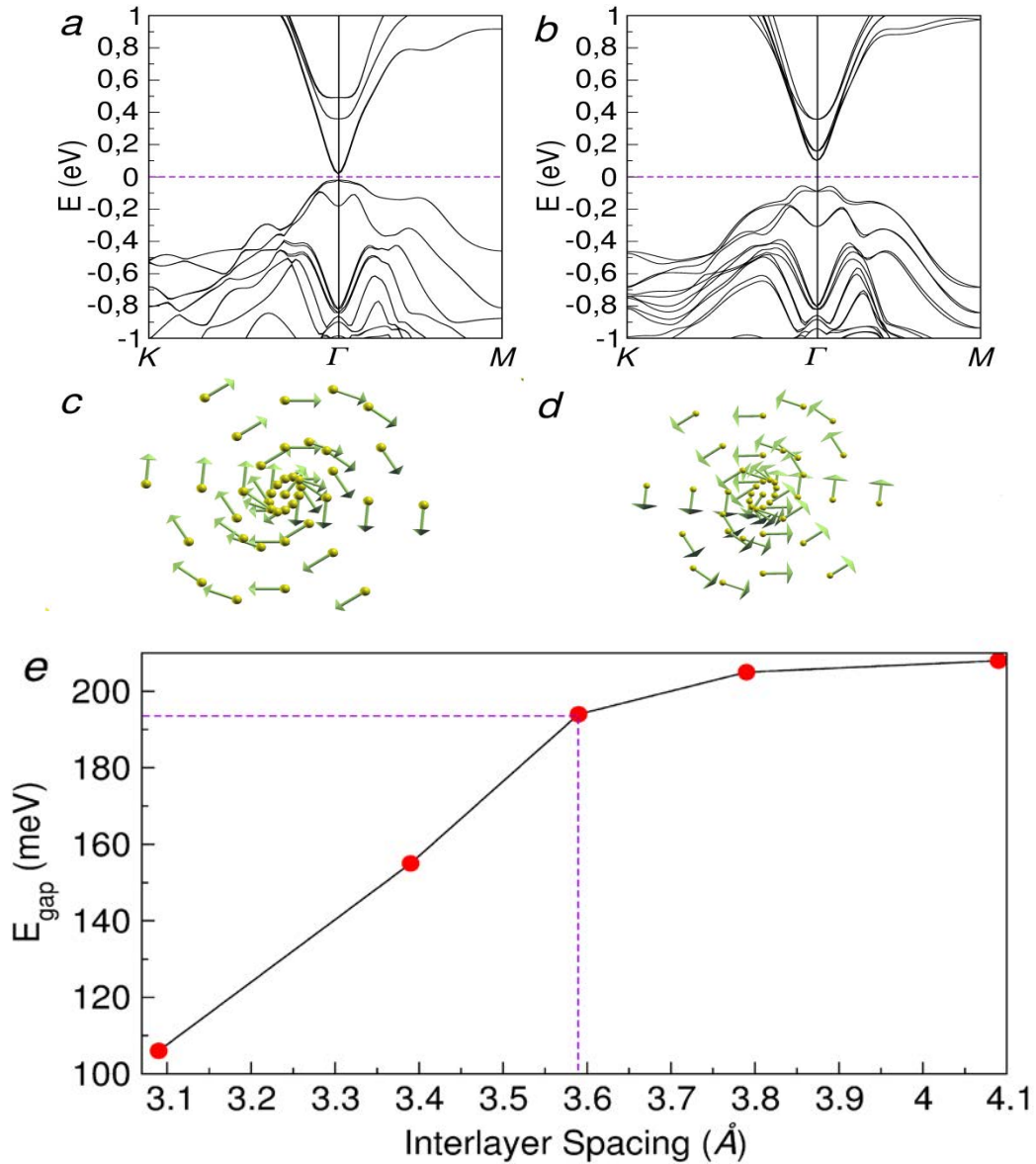


Fig. 3.3 Band structures of 3QL Bi_2Se_3 pristine (a) and with the bottom QL rotated by 180° (b). Spin textures of the topological surface states in absence (c) and in presence (d) of the twin grain boundary. The spin polarization is calculated from the bottom of the conduction band to $E=0.15$ eV. (e) Evolution of the band gap while increasing the spacing between the middle and the rotated bottom QLs. The dashed lines show the equilibrium distance

Figs. 3.4a and 3.4b reports the band structure projection on the first two b and bottom rotated a QLs. The projection exhibits a very different gap for each substructure owing to the large variation of the distance between QLs induced by the twin GB. In particular, the band structure projection on the first 2QL is almost identical to the 2QL case shown in Fig. 3.2. Indeed the concave shape of the conduction bands are recovered, which might be related to a non-trivial to trivial phase transition. Such impact on the electronic band structure likely stems

from the fact that the Se layers between the rotated and the original QLs become aligned in x - y plane after the rotation, increasing the Coulomb repulsion. This results in a larger interlayer spacing and the gap enlargement. It is interesting to mention that, despite the large increase of the gap, the spin texture corresponding to the topological surface states is still preserved (Fig. 3.3d), which is different from that in 2QLs case. This means that the middle QL could act like a buffer zone and help maintain the *Rashba* spin texture on the top QL.

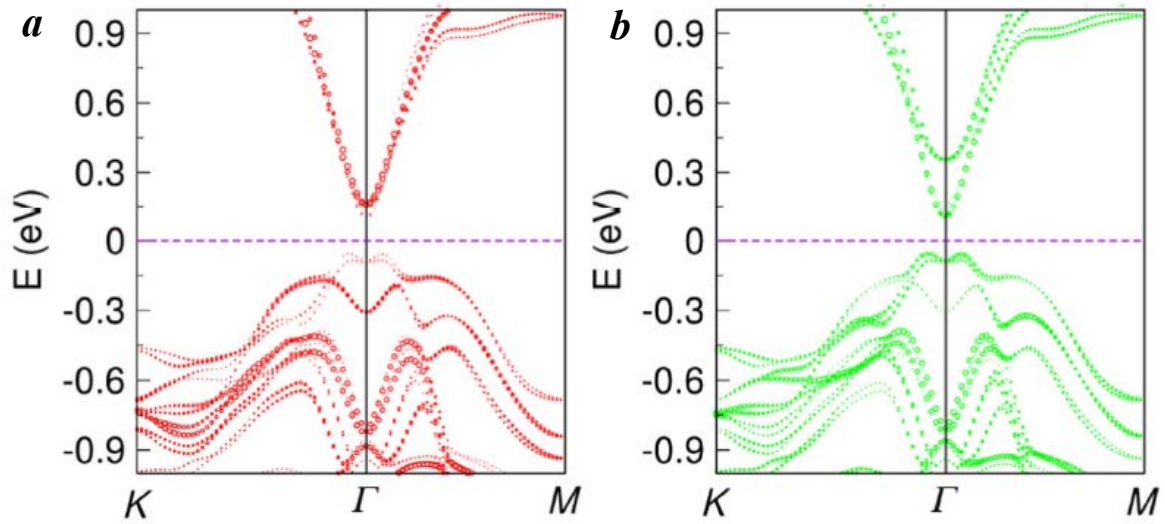


Fig. 3.4 *a* and *b* band structure projection on the bottom rotated QL and the first two QLs respectively. The projection on the first 2QLs resembles the band structure of the 2QL slab

To confirm that the increased gap value is related to the interlayer spacing between the last two QLs, we compute the magnitude of the gap while varying the distance between middle and bottom QLs starting from the relaxed structure. The results are plotted in Fig. 3.2e and, as expected, they show an increase of the band gap for larger interlayer spacing. The presence of such grain boundaries in the 3 nm ultrathin film also induces a very small energy level splitting due to the breaking of inversion symmetry.

4QL slab—the 4QL slab admits two different structures associated with the presence of a twin GB, namely, the 3 + 1 and 2 + 2 cases. Fig. 3.5a shows the band structure of the pristine 4QL Bi_2Se_3 film showing a small band gap of the order of 20 meV. By rotating only the top or bottom QLs one gets the 3 + 1 case whose band structure is given in Fig. 3.5b. Fig. 3.5c shows the band structure when the GB is located in the center of the slab (2 + 2 case). Interestingly, the band gap is barely changed. This is easily understood by analysing the variation of the distance between QLs in absence or in the presence of the twin GB. The van der Waals

distances after geometry relaxation are $\Delta d (3 + 1) \gg 0.03 \text{ \AA}$, and $\Delta d (2 + 2) \gg 0.1 \text{ \AA}$. These are much smaller than the ones obtained in the $2 + 1$ case described above. On the other hand, the Rashba splitting induced by breaking the inversion symmetry through the incorporation of a twin GB shifts from the surface state in the $3 + 1$ case to the first bulk conduction band in the $2+2$ case. This may serve as a guidance to obtain valuable information regarding the position of the GB within the thin film. Figs. 3.5*d* – 3.5*f* show the band structure projection for both configurations, namely $3 + 1$ and $2 + 2$. The three projections are very similar and the substructures (or grains) formed in presence of the GB seem to remain strongly connected. This is reasonable given the small modifications of the van der Waals distances induced by the twin GB.

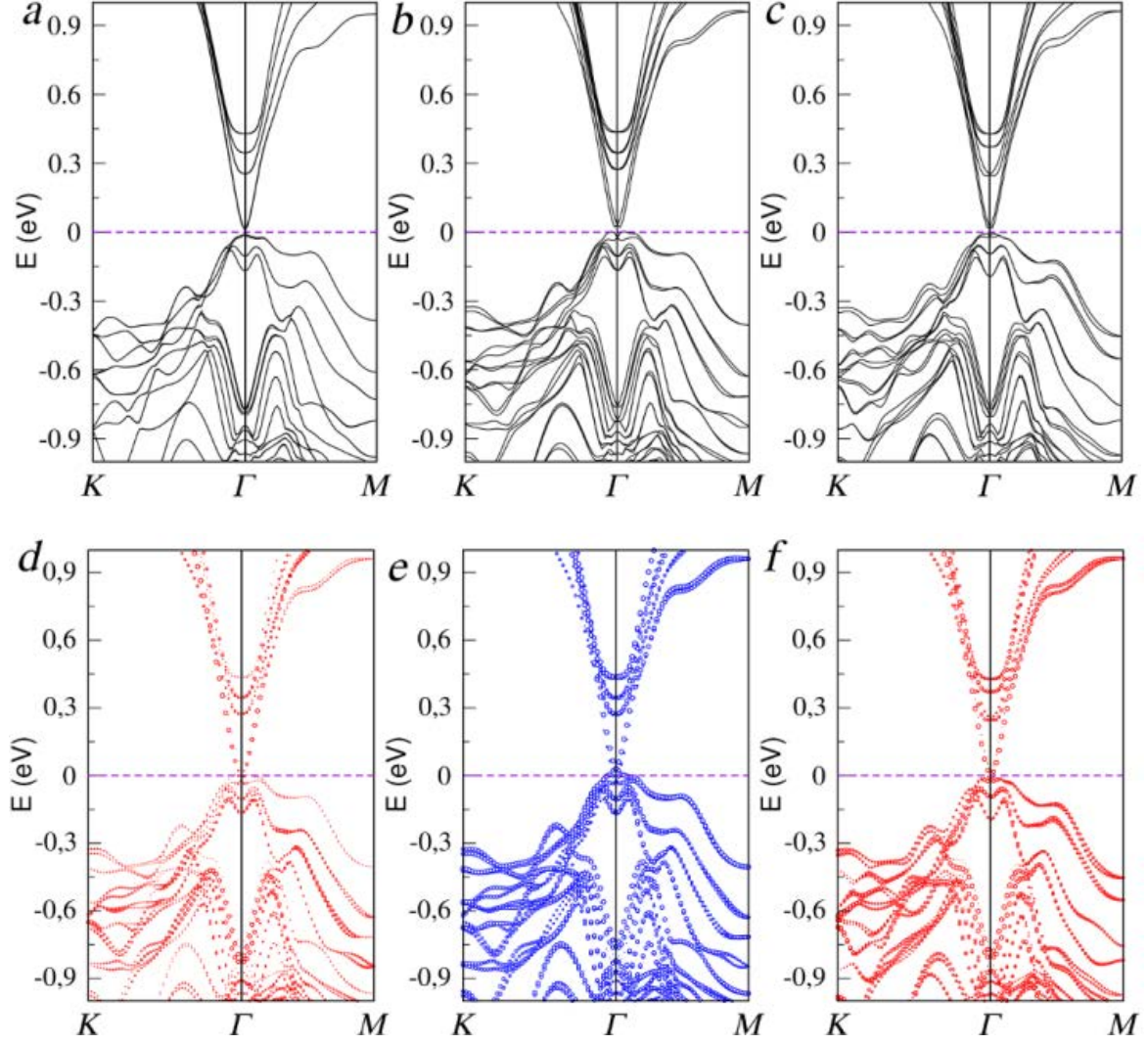


Figure 3.5 Band structure of 4QL Bi_2Se_3 pristine (a), the bottom QL rotated by 180° (3+1 structure) (b) and the two bottom QLs rotated (2+2 structure) (c). It is interesting to note that the Rashba splitting induced by the presence of the twinGB is more pronounced in the surface band in the 3+1 case and in the first bulk band in the 2+2 case. Band structure projection on the bottom rotated QL(d) and the first fixed 3QLs (e) corresponding to the 3+1 case. (f) Band structure projection on the top 2QLs corresponding to the 2+2 structure

5QL slab—the 5QL case also admits two different geometries in presence of a twin GB, namely, the 4 + 1 and the 3 + 2. The band structures of the pristine and the two polycrystalline cases are shown in Figs. 3.6a – 3.6c. The band structure projections are plotted in Figs. 3.6d – 3.6g. The two different configurations show a very different behavior. While the 4 + 1 case presents a strongly disconnected rotated QL from the remaining QL (Figs. 3.6d and 3.6e), the 3 + 2 case shows a similar band structure projection for both substructures (Figs. 3.6f and 3.6g). This is also related to the different distance variation in the 4 + 1 and the 3 + 2

cases. Indeed, while in the first case the distance changes dramatically from $\gg 2.63$ to $\gg 3.61$ Å, in the second case it is slightly modified by the presence of the twinGB, $\Delta d = 0.082$ Å.

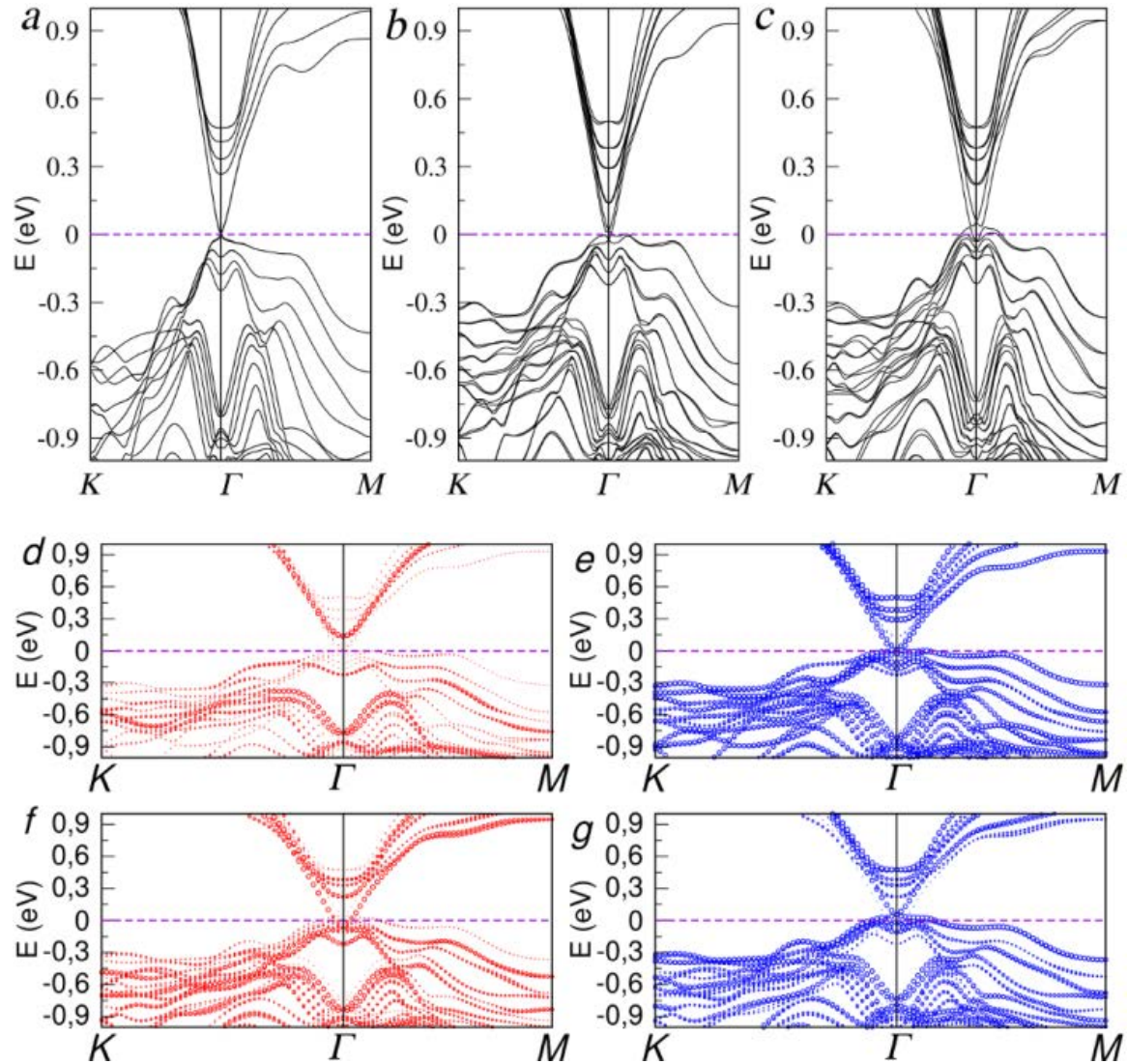


Fig. 3.6 Band structure of 5QL Bi_2Se_3 pristine (a), the bottom QL rotated by 180° (4+1 structure) (b) and the two bottom QLs rotated (3+2 structure) (c). Band structure projection on the bottom rotated QL (d) and the first fixed 4QLs (e) corresponding to the 4+1 case. Band structure projection on the bottom rotated 2QLs (f) and the first fixed 3QLs (g) corresponding to the 3+2 structure

In a similar work by Aramberri et al on thicker Bi_2Se_3 films [12], it was shown that twin boundaries induce either n - or p -type self-doping on the surface states (up to 300 meV), depending on the relative orientation of adjacent QLs. Such self-doping stems from spontaneous polarization generated by the dipole moments associated with the lattice defects. However in such study on thicker TI-films, no gap opening due to the presence of this type of defects was observed. This highlights the importance of reducing the number of defects when producing low dimensional TIs. According to the projection, the Dirac point (DP) of the top

QL surface is shifted upwards (Figs. 3.6e and 3.6g); while that on the rotated QL surface remains below Fermi energy level (Fig. 3.6f). Fig. 3.6g shows that the DP of top QL surface is shifted above the Fermi energy level. This indicates that the rotation scheme for the 5QL Bi_2Se_3 can help reducing the bulk contribution to the surface conductivity and preserve the spin-momentum locking feature.

3.4 Surface doping on Bi_2Se_3 thin films

Another important effect that may appear when ultrathin TI films are grown or deposited on top of a substrate is surface doping. To mimic this effect, we have fully saturated one of the surfaces of our Bi_2Se_3 slab with hydrogen atoms (see Fig. 3.1c). After full relaxation, the distance between H and Se atoms was found to be 1.52 Å. Fig. 3.7 shows the band structures and spin textures of the partially hydrogenated 3QL Bi_2Se_3 slabs projected onto the hydrogen terminated top QL (red circles) and the pristine bottom QL (green circles) while varying the H–Se distance. First, we observe the formation of surface dipoles when the hydrogen atoms start to approach the surface leading to a downward shift of the surface bands at the Γ -point, and also to the formation of Rashba-like states as experimentally observed on potassium doped Bi_2Se_3 samples [13]. Second, and more importantly, the gapless surface states remain metallic after hydrogen absorption. This is mainly driven by the breaking of inversion symmetry which splits the DPs at both surfaces reducing surface-to-surface interaction. Meanwhile, the spin texture at the Γ -point corresponding to the undoped topological surface states, reflects the usual in-plane polarization (see Fig. 3.7d) thus preserving the spin-momentum locking.

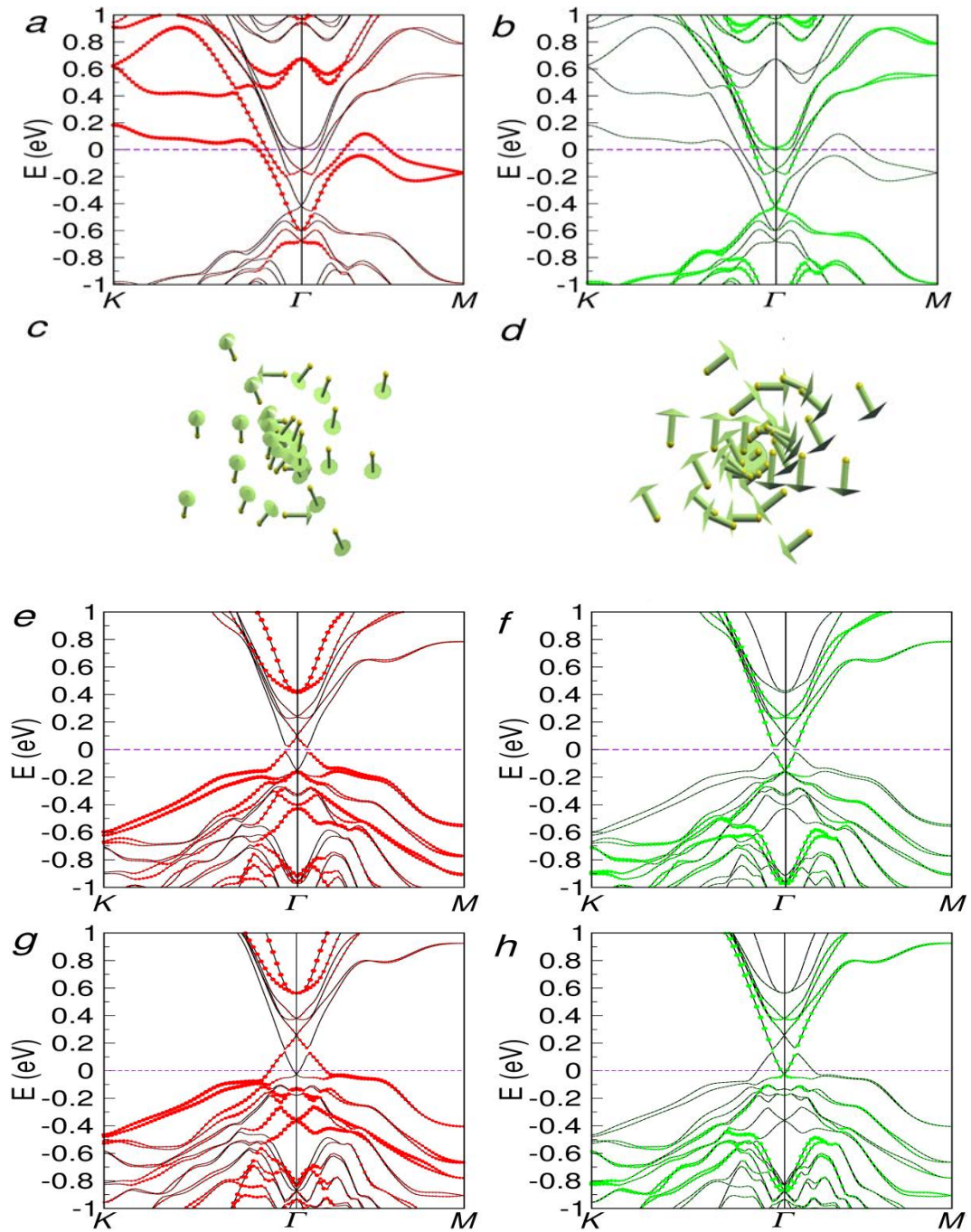


Fig. 3.7 Top panel shows the band structure of fully relaxed 3QL Bi_2Se_3 slab with top QL hydrogenation (H–Se distance is 1.52 Å). Red and green circles indicate the projection on the top (a) and bottom (b) QLs. Second panel shows the spin texture at one of the M points (c) and at the Γ -point (d). Rest of the panels show the band structure of the same system, but for larger H–Se distance: 3.52 Å (e)–(f) and 5.52 Å (g)–(h)

As previously observed [14, 15], surface modification of Γ centered TIs may give rise to new nontrivial surface states centered at the three M points of the Brillouin zone (figure 3.7a). The origin of such new surface states seem to be related to the presence of dangling bonds

appearing during cleaving process [16] due to the formation of non-stoichiometric surface terminations like Se–Bi–Se or Se–Bi. Here, the new surface or mid gap states appear by a simple chemical saturation of the top Se atoms by hydrogen. This case is even more interesting than non-stoichiometric surface terminations since the latter ones are highly reactive and may tend to reconstruct.

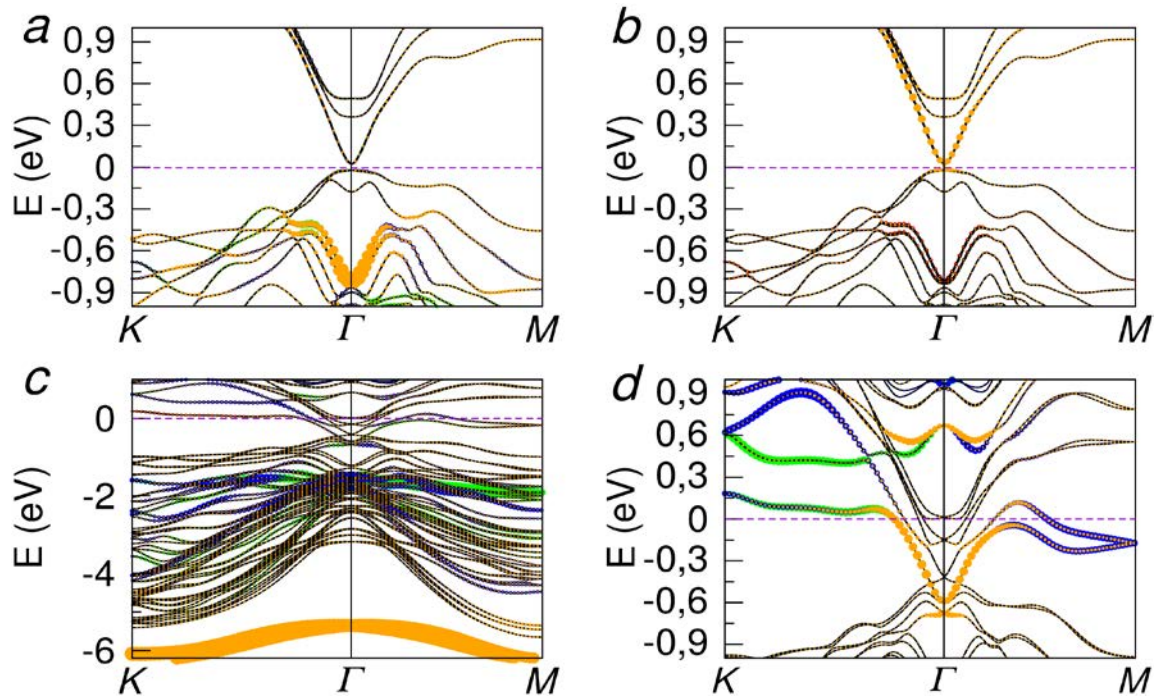


Fig. 3.8 Atomic orbital projection of the top Se (left panel) and Bi (right panel) atoms on the band structures corresponding to the pristine 3QL Bi₂Se₃ case (a), (b) and the hydrogenated case (c), (d). The different colors correspond to 1s (red), p_x (green), p_y (blue) and p_z (yellow)

A detailed analysis of the atomic orbitals involved on the formation of this new state is shown in Fig. 3.8, where we plot the band structures of pristine (a), (b) and hydrogenated (c), (d) slabs projected onto the atomic orbitals of the surface Se (left panel) and Bi (right panel) atoms. After hydrogenation, the bands corresponding to the p_z orbitals of the Se atoms (yellow circles) disappear from the low-energy region due to the hybridization with the 1s orbitals of the H atoms. On the other hand, the p_z orbitals of the Bi surface atoms that mainly contribute to the formation of the topological surface states in the pristine case, are still present after the hydrogenation but at lower energy (Figs. 3.8b and 3.8d). More interestingly, while typical topological surface states centered at the Γ - point show a strong p_z contribution from the top QL atoms, now the contribution of the p_y orbitals from the Bi atoms of the second layer on the new topological surface states at M is even stronger than the p_z orbital contribution, which

manifests the presence of in-plane dangling bonds in the top Bi–Se interface. Also, the spin texture associated with this new Dirac cone shows a spin-momentum locking configuration which resembles that of a Dresselhaus spin–orbit interaction typical of 3D materials, with a strong out-of-plane spin polarization (Fig. 3.7c).

3.5 Combining twin grain boundaries and surface doping in Bi₂Se₃ thin films

We finally consider the joint contribution of both twin grain boundary and hydrogenation introduced into the 3QLs Bi₂Se₃ film. Se atoms on the top surface are fully saturated by hydrogen atoms while the bottom QL is rotated by 180° (Fig. 3.1d). Fig. 3.9 shows the resulting band structures at opposite surfaces. Interestingly, the formation of the additional Dirac cone at *M*-point is insensitive to the twin grain boundary. It is important to note that the presence of the twin boundary along the (111)-direction and the saturation of the top Se atoms give rise to an interesting situation in which electrons may flow easily on the top surface due to the formation of the new surface state band coming from the dangling bonds (red circles), while this flow will not be allowed in the opposite surface due to the appearance of a new gap of about 200 meV (green circles).

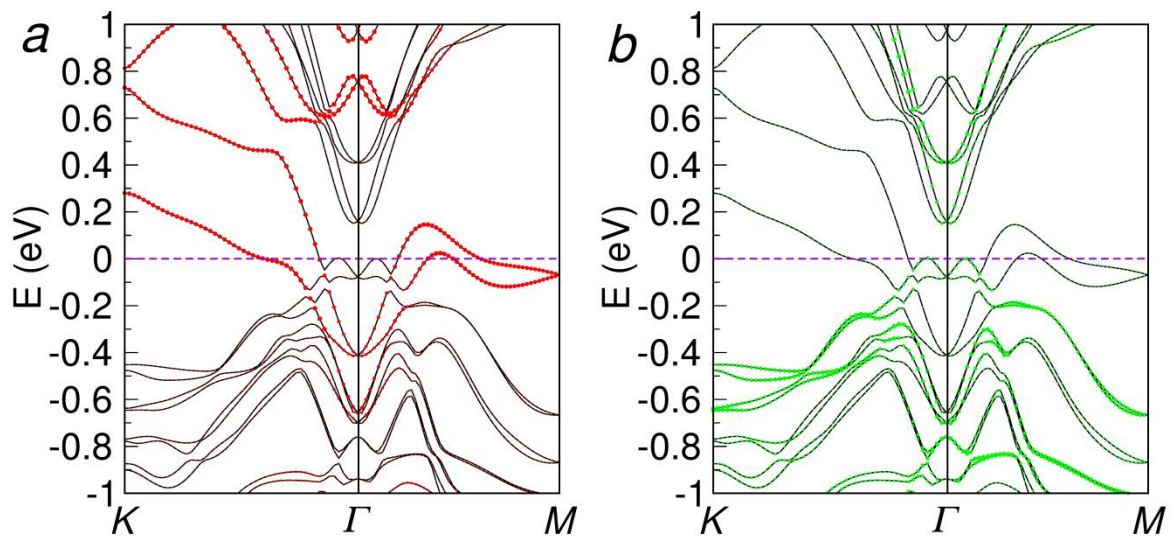


Figure 3.9 Band structure of 3QL Bi₂Se₃ with the bottom QL rotated by 180° and the top layer fully hydrogenated. Red and green circles show the projection onto the top and bottom QLs respectively

3.6 Conclusions

In conclusion, we have studied the impact of different defects on the electronic properties of ultrathin films of TIs. Twin grain boundaries are found to enhance the electronic band gap of

the film, without changing the spin texture of surface states, contrary to the case of hydrogen adatoms which modify the spin texture symmetry (similar to Dresselhaus spin-orbit interaction type) of the electronic states and generate a new Dirac cone at M -point in the Brillouin zone of the hydrogenated surface. Our results evidence that in the ultrathin limit and when the thickness is less than 2nm, the nature of twin boundary defect crucially impacts on the variability of the spin-dependent features of the electronic spectrum, which is simultaneously a limitation for fine-tune control of surface states in situation of large surface versus bulk ratio, but also suggests interesting directions to explore the spin dynamics of new electronic excitations generated by impurity bands. Similar studies of disorder effects in more complex heterostructures, such as graphene/TI [17] deserve further consideration.

References

- [1] Wang, C.; Bian, G.; Miller, T. and Chiang, T-C *Phys. Rev. B* (2013) 87, 235113
- [2] Richardella, A.; Kandala, A.; Lee, J. S. and Samarth, N. *Appl. Phys. Lett. Mater.* (2015) 3, 083303
- [3] Kastl, C.; Seifert, P.; He, X.; Wu, K.; Li, Y. and Holleitner, A. *2D Mater.* (2015) 2, 024012
- [24] Kresse, Gand and Furthmüller, *J. Comput. Mater. Sci.* (1996) 6, 15
- [5] Blöchl, P. E. *Phys. Rev. B* (1994) 50, 17953
- [6] Kresse, G. and Joubert, D. *Phys. Rev. B* (1999) 59, 1758
- [7] Perdew, J. P.; Burke, K. and Ernzerhof, M. *Phys. Rev. Lett.* (1996) 77, 3865
- [8] Tkatchenko, A. and Scheffler, M. *Phys. Rev. Lett.* (2009) 102, 073005
- [9] Liu, Y.; Li, Y. Y.; Rajput, S.; Gilks, D.; Lari, L.; Galindo, P. L.; Weinert, M.; Lazarov, V. K. and Li, L. *Nat. Phys.* (2014) 10, 294
- [10] Liu, C-X; Zhang, H.; Yan, B.; Qi, X-L; Frauenheim, T.; Dai, X.; Fang, Z. and Zhang, S-C *Phys. Rev. B* (2010) 81, 041307(R)
- [11] Lu, H-Z; Shan, W-Y; Yao, W.; Niu, Q. and Shen, S-Q *Phys. Rev. B* (2010) 81, 115407
- [12] Aramberri, H.; Cerdá, J. I. and Muñoz, M. C. *Nano Lett.* (2015) 15, 3840
- [13] Zhu, Z-H; *et al.* *Phys. Rev. Lett.* (2011) 107, 186405
- [14] Bian, G.; Wang, X.; Liu, Y.; Miller, T. and Chiang, T-C *Phys. Rev. B* (2011) 84, 235414
- [15] Zhu, X-G and Hofmann, P. *Phys. Rev. B* (2014) 89, 125402
- [16] Lin, H.; *et al.* *Nano Lett.* (2013) 13, 1915
- [17] Cao, W.; Zhang, R-X; Tang, P.; Yang, G.; Sofo, J.; Duan, W. and Liu, C-X *2D Mater.* (2016) 3, 034006

Chapter Four: Electronic Properties of Graphene/Topological Insulator Heterostructures

4.1 Introduction to Graphene/TI Heterostructures

Some parts of this chapter was published on Nano letter.[74] Following the discovery of graphene and the large family of Van der Waals heterostructures based on two dimensional materials,[1~5] the spectrum of practical applications harnessing the uniqueness of such materials has grown continuously.[6] In the area of spintronics,[7, 8] the long room-temperature spin lifetime in graphene opens the possibility of large-scale integration of lateral spintronic devices and architectures.[9~11] Additionally, many recent reports indicate the benefit of using proximity effects to tune the spin properties inside the graphene layer and to engineer devices such as spin field-effect transistors.[12, 13] This provides exciting opportunities in the search for innovative spin manipulation strategies and the development of non-charge-based information-processing technologies. Proximity effects have been studied by combining graphene with magnetic insulators; for instance, J. C. Leutenantsmeyer *et al.* attached graphene layer with yttrium-iron-garnet (YIG) substrate, which is a ferromagnetic insulator, and found that an average exchange field of 0.2 T could be induced onto the graphene layer, resulting in a magnetic-gate tunable spin[14]; while, H. X. Yang *et al.* carried out the first principle calculations and reported that EuO could induce 24% of spin polarization in the graphene states, while, the exchange band splitting gap would be about 36 meV.[15] In Ali Hallal *et al.*'s work, cobalt ferrite (CFO) was found to shift the Dirac cone of graphene downwards by 0.5 eV and induce a spin-gating in the graphene layer.[16] Singh, S. *et al.* could control the direction of the exchange field in the ferromagnetic insulator (FMI) in graphene/FMI heterostructures and then, modulate the spin current on graphene layer in the experiment[17]

The other usual way is to magnify the spin-orbit coupling (SOC) in graphene through extrinsic chemical functionalization. Avsar, A. *et al.* observed enhanced SOC strength of graphene

with value of 9.1 meV as they deposited 0.06% of fluorine atoms on the graphene layer, observing the spin hall effect at room temperature[18] Cresti, A. *et al.* theoretically reported the emergence of the spin hall effect induced to graphene by gold ad-atoms,[19] with spin hall angle of ~ 0.1 deduced from nonlocal resistance simulations.[20]

Besides these two studies, another route recently proposed is to interface graphene with transition metal dichalcogenides (TMDCs)[21, 22] such as WS_2 or WSe_2 , which leads to phenomena such as weak antilocalization (WAL)[23~25] For instance, Schmidt, H. *et al.* observed the transition from WL to WAL in graphene/ MoS_2 system with an experimental spin relaxation based on Dyakonov-Perel mechanism.[21] Wang Z. *et al.* used both experiment and first principles calculations to prove that graphene/ WS_2 heterostructure manifests strong spin orbit interaction as revealed by a pronounced WAL in the graphene layer.[23] Avsar, A. reported very large nonlocal hall signals on graphene layer in graphene interfaced with a few layer WS_2 . [26] Additionally, the fact that electronic states in Gr/TMDC systems are spin-polarized primarily along the out-of-plane direction[27] results in large spin lifetime anisotropy between in-plane and out-of-plane spin-polarized electrons, which is, however, weakly energy-dependent and, therefore, not tunable.[28~30] However, although all reports mentioned above could induce exchange field or strong SOC to graphene layer and results in band splitting or WAL effects, but spin and momentum vectors are not locked to each other and the spin is always pointing along out-of-plane direction no matter how the direction of current is altered.

Recently, a lot of attention has been paid to heterostructures of graphene and topological insulators (TIs), with reports of anomalous magnetotransport, giant Edelstein effect, and gate tunable tunneling resistance; for example, Kim, N. *et al.* measured the magnetotransport in graphene with Bi_2Se_3 heterosystem and revealed the topological surface state, which is spin-momentum locking, on graphene layer[31] Zhang, L. *et al.* observed the gate tunable resistance on graphene layer in heterostructure with Bi_2Se_3 , which indicated graphene as the quantum hall insulator,[32] and, in another paper, they also reported a giant negative magnetoresistance with nontrivial spin texture on graphene interfaced with Bi_2Se_3 . [33] In Zalic, A. *et al.*'s work [34], bilayer graphene was found to possess the Landau level due to carriers of large fermi surface when it is attached with Bi_2Se_3 ; while, Rodriguez-Vega, M. *et al.* showed that monolayer or bilayer graphene interfaced with TIs could have giant Edelstein effect and spin-orbit torque.[35] Meanwhile, other works also pointed out the possible existence of a

quantum spin Hall phase on graphene adjacent to TI films.[36, 37] On the more applied side, the fabrication of broadband photodetectors based on Gr/TI heterostructures has been realized[38] as well as the injection of spin-polarized current from an ultrathin Bi₂Te₂Se nanoplatelet into graphene.[39] TI materials are distinguished by their strong intrinsic SOC, which leads to the formation of a bulk band gap and 2D surface states that host massless Dirac Fermions with spin-momentum locking.[40~45] Proximity to a TI leads to a band gap opening and spin-split bands in graphene, as discussed theoretically for the case of Bi₂Se₃,[46, 47] or for graphene interfaced with Sb₂Te₃. [37] Furthermore, graphene layer had already been reported to show the similar spin-momentum locking feature as that on TI surface state, which is quite different from those methods mentioned in previous parts. Dmitrii Khokhriakov *et al.* combined graphene with Bi₂Se₃ film together and measured spin transport and precession and reported that the spin signal and lifetime could be tuned and suppressed, owing to the hybridization between graphene and TI bands, which could open up a new opportunities for device functionalities controlled by topological proximity effects.[74]

However, currently there is substantial variability in the literature concerning the precise spin characteristics of Gr/TI systems. Rajput and co-workers measured and calculated a spin splitting of ~80 meV in graphene on Bi₂Se₃,[47] while Lee *et al.* calculated a band gap of up to 20 meV induced in graphene by Bi₂Te₂Se when all Dirac cones coincided.[48] Kou *et al.* predicted a SOC of ~2 meV induced in graphene sandwiched between two layers of Sb₂Te₃. [49] They also pointed out, as did Lin *et al.*, [50] the importance of the *Kekulé* distortion on the magnitude of the band gap in graphene. Jin and Jhi reported a TI thickness dependence of SOC induced in graphene by Sb₂Te₃, and they also hinted at unusual spin textures induced in the graphene bands.[51] Meanwhile, De Beule *et al.* [52] concluded that the spin texture imprinted on the graphene states should resemble the standard *Rashba* texture, as also found in Zhang *et al.* [53] Overall, these works indicate that TIs clearly induce strong proximity effects, resulting in gap opening and spin splitting of the bands, but the precise nature of the spin texture induced in the graphene layer, and the ways to detect it experimentally are crucially lacking. Additionally, such information is not only essential for clarifying how proximity effects between graphene and TIs generate the measured properties but also could enlarge the possibilities for tailoring spintronics applications.

To explain this experimental phenomenon and examine this heterostructure in this chapter, fundamental electronic properties, including both band structure and spin transport properties

of Gr/TI heterostructures, were computed based on *ab initio* calculations and then the results were fitted to tight-binding (TB) models that could fully reproduce both the band structure and the spin texture in the graphene layer. Structures with different twist angles between the graphene and the TI are considered, but in all cases, a giant spin lifetime anisotropy in the graphene layer, with in-plane spins relaxing much faster than out-of-plane spins, is obtained. In the highly commensurate structure, with a twist angle of 30° , the anisotropy is maximal near the graphene Dirac point, reaching values of tens to hundreds, and decays to $1/2$ at higher energies. Meanwhile, in the larger unit cell, with a twist angle of 0° , the anisotropy remains high at all Fermi energies and exhibits a strong electron–hole asymmetry. The difference in these behaviours is driven by the dominating SOC terms in each structure, which depend on the specific interface symmetry. This contrasts with prior calculations of the spin texture in Gr/TI systems, which predicted a purely *Rashba*-like spin texture with an energy-independent anisotropy of $1/2$. [52, 53]

Theoretical predictions in this work could be experimentally confirmed by performing a gate-dependent measurement of the anisotropy as recently achieved in Gr/TMDC samples, [29, 30, 54, 55] heterostructures that, however, do not exhibit any gate dependence. Differently, Gr/TI allows for a strong gate dependent anisotropy, enabling the fabrication of tunable spin filtering devices, while the in-plane spin-momentum locking could also make it possible to convert charge current to spin current and to control the spin orientation of the current. [39]

4.2. Parameter settings for DFT calculations

AB initio calculations of the electronic structure of Gr/TI heterostructures were carried out using density functional theory (DFT), [56] implemented in the Vienna *Ab initio* Simulation Package (VASP), [57] with the wave functions expanded in a plane wave basis with an energy cutoff of 600 eV using the projector-augmented wave method. [58] The PBE form of the generalized gradient approximation [59] was used to compute the exchange-correlation energy. Due to the different cell size for Gr/TI heterostructure with different twisted angle, a $24 \times 24 \times 1$ and $9 \times 9 \times 1$ k-point meshes were adopted for the small and large unit cells together with a convergence criterion of 10^{-6} eV. The spin–orbit coupling was included through noncollinear calculations, while the Van der Waals force was accounted for based on the Tkatchenko–Scheffler method, [60] and all structures were fully relaxed until forces were smaller than 10^{-2} eV/Å.

4.3. Band structure of Gr/1QL Bi₂Se₃ system with hollow configuration

In our simulations we found that the relaxed interlayer spacing between graphene and TI surface could vary a lot with the initial geometry, therefore, several initial settings were tested for this interlayer spacing; then, graphene layer and atoms on 1st TI layer were fixed along *z*-axis; while, coordinates in other two axes (*x* and *y*) were fully relaxed with the rest atoms in the system relaxed along all three axes. Through comparing energy of relaxed system with different initial interlayer spacing, that with lowest energy was adopted for the following study of electronic properties.

Taking the simulated Gr/TI heterostructure, which contains a Bi₂Se₃ film with one quintuple (1QL) thickness and one monolayer of graphene in a $\sqrt{3} \times \sqrt{3}$ supercell as an example, both top and side views are shown in Figs. 4.1*a*. and 4.1*b*. Se atom on 1st TI layer are labelled by green colour and it is placed on the centre of hexagon of graphene layer, which is called hollow alignment position. All energy data (energy v.s. interlayer distance), corresponding to different spacing cases, are listed in the table attached to the end of Fig. 4.1 and it is clear to see the most stable spacing corresponding to the lowest is 3.51 Å. Because the graphene layer is attached to the TI substrate, the minimum-energy lattice constant of bulk Bi₂Se₃, 4.196 Å, was adopted.

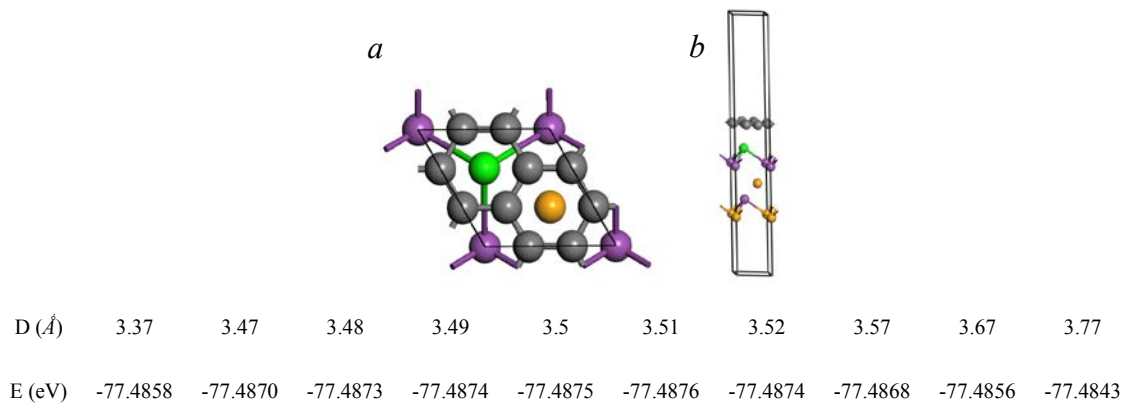


Fig. 4.1 Crystal structure Gr/1QL Bi₂Se₃ heterostructure in the hollow configuration and total energy of structure with different interlayer spacing. *a* and *b* – top and side view of the heterostructure; table – energy data for different spacing cases

The relaxed crystal structures exhibit a lattice mismatch of less than 3% and for the small unit cell, a different thickness (six quintuples) was also considered and will be simulated and compared with 1QL case in the following section. After the structure relaxation, the obtained bonding lengths for graphene layer are shown in Fig. 4.2. One determines the carbon bonding,

which structures the hexagon and surrounds the Se atom on 1st TI layer, while the other bonding length is along the connection between these hexagons. In other words, the interface mismatch results in two different carbon bondings on the graphene layer that can be seen as a *Kekulé* distortion. It has already been claimed that this distortion could play an unusual role in the band gap opening of graphene bands.[50]

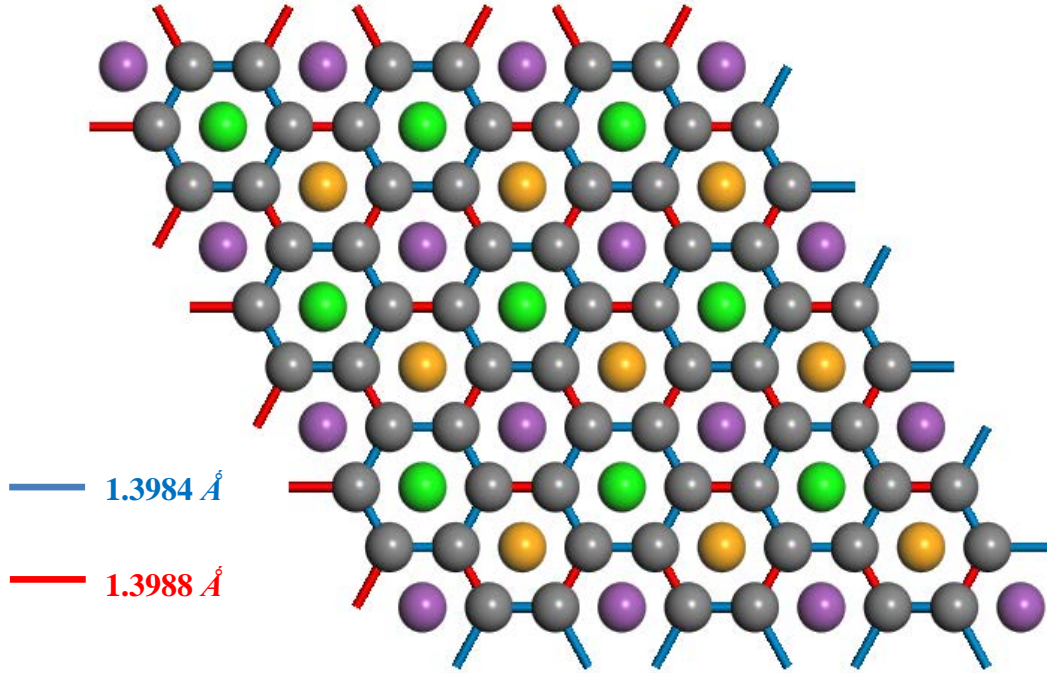


Fig. 4.2 Top view of graphene in Gr/1QL Bi₂Se₃ with relaxed carbon bonding length

In order to analyze the effect of this distortion, the band structure for the heterostructure was computed in the collinear case, which means that the SOC effect was switched off in the calculation, and the band structure for pristine graphene with 1×1 unit cell was also computed for the comparison with that with $\sqrt{3} \times \sqrt{3}$ supercell. Fig. 4.3a shows that the band structure for pristine graphene has a Dirac point (DP) located at Fermi energy level and this DP only shows at six K points in the First Brillouin zone. A very tiny gap around 18 μeV is given at K/K' point which comes from the weak intrinsic SOC effect, and it can neither be seen in the zoom-in Fig. 4.3b nor be detected in experiments, so graphene basically remains a semimetal material, despite the interaction with the TI in heterostructure of Gr/TI. On the other hand, Fig. 4.3c shows a very different band structure for graphene, which is labelled by red colour, in the heterostructure. First, the graphene DP shifts from the K to the Γ point because the $\sqrt{3} \times \sqrt{3}$ supercell can have different lattice vector in real space and this different lattice vector is used to compute those in reciprocal space. Then the different reciprocal lattice vector deter-

mines the first Brillouin zone with different size, due to the band folding. This band folding has already been reported in other studies[62] as well and with different real lattice vectors, the graphene DP could be folded to different k points. In the pristine case, there is only one DP sitting at each K point; while, in the $\sqrt{3} \times \sqrt{3}$ supercell case, the two DPs sitting at K and K' point pair are folded to the Γ point; thus, there are two valence and two conduction bands respectively. In the collinear calculation, the intrinsic SOC is switched off and there is no band splitting and each graphene valence or conduction band is doubly degenerate. Meanwhile, Fig. 4.3d shows an obvious band gap (~ 3.0 meV) opening in the graphene layer indicating that the *Kekulé* distortion can truly result in a relatively large gap opening, which is in line with the conclusion from Lin Z. *et al.*'s work.[5] The different carbon bonding lengths related to the different overlap between p -shell orbital on neighbour carbon atoms.. This will be explained with more details in the tight binding model section.

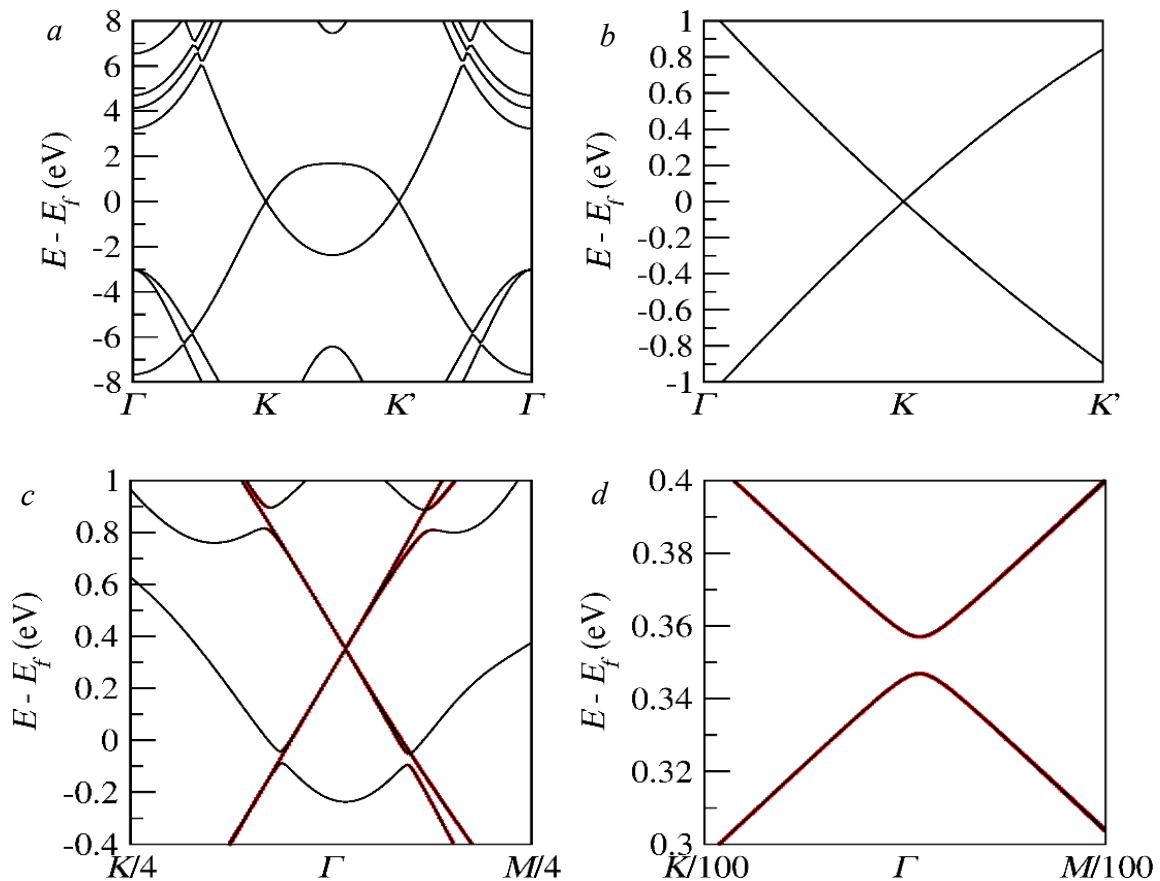


Fig. 4.3 Band structures of pristine graphene and Gr/1QL Bi_2Se_3 in the hollow configuration without SOC. *a* – band structure of pristine graphene with 1×1 unit cell; *b* – zoom-in band for *a* case; *c* – band structure of graphene with $\sqrt{3} \times \sqrt{3}$ supercell in Gr/1QL Bi_2Se_3 without SOC included; *d* – zoom-in band for *c* case. Red colour denotes the projection onto graphene bands

Besides the *Kekulé* distortion, the intrinsic SOC can also give rise to the gap opening, as already discussed in the literature; for instance, heavier ad-atoms on graphene layer can enhance the intrinsic SOC on graphene, which leads to the larger gap opening compared with the pristine case with very weak SOC strength.[20] Because of the strong intrinsic SOC, TI has its surface band inverted and this strong SOC could be transferred to graphene as well when they are combined together. Figs. 4.4a and 4.4b show the band structure of graphene with SOC included and the structure is same as that in Figs. 4.3c and 4.3d. Through the comparison, it is clear that the band gap is narrowed down in the case with non-collinear calculations and one can also see the non-equal band splittings for the graphene electronic bands. This effect actually comes from two elements. Attached to TI surface, the graphene layer its other surface exposed to vacuum zone, which breaks the inversion symmetry, and as a consequence TI surface exerts an external electric field onto the graphene layer. In the simulation, Se on 1st layer and Bi on 2nd layer are relatively close to graphene and they form charge dipole, tilted from z axis, which has both in-plane and out-of-plane components. Looking at the top view of this hollow configuration, there are three in-plane dipole components induced onto graphene and they are crossing three alternative carbon bondings and pointing from outer to inner of graphene hexagon. Finally, these three in-plane dipole components cancel each other leading to zero in-plane dipole; while, the three out-of-plane dipole components all point along z axis with same direction, resulting in out-of-plane electric field onto graphene layer. This induced electric field is also called *Rashba*-type spin orbit coupling (SOC) and it generates π bonding for electron on graphene layer experience a superimposed potential, which can lift up one set of graphene valence and conduction bands at one K point in Brillouin zone and release the double degeneracy; therefore, causing the splitting to the bands, which is illustrated in Fig. 4.4c.

However, this splitting should be equal for both valence and conduction bands as shown in Fig. 4.4c. In 4.4b, it is clear that graphene layer have relatively larger splitting on conduction bands (~ 2.6 meV) but very tiny splitting on valence bands (~ 0.4 meV), which is apparently not the case discussed in Fig. 4.4c. As for pristine TI, the intrinsic SOC is very strong and could bring the band inversion to the surface state which lifts valence surface band upwards and pushes the conduction surface state downwards and; finally, results in the fact that valence band is located above conduction band. When the graphene layer is attached to TI surface, the strong SOC of TI could also pushes the graphene bands upwards with different magnitude. Both valence and conduction graphene bands on one set of the K points in Brillouin zone.

lounin zone are pushed towards the centre of graphene gap, which narrows down the gap opened up by the *Kekulé* distortion. In other words, the final value of the band gap of the graphene layer comes from the combined effects from the *Kekulé* distortion, the *Rashba* and intrinsic SOC and the bonding distortion which contribute to enlarging the band gap; while, the intrinsic SOC makes a counter contribution and narrows down the gap and finally, the *Rashba* SOC is responsible for the band splitting.

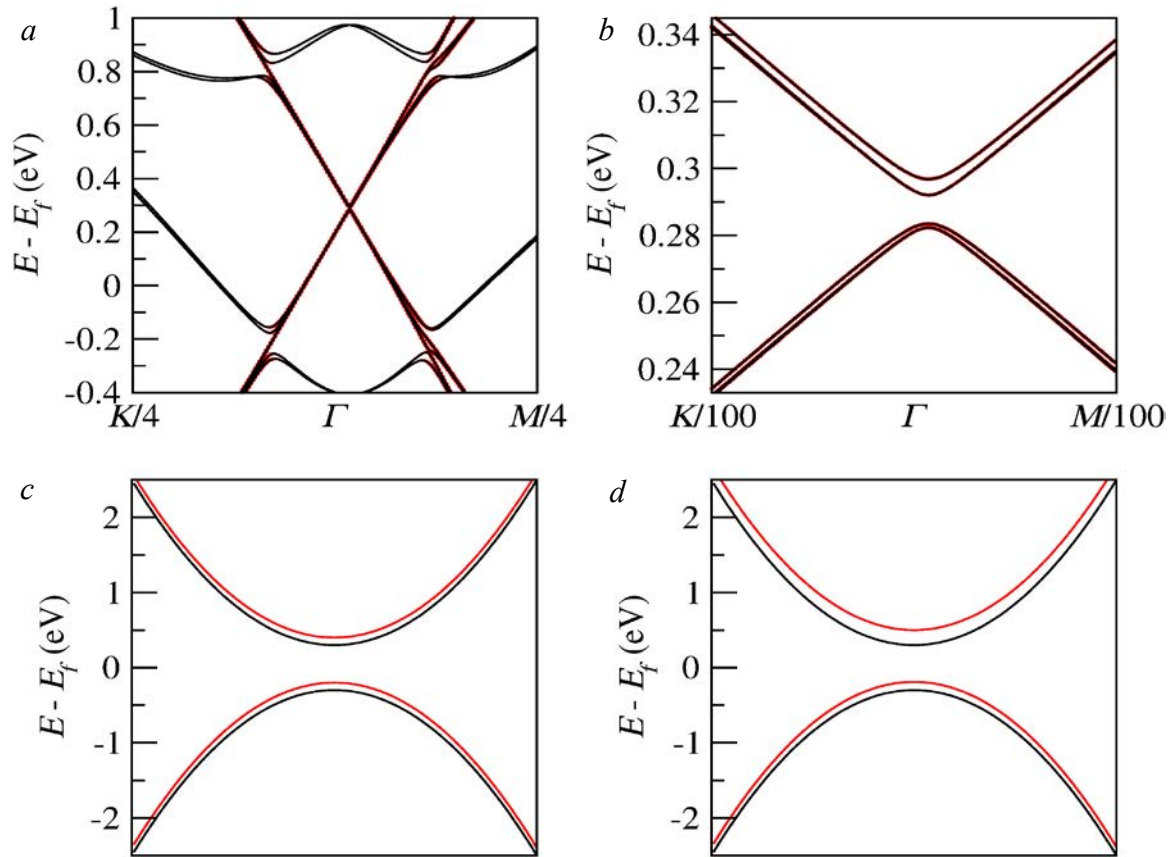


Fig. 4.4 Band structure of Gr/1QL Bi_2Se_3 in the hollow configuration with SOC and mechanism of *Rashba* and intrinsic SOC. *a.* – band structure for graphene with $\sqrt{3} \times \sqrt{3}$ supercell in Gr/1QL Bi_2Se_3 with SOC included; *b.* – zoom-in band structure for graphene with $\sqrt{3} \times \sqrt{3}$ supercell in Gr/1QL Bi_2Se_3 with SOC included; *c.* – illustration of *Rashba* SOC induced band splitting; *d.* – illustration of intrinsic SOC induced different band splitting

Another issue worth of pointing out is the interaction between graphene and TI bands. One clearly sees that the graphene bands are located in the conduction bands of Bi_2Se_3 film, dictating the charge transfer from the graphene layer to the TI surface indicating *p*-type doping in graphene. On the other hand, graphene bands also strongly hybridize with Bi_2Se_3 bands, which can be seen in Fig. 4.4*a* and these TI bands not only come from the surface state but also from the bulk because the thickness is just 1QL and the atom layer inside the TI film in-

teracts with graphene as well. It is also clear that the graphene DP shares the same energy window with TI bands, implying that injection of current on graphene layer could spread onto the TI surface as well and the signal measured include contribution from both graphene layer and TI film.

Due to quantum tunneling effect (QTE), charge potentials on the two surfaces in the TI thin film with thickness no larger than six nanometers (6 QLs) can affect each other, which causes the surface gap opening, and this is also the reason why TI films are usually produced with thickness larger than 6QLs in order to view the topological surface DP. In other words, the thickness of the TI affects the band structure, determining the formation and location of DP. It is therefore interesting to examine the thickness effect on the graphene layer in such Gr/TI heterostructures. For comparison with the 1QL TI case, graphene with 6QLs Bi_2Se_3 system is discussed below to explore the differences between these two cases.

4.4. Band structure for Gr/6QL Bi_2Se_3 system with hollow configuration

The calculation procedure for this case is similar to that in 1QL TI case and Figs. 4.5a and 4.5b show the top and side views of the heterostructure with the same hollow configuration. Through the comparison of total energy corresponding to different interlayer spacing cases, it is clear that the most stable distance remains identical (3.51 Å) and the relaxed carbon bonding length also follows the same rule that is the hexagon, surrounding Se atom on 1st layer, has the same length for all carbon bondings; while, the bonds connecting hexagons, has another different length. The relaxed carbon bond has the same length value as those in the Gr/1QL Bi_2Se_3 system, dictating that the *Kekulé* distortion is the same as that in 1QL TI case, and this also means that the gap opening in graphene layer could be same for both cases.

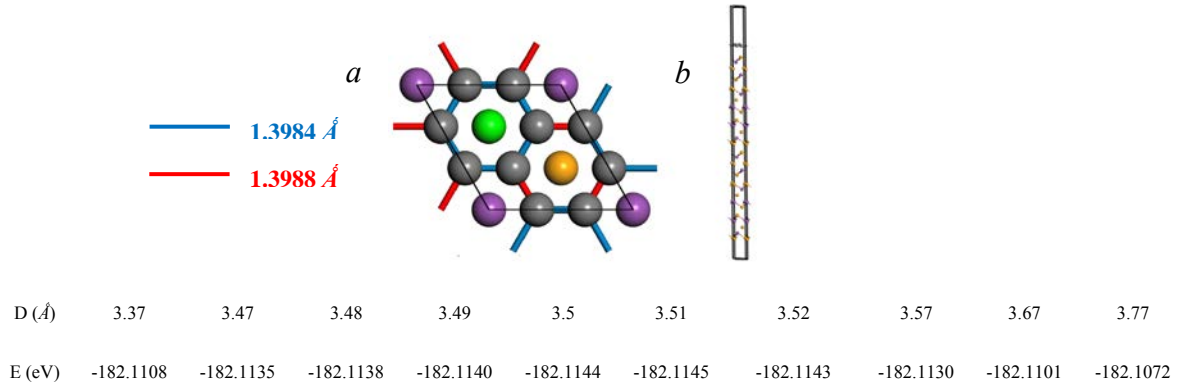


Fig. 4.5 Crystal structure Gr/6QLs Bi₂Se₃ heterostructure in the hollow configuration and total energy of structure with different interlayer spacing. *a* and *b* – top and side view of Gr/6QLs Bi₂Se₃ heterostructure with the relaxed carbon bonding length shown in *a*.; table – energy data for different spacing cases

On the other hand, the band structure of the Gr/6QLs Bi₂Se₃ is shown in Fig. 4.6*a* and, differently from the one quintuple case, the TI surface states are gapless because 6QLs is thick enough to avoid QTE, and the TI surface DPs are labelled by blue and green colours respectively, which correspond to the surface beneath graphene layer and surface far away from graphene. Because of the asymmetry in this heterostructure, the graphene layer also exerts external electric field to the TI, which acts as a dipole and lifts up the TI DP on the surface close to graphene; while it shifts the DP on the other surface below, and this is why two TI DPs are separated from each other and the double degeneracy is released. Meanwhile, Fig. 4.6*a* also shows the difference that more Bi₂Se₃ bands appear within the energy window where graphene DP sits, and they are from TI bulk state. The hybridization between graphene and Bi₂Se₃ becomes much stronger than that in 1QL case, indicating that the signal measured in experiments could have more contribution from the TI bands; especially, the bulk state. Since only TI surface states exhibit spin-momentum locking, if one likes to have a dominated surface state transport, current injection should be very careful in order to avoid the bulk contributions.

Given the same reason for the gap opening on the graphene bands in both 1QL and 6QLs cases, Fig. 4.6*b*. shows that the gap value does not change a lot and is the same as that in 1QL TI case because of the same magnitude of the *Kekulé* distortion, shown in Fig. 4.5*a*., while, the band splitting also has the same origin in both 1QL and 6QLs cases, as the splitting value is about 2.6 meV and 0.04 meV for conduction and valence graphene bands respectively. This means that the thickness of TI in this heterostructure does not affect significantly the

graphene bands; particularly, the gap and band splitting values. One explanation here is that TI film here is not thick enough to induce any change to charge distribution on the graphene layer, although it could definitely affect the TI film itself. Graphene with even thicker TI film could be very heavy for DFT computation and it is beyond the calculation capability of the VASP code. Therefore, based on all the current results, one conclusion is that the thickness of the TI film does not alter too much the graphene bands. However, one should note that the experimental work on such heterostructure often involves graphene layer attached to TI film with a few hundreds of nanometer-thickness and this could affect the charge potential on graphene layer; especially, the band gap value, because it has already been reported that the surface gap of TI film could follow an ‘open-close’ repetition rule as the thickness of TI continuously increases.

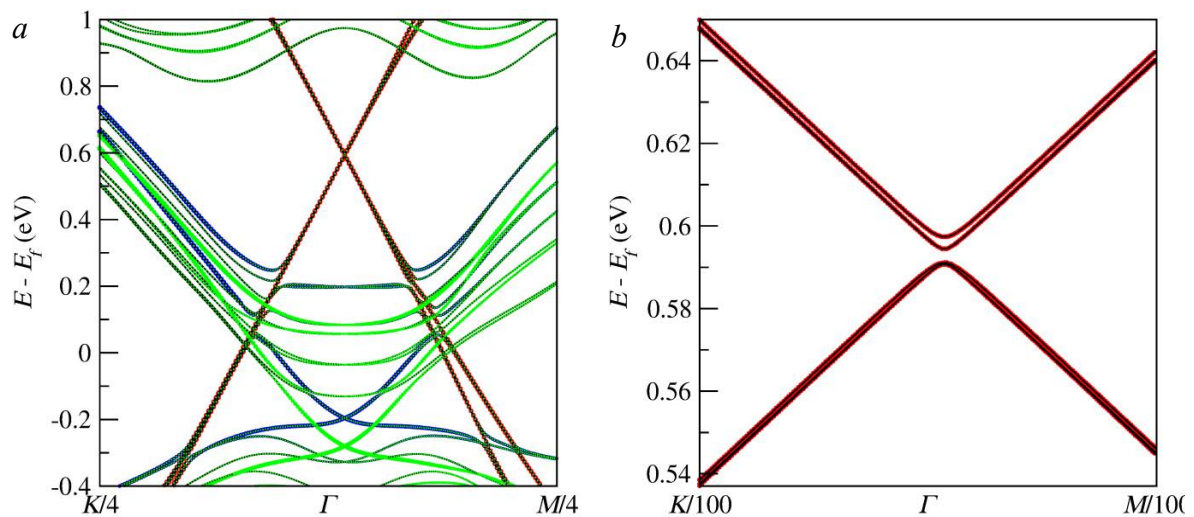


Fig. 4.6 Band structure of Gr/6QLs Bi_2Se_3 in hollow configuration. *a* – band structure of Gr/6QLs Bi_2Se_3 ; *b* – zoom-in band structure of graphene layer in this heterostructure

Since the thickness of TI film does not affect significantly the graphene band structure; the calculation of the electronic properties was restricted to the Gr/1QL TI heterostructure. It should be noted that, beyond the hollow configuration already studied in previous sections, other different configurations; such as top or bridge position, could alter the electronic properties of graphene as well due to the different effective Hamiltonian. Therefore, it is necessary to examine such structure with different alignment between the graphene and the TI.

4.5. Band structure for Gr/1QL Bi_2Se_3 system with bridge configuration

In the bridge configuration, the Se atom on 1st TI layer stays in the centre of one carbon bond of the graphene layer and Fig. 4.7 shows both top and side views of this structure. The struc-

ture relaxation procedure is similar to the prior cases and the total energy v.s. spacing is given in the table attached to Fig. 4.7. Compared with that in Fig. 4.1 table, the bridge configuration obviously gives higher energy than hollow one and the most stable interlayer distance between graphene and TI surface is also larger ($\sim 3.52 \text{ \AA}$) than for the hollow case, dictating that the hollow configuration is much more stable, compared with the bridge one. Another difference is that the relaxed carbon bonds in the graphene layer in this configuration has a uniform value without *Kekulé* distortion, which means that graphene band gap could remain small, since this distortion is the main origin of the gap opening in graphene. Additionally as already discussed in the hollow configuration, Se and Bi atoms on 1st and 2nd layers form the dipole, which has both in-plane and out-of-plane components, and the in-plane components cancel each other in the hollow configuration case and only the out-of-plane component can survive. There is no symmetric alignment for the in-plane component in this bridge position case as it is clear that one Se on 1st layer is moved beneath the centre of carbon bond and the other two Se on 1st layer is moved within the hexagon zone and the resulting dipoles exerted by these three Se-Bi interactions cannot cancel the in-plane components. This also indicates that both nonzero in-plane and out-of-plane *Rashba* SOC, induced by these dipoles, should also alter the Hamiltonian with different terms. Meanwhile, the intrinsic SOC could also be different as the electron will experience different potential from that in the hollow configuration, when jumping between second neighbour carbon orbitals. Based on the discussion for bridge configuration, it is reasonable to expect quite different band structure for graphene layer.

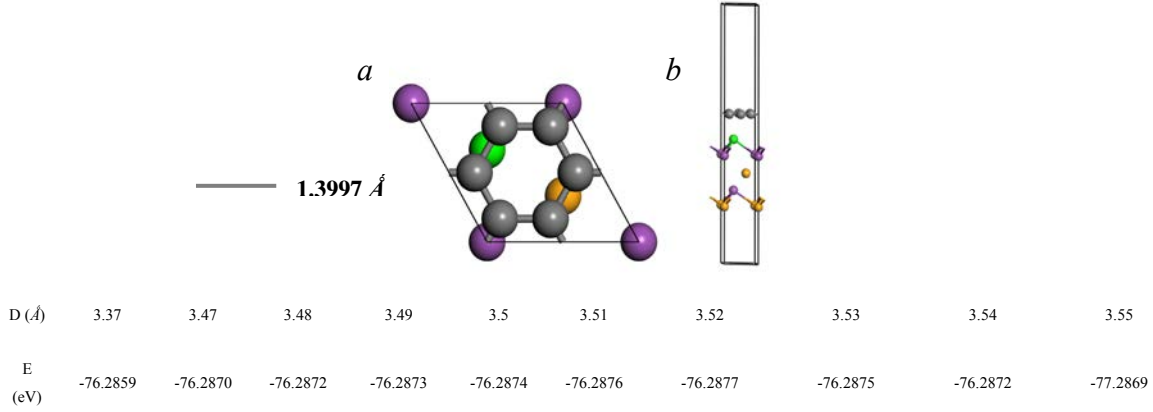


Fig. 4.7 Crystal structure Gr/1QL Bi_2Se_3 heterostructure in the bridge configuration and total energy of structure with different interlayer spacing. a and b – top and side view of Gr/1QL Bi_2Se_3 heterostructure with bridge configuration with the relaxed carbon bonding length shown in a ; table – energy data for different spacing cases

Fig. 4.8 shows the band structure for Gr/1QL Bi_2Se_3 with bridge configuration with the graphene DP which is still folded to Γ point in the Brillouin zone because the supercell ($\sqrt{3} \times \sqrt{3}$) remains the same. The gap of graphene remains very tiny (~ 0.03 meV), which is consistent with the discussion on the uniform carbon bond length on graphene layer. Furthermore, a prominent lateral splitting of bands is also observed in the graphene layer. In section 4.3, Fig. 4.4c shows that out-of-plane *Rashba* SOC induces a band splitting in the vertical direction since the external electric field is along the z axis; while, in this bridge configuration, the in-plane *Rashba* SOC is non zero as well, which could thus definitely exert an in-plane electric field, and triggers a band splitting in the lateral direction. J. Borge *et al.*[62] and Ka Shen *et al.*[63] have discussed a situation where electrons, moving within an electric field, could feel an effective magnetic field (MF), even without external magnetic field, and this effective MF has the direction related to its momentum direction. The electric field is induced on the interface with the heterostructure; for instance, electrons in the graphene layer could feel the external electric field induced from the TI film, and meanwhile, this effective MF would result in the band structure with opposite spin vectors on the split bands (shown in Fig. 4.8c), which indicates spin polarization with certain direction corresponding to specific momentum direction. When electron moves on such electronic bands, the non-even distribution of momentum would exist in specific direction and, since the spin polarization is highly related to the momentum direction, this non-equilibrium direction for momentum could involve the non-equilibrium distribution of spin polarization and; thus, the accumulation of spin along specific direction (shown in Fig. 4.8d). This process is called Edelstein effect and leads to the conversion of charge current into spin current and vice versa.

M. Rodriguez-Vega *et al.* found that substantial current-induced spin density accumulation should be generated on graphene/bilayer graphene interfaced with the magnetic TI film due to a giant Edelstein effect[64]. Fig. 4.8b shows that the Gr/1QL Bi₂Se₃ with bridge configuration, the nonzero in-plane *Rashba* SOC could induce the lateral band splitting to graphene layer even without external MF, involving the this non-even distribution for spin polarization. Finally, the charge current, moving on this graphene layer, could bring the accumulation of spin along specific direction and be converted into spin current. In other words, bridge configuration could have Edelstein effect on graphene layer; while, hollow configuration does not have this feature since, in hollow position case, only the out-of-plane *Rashba* SOC remains and no lateral band splitting is observed. This could provide an useful guide to the experimentalist for optimising the spin current conversion in such heterostructure.

Apart from the Edelstein effect on in this bridge configuration, the band structure in Fig. 4.8a also shows some similar features as those in the hollow configuration case. First, the graphene DP stays within the conduction band of Bi₂Se₃, indicating that charge transfer from graphene to TI surface. Second, strong hybridization between graphene and TI bands also exists in this bridge position case. The third point is that TI bands also appear within the energy window where the graphene DP is located; implying that the spin signal measured on graphene layer could also diffuse onto TI surface and have same contribution from TI.

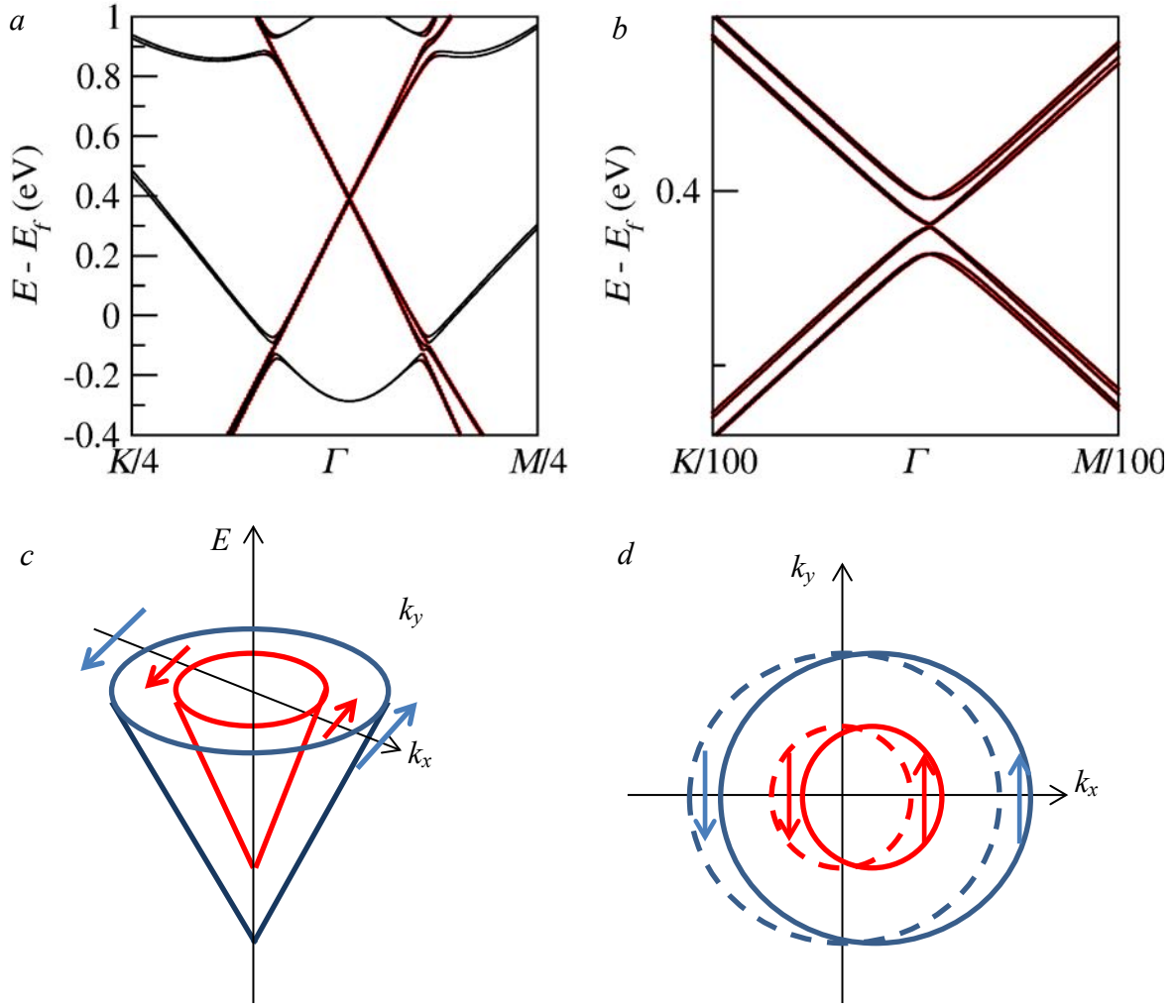


Fig. 4.8 Band Structure of Gr/1QL Bi_2Se_3 in bridge configuration and illustration of Edelstein effect. *a.* – band structure of Gr/1QL Bi_2Se_3 with bridge configuration; *b.* – zoom-in band structure of graphene layer in this heterostructure; *c.* – energy dispersion relation under strong Rashba SOC; *d.* – illustration of Edelstein effect

4.6. Band structure for Gr/1QL Bi_2Se_3 system with top configuration

Following the same calculation procedure, the Gr/1QL Bi_2Se_3 with top configuration was also examined and Figs. 4.9*a* and 4.9*b* display the top and side views of Gr/1QL Bi_2Se_3 for the top configuration. In this case, one carbon atom sits right above the Se atom on 1st TI layer and different interlayer spacing were examined with the corresponding the total energy of the whole system. It is obvious that top configuration gives the highest energy among these three position cases and the stable interlayer distance is also the largest one ($\sim 3.57 \text{ \AA}$), dictating that the most stable alignment is the hollow one and the most unfavourable configuration is the top one, in the point view of total energy. Similarly for the bridge position case, a uniform carbon bonding also shows up in the top position (shown in Fig. 4.9*a*), implying that there is

no *Kekulé* distortion of the graphene layer which presents no sizable bandgap. From the top view, one clearly sees the asymmetry alignment for dipole, resulting from Se and Bi atoms on 1st and 2nd TI layers, and this means that nonzero in-plane *Rashba* SOC could exist in this top configuration as well. Furthermore, the displacement of Se on 1st TI layer from the centre of carbon hexagon on graphene layer could also make electrons, jumping between second neighbour carbon atoms, feeling different intrinsic SOC. For instance, orbitals on top of Se atom on 1st TI layer could experience different potential from those not located on Se atom and electron could have different additional energy. All these difference in geometry could affect the band structure a lot and bring different electronic properties.

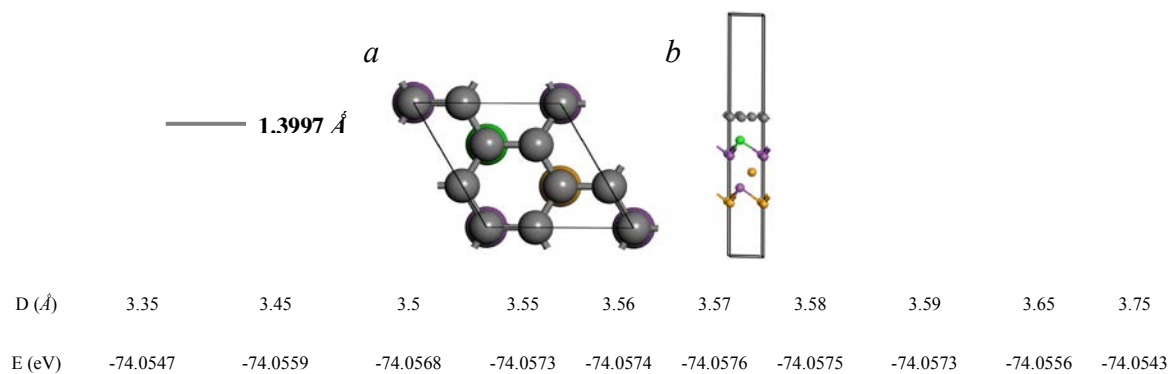


Fig. 4.9 Crystal structure Gr/1QL Bi₂Se₃ heterostructure in the top configuration and total energy of structure with different interlayer spacing *a* and *b* – top and side view of Gr/1QL Bi₂Se₃ heterostructure with top configuration with the relaxed carbon bonding length shown in *a*; table – energy data for different spacing cases

Based on the top configuration, the band structure of the heterostructure was computed (see Fig. 4.10). Apparently, the top configuration case only manifest a very tiny band gap, owing to a negligible *Kekulé* distortion of the graphene layer whereas graphene bands split in the lateral direction, indicating that the in-plane *Rashba* SOC is also non zero in the top position case. This means that a displacement of the alignment from the hollow configuration could always involve a finite in-plane *Rashba* SOC value, responsible for the lateral band splitting, and inducing a possible Edelstein effect for the graphene states. This feature could result in a conversion of charge current to spin one in the experimental measurements. Similarly, the top configuration also shows strong hybridization between graphene and TI and the TI bands co-exist with graphene DP within the same energy window, dictating the signal mixing between that from graphene layer and that from TI film. This could be an important element in interpreting spin transport measurements and affect the detected electronic properties.

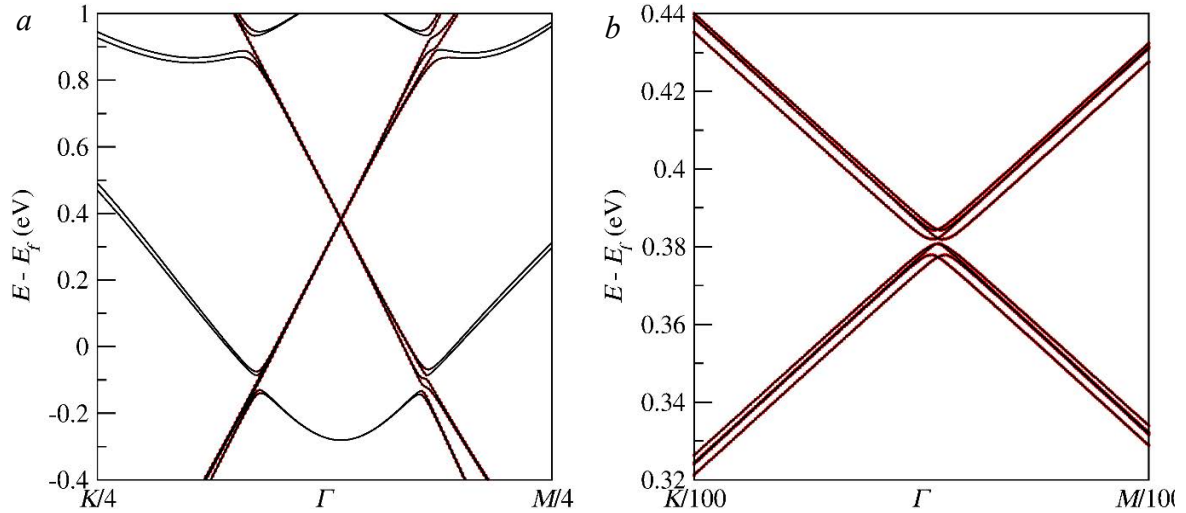


Fig. 4.10 Band structure of Gr/1QL Bi_2Se_3 in top configuration. *a* – band structure of Gr/1QL Bi_2Se_3 with top configuration; *b* – zoom-in band structure of graphene layer in this heterostructure

In the above sections, the impact of both thickness and configuration elements on the band structure of Gr/ Bi_2Se_3 heterostructure have been compared and discussed. The most common situation in experiment is that all three configurations should coexist in such device, because both alignment and interlayer spacing between graphene and TI surface are very difficult to control and one usually measures the signal based on the average effect of all different configurations. Thus, the next point is to include different configurations in the same structure and examine the band structure for the average effect.

4.7. Band structure for Gr/1QL Bi_2Se_3 system with three configurations

There are three common positions (hollow, bridge and top) included in graphene layer with 5×5 supercell/1QL Bi_2Se_3 with 3×3 supercell as shown in Fig. 4.11. Therein to, one Se atom, sitting at the four corners, is located in the hollow position; while, two are in the top position and another two are in the bridge positions. Following prior discussion, concluding that different configurations could give different Van der Waals interlayer spacing, this big unit cell should produce different spacing between the graphene and the TI surface. For instance, the hollow configuration at four corners of the supercell could have smallest distance; while two carbon atoms right on top of Se atom could have largest spacing. In the structure relaxation step, the initial spacing was taken as the average value from those in three single configuration cases and 9×9 k point mesh was adopted in the self-consistent calculation step, due to the size of the large unit cell. According to the relaxed structure (shown in Fig. 4.11*a*), it is clear that the whole graphene layer has the uniform bond and bond length is larger than that

in hollow case but smaller than that in bridge configuration. This whole relaxed structure is based on the average effect of these three configurations, indicating that the graphene band gap could be zero because there is no *Kekulé* distortion.

Meanwhile, only the in-plane *Rashba* SOC contributions in hollow position (four corners) cancel each other whereas those in bridge and top positions keep some residual value, based on the local asymmetric geometries. Based on the previous discussions, all three configurations contribute to the non-zero in-plane *Rashba* SOC so this large unit cell should have the non-zero total in-plane *Rashba* SOC and out-of-plane *Rashba* SOC always exist. Besides that, the intrinsic SOC induced on the graphene layer could also be different at different local configurations and this should affect the electronic environment as well.

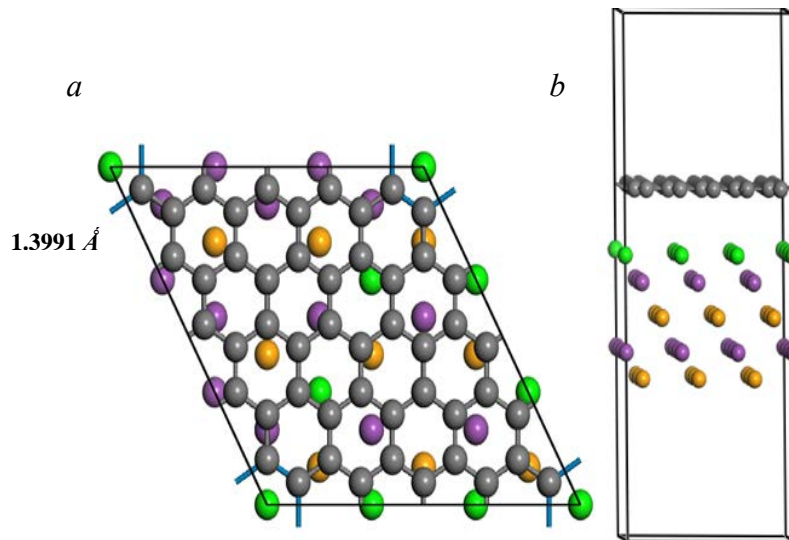


Fig. 4.11 Structure of Gr/1QL Bi_2Se_3 with big supercell. *a* and *b* – top and side view of Gr/1QL Bi_2Se_3 heterostructure with three configurations and the relaxed carbon bonding length shown in *a*

The band structure of this large unit cell is shown in Fig. 4.12 and our works on this system have already been published.[74] Given the different lattice vectors from those in $\sqrt{3} \times \sqrt{3}$ supercell in real space, the graphene bands are not folded to the Γ point anymore but are located at the K/K' points of the Brillouin zone. Accordingly, there are only two valence and two conduction graphene bands located at each K point, which is different from the case of the single configuration with $\sqrt{3} \times \sqrt{3}$ supercell. Meanwhile, the graphene layer does not exhibit any band gap because of the uniform bonding length. On the other hand, the lateral band splitting (Fig. 4.12*b*) is also observed, which indicates that the Edelstein effect could be detected as the charge current converted to spin for specific momentum direction. Another different point from the previous single configuration case is that there is no strong hybridiza-

tion between the graphene and TI bands since no TI bands show up within the energy window where graphene bands sit. Such large unit cell is more realistic in view of experiments, so one could expect to detect specific spin signals, only due to the graphene layer, which is suitable for examining modified graphene properties.

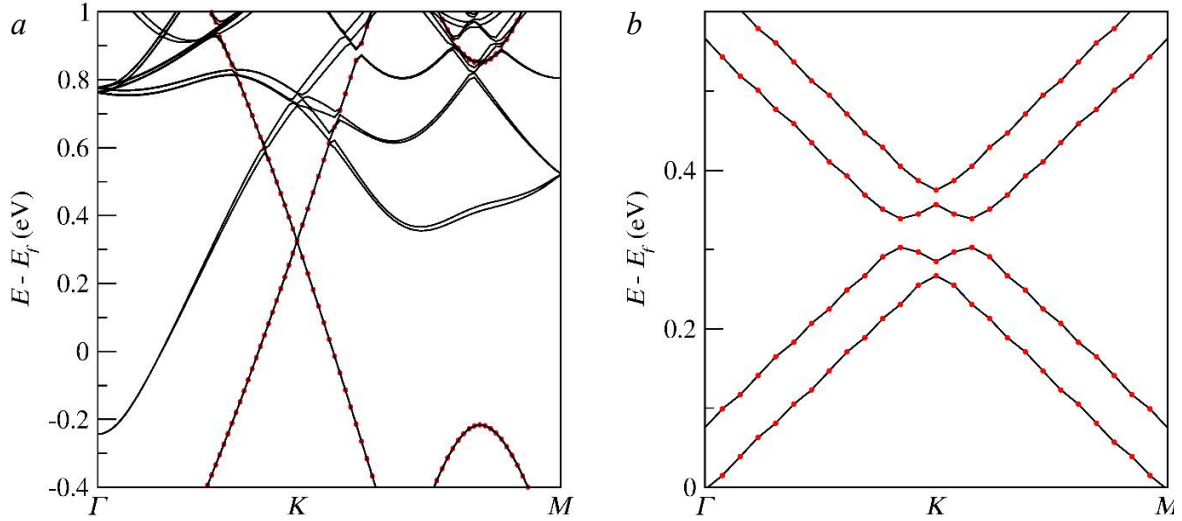


Fig. 4.12 Band structure of Gr/1QL Bi₂Se₃ with big supercell. *a* – band structure of Gr/1QL Bi₂Se₃ with three configurations; *b* – zoom-in band structure of graphene layer in this heterostructure

Besides the Bi₂Se₃, there are other 3D TI crystals, sharing the same space group but with different lattice constants. They also show topological surface states as for the strong intrinsic SOC case due to the band inversion; however, they also show some difference from each system. For instance, the pristine Bi₂Se₃ thick enough (> 6 QLs) shows surface DP weakly shifted in the valence band maximum (VBM), dictating the measured surface signal should also include some contribution from the bulk bands; while, Sb₂Te₃ has its surface DP right within the bulk band gap, which will make the spin signal uniquely driven by surface states. Such different electronic properties could induce different spin transport behaviours onto the graphene layer and since the lattice constant for different TIs are also different, the bonding distortion on graphene could also be different in the various possible Gr/TI systems. Therefore, it is necessary to examine these different substrates with different interface configurations.

4.8. Band structure for Gr/1QL Bi₂Te₃ system with three different configurations

The lattice constant for Bi₂Te₃ are smaller than that for Bi₂Se₃ and more much more different from that of graphene; therefore, the lattice mismatch ($\sim 2.8\%$) between graphene and Bi₂Te₃ is larger than that ($\sim 2.1\%$) in Gr/Bi₂Se₃ with $\sqrt{3} \times \sqrt{3}$ supercell. The structure relaxation procedure is identical to that used for the Gr/Bi₂Se₃ case and different initial interlayer spacing

has been tested and plot against the total energy of the whole system to get the most stable distance. For the sake of simplicity, only the relaxed structures with the most stable interlayer distance are shown in Fig. 4.13 for three different single configurations.

The difference for these three position cases appears clearly since the hollow configuration gives a *Kekulé* distortion, with two different bonding lengths forming in the graphene layer. One lies inside the hexagon, surrounding the Te on the 1st Bi₂Te₃ film, while the other one is between this hexagon, which is the same as that in the Gr/Bi₂Se₃ system for the hollow configuration. The different point is that the value of the bonding length in Bi₂Te₃ case, is larger than that of the Bi₂Se₃ because of the different lattice constants in these two crystals. In other words, the band gap should be different from that in the Gr/Bi₂Se₃ system because of the varying bonding distortion with different magnitude. Meanwhile, both bridge and top configurations show uniform carbon bonding lengths, similarly to the case of Gr/Bi₂Se₃ case as well.

Because the geometry in the Bi₂Te₃ case also remains the same, it is reasonable to deduce that the in-plane *Rashba* SOC is nonzero for both bridge and top ones and this is the reason why lateral band splitting happens in bridge and top cases; in contrast to the hollow one. The difference is the magnitude of splitting in these two heterostructures because of the different dipole strengths induced by Se-Bi and Te-Bi. The out-of-plane *Rashba* SOC should be uniform on graphene but with a different magnitude and could result in a different band splitting value.

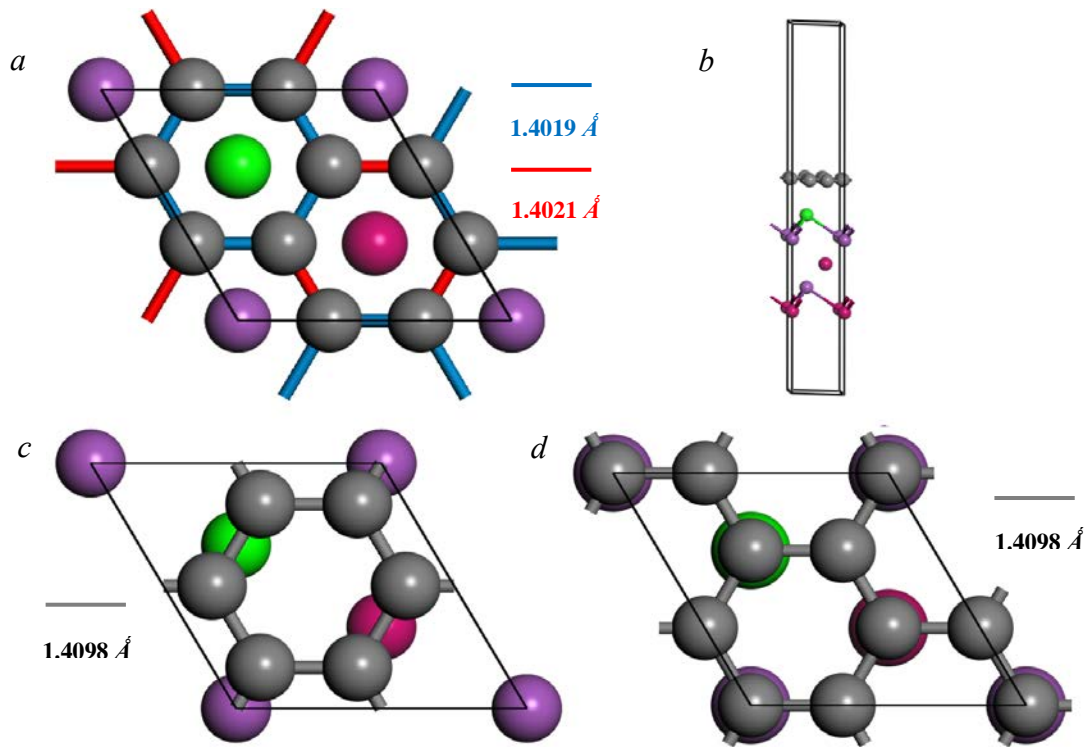


Fig. 4.13 Structure of Gr/1QL Bi_2Te_3 heterostructure in three different configurations. *a* and *b* – top and side view of Gr/1QL Bi_2Te_3 heterostructure with hollow configurations; *c* and *d* - top views of Gr/1QL Bi_2Te_3 heterostructure with bridge and top configurations.

The relaxed carbon bonding lengths are shown in *a*, *c* and *d* respectively

The band Structure for three configurations are shown in Figs. 4.14 and 4.15 from which it is clear that some differences from those in Gr/1QL Bi_2Se_3 system are evident, though the geometry and supercell are identical in each corresponding configuration. First, Fig. 4.14*b* shows that the band gap is much larger than that of the Gr/ Bi_2Se_3 system in the hollow position, which is consistent with the carbon bonding distortion in the Bi_2Te_3 case is larger than that of the Bi_2Se_3 system. Second, another different feature is that the graphene DP is located at the Fermi energy level; rather than in Bi_2Te_3 conduction bands, indicating that there is no charge transfer between them. In the Gr/ Bi_2Se_3 system, the graphene DP is located in the TI conduction band, dictating that any spin signal measured on graphene, within the energy window of graphene DP, always include contribution from the bulk bands of Bi_2Se_3 . Because of this, the Bi_2Se_3 surface states are pushed downwards inside the bulk valence bands for the 6QLs TI case. However, in this system, there are no TI bands, bulk bands in particular, around the Fermi energy level and this means that any spin signal measured within this window would only have contribution from graphene layer. This is a better situation to examine the properties of any spin current propagating in the graphene layer. Regarding the band splitting, the results are same as that in the Gr/ Bi_2Se_3 case and the explanation is same as well.

The dipole induced by Te-Bi brings the out-of-plane *Rashba* SOC is along z axis in Bi_2Te_3 , resulting in the large splitting in conduction band and small splitting in valence band (as seen in Figs. 4.14c and 4.14d).

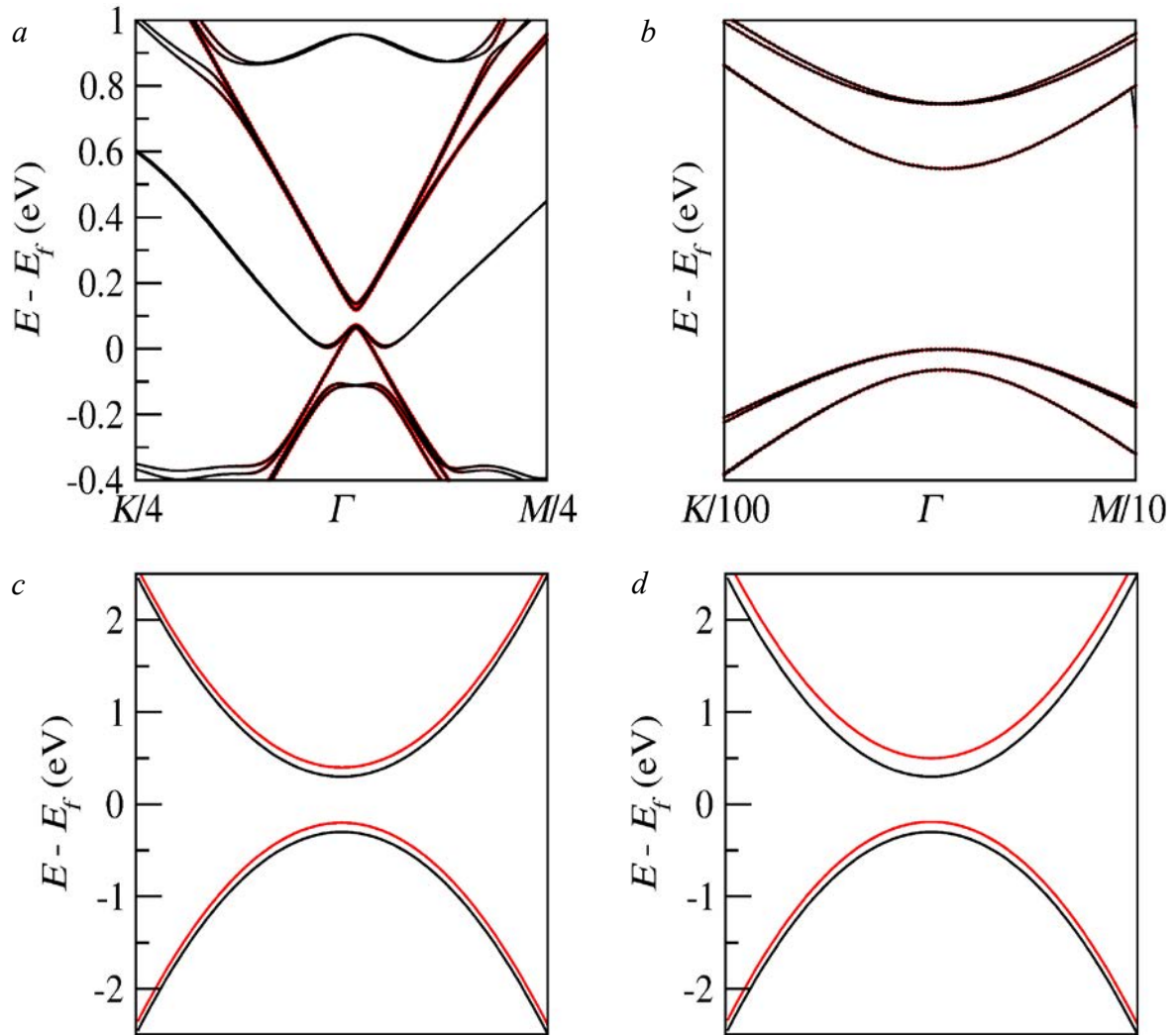


Fig. 4.14 Band structure of Gr/1QL Bi_2Te_3 heterostructure in the hollow configuration and mechanism of *Rashba* and intrinsic SOC. *a* – band structure of Gr/1QLs Bi_2Te_3 with hollow configuration; *b* – zoom-in band structure of graphene layer *a*; *c* – illustration of *Rashba* SOC induced band splitting; *d* – illustration of intrinsic SOC induced different band splitting

As far the other two configurations are concerned, in both cases it is obvious that the lateral band splitting is observed (shown in Fig. 4.15), owing to that the non-zero in-plane *Rashba* SOC remains but the difference between these two cases is that the lateral splitting in the top position is larger than that in the bridge one, dictating that top position case has larger residual in-plane *Rashba* SOC than bridge configuration. This means that the geometry really plays an important role in the morphology of the graphene band structure and originates a non-zero electric field, no matter what the TI substrate is. This also indicates that the Edelstein effect

could exist for the spin current conversion. On the other hand, it can also be seen that the graphene DP is located at the Fermi energy level in the Gr/Bi₂Te₃ system for all three configurations and only two TI bands hybridize with graphene close to Fermi level, suggesting that the spin signal measured on graphene in this system should preferentially come from graphene layer.

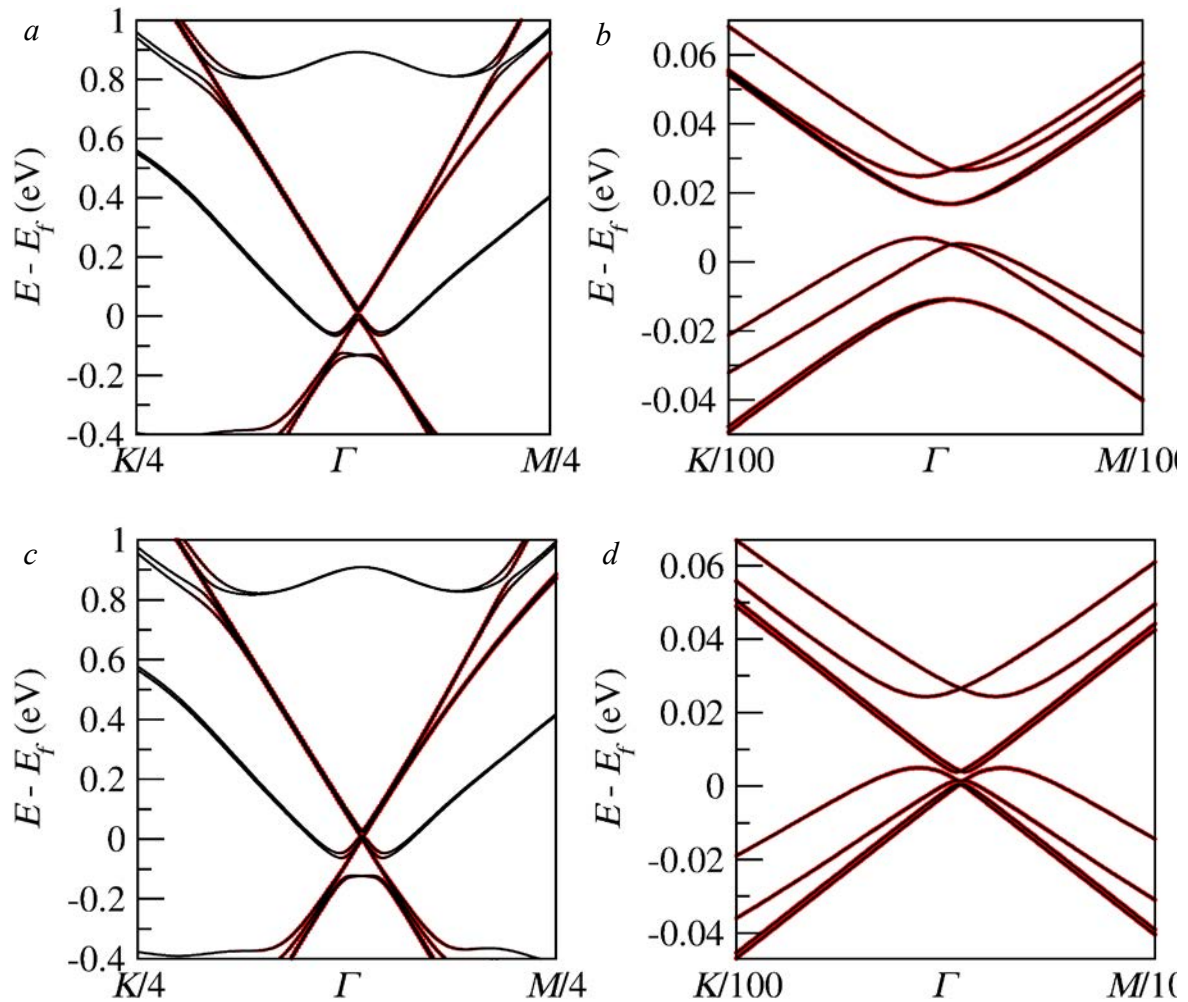


Fig. 4.15 Band structure of Gr/1QL Bi₂Te₃ with bridge and top configurations. *a* - band structure of Gr/1QL Bi₂Te₃ with bridge configuration; *b* - zoom-in band structure of graphene layer *b*; *c* - band structure of Gr/1QLs Bi₂Te₃ with top configuration; *d* - zoom-in band structure of graphene layer *c*

For the same geometry but with a large unit cell, including all three configurations for the Gr/Bi₂Te₃ system, it is expected to have the same electronic features as that in Gr/Bi₂Se₃ case. The only difference could be that the hybridization between the graphene and the TI band is not strong around Fermi energy level; then, other features (such as band splitting) should be similar. Besides Bi₂Se₃ and Bi₂Te₃, another type of 3D TI that belongs to Bi₂Se₃ family TI is the Sb₂Te₃ and the surface DP in this system is located inside the bulk band gap for the thick

film (> 6 QLs). It is also interesting to actually study such heterostructure made by combining graphene with this TI.

4.9. Band structure for Gr/1QL Sb_2Te_3 system with three different configurations

Following the same procedure as in previous sections (4.4 ~ 4.5 and 4.8), the most stable interlayer spacing between the graphene layer and the Sb_2Te_3 film was found, through the analysis of the total energy of the heterostructure. Fig. 4.16 shows all three different configurations with relaxed bonding length for this system and it is clear that the Gr/1QL Sb_2Te_3 has the largest *Kekulé* distortion in the hollow configurations among three TI substrate films, indicating that the band gap in such position should have the largest value. Meanwhile, the geometry in bridge and top configurations are also similar as those in the Bi_2Se_3 and Bi_2Te_3 cases so that a residual in-plane *Rashba* SOC is expected to be nonzero as well and a lateral splitting for graphene bands.

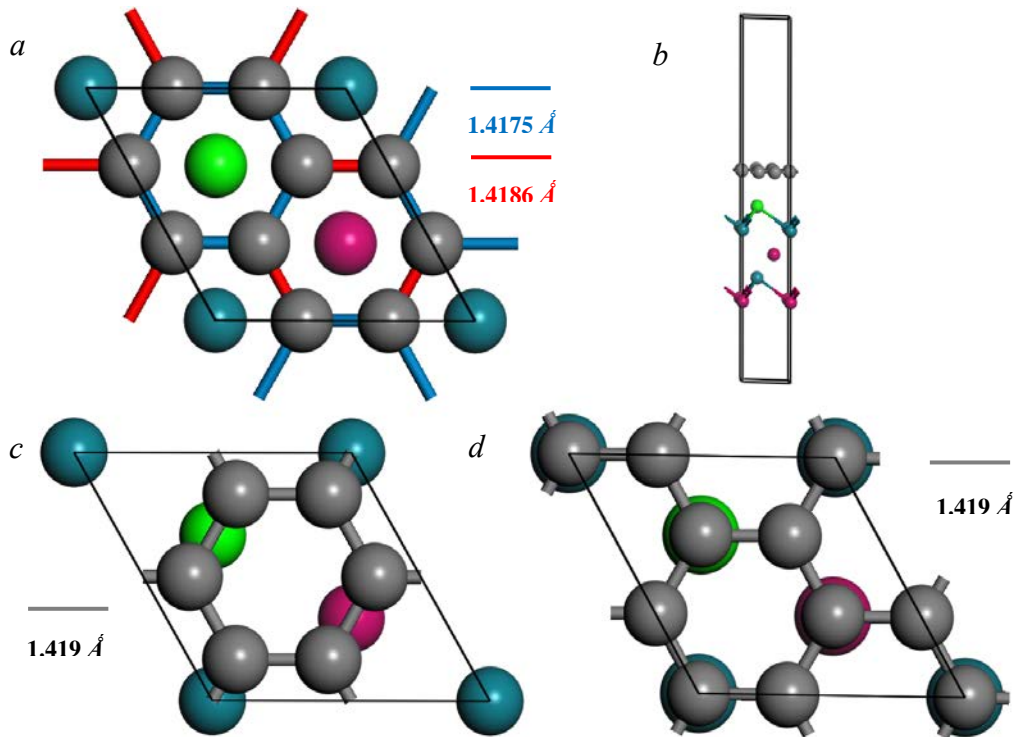


Fig. 4.16 Structure of Gr/1QL Bi_2Sb_3 heterostructure in three different configurations. *a* and *b* – top and side view of Gr/1QL Sb_2Te_3 heterostructure with hollow configurations; *c* and *d* - top views of Gr/1QL Sb_2Te_3 heterostructure with bridge and top configurations.

The relaxed carbon bonding lengths are shown in *a*, *c* and *d* respectively

The band structures for all three configurations in this case are shown in Fig. 4.17 and, as discussed based on geometry in Fig. 4.16, the hollow position gives rise to the largest band gap for the graphene layer due to the largest carbon bonding distortion, compared with the other

two substrate systems. The splitting is indeed large in graphene conduction bands; while it appears small in the valence bands for the same reason as discussed in section 4.8. Meanwhile, an obvious lateral splitting on the graphene bands is seen in the bridge and the top positions as well; noteworthy, the top position has the largest splitting value. This proves that the geometry of the interface is very important for the final band structure. For the Sb_2Te_3 substrate case, the graphene DP is located at the Fermi energy level, like in the Bi_2Te_3 case, indicating that there is no charge transfer between these two graphene and TI materials. Furthermore, there are even fewer Sb_2Te_3 bands around the graphene DP zone, meaning that a spin signal measured experimentally would mainly be driven by the graphene layer within this Fermi energy window, which is the most suitable situation for a maximum control of spin transport properties.

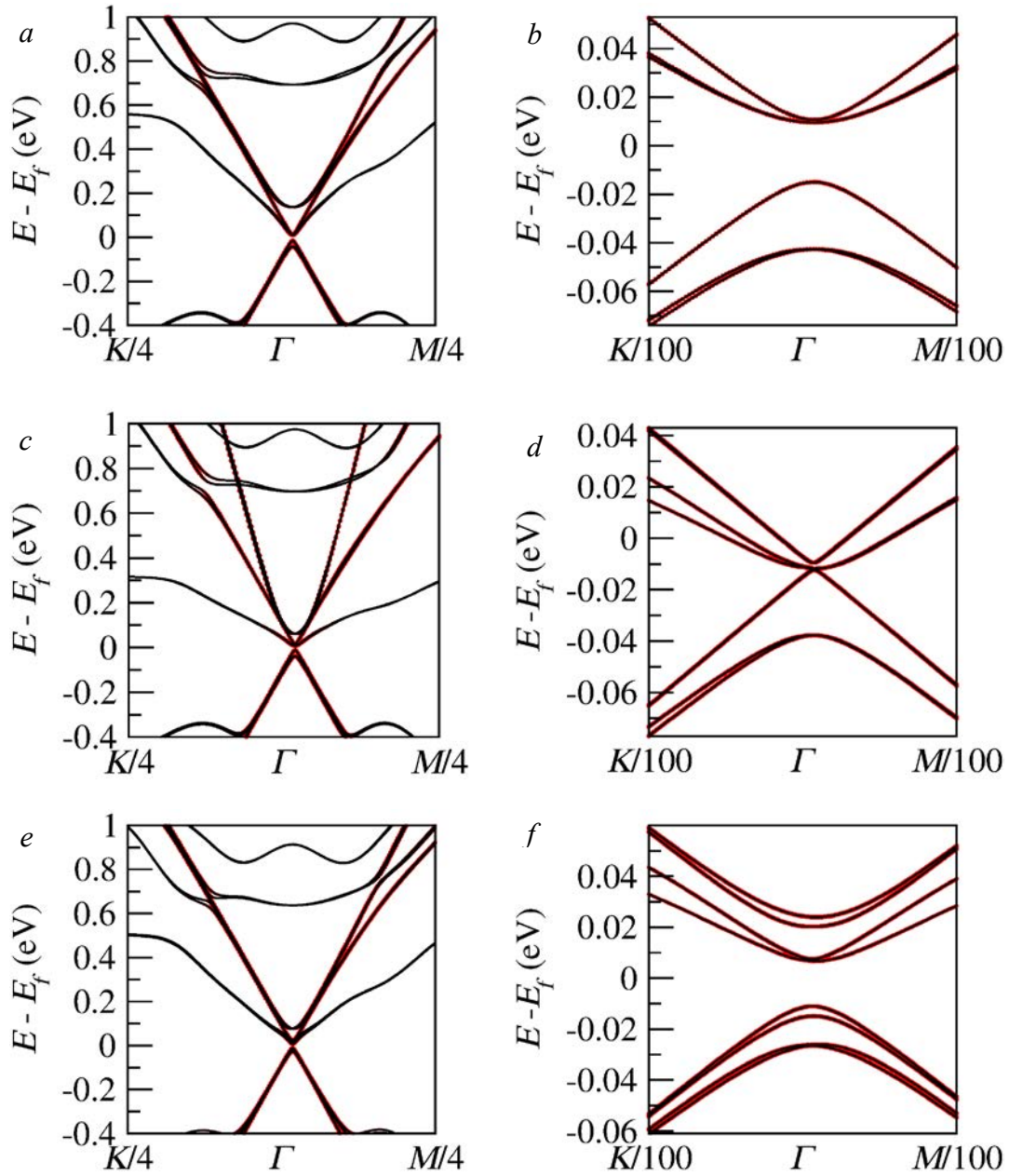


Fig. 4.17 Band structure of Gr/1QL Sb_2Te_3 heterostructure with three different configurations. – band structure of Gr/1QLs Sb_2Te_3 with hollow configuration; *b* – zoom-in band structure of graphene layer *a*; *c* – band structure of Gr/1QLs Sb_2Te_3 with bridge configuration; *d* – zoom-in band structure of graphene layer *c*; *e* – band structure of Gr/1QLs Sb_2Te_3 with top configuration; *f* – zoom-in band structure of graphene layer *e*

It can be concluded that all three TI substrates induce interesting electronic and spin features to the graphene layer; such as a band gap opening in the hollow position and a lateral band splitting in the bridge and the top configurations, because the relative interface geometry between the graphene layer and the TI surface remains identical. The only difference remains the magnitude of the SOC effects imprinted onto the graphene band. For instance, graphene in the Gr/1QL Sb_2Te_3 has the largest gap value; follows by the Gr/1QL Bi_2Te_3 and the

Gr/1QL Bi₂Se₃ structure which has the smallest gap with the same hollow configuration, due to the different magnitude of the *Kekulé* distortion. This also happens to the lateral splitting of graphene bands with different magnitude in different TI cases for both bridge and top positions. Therefore, it can be concluded that the TI substrate affects the magnitude more than the morphology of the graphene bands in function of the relative position between carbon and Se or Te on 1st layer. The cell size ($\sqrt{3} \times \sqrt{3}$) remains same no matter what TI substrate is.

In the very beginning of this chapter, a comparison between the different methods has already been mentioned, regarding the proximity effect induced onto graphene layer, and, in contrast with the effect of FMI or heavy atom doping, TI have very special properties that is spin-momentum locking of the surface state, which can be imprinted to graphene states as well. It is also, thus, necessary to examine the spin texture properties of graphene in such heterostructures.

4.10. Spin texture for graphene layer in Gr/Bi₂Se₃ system with hollow configuration

Since the 1QL TI film shows QTE between the two surface states, resulting in a surface gap opening, Gr/6QLs Bi₂Se₃ system has been shown and the comparison of the spin texture on both graphene and TI surface state. A k point mesh with ten circles round Γ point was built up because DPs on both graphene and TI stays at the Γ point and further away from the Γ point, more points were chosen on the circle so as to capture enough information for a high resolution of the spin expectation value and direction. It has already been reported that the Fermi surface for the TI surface states exhibit circular shape within a small energy window ($\sim \pm 200$ meV)[65] so that the spin texture is only taken on the k point mesh within a small zone around Γ point. In the NSCF calculation step, the expectation value for the spin operator along three axes were computed for all the bands of graphene and TI surface states.

Fig. 4.18a shows the band structure for such system where red, blue and green colours denote the graphene, TI surface beneath graphene and TI surface on the other side respectively. Figs. 4.18b and 4.18c show the top view of spin texture for blue and green surface states respectively. To have a clear view, only five k points of the circle meshes are plot here and each arrow denotes the direction of the spin vector in 3D space. From the texture, it is clear that spin and momentum vectors are always perpendicular to each other; while, side views in Figs. 4.18d and 4.18e show zero out-of-plane component. This indicates that the spin texture on TI surface follows the standard *Rashba* type texture symmetry with the expectation value for the

spin v.s. momentum angle following SIN and COS function shapes for the component along x and y axes respectively. Meanwhile, the band inversion for the two surface states brings the opposite helical texture with opposite direction for spin vectors. All these features are in line with the reference works.[66-68]

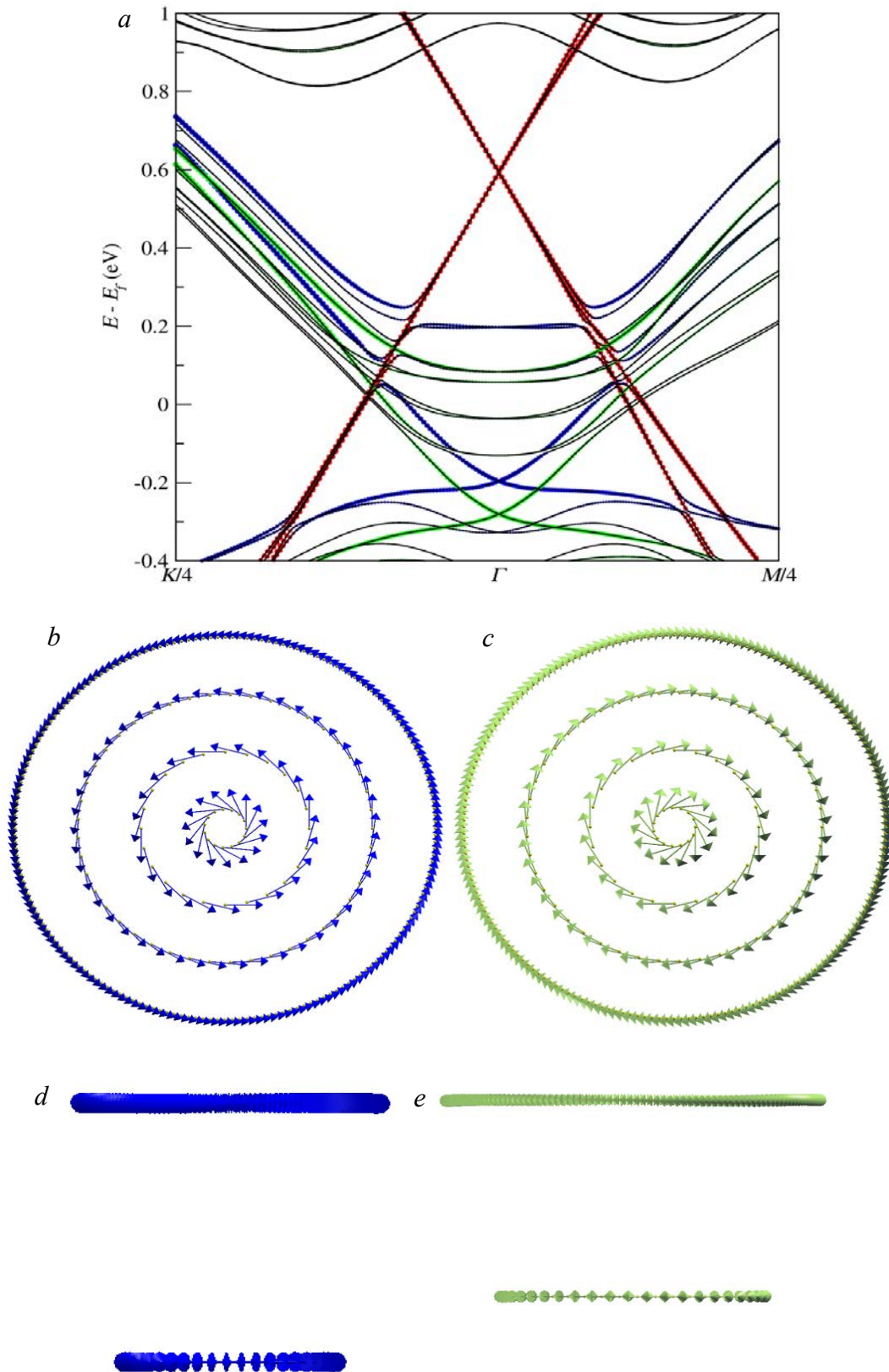


Fig. 4.18 Band structure of Gr/6QLs Bi_2Se_3 and spin texture for TI surface states. *a* – band structure of Gr/6QLs Bi_2Se_3 and red, blue and green colour denote graphene, TI surface states close to and away from graphene respectively; *b* and *c* – top views of spin texture for blue and green bands; *d* and *e* – side views of *b* and *c* cases

There are eight graphene bands folded to the Γ point in this $\sqrt{3} \times \sqrt{3}$ supercell with every two bands on the degenerate K and K' pair. It was found that every double degenerate graphene bands show the same spin texture (same magnitude but opposite direction for spin) and, to save space, only one of them is taken to illustrate the texture in Fig. 4.19 so as to compare the differences. From the top views of all bands shown in Fig. 4.19, spin and momentum vectors are not perpendicular to each other anymore and, from the side views, spin vector also shows non zero out-of-plane component for some bands, which indicates that the texture of the graphene states is not a standard *Rashba* type texture. On the other hand, spin vectors on different k point circles show the same direction along the same radial momentum angle and, once the momentum changes direction, spin also changes accordingly. This implies that the graphene bands also have a spin-momentum locking feature but this locking is different from the standard *Rashba* one for the TI surface states. Every double degenerate graphene band shows texture with opposite spin directions (not shown in Fig. 4.19), which is similar to those of the TI surface states. Furthermore, side views also show that some graphene bands (1st and 5th) have finite out-of-plane spin components; while, some have negligible ones. This phenomenon could be related to the fact that different graphene bands on different k points have different behaviours and one valley show zero out-of-plane spin; while, the other one does not. Besides these characteristics, another prominent issue is that, for those bands with non-zero out-of-plane spin components, k point circle close to Γ point only has out-of-plane spin component and zero in-plane spin; while, those circles away from Γ point have both non zero in-plane and out-of-plane spin component. This means that the ratio of in-plane and out-of-plane spin components is k point-dependent and, in other words, there is spin anisotropy on the graphene layer in such heterostructure system. This is an important feature that is worth of attention in experimental studies, because the spin current propagating in different momentum direction could have different spin relaxation time which will highly affect the final signal measured.

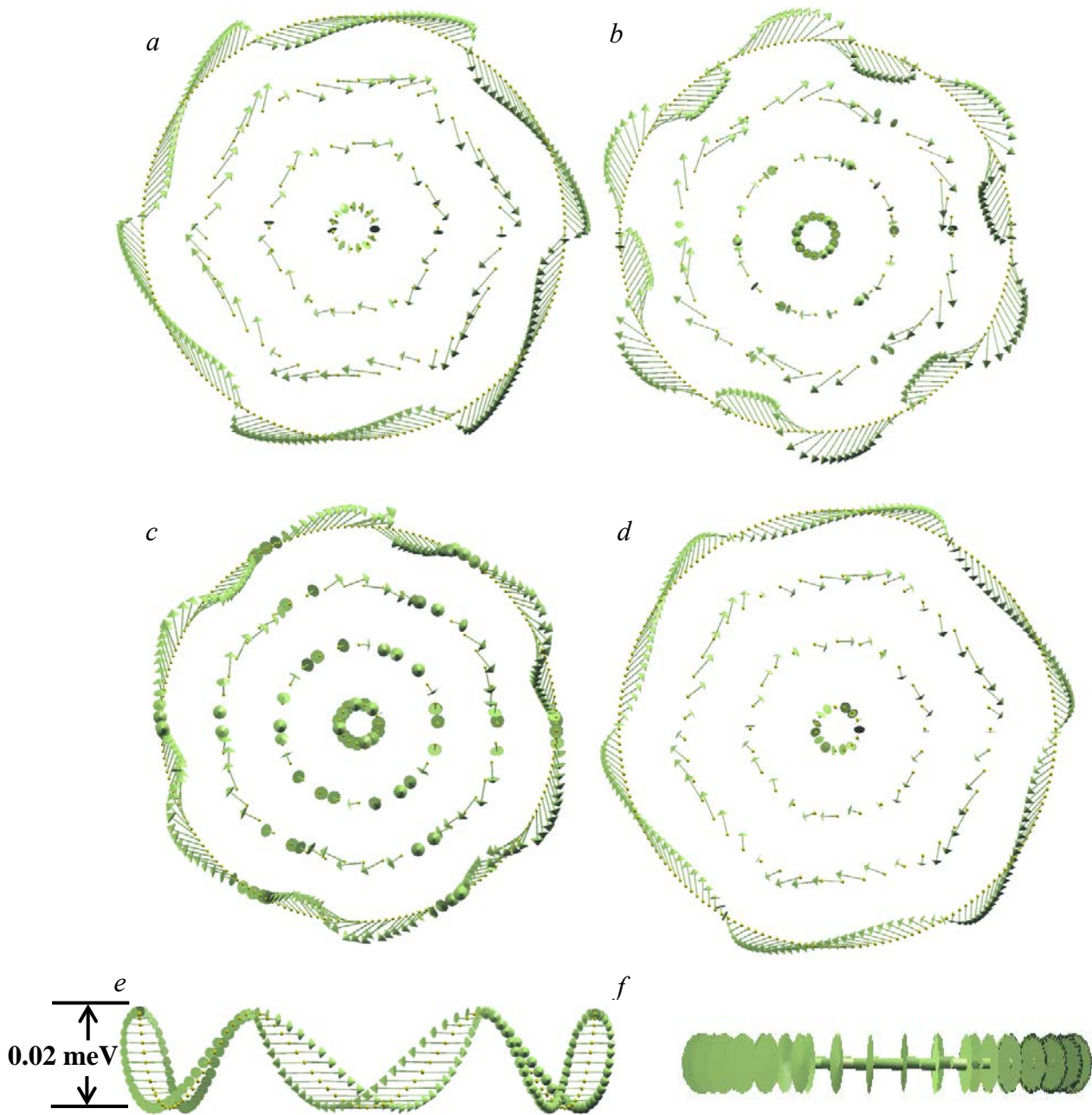


Fig. 4.19 3D spin texture for graphene bands. *a, b* – top views of texture for 1st and 3rd graphene bands; *c, d* – top views for 5th and 7th graphene bands; *e, f* – side views corresponding to *c* and *d*

In order to have an even clearer view of the texture, the expectation value of spin v.s. momentum angle is plot in Fig. 4.20, with correspondences to those bands in Fig. 4.19, and where 0° corresponds to the direction along x axis with different colour denote different k point circles and where red to black indicates circles moving away from the Γ point continuously. It is obvious that some graphene bands have non-zero $\langle S_z \rangle$; while, other have zero one. On the other hand, $\langle S_x \rangle$ and $\langle S_y \rangle$ for all bands follow SIN and COS functions-like shapes

respectively; except that there are peaks, showing up every 60° , so this is an atypical *Rashba* type spin texture. Regarding different colours, denoting k circles at different energy, it is also evident that the in-plane spin component reduces continuously as the circle contour gets closer and closer to the Γ point (from purple to red colour contour); while, the out-of-plane spin does not change with the energy, implying that the ratio between them is energy/ k point-dependent. This is consistent with the conclusion deduced from the analysis of Fig. 4.19 indicating that it is necessary to study this spin anisotropy since it matters a lot in the experimental measurement for spin current.

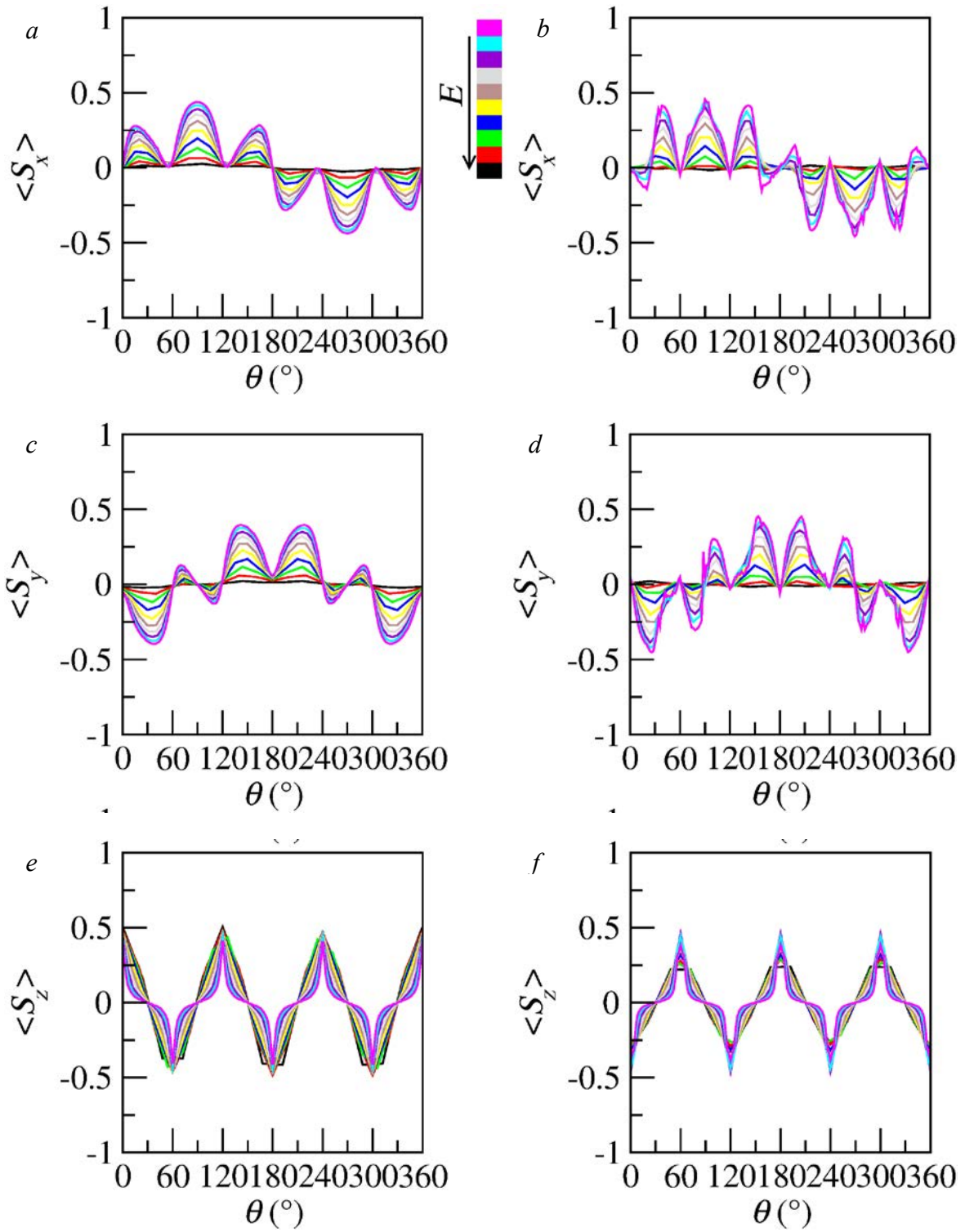


Fig. 4.20 2D expectation value of spin texture v.s. momentum angle for graphene bands. *a*, *b* – $\langle S_x \rangle$ for 1st and 5th graphene bands; *c*, *d* – $\langle S_y \rangle$ for 1st and 5th graphene bands; *e*, *f* – $\langle S_z \rangle$ for 1st and 5th graphene bands

Based on the computed spin textures, the spin lifetime anisotropy of the system was predicted and defined as the ratio of out-of-plane to in-plane spin lifetime.

$$\zeta \equiv \frac{\tau_{sz}}{\tau_{sx}}$$

Assuming the Dyakonov–Perel regime[69] of spin relaxation, the lifetime of spins polarized along α is given by

$$\tau_{s,\alpha}^{-1} = \tau_{\beta}^* \left(\overline{|\Omega|^2} - \overline{\Omega_{\alpha}^2} \right)$$

where, Ω is the momentum-dependent effective magnetic field arising from SOC in units of spin precession frequency, τ_{β}^* is the time to randomize the β -component of Ω , with $\beta \perp \alpha$, and the overline represents an average over the Fermi surface at a particular Fermi energy. For a given energy band, the effective magnetic field can be decomposed as

$$\Omega = \omega \cdot S$$

where, $\omega = \Delta E / \hbar$ is the spin precession frequency associated with the spin splitting ΔE of the band, and $S = \langle \psi | s | \psi \rangle$ is the spin polarization of the eigenstates ψ associated with the band.

The spin lifetime anisotropy arising from the spin-split band structure can then be written as:

$$\zeta = \frac{\tau_z^* \sum_{i=1}^4 \left(\overline{|S|^2} - \overline{S_x^2} \right)_i}{\tau_x^* \sum_{i=1}^4 \left(\overline{|S|^2} - \overline{S_z^2} \right)_i}$$

where, the sum over i includes each of the four conduction or valence bands in the Fermi surface average. In the $\sqrt{3} \times \sqrt{3}$ supercell, because both Dirac cones are folded to the Γ point, the following relation exists.

$$\tau_x^* = \tau_z^* = \tau_p'$$

Therefore, all k points on the same energy contour were counted together in order to compute the expectation value of spin vector and the resulting anisotropy results are given in Fig. 4.21. There are ten points along each valence/conduction side, denoting each energy contour, and the corresponding eigenvalue is used so as to see the relative position between each contour and the centre of graphene Γ point, which is shifted ($E - E_{DP}$) to 0 eV in the figure.

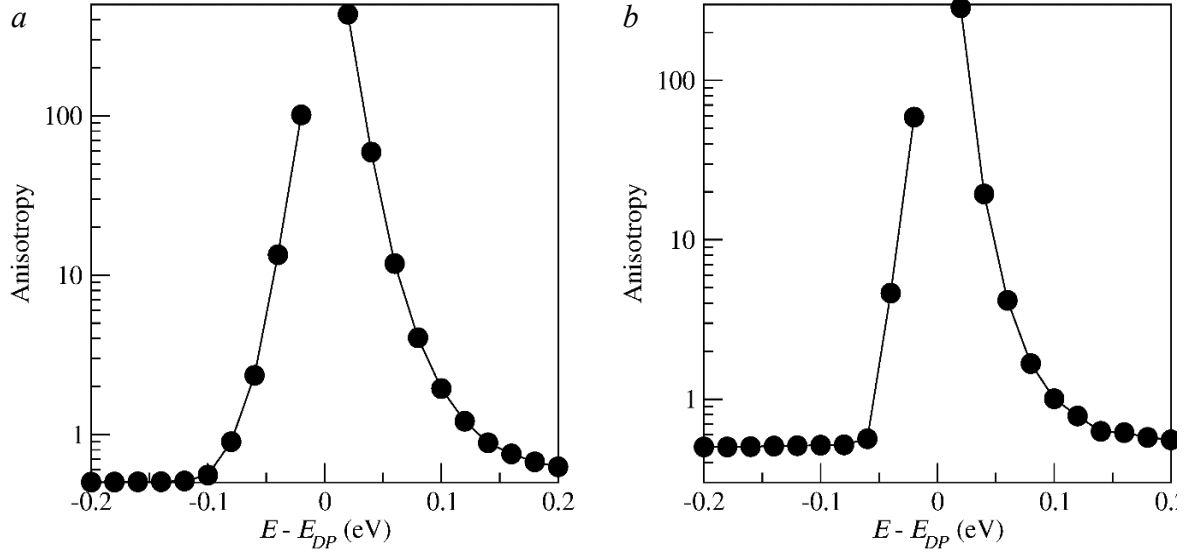


Fig. 4.21 Spin lifetime anisotropy of Gr/Bi₂Se₃ heterostructure as a function of energy relative to the graphene Dirac point. *a* – 1QL case; *b* – 6QLs case

In Fig. 4.21*b* for the $\sqrt{3} \times \sqrt{3}$ supercell as the example, one reports the spin transport anisotropy which is seen to remain negligible away from the graphene DP, in the order of 1/2, while it reaches values in the hundreds at the lowest energies. This trend (alteration of anisotropy with energy) also holds within the Bi₂Se₃ band gap, where the graphene bands are completely in-plane and the anisotropy is 1/2. Such behavior results from the increase in weight of $\langle S_z \rangle$ near the DP and the corresponding decrease of $\langle S_x \rangle$ and $\langle S_y \rangle$. Based on this result, the hollow configuration could give different spin lifetime along different spin current directions.

4.11 Spin texture and anisotropy for graphene layer in Gr/Bi₂Se₃ system with bridge, top and all three configurations

Following the same computational method, both bridge and top configurations were examined for the analysis of spin texture and lifetime anisotropy and due to the similarity in all graphene bands, only the 5th graphene conduction band in the bridge configuration is taken as an example to show the expectation value of spin v.s. momentum direction along three axes. Fig. 4.22 shows that both cases do not exhibit variation of the in-plane spin component with energy; while, both in-plane and out-of-plane spin components are in the same magnitude. This, directly, results in a very small spin lifetime anisotropy and the value is very close to 1/2, indicating that geometrical configurations not only affect the band structure but also alter the spin lifetime a lot. On the other hand, the most common configuration in reality includes

all different positions; therefore, the large unit cell with all hollow, bridge and top positions was also examined for this spin lifetime anisotropy.

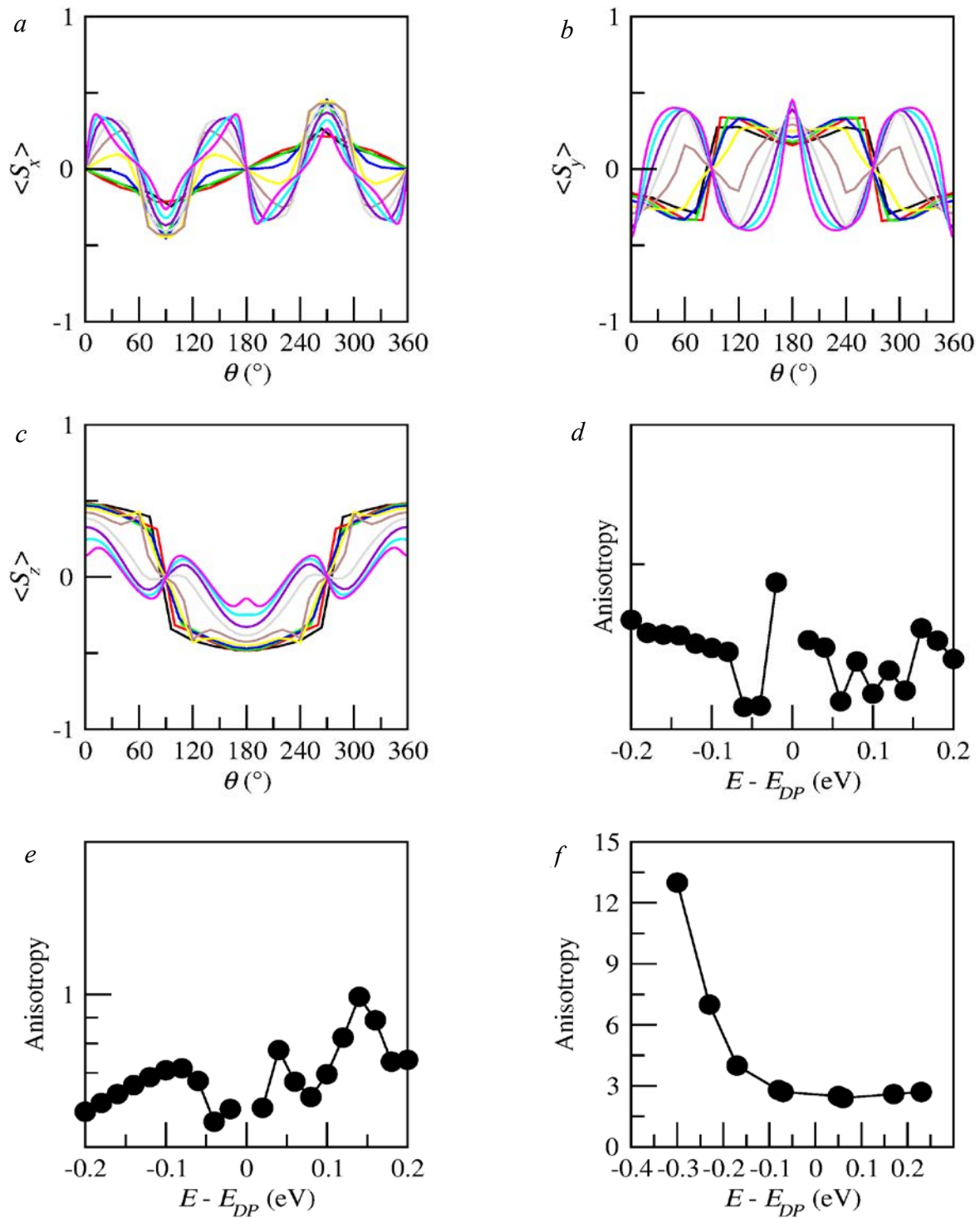


Fig. 4.22 Spin texture and lifetime anisotropy of Gr/1QL Bi_2Se_3 heterostructure as a function of energy relative to the graphene Dirac point. *a*, *b* and *c* – $\langle S_x \rangle$, $\langle S_y \rangle$, $\langle S_z \rangle$ v.s. momentum angle for 5th graphene band in bridge position. *d* – anisotropy for bridge configuration case; *e* – anisotropy for top configuration case; *f* – anisotropy in large unit cell with all three configurations

In the large supercell case, the anisotropy is characterized by a strong electron–hole asymmetry, which is driven by the relatively large value of λ_{PIA} ; as shown in ref[28], the out-of-plane spin relaxation rate is proportional to $(a \times k_F \lambda_{PIA} \pm \lambda_R)^2$, where a is the graphene lattice constant, k_F is the Fermi wavenumber, and the $+$ ($-$) is for the conduction (valence) band. At sufficiently negative energies, when $a \times k_F \lambda_{PIA} = \lambda_R$, this model predicts that the spin lifetime anisotropy will diverge. In reality, when $\tau_{s,z}$ becomes sufficiently long, another source of spin relaxation, such as contact dephasing or magnetic impurities, would take over, placing an upper bound on ζ . In systems without a strong PIA SOC, the anisotropy would be independent of the Fermi energy. In this large unit cell, the anisotropy is driven by the SOC and the charge scattering through τ_{iv}/τ_p . In general, intervalley scattering is caused by structural defects such as dislocations, grain boundaries, vacancies, *etc.*, as well as chemical adsorbates such as hydrogen, oxygen, or other hydrocarbons that could be deposited during device fabrication.[70] Bi_2Se_3 is known to suffer from Se vacancies, which might also induce short-range Coulomb potentials and intervalley scattering in graphene.[70] Measuring τ_p is straightforward because it can be deduced from the mobility and charge density. For example, a typical carrier density of $2 \times 10^{12} \text{ cm}^{-2}$ coupled with a mobility of $6000 \text{ cm}^2/\text{V}\cdot\text{s}$, as measured recently for a graphene/ Bi_2Se_3 system,[33] yields $\tau_p \approx 100 \text{ fs}$. Determining τ_{iv} requires a measurement of weak localization (WL), but in Gr/TI or Gr/TMDC systems, the strong SOC leads to weak antilocalization (WAL), making it difficult to extract τ_{iv} . So far, the best that has been done for a Gr/TMDC system is to measure WL in a region of the device that is not covered by the TMDC and to assume that value as an upper bound of τ_{iv} in the Gr/TMDC region.[25] We are not aware of any estimates of τ_{iv} in Gr/TI systems. Measurements of WL in graphene systems yield τ_{iv}/τ_p in the range of 3–20 depending on the sample quality and Fermi energy.[25, 72 and 73] Very generally, τ_p is in the range of tens of femtoseconds, and τ_{iv} is on the order of hundreds of femtoseconds to a few picoseconds. Assuming $\tau_{iv} \approx 10 \tau_p$ as a typical experimental situation, we would expect an anisotropy on the order of a few tens over the full range of gate voltage.

4.12. Spin texture for graphene layer in Gr/IQL Bi_2Te_3 and Sb_2Te_3 systems with hollow, bridge, top configurations

To analyze the differences between different TI substrates, regarding the spin texture and lifetime anisotropy, Bi_2Te_3 and Sb_2Te_3 cases were also examined and compared with the Bi_2Se_3 system for the corresponding configurations. Fig. 4.23 shows results for Bi_2Te_3 ; while, Fig. 4.24 shows that for Sb_2Te_3 cases and, due to the similarity between each band, only the 5th

graphene band is considered to illustrate the spin texture in hollow and bridge configurations. It is clear that, for Gr/Bi₂Te₃ system, hollow configuration provides a texture with in-plane spin component, varying with energy, and the out-of-plane spin vector remains same; while, bridge configuration delivers a texture with equal in-plane and out-of-plane spin components, dictating a larger spin lifetime anisotropy in the hollow case and 1/2 for the bridge one. The top position case also shows similar results like the bridge one. This is consistent with the anisotropy figure for all three cases, which points to the same conclusion that the hollow position has obvious anisotropy; while, the other two do not. A subsequent issue is anisotropy magnitude, which is large in Bi₂Se₃ case and relatively small in Bi₂Te₃ one and mainly results from the potential with different proximity effect exerted by the substrate TI films.

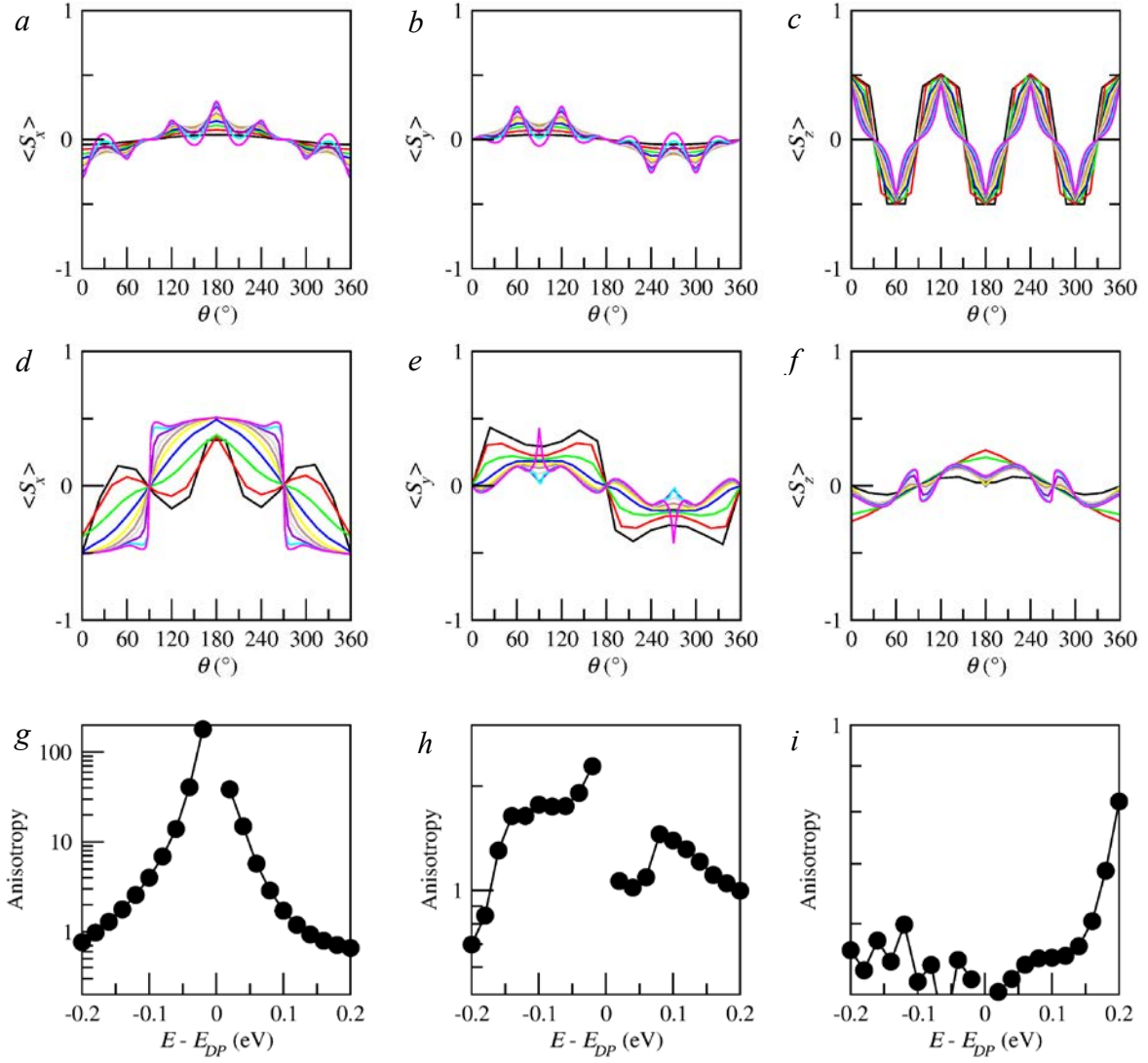


Fig. 4.23 Spin texture and lifetime anisotropy of Gr/1QL Bi_2Te_3 heterostructure as a function of energy relative to the graphene Dirac point. *a*, *b* and *c* – $\langle S_x \rangle$, $\langle S_y \rangle$, $\langle S_z \rangle$ v.s. momentum angle for 5th graphene band in hollow position; *d*, *e*, and *f* – $\langle S_x \rangle$, $\langle S_y \rangle$, $\langle S_z \rangle$ v.s. momentum angle for 5th graphene band in bridge position. *g*, *h* and *i* – anisotropy for hollow, bridge and top configuration case

Fig. 4.24 show the results for Gr/1QL Sb_2Te_3 system, which displays similar features as those in previous two cases and it can be seen that the anisotropy reaches the largest value in this system followed by the Bi_2Se_3 and finally the Bi_2Te_3 which exhibits the smallest anisotropy. All these results provide guidelines that graphene interfaced with Bi_2Se_3 family TI films should present atypical *Rashba* spin texture with peak showing up every 60° , and in-plane spin components decreasing as the k point approaches Γ point for hollow configuration; while, the out-of-plane spin component remains unchanged no matter how the k point varies in Brillouin zone, dictating a specific spin anisotropy in this configuration. Regarding the bridge and top positions, the spin anisotropy is very small and remains close to 1/2 for graphene lay-

er combined with all three substrate TI films. On the other hand, different TI substrates could induce some anisotropy with different magnitudes for the same hollow configuration, implying that the TI film does not alter the general rule but could change the magnitude, because of the charge potential with different strengths from different TI surface state, which still matters a lot for the measurement in spintronic experiments.

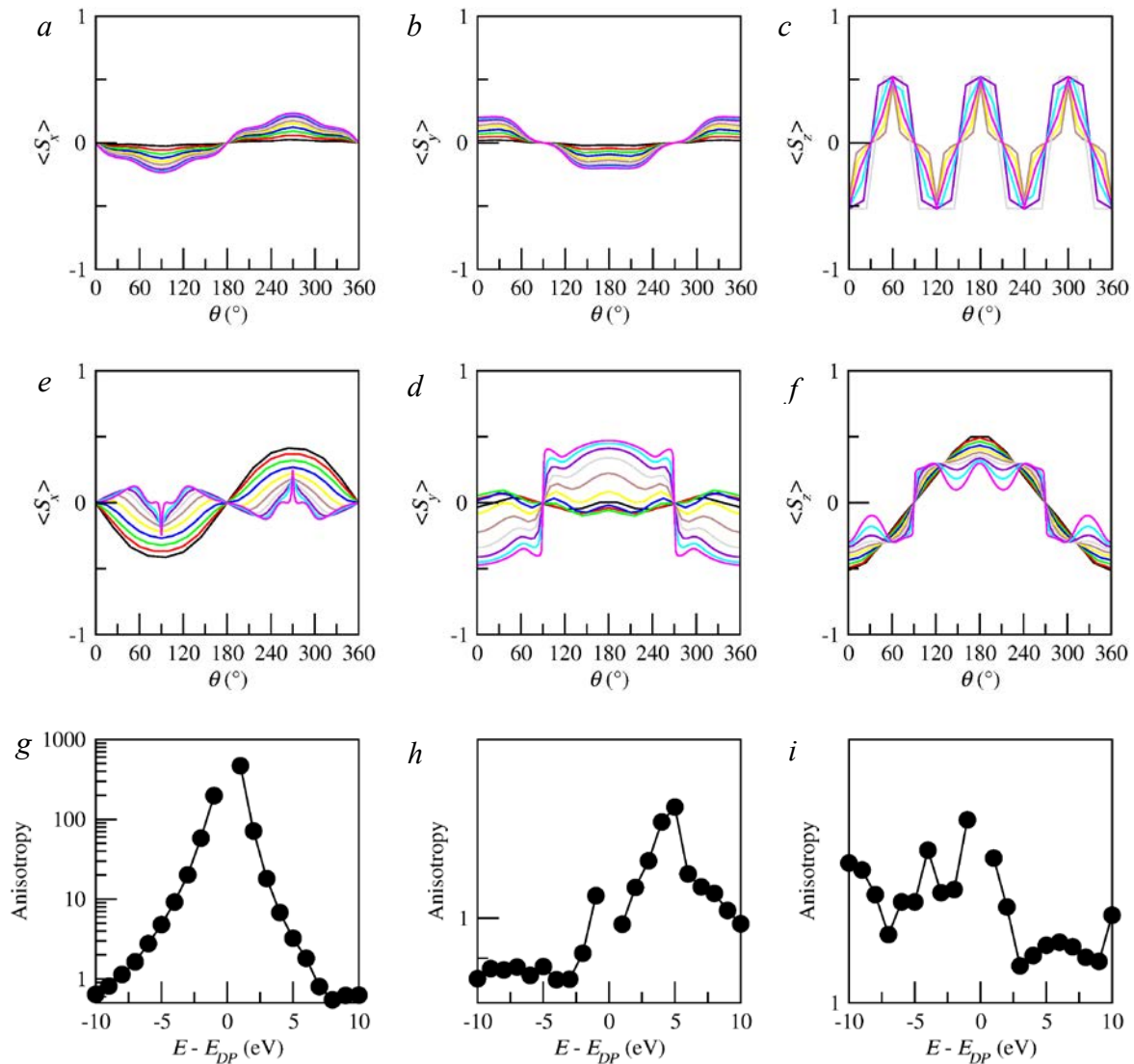


Fig. 4.24 Spin texture and lifetime anisotropy of Gr/1QL Sb_2Te_3 heterostructure as a function of energy relative to the graphene Dirac point. *a*, *b* and *c* – $\langle S_x \rangle$, $\langle S_y \rangle$, $\langle S_z \rangle$ v.s. momentum angle for 5th graphene band in hollow position; *d*, *e*, and *f* – $\langle S_x \rangle$, $\langle S_y \rangle$, $\langle S_z \rangle$ v.s. momentum angle for 5th graphene band in bridge position. *g*, *h* and *i* – anisotropy for hollow, bridge and top configuration cases

In all previous sections, DFT results for the Gr/TI with different configurations, substrates and thickness were investigated and the band structure and spin texture induced to graphene layer. Some peculiar features were also observed and discussed; however, it is still necessary to examine the origin of each electronic feature through more concrete method, and for that

purpose tight binding (TB) models were developed to reproduce and better understand all electronic properties in such heterostructures.

4.13. TB method for pristine graphene system

The TB method is used to compute the band structure and is based on a superposition of wave functions for isolated atoms at each atomic site within the crystal structure. In graphene, p -shell orbital electron of carbon form two main types of bondings. One is the in-plane σ bond, which is strongly covalent, determining the energetic stability and the elastic properties of graphene; while, the other one is perpendicular to graphene plane, forms the π bond in graphene. The calculation for the energy ranges of σ and π bands shows that only electrons in the π bond contribute to the electronic properties of graphene because the σ bands are far away from the Fermi level. Because of this, it is sufficient to treat graphene as a collection of atoms with single p_z orbitals per site. In graphene, carbon atoms are located at the vertices of a hexagonal lattice. Graphene is a bipartite lattice which consists of two sublattices A and B and basis vectors (\mathbf{a}_1 , \mathbf{a}_2), which is shown in Fig. 4.26:

$$a_1 = a \left(\frac{\sqrt{3}}{2}, \frac{1}{2} \right), a_2 = a \left(\frac{\sqrt{3}}{2}, -\frac{1}{2} \right)$$

with $a = \sqrt{3}a_{cc}$, where $a_{cc} = 1.42 \text{ \AA}$ is the carbon-carbon distance in graphene. These basis vectors build a hexagonal Brillouin zone with two inequivalent points K and K_- ($K+$ and $K-$ respectively in Fig. 4.25) at the corners

$$K = \frac{4\pi}{3a} \left(\frac{\sqrt{3}}{2}, -\frac{1}{2} \right), K' = \frac{4\pi}{3a} \left(\frac{\sqrt{3}}{2}, \frac{1}{2} \right)$$

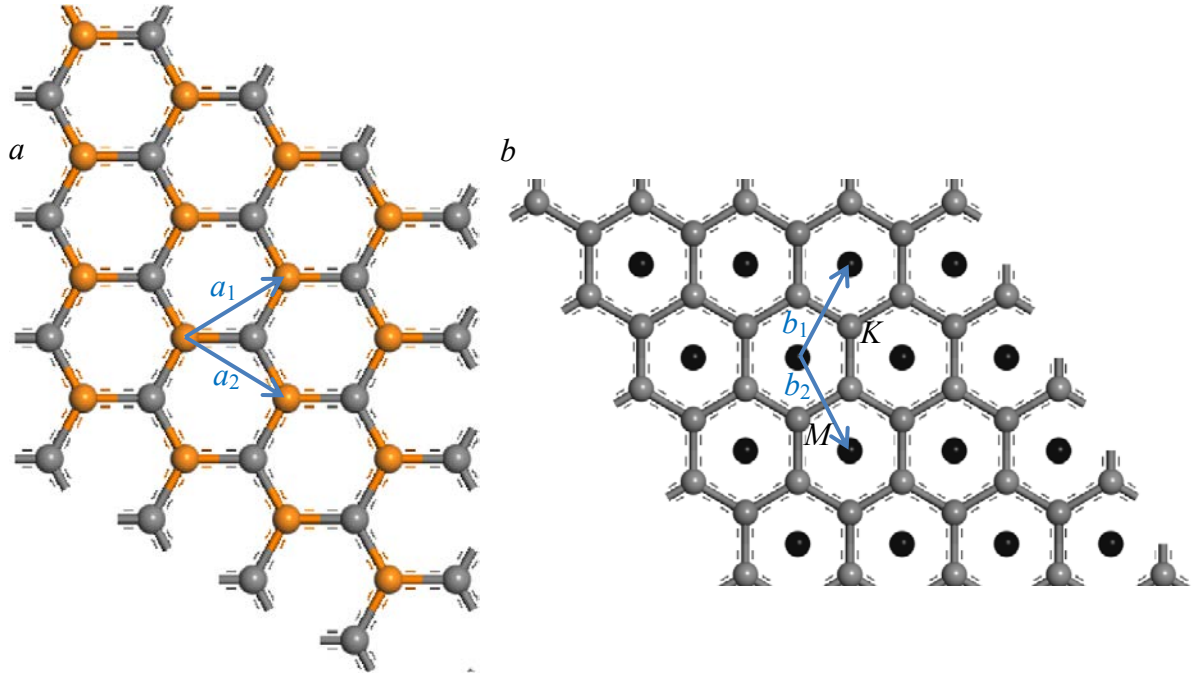


Fig. 4.25 Lattice vector for graphene in both real and reciprocal spaces

As mentioned above and from Bloch's theorem, wave function can be written in the form of p_z orbitals wave function at sublattices A [$\phi(r-r_A)$] and B [$\phi(r-r_B)$]

$$\psi(k, r) = c_A(k)\phi^A(k, r) + c_B(k)\phi^B(k, r)$$

where,

$$\phi^A(k, r) = \frac{1}{\sqrt{N}} \sum_{R_j} e^{ikR_j} \phi(r - r_A - R_j)$$

$$\phi^B(k, r) = \frac{1}{\sqrt{N}} \sum_{R_j} e^{ikR_j} \phi(r - r_B - R_j)$$

where, k is the electron wavevector, N is the number of unit cells in the graphene sheet and R_j is a Bravais lattice point. Using the Schrödinger equation, $H\Psi(k, r) = E\Psi(k, r)$, one obtains a 2×2 eigenvalue problem,

$$H(k) \begin{pmatrix} c_A(k) \\ c_B(k) \end{pmatrix} = \begin{pmatrix} H_{AA}(k) & H_{AB}(k) \\ H_{BA}(k) & H_{BB}(k) \end{pmatrix} \begin{pmatrix} c_A(k) \\ c_B(k) \end{pmatrix} = E(k) \begin{pmatrix} S_{AA}(k) & S_{AB}(k) \\ S_{BA}(k) & S_{BB}(k) \end{pmatrix} \begin{pmatrix} c_A(k) \\ c_B(k) \end{pmatrix}$$

where, $S_{\alpha\beta}(k) = \langle \phi_\alpha(k) | \phi_\beta(k) \rangle$ and the matrix elements of the Hamiltonian are

$$H_{AA}(k) = \frac{1}{N} \sum_{R_i, R_j} e^{ik(R_j - R_i)} \langle \phi^{A, R_i} | H | \phi^{A, R_j} \rangle$$

$$H_{AB}(k) = \frac{1}{N} \sum_{R_i, R_j} e^{ik(R_j - R_i)} \langle \varphi^{A, R_i} | H | \varphi^{B, R_j} \rangle$$

with $H_{AA} = H_{BB}$ and $H_{AB} = H_{BA}^*$ and introducing the notation: $\varphi^{A, R_i} = \varphi(r - r_A - R_i)$ and $\varphi^{B, R_i} = \varphi(r - r_B - R_i)$.

If we neglect the overlap $s = \langle \varphi^A | \varphi^B \rangle$ between neighboring p_z orbitals, then,

$S_{\alpha\beta}(k) = \delta_{\alpha\beta}$ and the eigenvalue function becomes

$$\begin{pmatrix} H_{AA}(k) & H_{AB}(k) \\ H_{BA}(k) & H_{BB}(k) \end{pmatrix} \begin{pmatrix} c_A(k) \\ c_B(k) \end{pmatrix} = E(k) \begin{pmatrix} c_A(k) \\ c_B(k) \end{pmatrix}$$

Here, only the first nearest neighbour interaction is taken into account; then,

$$H_{AB}(k) = \langle \varphi^{A,0} | H | \varphi^{B,0} \rangle + e^{-ika_1} \langle \varphi^{A,0} | H | \varphi^{B,-a_1} \rangle + e^{-ika_2} \langle \varphi^{A,0} | H | \varphi^{B,-a_2} \rangle = -\gamma_0 \alpha(k)$$

where, γ_0 stands for the transfer integral between first neighbour π orbitals ($\gamma_0 = 2.7\text{eV}$ in this thesis) and $\alpha(k)$ is given by:

$$\alpha(k) = 1 + e^{-ika_1} + e^{-ika_2}$$

Taking $H_{AA} = H_{BB} = 0$ as the energy reference, we can write $H(k)$ as:

$$H(k) = \begin{pmatrix} 0 & -\gamma_0 \alpha(k) \\ -\gamma_0 \alpha^*(k) & 0 \end{pmatrix}$$

Diagonalizing this hamiltonian gives the energy dispersion relations for π^* (conduction) band (+) and π (valence) band (-):

$$\begin{aligned} E^\pm(k) &= \pm \gamma_0 |\alpha(k)| = \pm \gamma_0 \sqrt{3 + 2 \cos(ka_1) + 2 \cos(ka_2) + 2 \cos[k(a_2 - a_1)]} \\ &= \pm \gamma_0 \sqrt{1 + 4 \cos \frac{\sqrt{3} k_x a}{2} \cos \frac{k_y a}{2} + 4 \cos^2 \frac{k_y a}{2}} \end{aligned}$$

This band structure is plotted in Fig. 4.26 with the symmetry between the conduction band and the valence band which touch at three K and K' points with zero density of state at this energy. Because of this, graphene is called gapless semiconductor or semi-metal. In neutral graphene, the Fermi level lies exactly at these points.

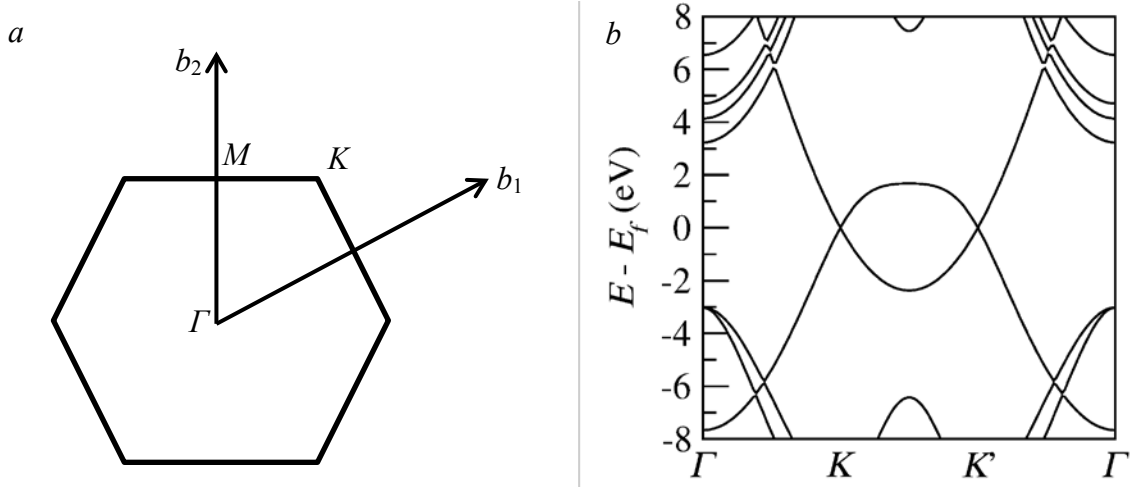


Fig. 4.26 Brillouin zone and band structure of graphene. *a* – First Brillouin zone of graphene; *b* - Band structure of pristine graphene

4.14. TB method for graphene band in Gr/1QL Bi₂Se₃ system with hollow configuration

In this heterostructure system, the graphene layer does not have different sublattices because of the broken symmetry induced by the TI substrate, indicating that there is no stagger potential in Hamiltonian. To describe the electronic properties of such graphene layer, the TB Hamiltonian is given by the following formula:

$$H = \sum_{a=0,p} t_a \sum_{\langle ij \rangle, s} c_{is}^+ c_{js} + \frac{i}{3\sqrt{3}} \sum_{\langle\langle ij \rangle\rangle, ss'} c_{is}^+ c_{js'} \lambda_I [v_{ij} s_z]_{ss'} + \frac{2i}{3} \sum_{\langle ij \rangle, ss'} c_{is}^+ c_{js'} [(\lambda_R^z \hat{Z} + \lambda_R^\rho \hat{\rho}) \cdot (s \times \bar{d}_{ij})]_{ss'}$$

where, c_{is}^+ (c_{is}) is the creation (annihilation) operator of an electron at lattice site i with spin s , d_{ij} (D_{ij}) is the unit vector pointing from site j to the nearest (next-nearest) site i , s is the spin Pauli matrix, v_{ij} is +1 (−1) for a clockwise (counter-clockwise) hopping path from site j to i and the single (double) brackets are sums over first (second) nearest neighbors. The first term in the formula describes the hopping between nearest-neighbor carbon atoms. As depicted in Fig. 4.27, this has two different strengths: t_0 is the hopping within the carbon ring surrounding the top (green) Se atom, and t_p is the hopping between carbon rings. This describes a *Kekulé* distortion of the graphene lattice in the hollow configuration and opens a band gap of $2|t_0 - t_p|$ in the absence of SOC. The second term describes intrinsic SOC in the graphene lattice,[69] λ_I , and is assumed nonzero only for the carbon ring surrounding the top Se atom, which is highlighted by the solid triangle in Fig. 4.27. The third term is a uniform *Rashba* SOC (λ_R^z) induced by an electric field perpendicular to the graphene plane. The fourth term is a second *Rashba* SOC (λ_R^ρ) arising from a radial in-plane electric field. In previous section, it

has already been discussed that in-plane *Rashba* SOC is only non-zero along scarlet arrows in Fig. 4.27 and this could also give good fitting to DFT results.

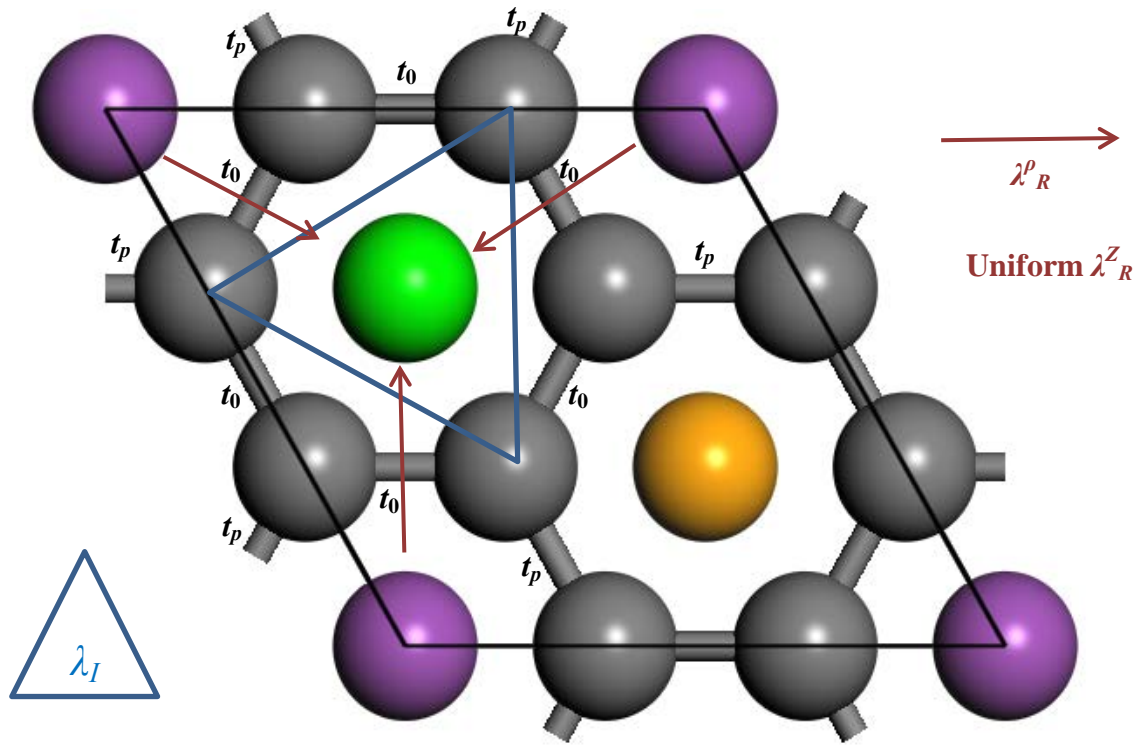


Fig. 4.27 Top of graphene with $\sqrt{3} \times \sqrt{3}$ supercell and hollow configuration and TB parameters are labelled

Fig. 4.28 shows the band structure of graphene layer based on the TB Hamiltonian model. To see the effect of each parameter, they were switched on one by one and the corresponding band structure is put together for comparison. It is clear that the uniform hopping on graphene without *Kekulé* distortion is insufficient to open a band gap and the energy and k point show linear dispersion relation; while, two different hopping terms could simulate the bonding distortion and the band gap opening, which is consistent with the DFT results. As the out-of-plane *Rashba* SOC term is switched on, a clear band splitting shows up in both valence and conduction bands but the splitting is equal in both, which is not the case in DFT results. Only after the intrinsic SOC term is added on, then the splitting shows large value in conduction bands and small value in valence bands. This is because the intrinsic SOC contributes in shifting the valence and one conduction band towards the centre of graphene DP with different magnitude. Through analysing this comparison, the main conclusion is that the *Kekulé* distortion is responsible for the band gap opening and the final gap value is total effect of both this bonding distortion, *Rashba* SOC and intrinsic SOC.

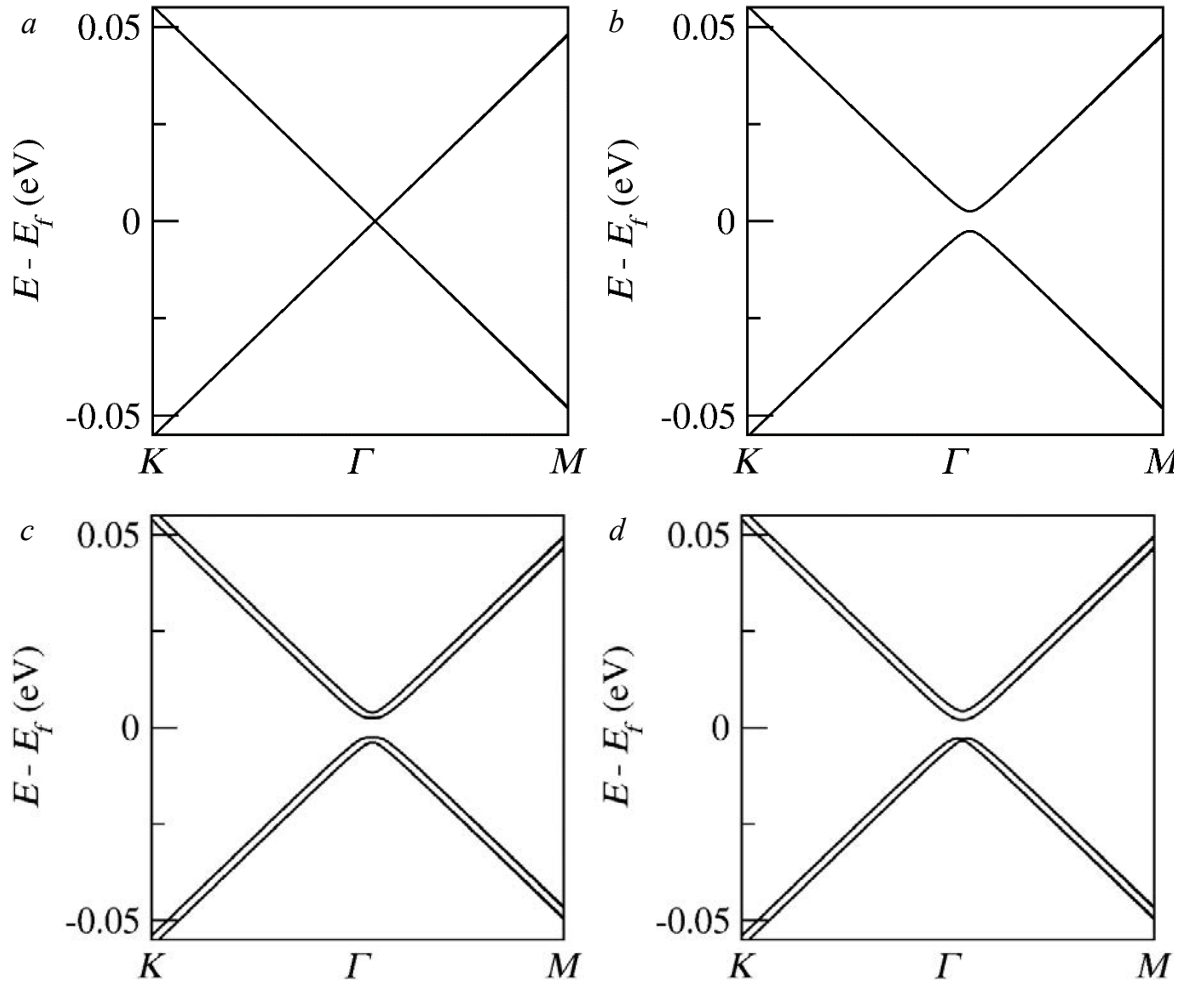


Fig. 4.28 Band structure graphene with $\sqrt{3} \times \sqrt{3}$ supercell and hollow configuration. *a* – uniform hopping; *b* - *Kekulé* distortion; *c* – with out-of-plane *Rashba* SOC; *d* – with intrinsic SOC

To further examine this TB model, the spin texture was also computed and compared based on the TB Hamiltonian with each parameter added on one by one (see Fig. 4.29). It is clear that only considering a uniform hopping does not give a correct spin texture as the in-plane spin component is zero; while, the out-of-plane one shows positive or negative 1. This is because the Hamiltonian matrix is spin polarized. Then, as the bonding distortion is switched on, the spin texture is more or less the same as in the uniform hopping case, indicating that the *Kekulé* distortion does not play the key role in forming the correct spin texture on graphene layer. Only after the *Rashba* SOC term is switched on, then the non-zero in-plane spin component shows up and, through modifying the relative strength between in-plane and out-of-plane *Rashba* SOC, the correct symmetry is grasped and peaks show around every 60° angle. However, the out-of-plane spin component still shows zero value, which is still different from the DFT results. Figs. 4.29j ~ 4.29l show the results and the intrinsic SOC is switched on and

it is clear that the out-of-plane spin component then shows non zero value and, through modifying this parameter carefully, the correct symmetry that negative and positive peak shows up by turn are drawn. Based on this comparison, the following conclusions can be reproduced. The *Kekulé* distortion does not play a fundamental role in determining the spin texture; while, the correct form of the in-plane spin vector mainly depends on the relative strength of the in-plane and the out-of-plane *Rashba* SOC terms, which are responsible for the spin precession. Meanwhile, the out-of-plane spin vector mainly comes from the intrinsic SOC term, which could give non zero $\langle S_z \rangle$ with the correct symmetry.

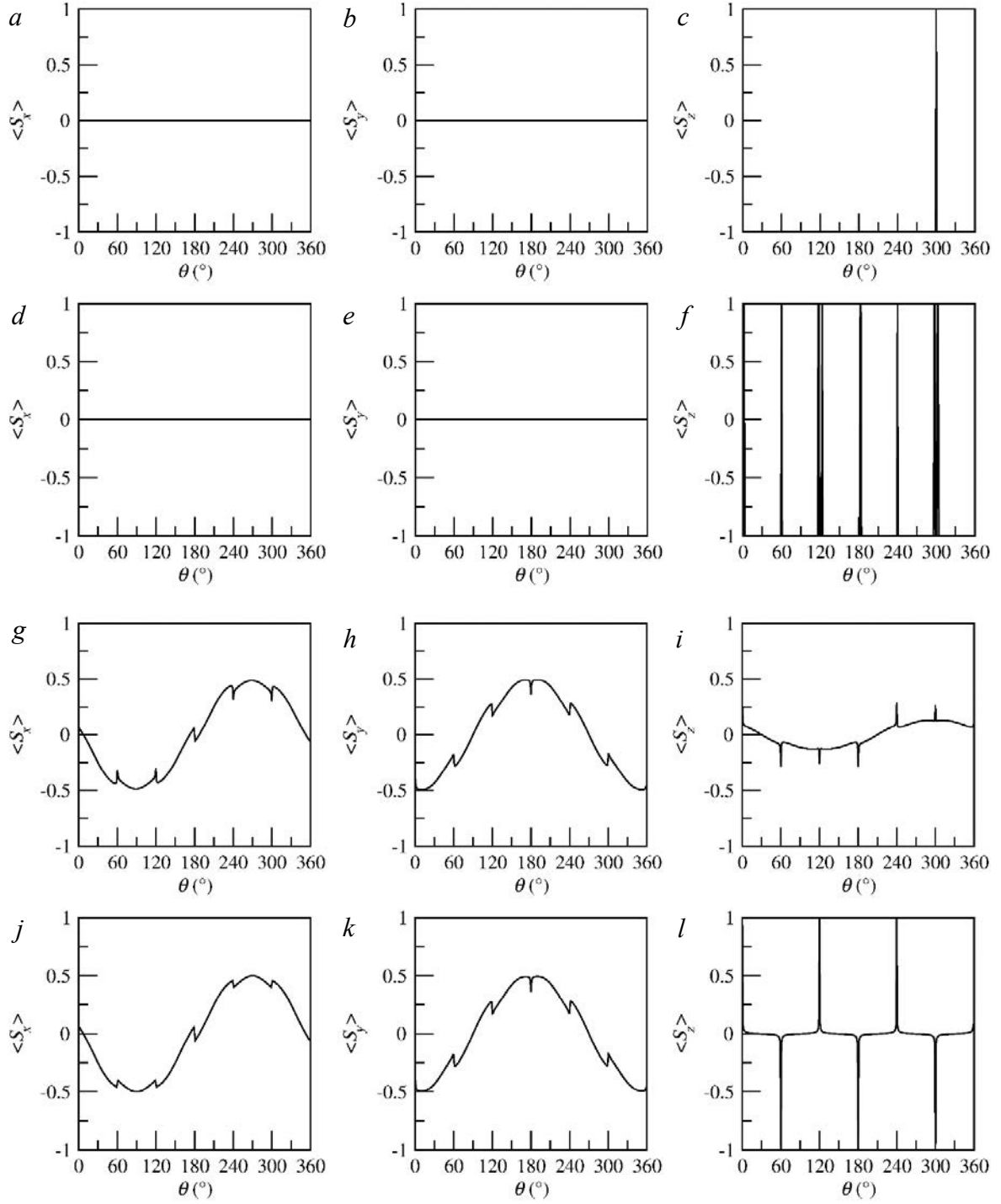
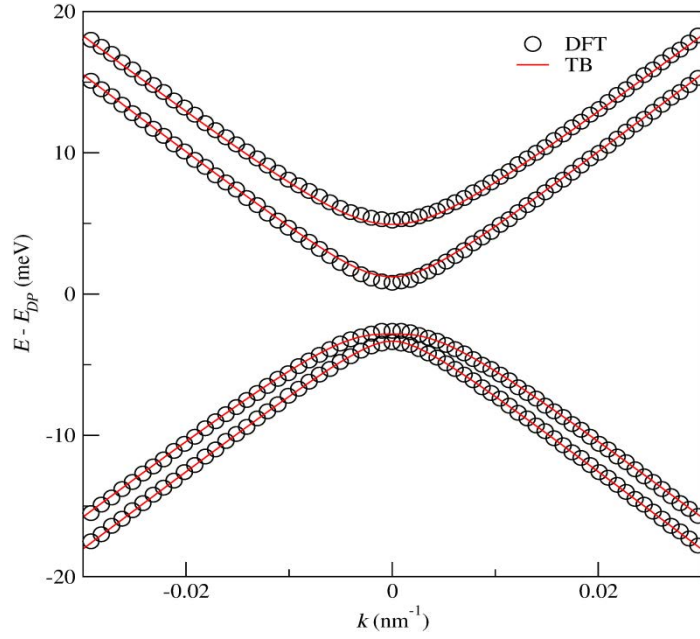


Fig. 4.29 Spin texture from TB model with different parameter added on. *a*, *b* and *c* – $\langle S_x \rangle$, $\langle S_y \rangle$ and $\langle S_z \rangle$ for only uniform hopping; *d*, *e* and *f* – $\langle S_x \rangle$, $\langle S_y \rangle$ and $\langle S_z \rangle$ for *Kekulé* distortion; *g*, *h* and *i* – $\langle S_x \rangle$, $\langle S_y \rangle$ and $\langle S_z \rangle$ for both in-plane and out-of-plane *Rashba* SOC case; *j*, *k* and *l* – $\langle S_x \rangle$, $\langle S_y \rangle$ and $\langle S_z \rangle$ for intrinsic SOC case

In order to have a better fitting between TB and DFT results, values for all TB parameters were tuned to best reproduce the DFT band structure and spin texture of the Gr/TI heterostructures. The TB fitted band structure is given in Fig. 4.30; while the spin texture appears in Fig. 4.31 respectively. The orbital gap induced by the *Kekulé* distortion is ~ 6 meV and the

SOC strengths are on the order of a few meV. A notable result is the relative magnitude of the in-plane and out-of-plane *Rashba* terms. Recent work has found good fits to the DFT band structure when assuming $\lambda_R^p \ll \lambda_R^z$, [51] but here, to obtain the proper in-plane spin texture, it is necessary to enforce $\lambda_R^p \gg \lambda_R^z$. The presence of the intrinsic SOC (λ_I) is necessary for a proper fit to the DFT band structure but has no impact on the spin texture. Meanwhile, the out-of-plane spin component $\langle S_z \rangle$ depends crucially on the presence of the *Kekulé* distortion, which hybridizes the K and K' bands; in its absence the magnitude of $\langle S_z \rangle$ drops by 3 orders of magnitude. Here, it is noted that this spin texture is quite different from that published in prior works, which predicted a purely *Rashba*-like behavior. [52, 53] This difference is attributed to the choice of model used; the earlier works used a continuum model for the graphene and TI bands that does not account for trigonal warping, the *Kekulé* distortion, or the in-plane *Rashba* terms. We have found that these terms are crucial for properly capturing the DFT spin texture.



Parameter	$\sqrt{3} \times \sqrt{3}$ supercell
t_0	-2.6 eV
$t_0 - t_p$	-3 meV
λ_i	-2.5 meV
λ_R^z	0.05 meV
λ_R^ρ	-1.9 meV

Fig. 4.30 TB fitted band structure and fitted value for TB parameters for Gr/TI with the hollow configuration

Based on these discussions, the spin texture with fitted TB parameters are shown in Fig. 4.31 with the DFT results for comparison. The calculation procedure is same as that in DFT one that ten energy contours were taken and expectation value of spin vectors were computed on all k points along each contour; then, the expectation value is plot against momentum direction from 0° to 360° , with the starting direction 0° pointing to the x axis. For simplicity, only one graphene conduction band was examined for the comparison, it can be seen that, with all these fitted value, TB calculation can basically reproduce all features of the spin texture from the DFT one. All in-plane spin components show the fold symmetry that a peak shows up every 60° and their magnitude decrease as the contour moves closer and closer to graphene

DP. Meanwhile, the out-of-plane spin component does not decrease no matter how the contour moves (close or away from graphene DP).

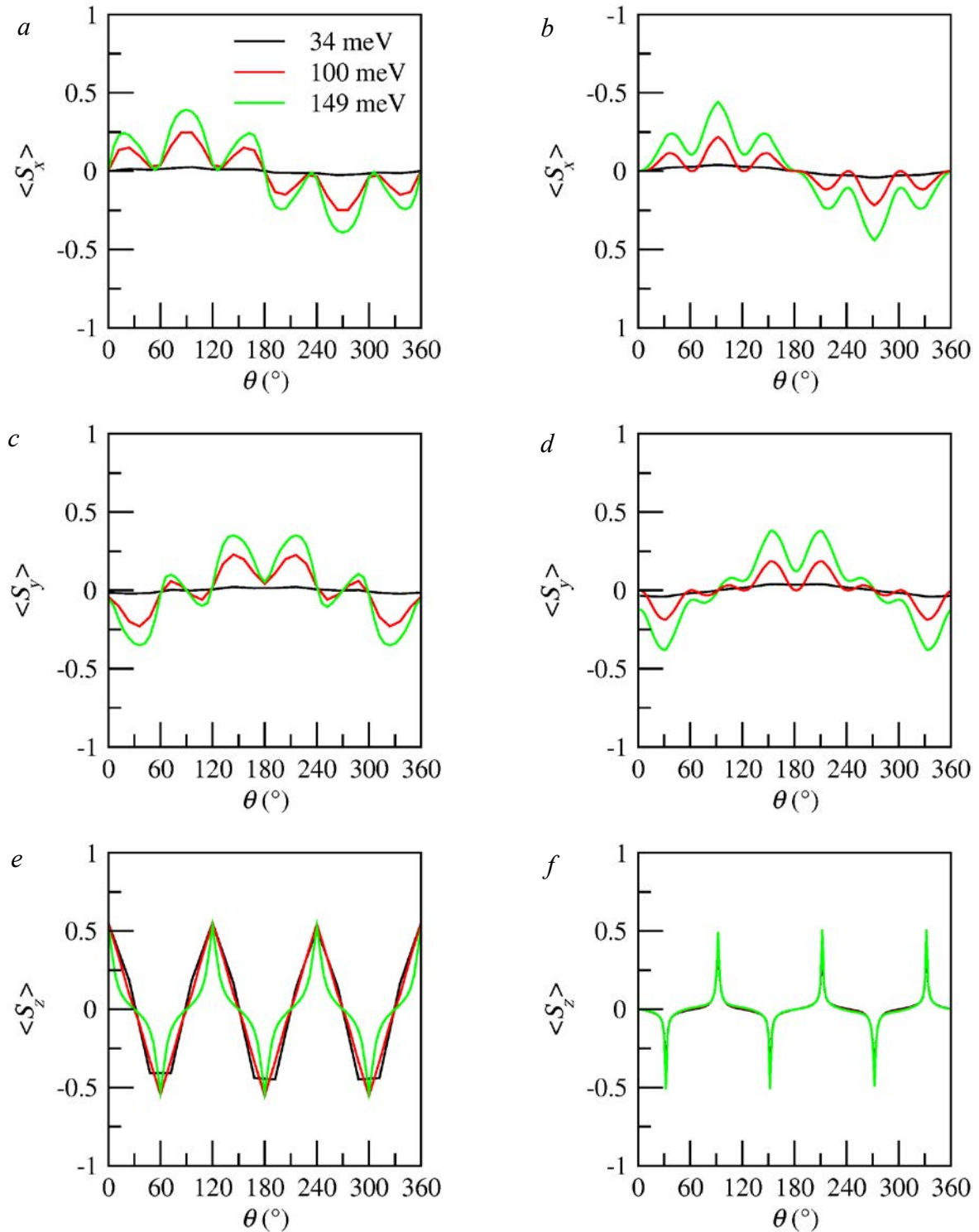


Fig. 4.31 Spin texture calculated by TB and DFT method. *a*, *c* and *e* - $\langle S_x \rangle$, $\langle S_y \rangle$ and $\langle S_z \rangle$ for graphene conduction band from DFT results; *b*, *d* and *f* - $\langle S_x \rangle$, $\langle S_y \rangle$ and $\langle S_z \rangle$ for graphene conduction band from TB results

According to Fig. 4.31, it is clear that the ratio of in-plane and out-of-plane spin component is k point dependent as well; therefore, it is necessary to examine the spin anisotropy based on this TB fitted model. Fig. 4.32 shows the results and it is clear that the anisotropy reaches its maximum value close to graphene DP; while, decreases gradually as the contour moves away from the DP and finally approach 1/2 value. This conclusion is in line with those for graphene/TMD heterostructures.[72] All these trends are the same as those in DFT one.

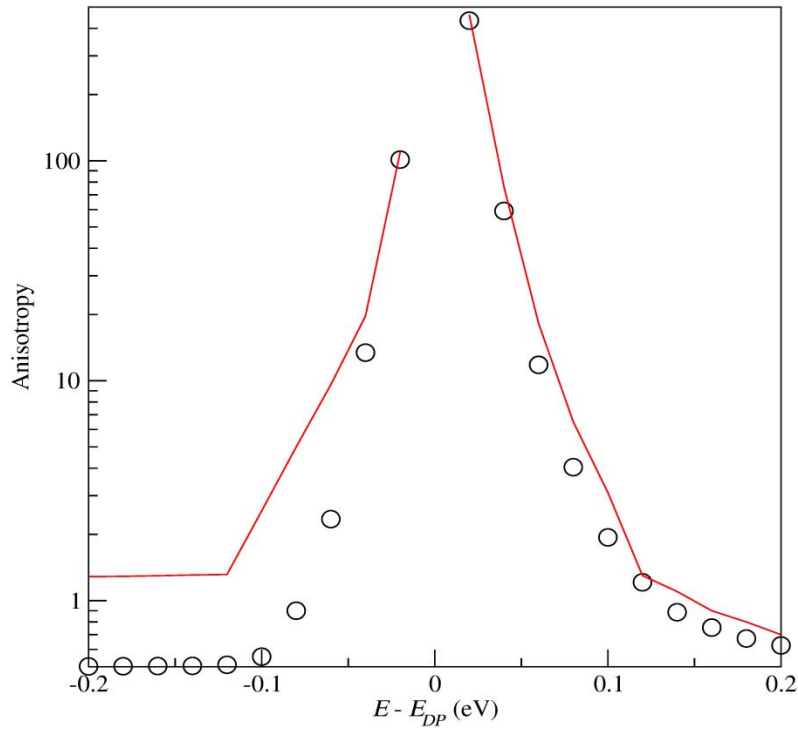


Fig. 4.32 Spin anisotropy of graphene in $\sqrt{3} \times \sqrt{3}$ supercell based on DFT and TB results

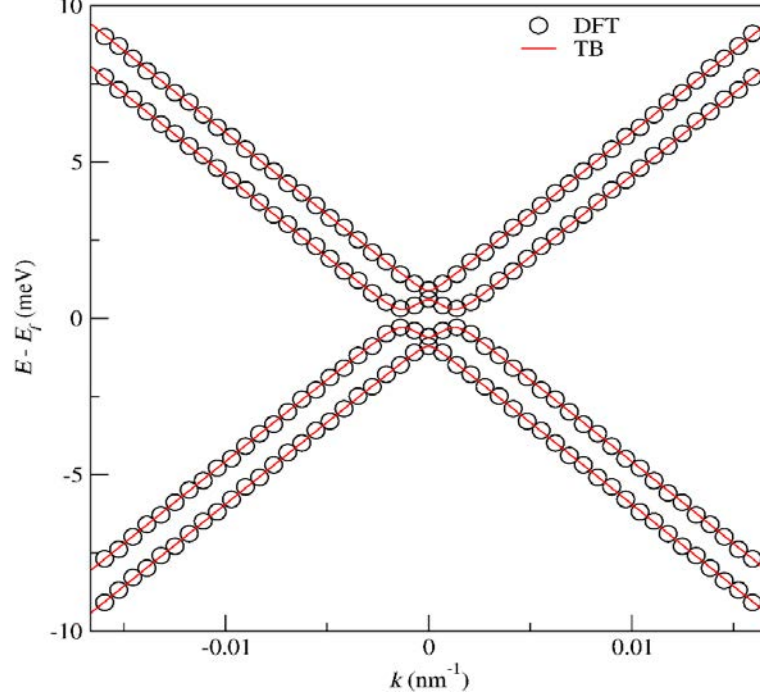
4.15 TB method for graphene band in Gr/1QL Bi₂Se₃ system with all three configurations

Since in section 4.7, DFT results show quite different electronic properties for the large unit cell with all three configurations, compared with those only with one configuration, it is necessary to examine this large unit cell based on the TB model. Different from the $\sqrt{3} \times \sqrt{3}$ supercell, the supercell for graphene layer here is 5×5 and, because of the TI substrate, the symmetry is broken, which means that some new terms should be added into the original one, which is built up for $\sqrt{3} \times \sqrt{3}$ graphene supercell case and the formula is written below.

$$H_{big} = H_{small} + \frac{i}{3\sqrt{3}} \sum_{\langle\langle ij \rangle\rangle, ss} c_{is}^{\dagger} c_{js} \xi_i \lambda_{iVZ} [v_{ij} s_z]_{ss} + \frac{2i}{3} \sum_{\langle ij \rangle, ss} c_{is}^{\dagger} c_{js} \left[(\xi_i \lambda_{PIA} \hat{Z}) \cdot (s \times \bar{D}_{ij}) \right]_{ss}$$

where, H_{big} and H_{small} are hamiltonian matrice for big (5×5) and small ($\sqrt{3} \times \sqrt{3}$) unit cell respectively. D_{ij} is the unit vector pointing from site j to the next-nearest site i . ξ_i is +1 (-1) on sublattice A (B). H_{small} is a little bit different from that discussed in the hollow configuration and since the *Kekulé* distortion does not exist in this big unit cell, because all carbon bonds show the same length. Meanwhile, in the larger unit cell, the in-plane *Rashba* SOC term does not exist, owing to the lack of radial symmetry. The second term in the formula describes the valley Zeeman SOC (λ_{VZ}), which couples spin and valley and arises when sublattice symmetry is broken in the graphene layer.[70] For this reason, it is only present in the larger unit cell. Finally, the last term is denoted *PIA* (pseudospin inversion asymmetry) SOC (λ_{PIA}), which is akin to a second-order *Rashba* SOC and leads to a k -linear spin splitting of the bands. This particular term only arises in the presence of sublattice symmetry breaking plus a perpendicular electric field.[70]

Fig. 4.33 shows the TB fitted band structure and it is clear that TB model fits quite well to DFT results. Owing to the different interface symmetry of the larger unit cell, there are significant differences in the band structure and relevant SOC parameters compared to the smaller unit cell. In the band structure, the graphene Dirac cones remain separated at the K and K' points of the Brillouin zone, while the charge transfer between the graphene and the TI remains large.



Parameter	$\sqrt{3} \times \sqrt{3}$ supercell
t_0	-2.4 eV
λ_{VZ}	-0.6 meV
λ_R^z	0.3 meV
λ_{PIA}	-1.1 meV

Fig. 4.33 TB fitted band structure and fitted value for TB parameters for Gr/TI with three configurations (hollow, bridge and top)

On the other hand, the spin textures are also plot for both K and K' points in Brillouin zone and shown in Fig. 4.34. One graphene conduction band is taken as an example to show the texture and owing to the fact that there is no band folding to Γ point, unlike that in hollow configuration case, the hybridization between the valleys no longer occurs, and the 60° periodicity of the spin texture disappears. Instead, $\langle S_z \rangle$ remains independent of the momentum direction, and its sign is valley dependent. This behavior is driven by the presence of valley-Zeeman SOC (λ_{VZ}), which is permitted by the sublattice symmetry breaking in the larger unit cell. The in-plane spin components follow the typical *Rashba* texture, and the *PIA* SOC determines their energy dependence. As mentioned above, the *Kekulé* distortion and in-plane

Rashba SOC are not present in this system. Additionally, the intrinsic SOC is found to be vanishingly small.[27]

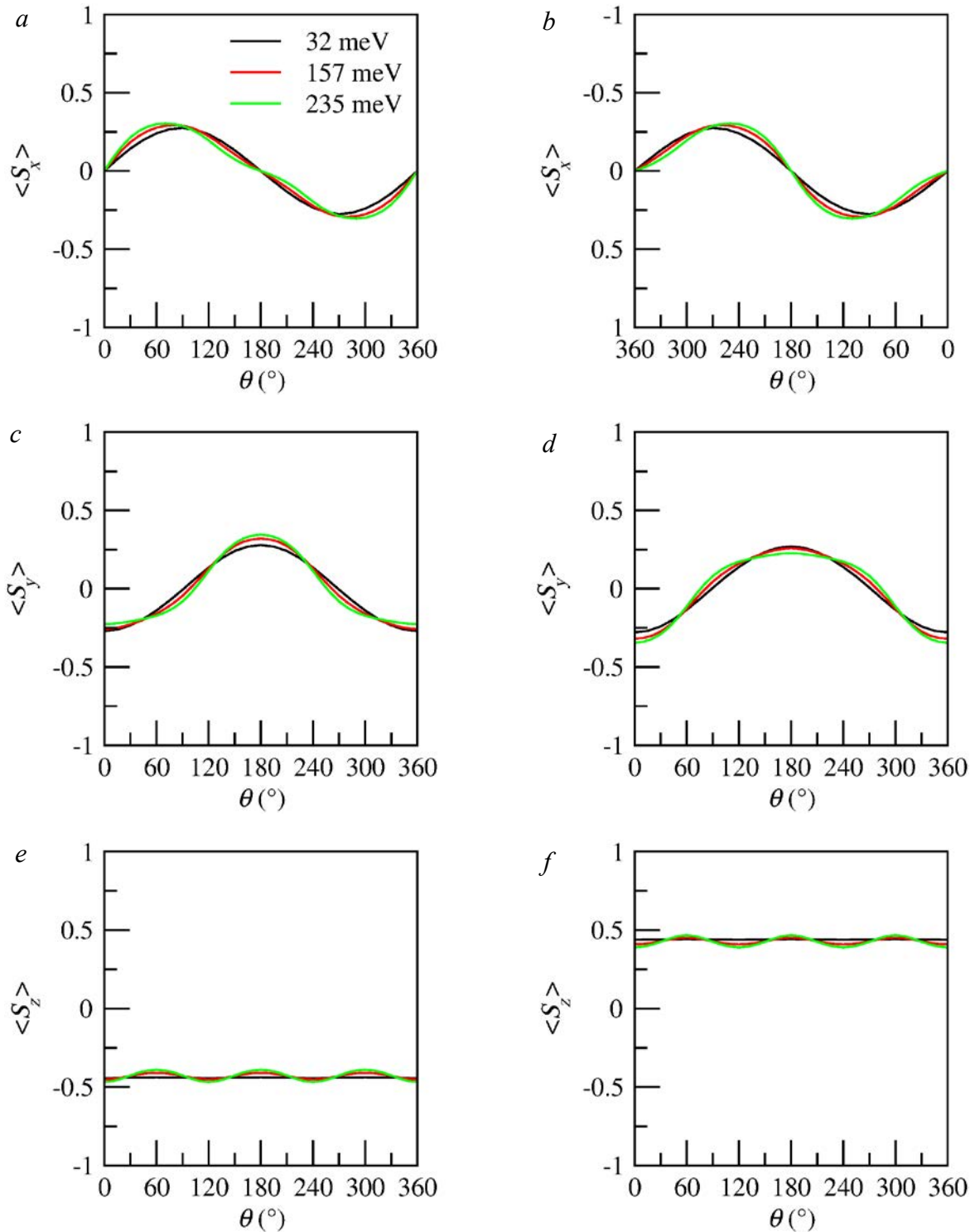


Fig. 4.34 Spin texture calculated by DFT method. *a*, *c* and *e* - $\langle S_x \rangle$, $\langle S_y \rangle$ and $\langle S_z \rangle$ for graphene conduction band at K point; *b*, *d* and *f* - $\langle S_x \rangle$, $\langle S_y \rangle$ and $\langle S_z \rangle$ for graphene conduction band at K' point

Furthermore, the in-plane spin component basically follow standard *Rashba* type texture and the out-of-plane spin part does not change a lot with the energy inn the conduction band so it can be concluded that the ratio of in-plane to out-of-plane spin component does not depend on the k point much above the graphene DP, like in the hollow configuration case. This can be appreciated in Fig. 4.35, which shows both DFT and TB fitting results for spin anisotropy, and, above graphene DP, anisotropy does not change significantly. However, the anisotropy increases a lot as the energy moves to the negative side of the graphene DP. This means that upon tuning the back gate voltage one could tailor the spin anisotropy value for this device since the large size supercell chosen should be more realistic for comparison with experimental data.

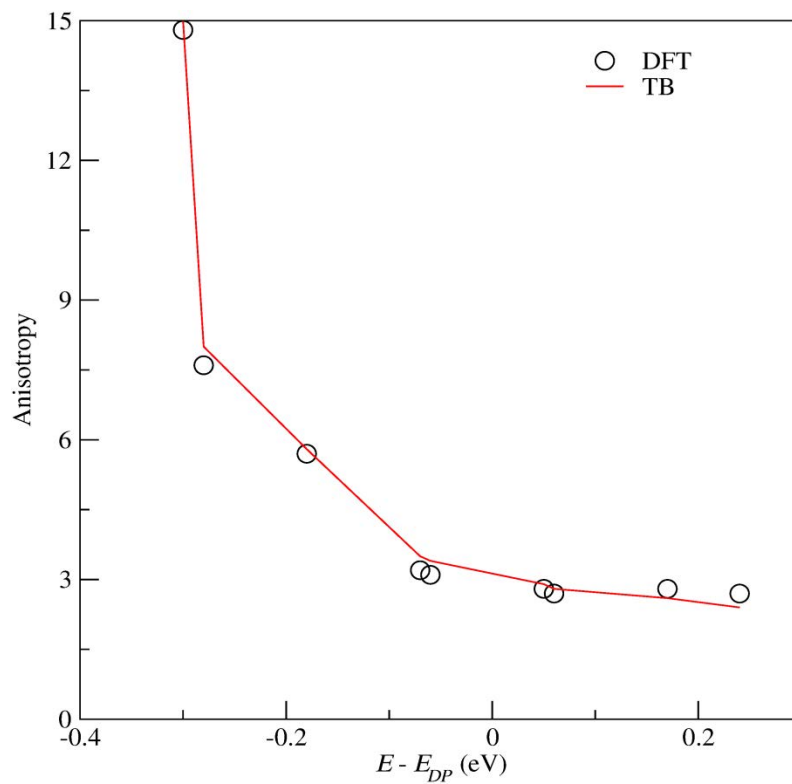


Fig. 4.35 Spin anisotropy of graphene in large unit cell based on DFT and TB results

4.16 Conclusions

In this chapter, Gr/TI heterostructures were investigated and discussed, showing the proximity effects of TI onto graphene layers. This study reveals the emergence of strong anisotropic spin transport feature in graphene in proximity with TIs, but the origin and energy dependence of this anisotropy varies significantly with the geometry of the interface. This arises from the very small lattice mismatch, which permits a highly commensurate unit cell at the appropriate twist angle. This is in contrast to the case of Gr/TMDC systems, which have a

much-larger lattice mismatch that precludes the formation of a small and highly commensurate unit cell.[23, 27] Similar to the case of Gr/TMDC, Gr/TI displays a relatively energy-independent anisotropy for zero twist-angle between the graphene and TI lattices. However, in the highly commensurate unit cell (with a twist angle of 30°), the spin anisotropy is connected to both a *Kekulé* distortion and an in-plane *Rashba* SOC induced in the graphene by the TI. As a result, the spin lifetime becomes highly anisotropic near the graphene Dirac point while vanishing at higher energies, suggesting a much stronger variability via electrostatic gating in experiments. Such a spin anisotropy could be playing a role in the debated experimental results reported to date in Gr/TI heterostructures[32, 33, 39]; while simultaneously suggesting new device engineering such as gate tunable linear spin polarizers, which remove the in-plane component of a spin-polarized current but leave the out of plane component intact.

One useful observation is that, as shown in Gr/Bi₂Se₃ case, the Fermi level initially lies in the Bi₂Se₃ conduction band, which will generate parallel transport in the graphene and TI layers. However, given that the spin lifetime in the TI bulk should be exceptionally short (a few femtoseconds),[68, 69] any measured spin signal may still carry features of the spin transport in the graphene layer. Different from Gr/Bi₂Se₃ system, Gr/Bi₂Te₃ and Gr/Sb₂Te₃ systems show that graphene DP lies in the bulk TI band gap. This could improve the purity of the measured spin signal on graphene although some hybridization between graphene and TI, dictating some contribution mixing also exist. To more optimally realize the conditions in which the TI surface states would play a role in the transport properties of Gr/TI heterostructures, ternary compounds, with the TI Fermi energy well within the TI bulk gap, would be even more desirable since there has already research work reported to show that graphene DP could remain located within the TI bulk band gap without any hybridization with TI bands.[70]

In order to build up the connection with experiments, a collaboration was developed with the group of Prof. Saroj Dash from Chalmers University.[71] Dash and co-workers could successfully measure various devices integrating graphene with two TI materials having different doping levels, Bi₂Se₃ and Bi_{1.5}Sb_{0.5}Te_{1.7}Se_{1.3}. They found some large modulation of the measured spin signal and spin-lifetime with gate voltage, evidencing a strong proximity-induced SOC, hence confirming substantial coupling of the graphene electronic bands in the heterostructure.

Fig. 4.36 shows a schematic of the performed non-local transport experiment in which a spin polarized current is injected onto graphene from a ferromagnetic (FM) source to a normal metal drain (left electrodes), whereas a non-local voltage is detected far away from the current flow (right side of the picture). The non-local spin signal is modulated by the presence of the deposited TI, as well as tuned by the presence of an external magnetic field (perpendicular to the graphene plane) which induces spin precession and relaxation detected and analysed through the non-local voltage. Fig. 4.36*b* gives the experimental measurement of the spin lifetime in Gr/Bi₂Se₃ device, whereas Fig. 4.36*c* is the deduced spin lifetime from our theoretical analysis. Our theoretical results give support to the experimental curves (not shown here).[71]

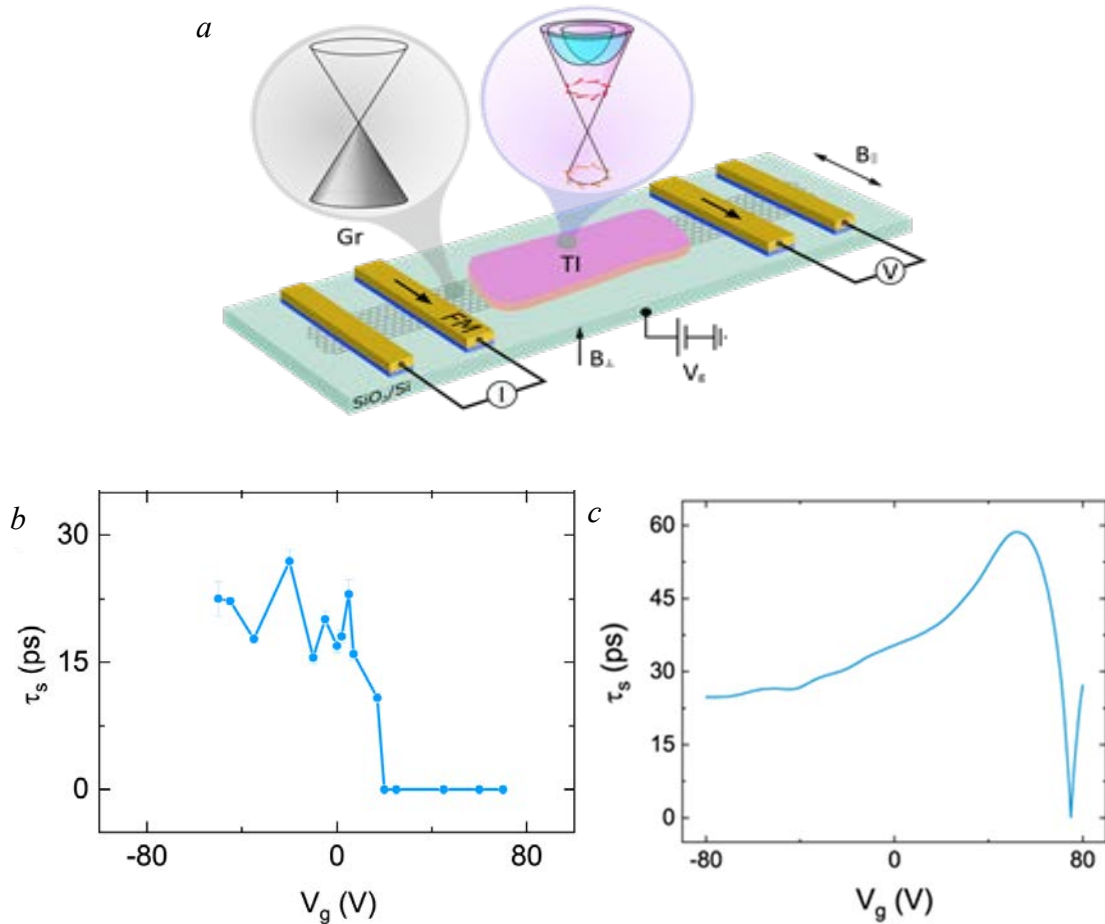


Fig. 4.36 Experimental work on Gr/ Bi₂Se₃ system. *a* – Schematic representation of the device consisting of a graphene (Gr)-topological insulator (TI) heterostructure channel and ferromagnetic (FM) tunnel contacts for spin injection and detection in a nonlocal transport geometry. The insets show the band structures of Gr and TI. The external magnetic field in both in-plane ($B_{||}$) and out-of-plane (B_{\perp}) direction and back gate voltage (V_g) are used to control the device functionality. *b* – Spin lifetime (τ_s) measured in the Gr/Bi₂Se₃ device. *c* - Estimated spin lifetime in graphene arising from the *ab initio* band structure and spin texture, assuming spin relaxation dominated by the Elliot-Yafet and D'yakonov-Perel' mechanisms.

Finally, it would be interesting to include defects and disorder in the *ab initio* simulations and TB models because this could locally alter the strength and nature of the SOC parameters. Such an analysis, beyond the scope of the present work, could be also extended by developing a full Gr/TI tight-binding model, using (for instance) the Fu–Kane–Mele model.[72, 73]

References:

- [1] Geim, A.; Grigorieva, I. *Nature* (2013) 499, 419
- [2] Butler, S. Z.; *et al.* *ACS Nano* (2013) 7, 2898–2926
- [3] Bhimanapati, G. R.; *et al.* *ACS Nano* (2015) 9, 11509–11539

- [4] Novoselov, K. S.; Mishchenko, A.; Carvalho, A.; Castro Neto, A. H. *Science* (2016) 353, 461
- [5] Lin, Z.; *et al.* *2D Mater.* (2016) 3, 042001
- [6] Ferrari, A. C.; *et al.* *Nanoscale* (2015) 7, 4598
- [7] Roche, S.; *et al.* *2D Mater.* (2015) 2, 030202
- [8] Kawakami, R. K. *2D Mater.* (2015) 2, 034001
- [9] Drögeler, M.; Volmer, F.; Wolter, M.; Terres, B.; Watanabe, K.; Taniguchi, T.; Güntherodt, G.; Stampfer, C.; Beschoten, B. *Nano Lett.* (2014) 14, 6050
- [10] Drögeler, M.; Franzen, C.; Volmer, F.; Pohlmann, T.; Banszerus, L.; Wolter, M.; Watanabe, K.; Taniguchi, T.; Stampfer, C.; Beschoten, B. *Nano Lett.* (2016) 16, 3533
- [11] Ingla-Aynés, J.; Meijerink, R. J.; van Wees, B. J. *Nano Lett.* (2016) 16, 4825
- [12] Yan, W.; Txoperena, O.; Llopis, R.; Dery, H.; Hueso, L. E.; Casanova, F. *Nat. Commun.* (2016) 7, 13372
- [13] Dankert, A.; Dash, S. P. *Nat. Commun.* (2017) 8, 16093
- [14] Leutenantsmeyer, J. C.; Kaverzin, A. A.; Wojtaszek, M.; van Wees, B. J. *2D Mater.* (2017) 4, 014001
- [15] Yang, H. X.; Hallal, A.; Terrade, D.; Waintal, X.; Roche, S.; Chshiev, M. *Phys. Rev. Lett.* (2013) 110, 046603
- [16] Hallal, A.; Ibrahim, F.; Yang, H.; Roche, S.; Chshiev, M. *2D Mater.* (2017) 4, 025074
- [17] Singh, S.; Katoch, J.; Zhu, T.; Meng, K.-Y.; Liu, T.; Brangham, J. T.; Yang, F.; Flatté, M. E.; Kawakami, R. K. *Phys. Rev. Lett.* (2017) 118, 187201
- [18] Avsar, A.; Hak Lee, J.; Koon, G. K. W.; Özyilmaz, B. *2D Mater.* (2015) 2, 044009
- [19] Cresti, A.; Nikolić, B. K.; García, J. H.; Roche, S. *Riv. Nuovo Cimento* (2016) 39, 587
- [20] Van Tuan, D.; Marmolejo-Tejada, J. M.; Waintal, X.; Nikolić, B. K.; Valenzuela, S. O.; Roche, S. *Phys. Rev. Lett.* (2016) 117, 176602
- [21] Schmidt, H.; Yudhistira, I.; Chu, L.; Castro Neto, A. H.; Özyilmaz, B.; Adam, S.; Eda, G. *Phys. Rev. Lett.* (2016) 116, 046803
- [22] Ge, J.-L.; Wu, T.-R.; Gao, M.; Bai, Z.-B.; Cao, L.; Wang, X.-F.; Qin, Y.-Y.; Song, F.-Q. *Front. Phys.* (2017) 12, 127210
- [23] Wang, Z.; Ki, D.-K.; Chen, H.; Berger, H.; MacDonald, A. H.; Morpurgo, A. F. *Nat. Commun.* (2015) 6, 8339
- [24] Wang, Z.; Ki, D.-K.; Khoo, J. Y.; Mauro, D.; Berger, H.; Levitov, L. S.; Morpurgo, A. F. *Phys. Rev. X* (2016) 6, 041020
- [25] Yang, B.; Tu, M.-F.; Kim, J.; Wu, Y.; Wang, H.; Alicea, J.; Wu, R.; Bockrath, M.; Shi, J. *2D Mater.* (2016) 3, 031012
- [26] Avsar, A.; Tan, J. Y.; Taychatanapat, T.; Balakrishnan, J.; Koon, G. K. W.; Yeo, Y.; Lahiri, J.; Carvalho, A.; Rodin, A. S.; O'Farrell, E. C. T.; Eda, G.; Castro Neto, A. H.; Özyilmaz, B. *Nat. Commun.* (2014) 5, 4875
- [27] Gmitra, M.; Kochan, D.; Högl, P.; Fabian, J. *Phys. Rev. B: Condens. Matter Mater. Phys.* (2016) 93, 155104
- [28] Cummings, A. W.; Garcia, J. H.; Fabian, J.; Roche, S. *Phys. Rev. Lett.* (2017) 119, 206601
- [29] Ghiasi, T. S.; Ingla-Aynés, J.; Kaverzin, A. A.; van Wees, B. J. *Nano Lett.* (2017) 17, 7528
- [30] Benítez, L. A.; Sierra, J. F.; Savero Torres, W.; Arrighi, A.; Bonell, F.; Costache, M. V.; Valenzuela, S. O. *Nat. Phys.* (2017) DOI: 10.1038/s41567-017-0019-2
- [31] Kim, N.; Lee, P.; Kim, Y.; Kim, J. S.; Kim, Y.; Noh, D. Y.; Yu, S. U.; Chung, J.; Kim, K. S. *ACS Nano* (2014) 8, 1154–1160
- [32] Zhang, L.; Yan, Y.; Wu, H.-C.; Yu, D.; Liao, Z.-M. *ACS Nano* (2016) 10, 3816

- [33] Zhang, L.; Lin, B.-C.; Wu, Y.-F.; Wu, H.-C.; Huang, T.-W.; Chang, C.-R.; Ke, X.; Kurttepeli, M.; Tendeloo, G. V.; Xu, J.; Yu, D.; Liao, Z.-M. *ACS Nano* (2017) 11, 6277
- [34] Zalic, A.; Dvir, T.; Steinberg, H. *Phys. Rev. B: Condens. Matter Mater. Phys.* (2017) 96, 075104
- [35] Rodriguez-Vega, M.; Schwiete, G.; Sinova, J.; Rossi, E. *Phys. Rev. B: Condens. Matter Mater. Phys.* (2017) 96, 085403
- [36] Lee, P.; Jin, K.-H.; Sung, S. J.; Kim, J. G.; Ryu, M.-T.; Park, H.-M.; Jhi, S.-H.; Kim, N.; Kim, Y.; Yu, S. U.; Kim, K. S.; Noh, D. Y.; Chung, J. *ACS Nano* (2015) 9, 10861
- [37] Cao, W.; Zhang, R.-X.; Tang, P.; Yang, G.; Sofo, J.; Duan, W.; Liu, C.-X. *2D Mater.* (2016) 3, 034006
- [38] Qiao, H.; Yuan, J.; Xu, Z.; Chen, C.; Lin, S.; Wang, Y.; Song, J.; Liu, Y.; Khan, Q.; Hoh, H. Y.; Pan, C.-X.; Li, S.; Bao, Q. *ACS Nano* (2015) 9, 1886
- [39] Vaklinova, K.; Hoyer, A.; Burghard, M.; Kern, K. *Nano Lett.* (2016) 16, 2595
- [40] Bernevig, B. A.; Hughes, T. L.; Zhang, S.-C. *Science* (2006) 314, 1757
- [41] Hsieh, D.; *et al.* *Science* (2009) 460, 1101
- [42] Moore, J. E. *Nature* (2010) 464, 194
- [43] Hasan, M. Z.; Kane, C. L. *Rev. Mod. Phys.* (2010) 82, 3045
- [44] Bercioux, D.; Lucignano, P. *Rep. Prog. Phys.* (2015) 78, 106001
- [45] Soumyanarayanan, A.; Reyren, N.; Fert, A.; Panagopoulos, C. *Nature* (2016) 539, 509–517
- [46] Popov, I.; Mantega, M.; Narayan, A.; Sanvito, S. *Phys. Rev. B: Condens. Matter Mater. Phys.* (2014) 90, 035418
- [47] Rajput, S.; Li, Y.-Y.; Weinert, M.; Li, L. *ACS Nano* (2016) 10, 8450
- [48] Lee, P.; Jin, K.-H.; Sung, S. J.; Kim, J. G.; Ryu, M.-T.; Park, H.-M.; Jhi, S.-H.; Kim, N.; Kim, Y.; Yu, S. U.; Kim, K. S.; Noh, D. Y.; Chung, J. *ACS Nano* (2015) 9, 10861
- [49] Kou, L.; Hu, F.; Yan, B.; Wehling, T.; Felser, C.; Frauenheim, T.; Chen, C. *Carbon* (2015) 87, 418
- [50] Lin, Z.; Qin, W.; Zeng, J.; Chen, W.; Cui, P.; Cho, J.-H.; Qiao, Z.; Zhang, Z. *Nano Lett.* (2017) 17, 4013
- [51] Jin, K.-H.; Jhi, S.-H. *Phys. Rev. B: Condens. Matter Mater. Phys.* (2013) 87, 075442
- [52] De Beule, C.; Zarenia, M.; Partoens, B. *Phys. Rev. B: Condens. Matter Mater. Phys.* (2017) 95, 115424
- [53] Zhang, J.; Triola, C.; Rossi, E. *Phys. Rev. Lett.* (2014) 112, 096802
- [54] Raes, B.; Scheerder, J. E.; Costache, M. V.; Bonell, F.; Sierra, J. F.; Cuppens, J.; Van de Vondel, J.; Valenzuela, S. O. *Nat. Commun.* (2016) 7, 11444
- [55] Raes, B.; Cummings, A. W.; Bonell, F.; Costache, M. V.; Sierra, J. F.; Roche, S.; Valenzuela, S. O. *Phys. Rev. B: Condens. Matter Mater. Phys.* (2017) 95, 085403
- [56] Kohn, W.; Sham, L. J. *Phys. Rev.* (1965) 140, A1133
- [57] Kresse, G.; Furthmuller, J. *Comput. Mater. Sci.* (1996) 6, 15
- [58] Kresse, G.; Joubert, D. *Phys. Rev. B: Condens. Matter Mater. Phys.* (1999) 59, 1758
- [59] Perdew, J. P.; Burke, K.; Ernzerhof, M. *Phys. Rev. Lett.* (1997) 78, 1396
- [60] Tkatchenko, A.; Scheffler, M. *Phys. Rev. Lett.* (2009) 102, 073005
- [61] Zhou, Yecheng; Zhang, Hao-Li and Deng, Wei-Qiao *Nanotechnology* (2013) 24(22):225705
- [62] Borge, J.; Gorini, C.; Vignale, G. and Raimondi, R. *Phys. Rev. B* (2014) 89, 245443
- [63] Shen, Ka; Vignale, G. and Raimondi, R. *Phys. Rev. Lett.* (2014) 112, 096601
- [64] Rodriguez-Vega, M.; Schwiete, G.; Sinova, J. and Rossi, E. *Phys. Rev. B* (2017) 96, 235419
- [65] Basak, Susmita; Lin, Hsin; Wray, L. A.; Xu, S.-Y.; Fu, L.; Hasan, M. Z. and Bansil, A. *Phys. Rev. B* (2011) 84, 121401(R)

- [66] Zhang, Haijun; Liu, Chao-Xing and Zhang, Shou-Cheng *Phys. Rev. Lett.* (2013) 111, 066801
- [67] Xie, Zhuojin, He, Shaolong; Chen, Chaoyu; Feng, Ya; Yi, Hemian; Liang, Aiji; Zhao, Lin; Mou, Daixiang; He, Junfeng; Peng, Yingying; Liu, Xu; Liu, Yan; Liu, Guodong; Dong, Xiaoli; Yu, Li; Zhang, Jun; Zhang, Shenjin; Wang, Zhimin; Zhang, Fengfeng; Yang, Feng; Peng, Qinjun; Wang, Xiaoyang; Chen, Chuangtian; Xu, Zuyan and Zhou, X.J. *Nature Communication* (2014) 5:3382
- [68] Liu, Chao-Xing; Qi, Xiao-Liang; Zhang, Hai-Jun; Dai, Xi; Fang, Zhong and Zhang, Shou-Cheng *Phys. Rev. B* (2010) 82, 045122
- [69] Fabian, J.; Matos-Abiague, A.; Ertler, C.; Stano, P.; Žutić, I. *Acta Phys. Slovaca* (2007) 57, 565
- [70] Kane, C. L.; Mele, E. J. *Phys. Rev. Lett.* (2005) 95, 226801
- [71] Khokhriakov, Dmitrii; Cummings, Aron W.; Song, Kenan; Vila, Marc; Karpiak, Bogdan; Dankert, André; Roche, Stephan and Dash, Saroj P.; Strong Proximity-Induced Spin Relaxation In Graphene - Topological Insulator van der Waals Heterostructures, submitted to Journal of Science Advances
- [72] Kochan, D.; Irmer, S.; Fabian, J. *Phys. Rev. B: Condens. Matter Mater. Phys.* (2017) 95, 165415
- [73] Cummings, Aron W.; Garcia, Jose H.; Fabian, Jaroslav and Roche, Stephan *Phys. Rev. Lett.* (2017) 119, 206601
- [74] Song, Kenan; Soriano, David; Cummings, Aron W.; Robles, Roberto; Ordejón, Pablo and Roche, Stephan *Nano Lett.* (2018) 18, 2033-2039

Chapter Five: The Effects of Non-Magnetic and Magnetic Dopants on the Electronic Properties of 3D Topological Insulators

5.1 Introduction to Fu-Kane-Mele Model

In 2007, Liang Fu, C. L. Kane and E. J. Mele proposed a theoretical model to predict the properties of three-dimensional topological insulators, which uses four Z2 topological invariants to distinguish between different quantum phases [1]. A corresponding tight-binding (TB) model, which is based on diamond cubic crystal structure and has four s -state bands, was also generated to discuss these phases based on the FKM TB model in equation (5.1):

$$H_{pristine} = t \sum_{\langle i,j \rangle} c_i^\dagger c_j + i \frac{8\lambda_{SOC}}{a^2} \sum_{\langle\langle i,j \rangle\rangle} c_i^\dagger \vec{s} \cdot (\vec{d}_{i,j}^1 \times \vec{d}_{i,j}^2) c_j \quad (5.1)$$

where, t is the hopping parameter between first neighbour atoms; λ_{soc} is the intrinsic spin-orbit coupling strength between second neighbour atoms; a is the bonding length between the two first neighbour atoms, \vec{s} is spin operator and $\vec{d}_{i,j}^1/\vec{d}_{i,j}^2$ is the unit bonding vector between the second neighbour atom.

Because the FKM Hamiltonian is defined in a 3D diamond lattice structure, there are two different hopping parameters to differentiate the inequivalent directions. One in-plane hopping parameter is denoted by t_{\parallel} , which describes the energy coupling, within the x - y plane between each atom and its three first neighbour atoms. The other coupling parameter, denoted by t_{\perp} , connects all 2D layers together. By tuning the relative magnitudes between t_{\parallel} and t_{\perp} , different topological (and trivial) phases can be achieved as illustrated in Fig. 5.1. Here, the structure was taken as a slab with 48 layers in the unit cell. If t_{\parallel} is larger than t_{\perp} , the interaction between each 2D layer structure is weak and the whole system just consists of several inde-

pendent layers of 2D QSH insulating phases. The surface band has an even number of Dirac points (DP) and the system behaves as a normal insulator, so it is called a weak topological insulator (WTI). If t_{\parallel} is equal to t_{\perp} , there is only one uniform hopping parameter in all directions and the whole system is similar to a semimetal. This phase is very interesting and resemble a Topological (or Dirac).[2] Topological semimetals are 3D analogues of Graphene where DP form due to spin-orbit effects and are protected against disorder as topological surface states. In presence of external magnetic fields or intrinsic magnetism may transform into Weyl semimetals. When t_{\parallel} is smaller than t_{\perp} , each 2D QSH phase is strongly connected to the others and the surface band has an odd number of DPs, which results in a robust topological state that cannot be easily destroyed by disorder, so it is called a strong topological insulator (STI).

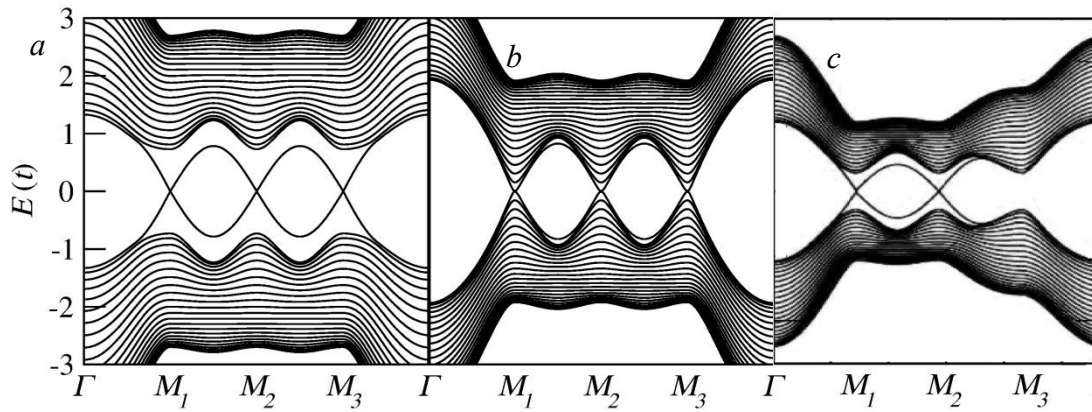


Fig. 5.1 Three phases TIs (*a.* - STI. *b.* - semimetal: *c.* - WTI)

Topological insulators are the main topic of this research project, therefore the discussion will be restricted to STI. The FKM model is built upon a diamond lattice symmetry which has a generic buckled structure where atoms belonging to different sub-lattices lie on different triangular planes in each layer. This constitutes the repeating unit of the crystal structure. Therefore the model allows for different surface terminations, either stoichiometric (T1) or not (T2). The stoichiometric one (or T1) is obtained by simply keeping the two triangular planes at the interface or removing an even number of triangular planes (see Fig. 5.2*a*). The non-stoichiometric one (or T2) is obtained by removing an odd number of triangular planes (see Fig. 5.2*b*). This makes the surface atoms to change coordination from three neighbour atoms in the same layer to just one single atom in the neighbouring layer. In a slab geometry made of a finite number of layers, we can have the same or different surface termination on each side (see Fig 5.2*a* ~ 5.2*c*). These different surface termination cases give rise to different

band structures, as shown in Fig. 5.2. Figs. 2a and 2d represent T1-T1 termination cases where three DPs appear at the three M points in the first Brillouin zone. In contrast, Figs. 2b and 2e represent the T2-T2 case with the presence of a single DP, sitting at Γ point. Figs. 2c and 2f illustrate the T1-T2 case and as this model has two terminations, the resulting band structures display both features from separate situations and the DPs show up at both Γ and three M points. Compared with the Bi_2Se_3 -family TIs, the T2-T2 termination case seems more “realistic” given its DP is located at the Γ point, although the internal crystal symmetries are different.

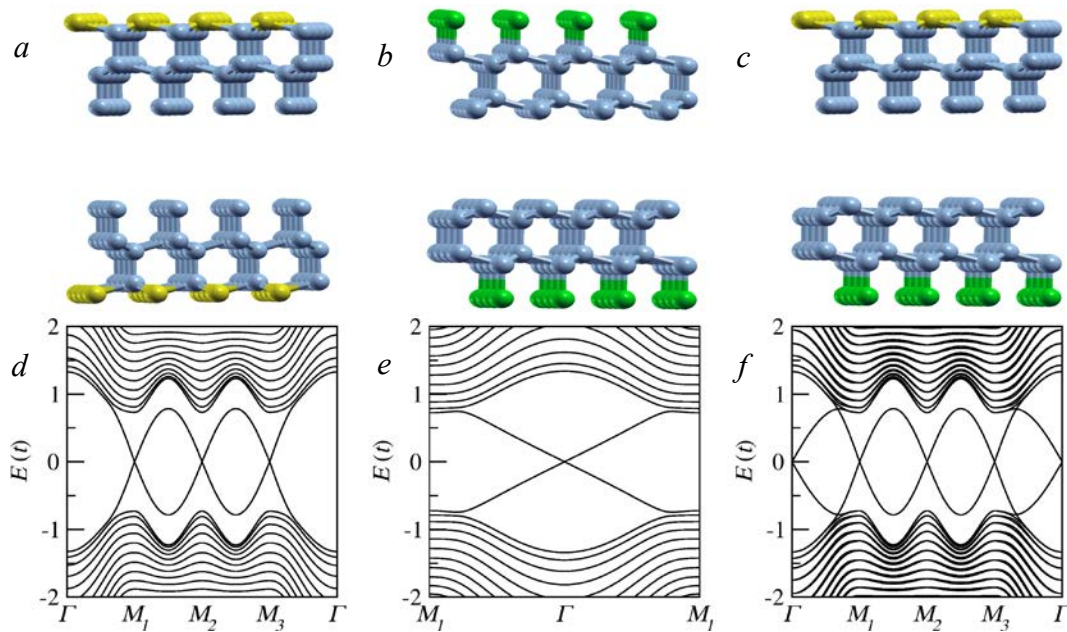


Fig. 5.2 Crystal and band structure. *a* & *d* – T1T1 case; *b* & *e* – T2T2 case; *c* & *f* – T1-T2 case. In *f*, there four DPs. One, which is located at Γ point, comes from T2 termination; while the other three DPs, which are located at three M points, come from T1 termination. Yellow and green colours denote atom on T1 and T2 terminations respectively.

It is instructive to also evaluate the effect of the thickness of the slab on the band structures as reported in Fig. 5.3. According to the figure, one can see a gap opening for the model with very few layers, since the surface states on both opposite surfaces overlap; while the gapless DP can be recovered for a thickness of at least 12 layers, which is thus enough to avoid state overlap and quantum tunnelling between opposite boundaries.[3]

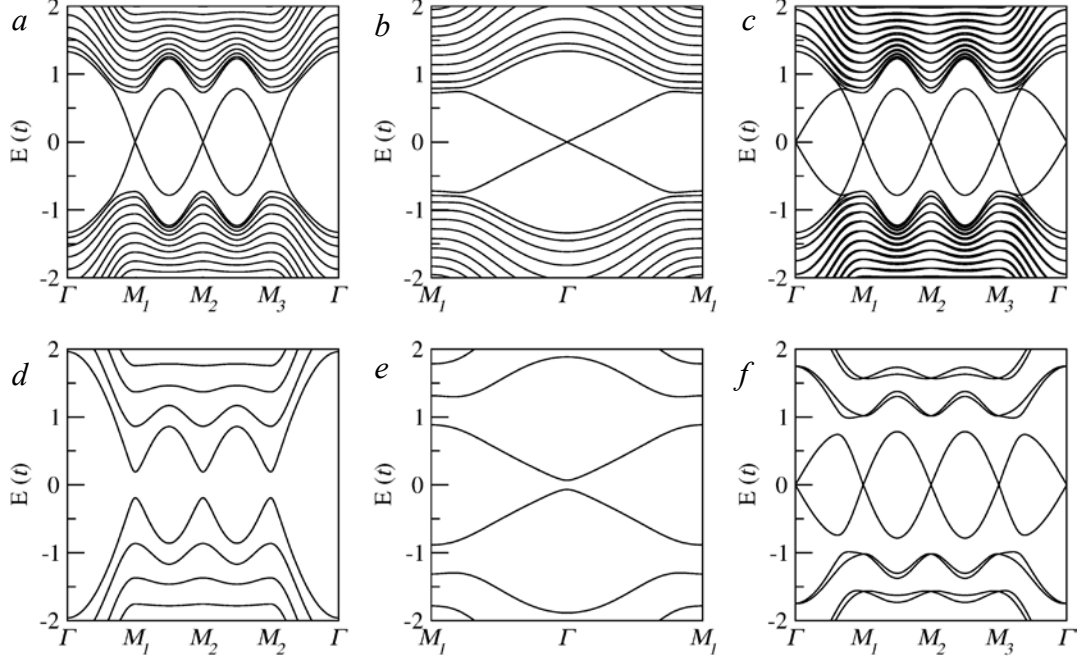


Fig. 5.3 Band structures versus the thickness of the FKM model. *a* & *d* – T1T1 case 12L & 4L; *b* & *e* – T2T2 case 12L & 4L; *c* & *f* – T1T2 case 11L & 3L

The spin texture of surface states of the FKM Hamiltonian can be computed from the equation (5.2).

$$\langle \hat{S}_j(\vec{k}) \rangle = \sum_{j \in \text{surface}} \langle \Psi_j(\vec{k}) | \hat{\sigma}_i | \Psi_j(\vec{k}) \rangle \quad (5.2)$$

where, $\langle S_i(\vec{k}) \rangle$ is the total expectation value of the spin operator for all surface atoms along different axes, $|\Psi_j(\vec{k})\rangle$ is the surface state from and $\hat{\sigma}_i$ is the Pauli matrix vector. Fig. 5.4 shows the typical spin textures for the two different surface terminations with a slab thickness of 48 atomic planes for the T1-T1 case and 46 atomic planes for T2-T2 one. The green arrows indicate the directions of spin expectation values centred on different high symmetry points in the Brillouin zone.

It is apparent that such spin textures on both surface terminations can manifest the spin-momentum locking mechanism, which means that the spin expectation values point in a direction perpendicular to the momentum direction (Fig. 4a). However, the textures also exhibit differences for the two cases. Fig. 4c shows the texture on the T1 surface and it can be seen that the angle between spin and momentum vectors does not keep at 90 degrees and varies with the momentum vector directions. This spin texture is usually observed in materials with

strong spin-orbit coupling and lacking of bulk inversion symmetry, and is known as Dresselhaus effect. It contrasts with the spin texture shown in Fig. 4a in which the spin and momentum are always perpendicular to each other over all the energy spectrum. Because different terminations exhibit DP at different k -points (T1 case - M point; T2 case - Γ point), the spin texture also shows up at different positions in the first Brillouin zone accordingly. Compared to real 3D TI film systems, such as Bi₂Se₃ films, where the spin texture on the surface is always perpendicular to the momentum, the T2-T2 slab seems again close to “reality”. In the following sections, we will focus on this type of slabs.

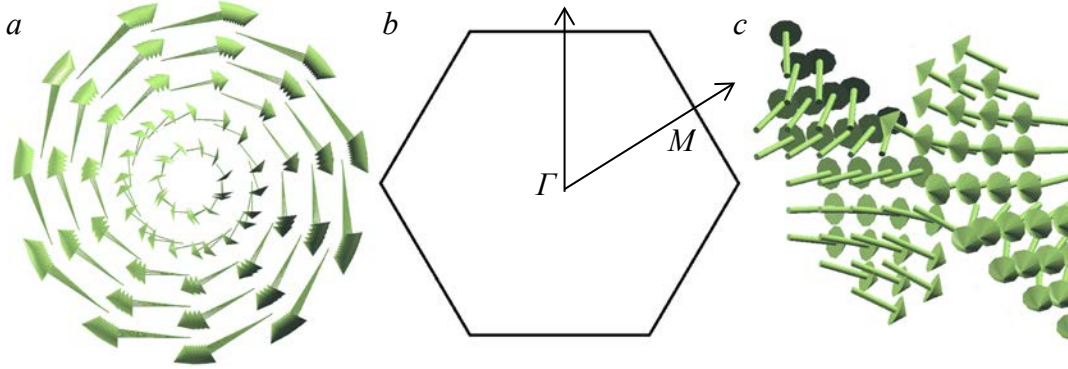


Fig. 5.4 Spin texture for FKM model on different surfaces. *a.* – T2 termination at the Γ point; *b.* – First Brillouin zone; *c.* – T1 termination at the M point

To further characterize the band structure properties, an effective four band Hamiltonian, initially proposed by Rui Yu *et al.*, [4] was used in our study to calculate the spectral properties of more realistic structures. In this way, the analytical expressions for the band gap and spin texture are obtained and more clear view for the electronic properties of TI surface state can be provided. To that end, the Schrödinger equation was solved using the Hamiltonian (5.3)

$$H_{TI_pristine} = \begin{pmatrix} 0 & a & 0 & 0 \\ a^+ & 0 & 0 & 0 \\ 0 & 0 & 0 & -a \\ 0 & 0 & -a^+ & 0 \end{pmatrix} \quad (5.3)$$

where, $a = ivKe^{-i\vartheta} = ivK(\cos\vartheta - i\sin\vartheta) = ivk_x + vk_y$ and a^+ is the Hermitian conjugate of a . v is the fermi velocity; K is the module of k -vector and $\vartheta = \arctan \frac{k_y}{k_x}$

$H_{TI_pristine_top} \Psi_{top} = \begin{pmatrix} 0 & a \\ a^+ & 0 \end{pmatrix} \times \begin{pmatrix} T_{\uparrow} \\ T_{\downarrow} \end{pmatrix} = \lambda \times \begin{pmatrix} T_{\uparrow} \\ T_{\downarrow} \end{pmatrix}$; then the eigenvalues are given by

$$\lambda^2 = a \times a^+ = v^2 K^2;$$

$$\lambda_{\pm} = \pm vK \quad (5.4)$$

and the eigenvectors

$$T_{\uparrow} = \frac{a}{\lambda} T_{\downarrow} \quad (5.5)$$

After normalization

$$\begin{pmatrix} T_{\uparrow}^+ & T_{\downarrow}^+ \end{pmatrix} \times \begin{pmatrix} T_{\uparrow} \\ T_{\downarrow} \end{pmatrix} = \begin{pmatrix} \frac{a^+}{\lambda} T_{\uparrow}^+ & T_{\downarrow}^+ \end{pmatrix} \times \begin{pmatrix} \frac{a}{\lambda} T_{\uparrow} \\ T_{\downarrow} \end{pmatrix} = \frac{aa^+}{\lambda^2} |T_{\downarrow}|^2 + |T_{\downarrow}|^2 = 2|T_{\downarrow}|^2 = 1$$

Then,

$$T_{\downarrow} = \frac{1}{\sqrt{2}} \quad (5.6)$$

and

$$T_{\uparrow} = \frac{1}{\sqrt{2}} \frac{a}{\lambda} = \frac{1}{\sqrt{2}} \frac{ivKe^{-i\theta}}{\pm vK} = \pm \frac{1}{\sqrt{2}} ie^{-i\theta} \quad (5.7)$$

For the bottom surface band, the eigenvalues and normalized eigenvector are given by

$$\lambda_{\pm} = \pm vK; B_{\uparrow} = \frac{1}{\sqrt{2}} \frac{-a}{\lambda} = \frac{1}{\sqrt{2}} \frac{-ivKe^{-i\theta}}{\pm vK} = \mp \frac{1}{\sqrt{2}} ie^{-i\theta}.$$

Therefore, the normalized eigenvector matrix is as follows (equation 5.8):

$$|\psi\rangle = \frac{1}{\sqrt{2}} \begin{pmatrix} ie^{-i\theta} & -ie^{-i\theta} & 0 & 0 \\ 1 & 1 & 0 & 0 \\ 0 & 0 & -ie^{-i\theta} & ie^{-i\theta} \\ 0 & 0 & 1 & 1 \end{pmatrix} \quad (5.8)$$

Fig. 5.5 shows the band structure calculated using this Hamiltonian from which the linear energy dispersion relation is evident for the pristine TI system. As the k point gradually moves close to Γ point, the energy spectrum shows a lowering of the density of states which disappears at the DP. This situation is the same as the T2-T2 termination case in the FKM model.

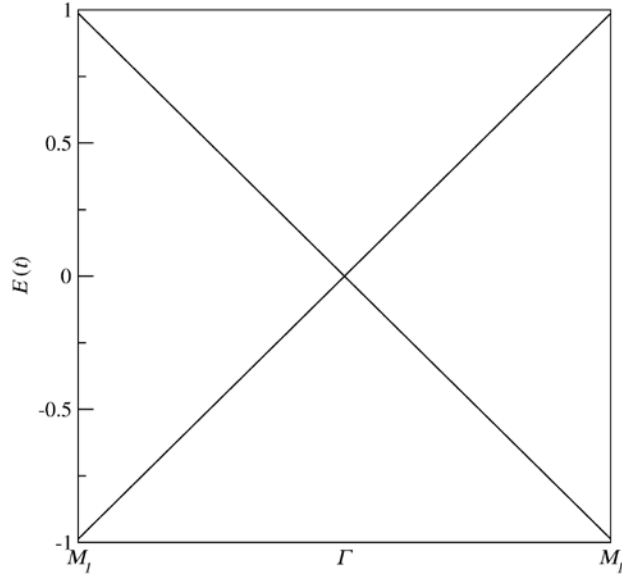


Fig. 5.5 Band structure, corresponding to T2 termination case from effective Hamiltonian model

5.2 Fu-Kane-Mele model with onsite non-magnetic potential

The study of disorder effects in TIs has been the subject of many theoretical studies. In Yan Yang Zhang *et al.*'s paper[17], the effect of disorder potential was studied in order to see how the band structure of a two dimensional topological insulator (HgTe/CdTe) evolves. The authors reported that disorder strength could lead to the touching of VB and CB, which may trigger the emergence of a topological Anderson insulating (TAI) phase. This type of disorder-driven phase has a cluster of nontrivial subgaps separated by almost flat and localized bands. Christoph P. Orth *et al.* also studied the HgTe/CdTe quantum well in presence of disorder using the Kane-Mele model and reported that such a system could be tuned into a TAI.[18]

Regarding three dimensional TIs, the effect of non-magnetic impurities on the electronic properties of TI cases has been investigated by Marco Bianchi *et al.*[5] who reported that Bi_2Se_3 film with adsorption of carbon monoxide (CO) molecules could exhibit band bending and energy downshift of the Dirac point due to doping when compared with the pristine TI system. This suggests that the adsorption of the CO molecules could cause aging of the TI surface state and degeneration between surface state and bulk bands. Tobias Forster *et al.*[6] performed theoretical calculations and studied the potassium (K) doping on different surface positions of the Bi_2Se_3 slab model. They pointed out that the hollow position is the most stable one and that K ad-atoms are likely to induce strong charge transfer and give rise to long-

range scattering potential. This effect could move the surface DP inside the bulk band, resulting in an *M*-shape valence maximum band and a *W*-shape conduction minimum band. Furthermore, a *Rashba*-type band splitting of the surface states was also observed below the conduction minimum. Hadj M. Benia *et al.*[7] performed an experiment in which a Bi₂Se₃ surface reacted chemically with water molecules. The result was a strong band bending with surface DP pushed into a valence band (VB) and a quantum well state (QWS) was observed on top of the VB. They argued that the distorted TI band could significantly alter the transport measurements, although the nontrivial characteristic of surface state remained with an odd number of crossings between the surface state and Fermi level. S. Jakobs *et al.*[8] modified the surface of Bi₂Se₃ film with organic molecules (H₂Pc^S) and reported a *Rashba*-type band splitting at the bottom of the conduction band with surface DP that could be shifted in a controlled way, through a careful tuning of the chemical interaction between H₂Pc^S and TI surface. G. L. Hao *et al.*[9] grew TI film on silicon substrate with both *p* and *n* -types and they reported that different types of substrates could enable tuning the position of the DP in the band structure. Other researchers have investigated the impact of non-magnetic doping on TI film systems, and most results conclude that doping effects, in the absence of magnetism, could induce large surface potentials, moving the surface DP into bulk bands and resulting in band bending.[10-19]

Based on all these reports, we use the FKM model with a random onsite non-magnetic potential ($V_{non-magnetic}$) in order to simulate the real situation that the non-magnetic disorder is randomly doped on TI surface. Equation (5.9) describes the Hamiltonian of the whole system:

$$H_{total} = H_{pristine} + V_{non-magnetic} \sum_{i \in surface} c_i^\dagger c_i \quad (5.9)$$

where, $H_{pristine}$ is the Hamiltonian for the pristine FKM model, $V_{non-magnetic}$ is the magnitude onsite potential with the value of $0.5t_{\parallel}$. Fig. 5.6 shows the band structure of the FKM model with T2-T2 terminations and 16.05% of nonmagnetic potential at random position on surface. It can be seen that the surface state remains, and also the DP, but its position is lifted up and become closer to the conduction band minimum than before. The results clearly show that this toy model could provide similar features than real TI system with non-magnetic doping. For instance, (1) the non-magnetic potential does not open the surface gap which is consistent with the experimental results; (2) the position of the surface DP is tuned with the onsite po-

tential. This is in line with the fact that tuning the charge potential with different nonmagnetic elements could shift the surface DP to different positions in VB or CB.

Meanwhile, the spin texture still shows spin-momentum locking (shown in Fig. 6 inset), which is the same as in the pristine case. This means the disorder potential only lifts the surface state but does not alter the nontrivial topological phase.

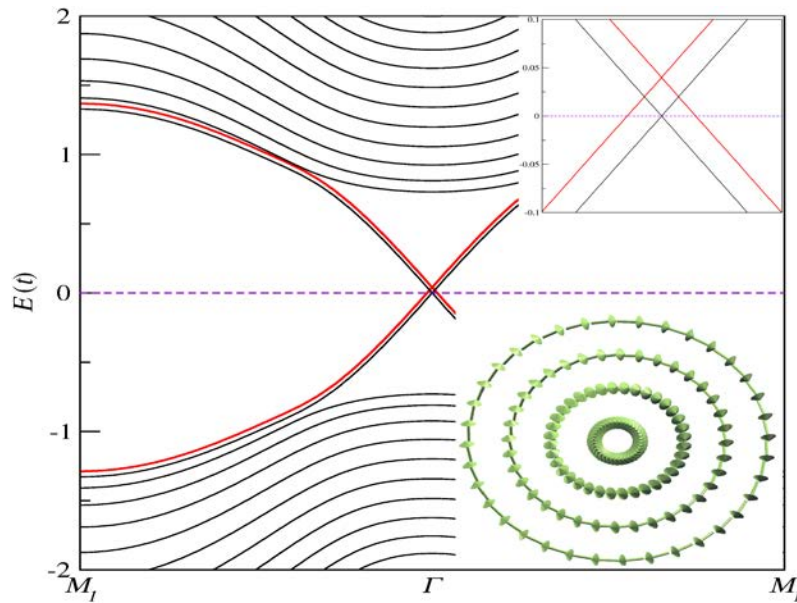


Fig. 5.6 FKM slab with T2-T2 termination doped with onsite non-magnetic potential and 48 layers. Red colour indicates the surface state doped with non-magnetic potential with spin texture shown in inset

5.3 Fu-Kane-Mele model with random onsite exchange potential

The previous section 5.2 has already shown that the FKM model on a diamond lattice could be used to reproduce the electronic structure of a topological insulator and also that non-magnetic doping on the surface does not break the time reversal symmetry of the system and only lifts the position of the surface DP. On the other hand, more and more studies have explored the effect of magnetic doping on TI because the Zeeman field exerted by the magnetic doping could break time reversal symmetry and cause the gap opening of the surface states. As introduced in chapter 2, the surface states of a topological insulator derive from band inversion, which derives from the strong spin-orbit coupling, so the gap opened by magnetic exchange can be non-trivial and induce a quantum anomalous hall effect (QAHE)[20]. For instance, Rui Yu *et al.* reported that Cr/Fe doped Bi_2Se_3 showed a topological non-trivial

band structure with quantized hall conductance without an external magnetic field[21], which means that the edge state of QAH phase could conduct charge current without any dissipation. Ke He *et al.*[22] also pointed out that $\text{Cr}_x(\text{Bi}_{0.2}\text{Sb}_{0.8})_{1-x}\text{Te}_3$ alloy exhibits nonzero Hall conductance, indicating that alloying with Cr could induce a QAH phase in TI materials. Cui-Zu Chang *et al.*[23] reported that Cr doped BiSbTe could achieve a quantized transverse conductance without a strong magnetic field. Mansoor B. A. Jalil *et al.*[24] studied theoretically a magnetically doped TI by using a Hamiltonian with spin-orbit coupling to evaluate the Hall conductance and reported an non-zero berry phase of the whole system. Besides that, other groups also studied many magnetic doping schemes on TI and reported surface gap opening and magnetism on TI systems.[25-33]

Therefore, it is quite important and interesting to study the effect of magnetic doping on the FKM model. Usually, the magnetic elements are distributed either onto the surface or inside bulk of TI in random positions with impurities distributed onto the surface and inside bulk of the FKM. In this section, we use the FKM model with magnetic doping using a spin dependent onsite exchange potential (V_{xc}) with different type of slab terminations. Fig. 5.7 shows a schematic picture for the model with a $9 \times 9 \times 1$ supercell and 24 atomic planes for T_2 - T_2 termination and 22 atomic planes for T_1 - T_1 termination. Red dots indicate the position of the magnetic dopant. The Hamiltonian used to study magnetic doping on TI takes the following form

$$H_{total} = H_{pristine} + \sum_{i,\sigma} [c_{i,\sigma}^\dagger (V_{xc} \cdot \sigma) c_{i,\sigma} + H.c.] \quad (5.10)$$

where, the first term ($H_{pristine}$) is the Hamiltonian for the pristine FKM model and the second term describes the onsite exchange potential. Here it was assumed that the doping elements do not have chemical bonding with TI and just induce localized Zeeman fields.

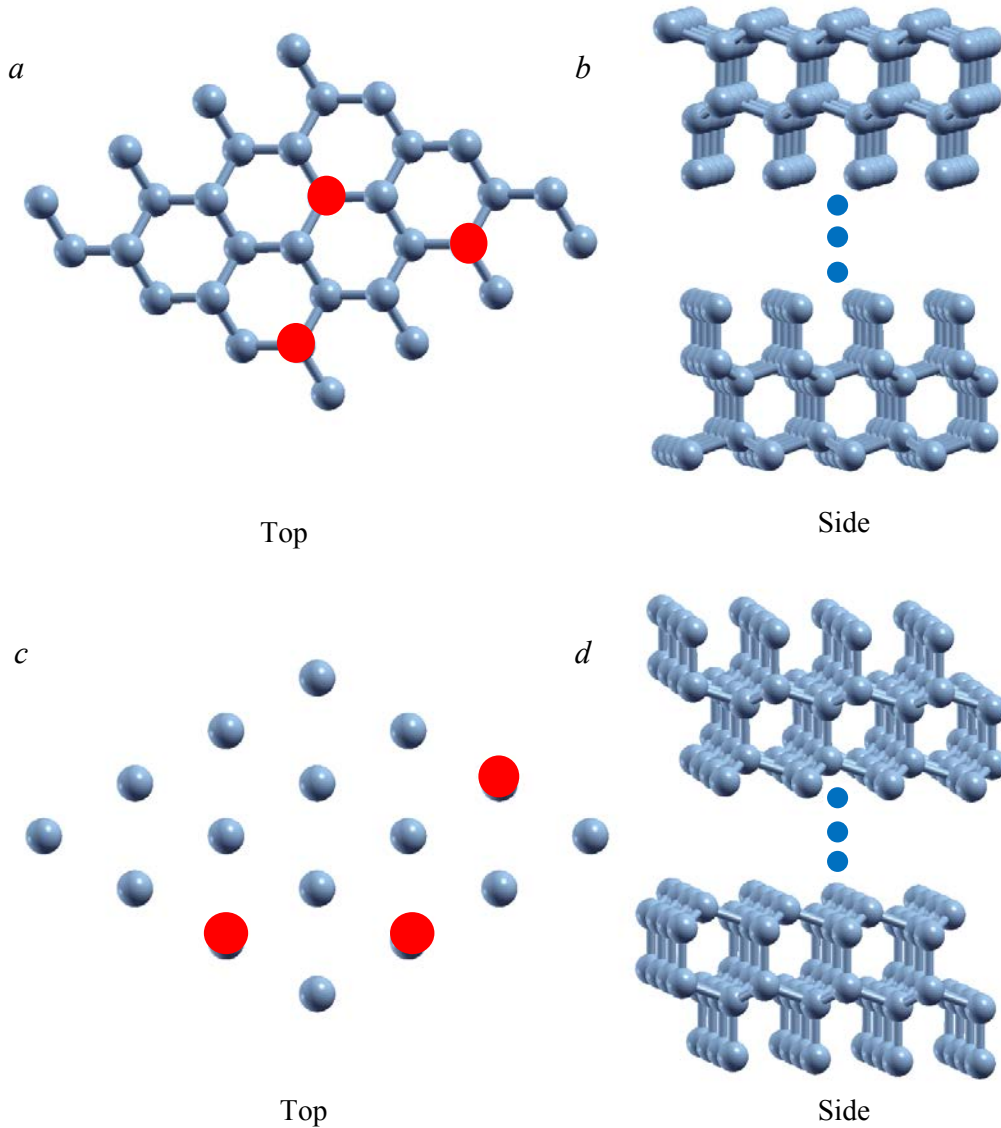


Fig. 5.7 Lattice structure of Fu-Kane-Mele model with both top and side views. *a*

According to Qin Liu's work[34], the reasonable value for the exchange potential ranges from $0.1t$ to $0.7t$ and t is the in-plane hopping parameter. Fig. 5.8 shows the band structure of the FKM model with unit cells doped with 100% magnetic impurities with a strength of the exchange potential which varies from $0.2t$ to $0.7t$. Both T_1 - T_1 and T_2 - T_2 terminations are investigated for this structure and the direction of potential is aligned along z axis. The red colour indicates the band projection over surface states. For the T_1 - T_1 case, DP shows up at M point and a gap opens (see Fig. 5.8(*a-c*)). The same occurs in the T_2 - T_2 case (see Fig. 5.8(*d-f*)), although the DP stays at Γ point instead. In both cases, the surface gap increases with the potential strength. This indicates that the stronger the exchange coupling, the larger the band

gap induced onto the surface band of TI. Due to the symmetry of the structure, the T_1 - T_1 termination shows different gaps opening for the M_1 , M_2 and M_3 points respectively; which clearly demonstrates that $M_1 \neq M_2 \neq M_3$. In the following theoretical calculations, the value of the exchange potential is taken as $0.5t$. We study the electronic properties of different structures and different magnetic doping schemes while keeping the strength of the magnetic exchange potential.

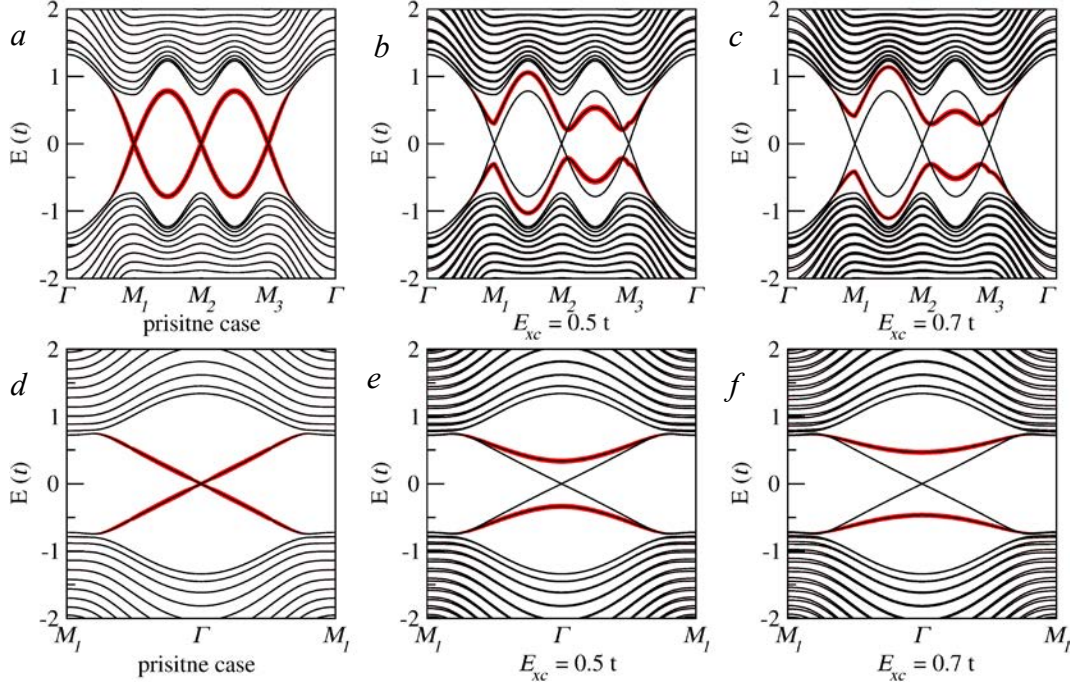


Fig. 5.8 Different strength of exchange potential doped onto an FKM model. $a \sim c$ - T_1T_1 termination; $d \sim f$ - T_2 - T_2 termination. Blue inset is the first Brillouin zone with three M points and Γ point

In unit cell, doping of impurities is 100% coverage but usually, TI film is adopted with different low doping percentage of impurities. This is why a larger supercell (shown in Fig. 5.7) was used in order to study the effect of different doping content on TI. Since the T_2 - T_2 termination shows the DP at the Γ point, similar to real topological insulators, we have adopted this case for the rest of this study. Fig. 5.9 shows the band structure of the FKM model with T_2 - T_2 termination and different percentages of the exchange potential on the top surface. The maximum magnetic doping percentage was 20% and the magnetic impurities were randomly distributed along the surface. The directions of all potentials were chosen to be along the z -axis at first. From Figs. 5.9a to 5.9c, it can be seen that the surface band gap increases with the doping percentage. The band gap values versus doping percentage are summarized in Fig. 5.10.

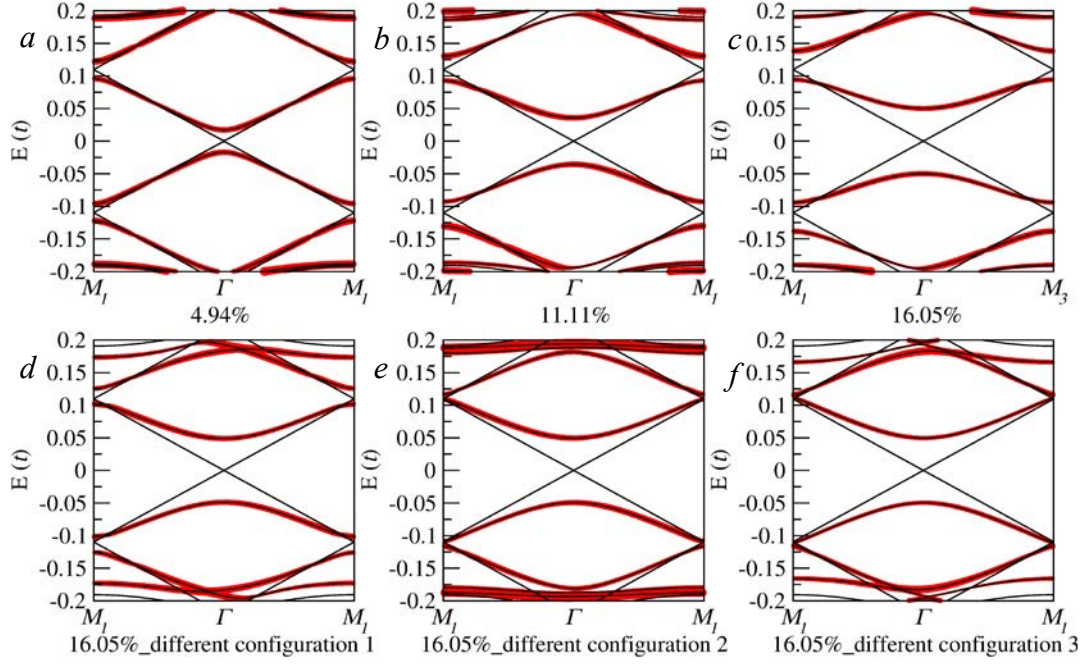


Fig. 5.9 Different doping percentage on T_2T_2 FKM model with $9 \times 9 \times 1$ supercell. The direction of potential is aligned along z axis. $a \sim c$ are different doping percents; $d \sim f$ are different configuration for the same doping percents corresponding to c

As discussed in chapter 2, because the TI surface bands are topological nontrivial, which means that Berry curvature around the gap is nonzero, the gaped TI is quite useful for the achievement of the quantum anomalous Hall effect, which shows quantized non-zero Hall conductance. In former experiments, the Hall conductance could only be observed on 2D electronic gas (2DEG) materials under a very strong magnetic field; for instance, Klaus Von Klitzing *et al.*[35] and D. C. Tsui *et al.*[36] reported the integer and fractional quantum Hall effect respectively. However, the achievement of the quantum Hall conductance requires external magnetic fields and low temperatures, which are usually not so easy to achieve in practice. On the other hand, in materials showing anomalous Hall conductance, such as ferromagnetic materials, the Lorentz force acting on the charge carriers necessary to induce the Hall current, comes from the intrinsic magnetization rather than from an external source. In this way, quantized Hall conductance is relatively easier to achieve. In topological insulators, the spin orbit coupling strength is very large and causes surface band inversion, which means that charge carriers with an opposite spin can move in opposite directions along the edges. This is known as quantum spin Hall effect (QSHE).[37] Since carriers with opposite spin sign move in counter-propagating paths, collision is avoided and the quantum transport become dissipationless. In other words, the study of the effect of magnetic impurities along z axis indicates

that the magnetic doping on TI makes it a useful applicant in the direction of quantized Hall effect without the requirement of external magnetic fields.

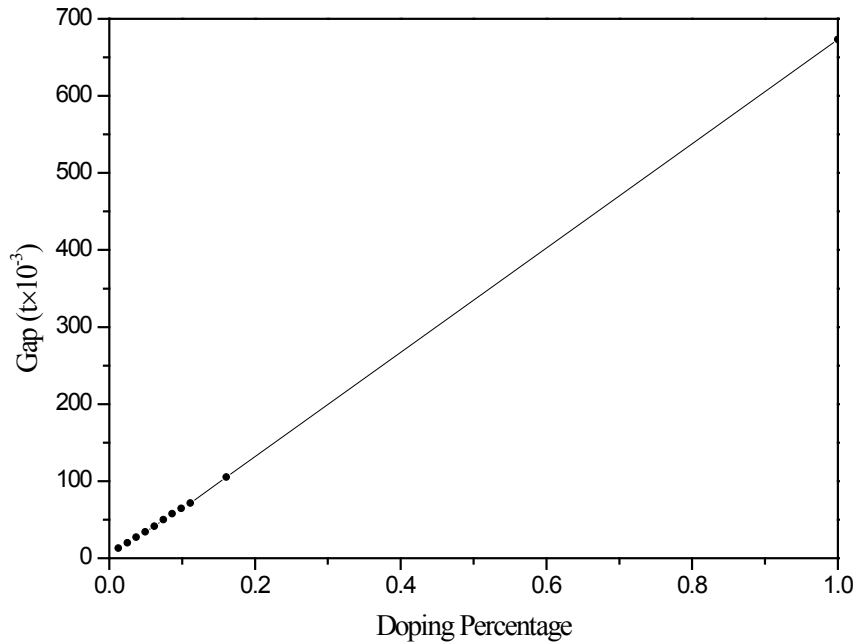


Fig. 5.10 Summary of band gap of FKM model with T2T2 termination configuration v.s. doping percentage

Since magnetic impurities are distributed at random surface positions, it is necessary to compare the influence between random configurations. Figs. 5.9d ~ 5.9f show the results for different surface doping configurations, corresponding to the same doping percentage from Fig. 5.9c. It is clear that randomness does not strongly affect the band structure; especially the band gap, although some small variations can be observed. Since it is very difficult to control the doping position on a TI surface in an experiment, these new results guarantee the generality of the results obtained previously for a fixed disorder percentage.

On the other hand, different magnetic elements may have a different easy axis in reality, which does not have to be only the z axis, therefore, it is important to study the effect of the easy axis for the exchange potential. For comparison, the supercell structure for FKM and the doping percentage were kept the same as that in Fig. 5.9c and the results for the FKM model with different magnetic easy axis are summarized in Fig. 5.11. Figs. 5.11a ~ 5.11c show the results for the magnetic moment aligned along the x axis; while Figs. 5.11d ~ 5.11e show the results for 16.05% doping with three different random doping configurations and the magnet-

ic moment is centred in the magnetic dopants. For the x -axis direction case, it is clear that the exchange potential does not induce any gap opening; instead it induces a translational shift of the surface DP which scales with doping percentage results in larger translational shift away from Γ point.

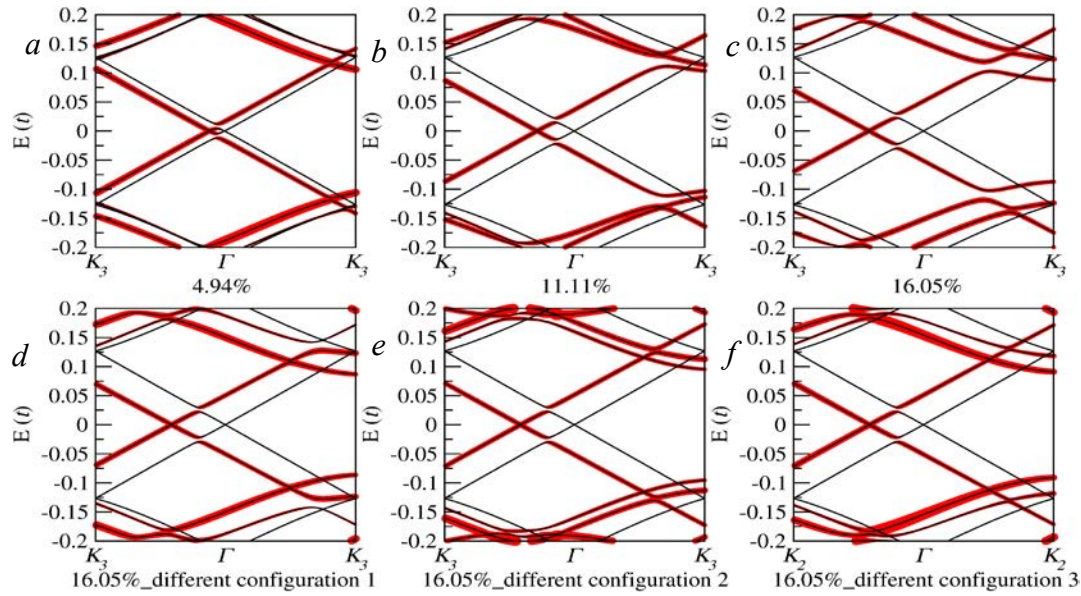


Fig. 5.11 Different easy axes for potentials adopted on an FKM model. $a. \sim c.$ are x -axis cases and doping percentages are the same as that in fig. 5.3. $d \sim e$ are different configurations of random axes in 3D space and the doping percentage is always fixed. $f. \sim$ is band structure along different k -paths. Red colour indicates the projection onto surface state doped with magnetic potential.

As can be seen in Fig. 5.12, the first Brillouin zone for the FKM model is hexagonal with three pairs of K - K' points occupying the diagonal corners. Since the magnetic moment points along the x -axis, which corresponds to the Γ - K direction in the reciprocal space, the surface DP position is shifted along this direction. The absence of a surface gap opening indicates that in-plane exchange potential does not break time reversal symmetry and this is the reason why the surface DP is preserved. The same conclusion can be extended to other in-plane exchange potentials.

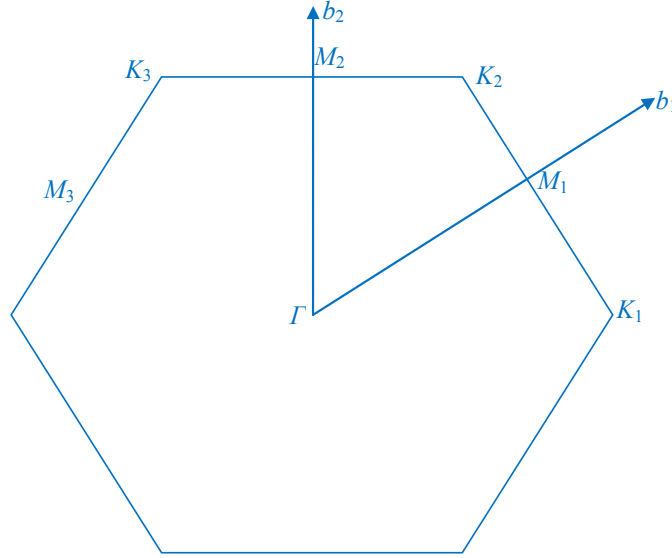


Fig. 5.12 First Brillouin zone for FKM model with reciprocal space lattice vector (b_1 and b_2)

In the experimental references there are many controversies regarding the mechanism inducing gap opening in topological surface states. For instance, M. Ye *et al.*[38] pointed out that Co atoms in Bi_2Se_3 are not able to order ferromagnetically. Indeed, no surface opening was observed by ARPES. On the contrary, Tome M. Schmidt *et al.*[39] reported on the possibility to induce an off-plane ferromagnetic interaction between Co dopants in TI and induce a gap opening. J. Honolka *et al.*[40] reported that Bi_2Se_3 films with Fe under 70 K could preserve TRS; while, Hosub Jin *et al.*[41]; T. Schlenk *et al.*[42]; T. Eelbo *et al.*[43] reported that Fe dopants on a TI surface could induce ferromagnetism and a gap opening.

A possible explanation for the different experimental results could come from the existence of different easy axis for different magnetic dopants. Once the easy axis is along an out-of-plane direction, like z -axis, the time reversal symmetry (TRS) is broken and the surface gap is formed; while when the axis is along any in-plane direction, like x -axis, the potential does not break TRS and the surface DP is just shifted away from Γ point along the in-plane easy axis. This implies that the expectation of the experimental results on magnetic doping on topological insulators greatly relies on the doping elements and the different alignments of the magnetic moments of impurities. It was noted that, for large enough magnetic dopants density, the resulting magnetic ordering (ferromagnetic, antiferromagnetic or diamagnetic) could determine the presence and width of the induced surface gap.

Meanwhile, the translational shift of the surface DP also brings the band crossing along a different k -path in the Brillouin zone. This means that the current signal measured in spintronic experiments could come from different surface states and one should pay attention to the contribution from different surface bands. According to Figs. 5.11d ~ 5.11f, it is clearly observed that the band gap does not vary a lot for different doping configurations.

On the other hand, different arbitrary configurations for the magnetic exchange can have different effects on the topological surface states and the band structure may vary a lot, especially the gap value. For instance, two magnetic impurities having opposite z -axis components will give rise to a zero out-of-plane magnetic moment; then, the remaining effect is dominated by the in-plane components, which does not trigger a gap opening. If two magnetic impurities on neighbouring surface atoms have the same z -axis components but opposite in-plane components, then the in-plane potential component is reduced while the out-of-plane components is enhanced, which results in a gap opening of the topological surface states. Furthermore, the surface band gap could also show translational shift away from the Γ point, due to the fact that the total in-plane component of the potential dominates and the out-of-plane is not totally cancelled. In contrast, some configurations could increase the surface gap at the Γ point if the out-of-plane potential component plays the key role. Because the angle between V_{xc} and the z axis was set up in a random way, the total V_z could vary a lot, depending on the angle θ (shown in the equation 5.11 and Fig. 5.13).

$$V_z = \sum_i V_{xc_i} \times \cos\theta_i \quad (5.11)$$

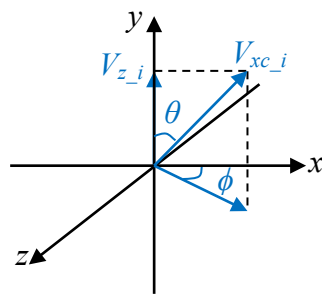


Fig. 5.13 Illustration for the configuration of the magnetic moment

In order to provide an energy window of the surface gap opening for the FKM model, we studied 40 different random configurations. The gap value was found to range between

$2.5 \times 10^{-2} \times t$ to $1.2 \times 10^{-1} \times t$. The band gap values v.s. z -axis component (V_z) of exchange potentials are shown in Fig. 5.14. Therefore, it is worth pointing out that this gap window could change for the doping percentage is lower than 100%, especially for very low doping percentage case where the distance between magnetic impurities becomes relatively large.

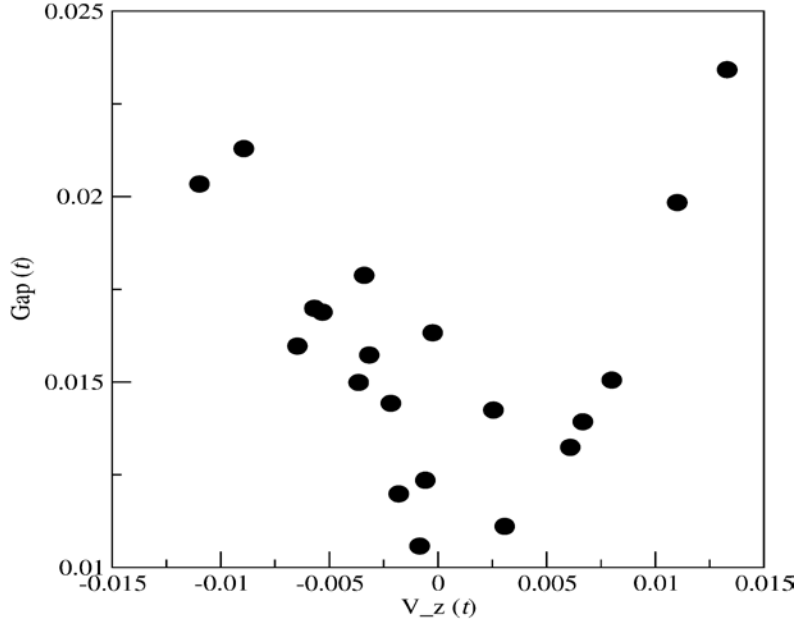


Fig. 14 Surface gap for different configurations for arbitrary-direction exchange potential on the surface in the FKM model

In order to provide an analytical expression for the electronic structure of the FKM model with magnetic dopants, we use a continuum model which allows to study the gap opening mechanism, Rui Yu *et. al's* work[44]. Here it is assumed that the TI is thick enough to avoid the quantum tunnelling effect between both surfaces. According to the equation 5.3 for the continuum model Hamiltonian of the TI, the onsite exchange potential (V_{xc}) is added to this Hamiltonian with two situations discussed below.

Situation 1: the exchange is aligned within the x - y plane.

According to the Pauli matrices $\sigma_x = \begin{vmatrix} 0 & 1 \\ 1 & 0 \end{vmatrix}$ and $\sigma_y = \begin{vmatrix} 0 & -i \\ i & 0 \end{vmatrix}$, the in-plane exchange potential is given by equation (5.12).

$$V = V_x \sigma_x + V_y \sigma_y = \begin{vmatrix} 0 & V_x - iV_y \\ V_x + iV_y & 0 \end{vmatrix} \quad (5.12)$$

Set $b = Ve^{-i\varphi} = V \times \cos\varphi + V \times i\sin\varphi = V_x - iV_y$ and $b^+ = Ve^{i\varphi} = V \times \cos\varphi + V \times i\sin\varphi = V_x + iV_y$

then, the in-plane exchange potential is

$$V = \begin{vmatrix} 0 & b \\ b^+ & 0 \end{vmatrix} \quad (5.13)$$

The in-plane exchange potential is only applied to the top TI surface, then the total Hamiltonian for TI becomes

$$H_{TI} = \begin{vmatrix} 0 & a+b & 0 & 0 \\ a^+ + b^+ & 0 & 0 & 0 \\ 0 & 0 & 0 & -a \\ 0 & 0 & -a^+ & 0 \end{vmatrix} \quad (5.14)$$

The off-diagonal terms are all zero, so the total Hamiltonian can be split into top and bottom surface parts.

For the bottom surface band, the Schrödinger equation writes in equation (5.15)

$$H_{TI_bottom}\Psi_{bottom} = \begin{vmatrix} 0 & -a \\ -a^+ & 0 \end{vmatrix} \times \begin{vmatrix} B_{\uparrow} \\ B_{\downarrow} \end{vmatrix} = \lambda \times \begin{vmatrix} B_{\uparrow} \\ B_{\downarrow} \end{vmatrix} \quad (5.15)$$

which gives eigenvalues for the bottom surface band of

$$\lambda^2 = a \times a^+ = v^2K^2 \text{ and } \lambda_{\pm} = \pm vK \quad (5.16)$$

The eigenvalues scales linearly with K, typical of a Dirac spectrum, and they touch at a single point (DP) at K=0.

For the top surface band, Schrödinger's equation is

$$H_{TI_top}\Psi_{top} = \begin{vmatrix} 0 & a+b \\ a^+ + b^+ & 0 \end{vmatrix} \times \begin{vmatrix} T_{\uparrow} \\ T_{\downarrow} \end{vmatrix} = \lambda \times \begin{vmatrix} T_{\uparrow} \\ T_{\downarrow} \end{vmatrix} \quad (5.17)$$

The eigenvalues are then

$$\lambda^2 = (a+b) \times (a^+ + b^+) = a \times a^+ + a \times b^+ + b^+ \times a + b \times b^+$$

$$= v^2K^2 + ivKV[e^{i(\varphi-\vartheta)} - e^{i(\vartheta-\varphi)}] + V^2 = v^2K^2 - 2vKP\sin(\varphi - \vartheta) + V^2$$

and

$$\lambda_{\pm} = \pm\sqrt{v^2K^2 - 2vKP\sin(\varphi - \vartheta) + V^2} \quad (5.18)$$

In particular, when the in-plane exchange potential is perpendicular to the k path, then

$$\varphi - \vartheta = \pm 90^\circ$$

and the eigenvalues become

$$\lambda_{\pm} = \pm\sqrt{v^2K^2 - 2vKP\sin 90^\circ + V^2} = \pm(vk - V) \quad (5.19)$$

For pristine TIs, DP is located at Γ -point; however, it is clear that the eigenvalue is no longer zero ($\pm V_{xc}$) at the Γ -point and instead reaches zero for $K = \frac{V}{v}$ case. Thus, it can be concluded that the in-plane exchange potential does not open any surface gap but just moves the surface DP somewhere away from Γ -point and, as the strength of exchange potential increases, the zero surface gap point is moved further away from Γ point in the Brillouin zone, because K increases with V_{xc} . This is illustrated in Fig. 5.15a.

On the other hand, when the in-plane exchange potential is perpendicular to the k -path ($\varphi - \vartheta = 0^\circ$), then the eigenvalues take the form

$$\lambda_{\pm} = \pm\sqrt{v^2K^2 - 2vKP\sin 0^\circ + V^2} = \pm\sqrt{v^2K^2 + V^2} \quad (5.20)$$

from which it is clear that the eigenvalues never reach zero and that there is always a band gap opening along this k path.

This conclusion is in agreement with the results from numerical calculations, which are shown in Figs. 5.11a ~ 5.11c which show the DP is shifted away from the Γ point. When examining the band structure of surface states obtained in calculation, one should pay attention to the k -path, because the surface DP could not be located at the Γ point anymore. Choosing different k paths, which does not include the Γ point, can result in different band structures from that with the Γ point.

Situation 2: The magnetization of impurities is aligned within the z axis.

In this case, the magnetization of the impurities is aligned out-of-plane. According to Pauli's matrix $\sigma_z = \begin{vmatrix} 1 & 0 \\ 0 & -1 \end{vmatrix}$, the out-of-plane exchange potential is written as

$$V = V_z \sigma_z = \begin{vmatrix} V_z & 0 \\ 0 & -V_z \end{vmatrix} \quad (5.21)$$

Following the same strategy as in Situation 1, we only apply the out-of-plane potential to the top TI surface, then the total Hamiltonian for TI is

$$H_{TI} = \begin{vmatrix} V_z & a & 0 & 0 \\ a^+ & -V_z & 0 & 0 \\ 0 & 0 & 0 & -a \\ 0 & 0 & -a^+ & 0 \end{vmatrix} \quad (5.22)$$

The bottom surface does not have magnetic doping so the surface state shows its DP at the Γ -point, which is same as in the previous deduction.

Regarding the top surface state, Schrödinger's equation becomes

$$H_{TI_top} \Psi_{top} = \begin{vmatrix} V_z & a \\ a^+ & -V_z \end{vmatrix} \times \begin{vmatrix} T_\uparrow \\ T_\downarrow \end{vmatrix} = \lambda \times \begin{vmatrix} T_\uparrow \\ T_\downarrow \end{vmatrix} \quad (5.23)$$

and the eigenvalues are

$$\lambda^2 = a \times a^+ + V_z^2 = v^2 K^2 + V_z^2,$$

thus,

$$\lambda_{\pm} = \pm \sqrt{v^2 K^2 + V_z^2} \quad (5.24)$$

This indicates that the eigenvalues have the minimum/maximum value at the Γ -point and is $\lambda = \pm V_z$. The band gap of the surface state is $2|V_z|$, which is in line with the numerical simulation shown previously using the FKM model. When the strength of the potential increases, the surface gap also increases. Fig. 15b shows the band structure for the out-of-plane magnetization.

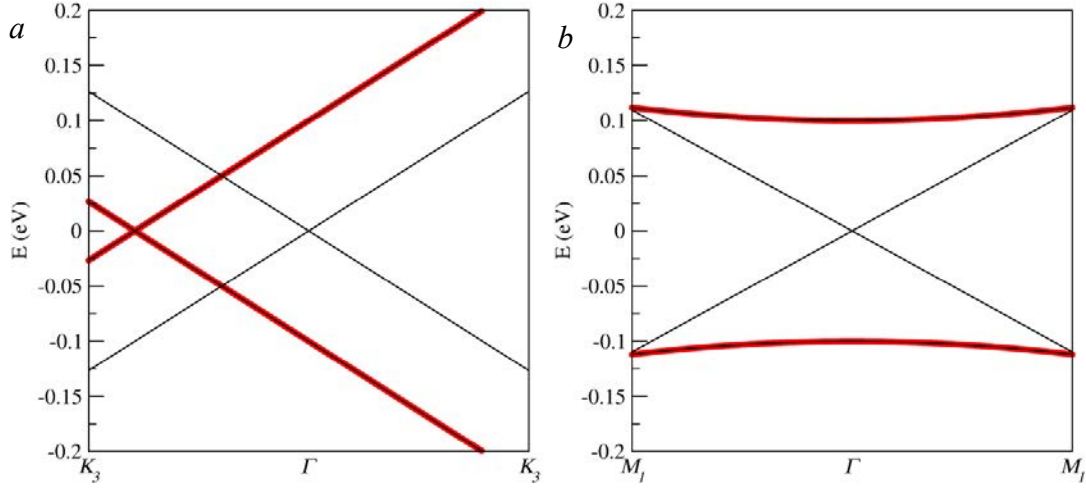


Fig. 5.15 Band structure of TI based on analytical calculations: *a* – in-plane exchange potential; *b* – out-of-plane magnetization

In addition to the surface doping scheme, one could also distribute the magnetic impurities inside the bulk and there have been many works on it; for instance, G. Rosenberg and M. Franz, for instance, used mean field theory to simulate random bulk doping with magnetic elements, which were aligned along an out-of-plane direction, and reported that a magnetic dopant could induce a window where the bulk was paramagnetic.[45] Similarly, Turgut Yilmaz *et al.* described the same situation when the surface state is magnetically ordered.[46] Cr dopants inside bulk of Bi_2Se_3 can open an energy gap at DP of the surface states, which is observable in the non-magnetic state.[47] Additionally, Kush Saha and Ion Garate performed theoretical calculations and studied coupling between the surface and bulk states when the Fermi level was pushed into the bulk band and poor conducting impurity band.[48]

In order to illustrate the effect of the magnetic doping away from the TI surface we have performed numerical calculations using the FKM model. The dopants were located at different positions with respect to the surface. Fig. 5.16 shows the band structure of the FKM model with different percentages of impurities moved beneath the TI surface. Figs. 5.16a ~ 5.16c show cases where the dopants are located in the second TI plane, which is right beneath the surface, and the direction of their magnetization is along the z -axis; Figs. 5.16d ~ 5.16f show the same results for the impurities with magnetization along the x axis. An explanation for these results is that the magnetic impurities interact with the surface band through the perpendicular hopping (t_{\perp}), which also controls the strong topological phase. As the impurity

moves away from the surface, the interaction through t_{\perp} becomes weaker and weaker; therefore, the effect on the surface band diminishes gradually.

Fig. 5.16 shows the same basic conclusions as those for doping on the TI surface. Figs. 5.16a ~ 5.16c all show a surface band gap, but the gap values are all smaller than those in Figs. 5.9a ~ 5.9c. Meanwhile, the impurity inside TI interacts with layers beneath the surface more than that on the TI surface and, taking Fig. 5.16a as an example, the red-colour impurity band hybridizes with other atoms on the 2nd layer and these bands are also pushed even further inside the bulk. Regarding Figs. 5.16d ~ 5.16f, the in-plane exchange potential also shifts the surface DP away from the Γ -point but not as far as in Figs. 5.11a ~ 5.11c and these impurity bands also hybridize with the bulk bands. It is clear that the effect of magnetic doping within the bulk becomes weaker and induces many hybridizations with the bulk states and this study can provide some general guidance to experimentalists.

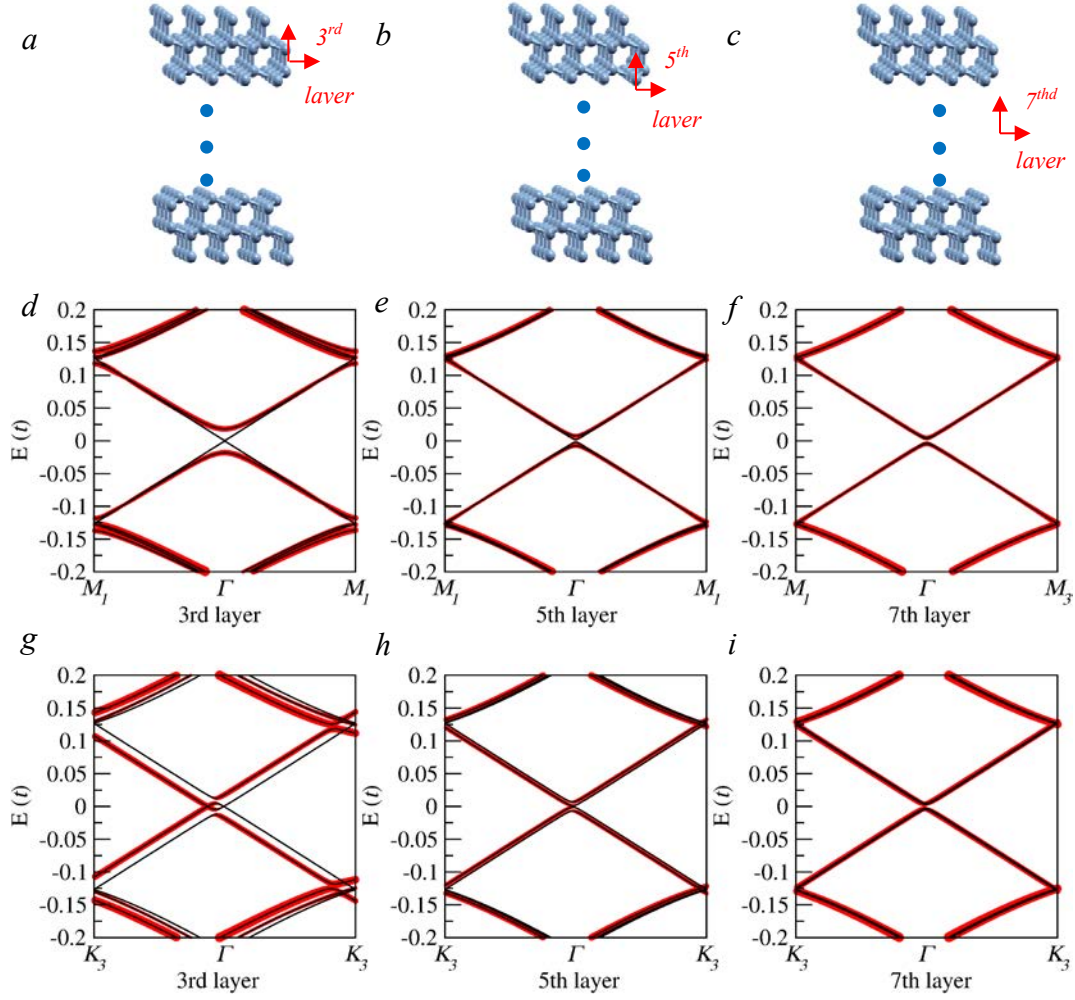


Fig. 5.16 FKM model with exchange potential doped on different layers, $a \sim c$ - doping positions onto different layers; $d \sim f$ - potential align along z axis; $g \sim i$ - potential align along x -axis

Fig. 5.17 shows the results when magnetic doping is restricted to the bulk of the FKM model and the doping percentage is 16.05%. Figs. 5.17c ~ 5.17d. correspond to cases where the magnetization of impurities points along the z -axis; while 5.17e ~ 5.17f shows the electronic structure when the magnetization points along the x -axis. This allows to simulate the effect of one ferromagnetic zone sandwiched by two TI films. It shows that when the ferromagnetic zone is far away from the TI surfaces, the magnetic elements do not influence the surface state, no matter how the potential is aligned (in-plane or out-of-plane direction). In other words, this magnetic impurities can act as a partition and divide the whole TI into two sub-films. Due to the fact that the thickness of each sub-TI film becomes thinner, the quantum tunnelling effect (QTE) manifests and a gap opening occurs in both out-of-plane and in-plane cases. This indicates that high percentage of bulk doping does not affect the surface state but

instead separates the whole system into sub films with thinner thicknesses which eventually may lead to surface gap opening because of QTE.

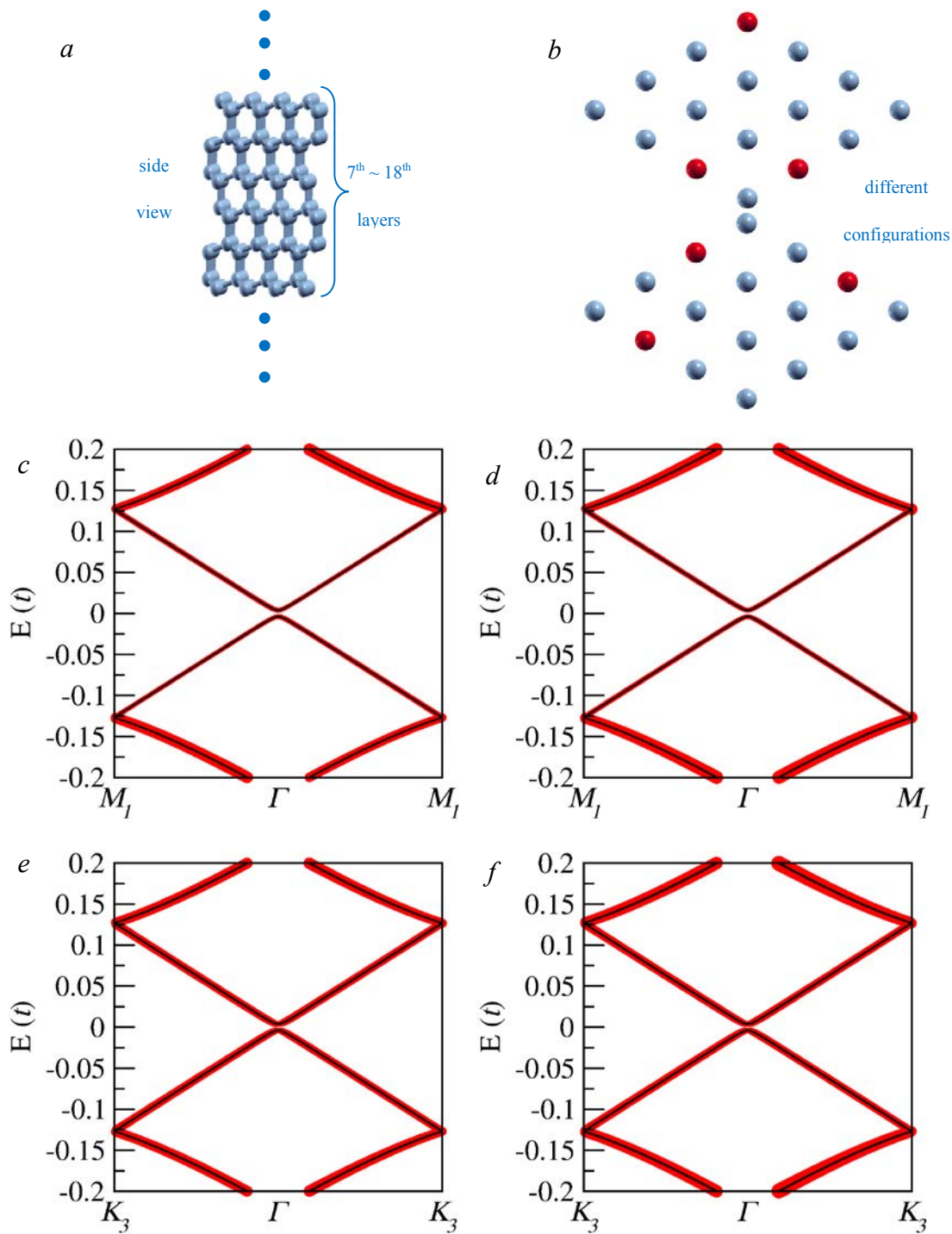


Fig. 5.17 FKM model with magnetic doping inside the bulk. *a, b* – side and top views for doping position, indicated by red colour; *c, d* - potential along z axis with

It is known that the surface states of TI exhibit the spin-momentum locking feature, *i.e.* that the spin and momentum of the surface state remains perpendicular to each other whatever the

energy and momentum values and the directions between them follows the right-hand rule. This also means that once the direction for one of them is known, that for the other one can be obtained through right hand rule. Fig. 5.18 shows the spin texture for the surface states in pristine TI, plotted in red, and the energy contours were taken around the Γ -point on this surface band. The green arrow indicates the direction of the spin vector, while the direction of the momentum vector is from centre of the contour circle to each point.

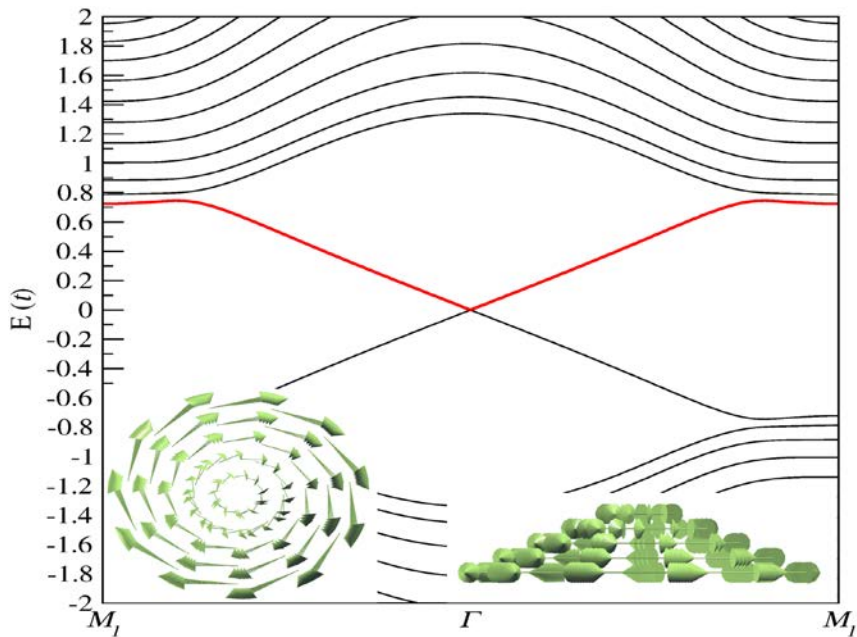


Fig. 5.18 Band structure and spin textures for pristine TI surface states

To have a better view of the spin textures, analytical calculations are performed. In the previous section, the eigenvalues and eigenvectors of pristine TI were already evaluated.

For the top surface, the eigenvalues are $\lambda_{\pm} = \pm vK$ and the eigenvectors are

$$|\Psi\rangle = \frac{1}{\sqrt{2}} \begin{pmatrix} ie^{-i\theta} & -ie^{-i\theta} \\ 1 & 1 \\ 0 & 0 \\ 0 & 0 \end{pmatrix} \quad (5.25)$$

Here, we only compute the spin texture corresponding to the top surface conduction band ($\lambda = vK$) with eigenvector (Remark: give a symbol to this eigenvector)

$$|\Psi_{\uparrow}\rangle = \frac{1}{\sqrt{2}} \begin{pmatrix} ie^{-i\theta} \\ 1 \\ 0 \\ 0 \end{pmatrix} \quad (5.26)$$

The expectation values of the spin operator along the three axes can be calculated as

$$\begin{aligned}\langle S_x \rangle &= (T_{\uparrow}^+ \quad T_{\downarrow}^+) \begin{vmatrix} 0 & 1 \\ 1 & 0 \end{vmatrix} \begin{pmatrix} T_{\uparrow} \\ T_{\downarrow} \end{pmatrix} = T_{\downarrow}^+ T_{\uparrow} + T_{\uparrow}^+ T_{\downarrow} \\ &= \frac{1}{\sqrt{2}} \times 1 \times \frac{1}{\sqrt{2}} \times ie^{-i\vartheta} + \frac{1}{\sqrt{2}} \times -ie^{i\vartheta} \times \frac{1}{\sqrt{2}} \times 1 = \sin\vartheta\end{aligned}\quad (5.27)$$

$$\begin{aligned}\langle S_y \rangle &= (T_{\uparrow}^+ \quad T_{\downarrow}^+) \begin{vmatrix} 0 & -i \\ i & 0 \end{vmatrix} \begin{pmatrix} T_{\uparrow} \\ T_{\downarrow} \end{pmatrix} = iT_{\downarrow}^+ T_{\uparrow} - iT_{\uparrow}^+ T_{\downarrow} \\ &= i \times \frac{1}{\sqrt{2}} \times 1 \times \frac{1}{\sqrt{2}} \times ie^{-i\vartheta} - i \times \frac{1}{\sqrt{2}} \times -ie^{i\vartheta} \times \frac{1}{\sqrt{2}} \times 1 = -\cos\vartheta\end{aligned}\quad (5.28)$$

$$\begin{aligned}\langle S_z \rangle &= (T_{\uparrow}^+ \quad T_{\downarrow}^+) \begin{vmatrix} 1 & 0 \\ 0 & -1 \end{vmatrix} \begin{pmatrix} T_{\uparrow} \\ T_{\downarrow} \end{pmatrix} = T_{\uparrow}^+ T_{\uparrow} - T_{\downarrow}^+ T_{\downarrow} \\ &= \frac{1}{\sqrt{2}} \times -ie^{i\vartheta} \times \frac{1}{\sqrt{2}} \times ie^{-i\vartheta} - \frac{1}{\sqrt{2}} \times 1 \times \frac{1}{\sqrt{2}} \times 1 = 0\end{aligned}\quad (5.29)$$

The expectation values of the spin operators are then plotted against the direction of the momentum vector, which is indicated by the angle ϑ , in Fig. 5.19. From both the analytical results and Fig. 5.19, it is clear that $\langle S_x \rangle$ and $\langle S_y \rangle$ follow a standard SIN and COS functions; while $\langle S_z \rangle$ is always zero, which is consistent with the numerical results shown in Fig. 5.19. This is very useful for the application of conversion from charge current to spin current in the field of spintronics, which was discussed in chapter 4 regarding the graphene/TI based heterostructures.

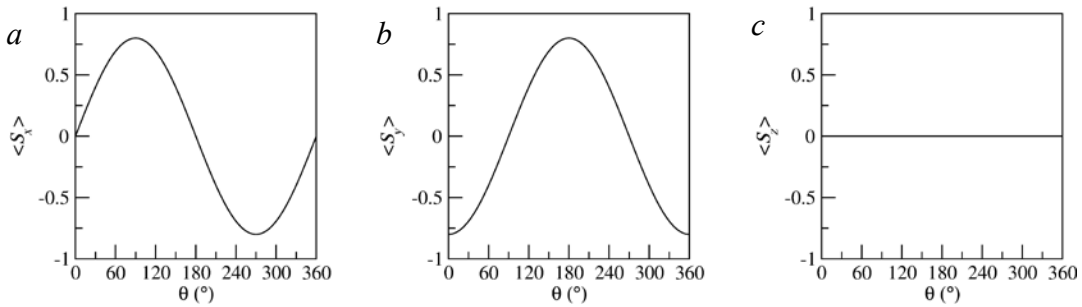


Fig. 5.19 Expectation value of spin along three axes on surface contour

Furthermore, the magnitude of the spin expectation value diminishes gradually as the contour moves close to Γ point. The spin lifetime anisotropy for the pristine TI is also calculated below and is defined as the ratio of out-of-plane to in-plane spin lifetimes. It is assumed that the

relaxation time follows a D'yakonov-Perel mechanism and the lifetime of spin polarized along α direction is given by the following equation (5.30)[49].

$$\frac{1}{\tau_\alpha} = \tau_{\alpha\perp}^* (\overline{|\Omega|^2} - \overline{\Omega_\alpha^2}) \quad (5.30)$$

where Ω is the momentum dependent effective magnetic field, which comes from SOC, and $\overline{\Omega_{\alpha\perp}^2}$ is the time to randomize the component of Ω which is perpendicular to α (spin polarization direction). The overline implies an average over the Fermi surface at a particular Fermi energy. For a given band, the magnetic field is decomposed in equation (5.31)

$$\Omega = \omega \cdot S \quad (5.31)$$

where, $\omega = \frac{\Delta E}{\hbar}$ denotes the spin precession frequency associated with the spin splitting ΔE of the band. S is the spin polarization of the eigenstates associated with the chosen band. Finally, the spin lifetime anisotropy, which comes from splitting bands, derives from equation (5.32)

$$A_f = \frac{\tau_z^* \sum_{i=1}^n (\overline{|S|^2} - \overline{S_x^2})_i}{\tau_x^* \sum_{i=1}^n (\overline{|S|^2} - \overline{S_z^2})_i} \quad (5.32)$$

where, the sum runs over all i , which are the band considered in the Fermi surface average. In the T₂-T₂ case, DP is located to Γ point, so $\tau_x^* = \tau_z^* = \tau_p$ and is the momentum relaxation time.[50]

In the pristine TI case, the lifetime anisotropy is found to be 0.5, which means that the standard *Rashba*-type texture always gives 50% anisotropy and the magnitude of $\langle S_x \rangle$ and $\langle S_y \rangle$ are equal to each other.

$$A_f = \frac{\overline{|S|^2} - \overline{|S_x|^2}}{\overline{|S|^2} - \overline{|S_z|^2}} = \frac{\overline{|S_y|^2} + \overline{|S_z|^2}}{\overline{|S_x|^2} + \overline{|S_y|^2}} = \frac{|S_y|^2 + |S_z|^2}{|S_x|^2 + |S_y|^2} = \frac{|S_y|^2}{|S_x|^2 + |S_y|^2} = \frac{1}{2} \quad (5.33)$$

On the other hand, the spin properties of TI with magnetic doping differ from the pristine TI case. Fig. 5.20 shows the spin texture for the FKM model with different impurity densities all polarized along the out-of-plane direction, and, from the top view, the results also show a

Rashba like texture. However, it is obvious that the spin component along the z axis is not zero from the side because the spin vector is tilted to the out-of-plane direction and, as the contour moves close to the Γ point, the spin vector is tilted more and more closely to the z axis. Furthermore, spin tends to align along the z axis as the doping density increases gradually ($a. \sim c.$). This means that the out-of-plane magnetization could align the spin on the surface state from an in-plane to an out-of-plane direction and closer to Γ point, more out-of-plane component spin vector has, dictating that the spin anisotropy is not 50%, like in the pristine TI case.

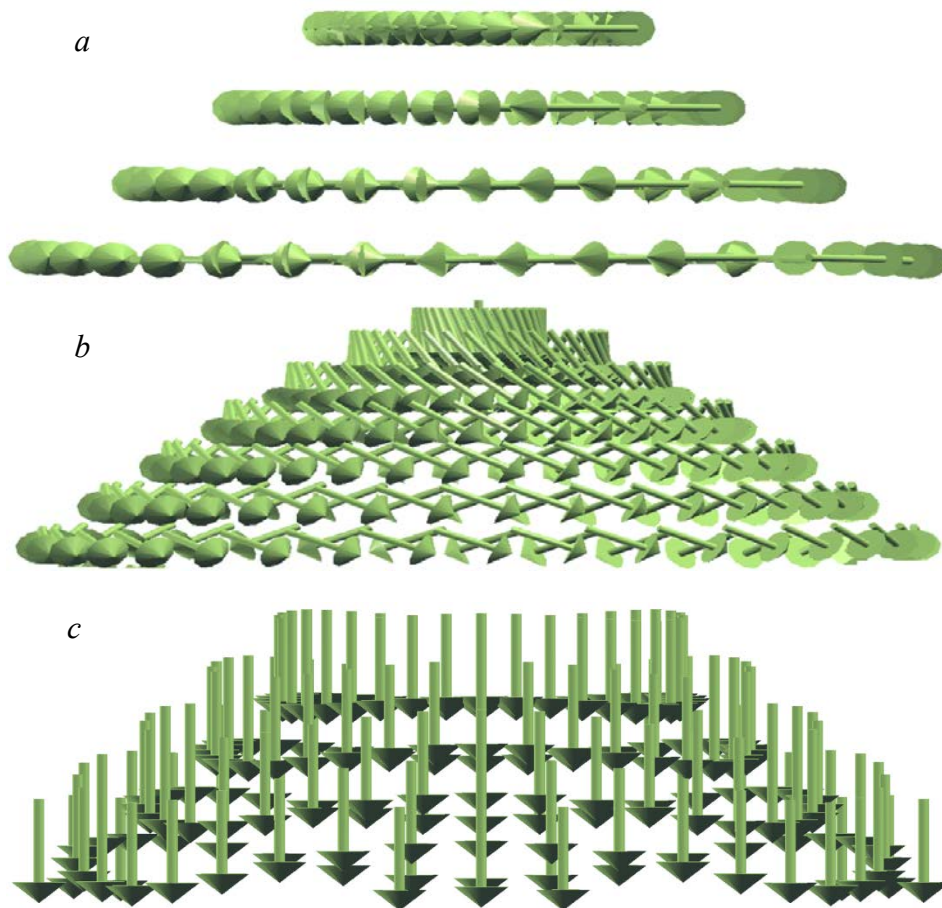


Fig. 5.20 Spin texture for FKM model doped with out-of-plane magnetization. *a.* – pristine case; *b.* – FKM doped with 16.05% exchange potential and *c.* - FKM doped with 100% magnetic doping

An analytical calculations were also carried out in order to give a clearer explanation of the computed spin textures. The eigen value and vector have been calculated in the previous content.

Top surface;

$$\lambda_+ = R \quad (R = \sqrt{v^2 K^2 + V^2}) \quad \text{and} \quad |\Psi_\uparrow\rangle = \sqrt{\frac{R-V}{2R}} \begin{pmatrix} \frac{a}{R-V} \\ 1 \\ 0 \\ 0 \end{pmatrix};$$

$$\lambda_- = -R \quad \text{and} \quad |\Psi_\uparrow\rangle = \sqrt{\frac{R+V}{2R}} \begin{pmatrix} \frac{a}{R+V} \\ 1 \\ 0 \\ 0 \end{pmatrix}$$

Here, only the surface states in the conduction band is considered and the expectation values of spin operator are

$$\begin{aligned} \langle S_x \rangle &= (T_\uparrow^+ \quad T_\downarrow^+) \begin{vmatrix} 0 & 1 \\ 1 & 0 \end{vmatrix} \begin{pmatrix} T_\uparrow \\ T_\downarrow \end{pmatrix} = T_\downarrow^+ T_\uparrow + T_\uparrow^+ T_\downarrow \\ &= \sqrt{\frac{R-V}{2R}} \times 1 \times \sqrt{\frac{R-V}{2R}} \times \frac{a}{R-V} + \sqrt{\frac{R-V}{2R}} \times \frac{a^+}{R-V} \times \sqrt{\frac{R-V}{2R}} \times 1 \\ &= \frac{vK \sin \theta}{R} \end{aligned} \quad (5.34)$$

$$\begin{aligned} \langle S_y \rangle &= (T_\uparrow^+ \quad T_\downarrow^+) \begin{vmatrix} 0 & -i \\ i & 0 \end{vmatrix} \begin{pmatrix} T_\uparrow \\ T_\downarrow \end{pmatrix} = iT_\downarrow^+ T_\uparrow - iT_\uparrow^+ T_\downarrow \\ &= i \times \sqrt{\frac{R-V}{2R}} \times 1 \times \sqrt{\frac{R-V}{2R}} \times \frac{a}{R-V} - i \times \sqrt{\frac{R-V}{2R}} \times \frac{a^+}{R-V} \times \sqrt{\frac{R-V}{2R}} \times 1 \\ &= -\frac{vK \cos \theta}{R} \end{aligned} \quad (5.35)$$

$$\begin{aligned} \langle S_z \rangle &= (T_\uparrow^+ \quad T_\downarrow^+) \begin{vmatrix} 1 & 0 \\ 0 & -1 \end{vmatrix} \begin{pmatrix} T_\uparrow \\ T_\downarrow \end{pmatrix} = T_\uparrow^+ T_\uparrow - T_\downarrow^+ T_\downarrow \\ &= \sqrt{\frac{R-V}{2R}} \times \frac{a^+}{R-V} \times \sqrt{\frac{R-V}{2R}} \times \frac{a}{R-V} + \sqrt{\frac{R-V}{2R}} \times 1 \times \sqrt{\frac{R-V}{2R}} \times 1 \\ &= \frac{V}{R} \end{aligned} \quad (5.36)$$

The expectation value of the spin operator against the direction of momentum vector is plotted in Fig. 5.21, from which it is clear that $\langle S_x \rangle$ and $\langle S_y \rangle$ still follow the SIN and COS function shape. However, $\langle S_z \rangle$ is no longer zero and within the same energy contour, $\langle S_z \rangle$ it is proportional to the strength of exchange potential. This contrasts with the pristine case.

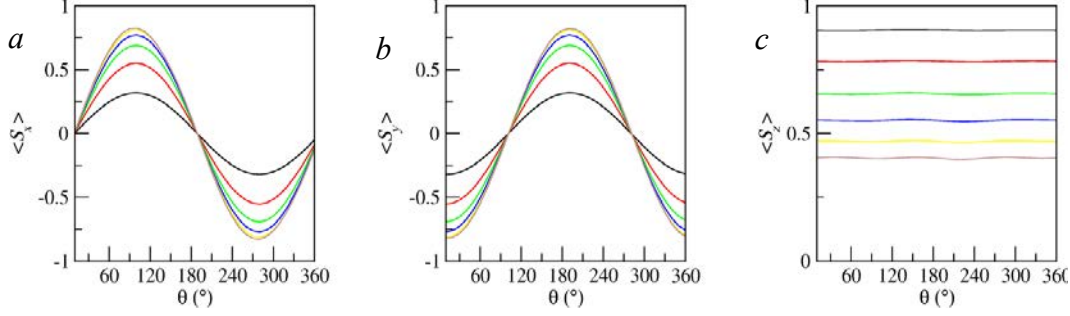


Fig. 5.21 Expectation value of spin along three axes in FKM doped with onsite exchange potential

Meanwhile, as the contours move close to the Γ point in the Brillouin zone, K ($K = \sqrt{K_x^2 + K_y^2}$) and, then, R ($R = \sqrt{v^2 K^2 + V^2}$) becomes smaller and the constant exchange potential, $\langle S_z \rangle$ then becomes larger. This means that the ratio of in-plane to out-of-plane spin component is k dependent and therefore, the spin lifetime anisotropy is expressed in equation (5.37).

$$\begin{aligned}
 A_f &= \frac{|\overline{S}|^2 - |\overline{S_x}|^2}{|\overline{S}|^2 - |\overline{S_z}|^2} = \frac{|\overline{S_y}|^2 + |\overline{S_z}|^2}{|\overline{S_x}|^2 + |\overline{S_y}|^2} = \frac{|\overline{S_y}|^2 + |\overline{S_z}|^2}{|\overline{S_x}|^2 + |\overline{S_y}|^2} = \frac{\sum_{i=1}^N \left(\frac{v^2 K_x^2}{R^2} + \frac{K^2}{R^2} \right)}{\sum_{i=1}^N \left(\frac{v^2 K_x^2}{R^2} + \frac{v^2 K_y^2}{R^2} \right)} \\
 &= \frac{\int_0^{2\pi} (v^2 K^2 \cos^2 \vartheta + V^2)}{\int_0^{2\pi} (v^2 K^2 \sin^2 \vartheta + v^2 K^2 \cos^2 \vartheta)} = \frac{v^2 K^2 + 2V^2}{2v^2 K^2} = \frac{1}{2} + \frac{V^2}{v^2 K^2} \quad (5.37)
 \end{aligned}$$

According to the analytical results, which are shown in Fig. 5.22, the following rules are apparent. First, on a fixed energy level, K is constant and A_f increase with exchange potential; second, with a constant exchange potential, A_f increases as the energy contour close to Γ point. When the contour moves away from Γ point, A_f decreases gradually and the minimum value is 50%.

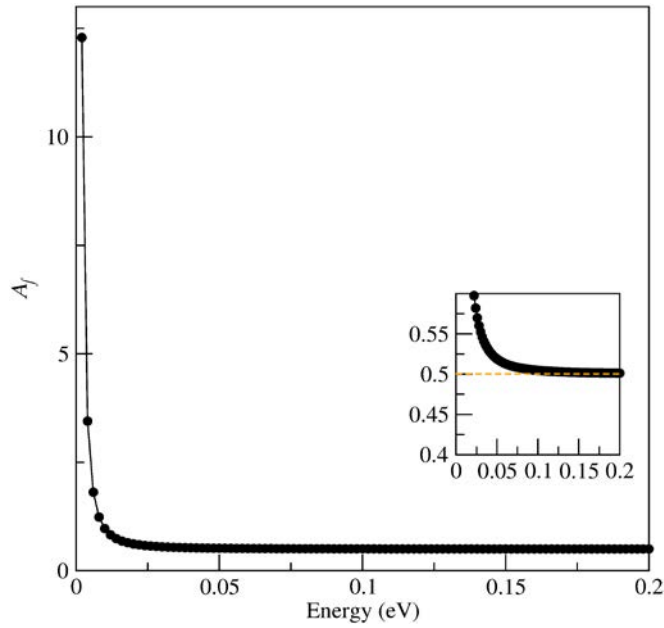


Fig. 5.22 Spin lifetime anisotropy of FKM doped with onsite exchange potential

These results are consistent with both the numerical results and increases in doping percentages shown in Fig. 5.23. Furthermore these findings can provide guidance for researchers investigating the effects of magnetic doping on TI surfaces: specifically, that magnetic doping on TI surfaces not only opens the surface gap and generates a quantum anomalous hall effect but can also induce spin anisotropy, which could affect the relaxation of the spin current signal on the TI surface.

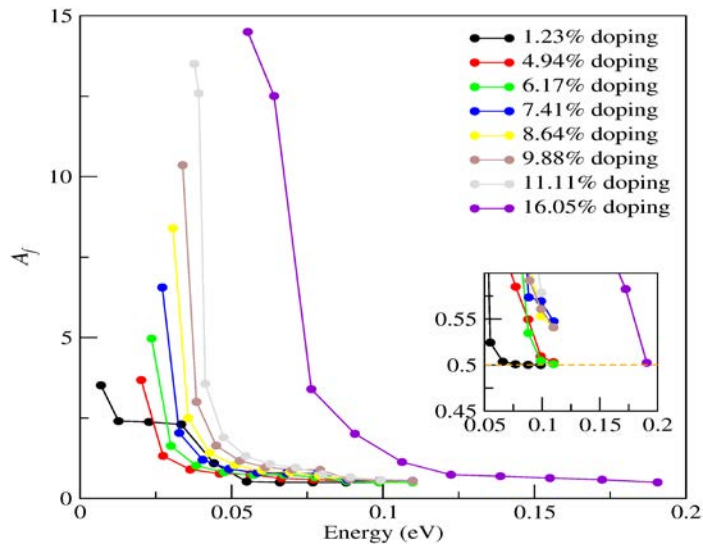


Fig. 5.23 Spin anisotropy v.s. doping percentage based on numerical calculation of

5.4 Conclusions

This chapter discussed Fu-Kane-Mele (FKM) model doped with different impurities, regarding the electronic properties, in order to provide a fundamental understanding on the property alternation of 3D topological insulator by impurity.

Section 5.1 explained this FKM model and showed how to simulate 3D TI with different phases (strong TI, semimetal and weak TI) through modifying hopping parameters along different axes; then, reported that DP could show up at different k points with different spin texture for different termination case in this model and it is worth to note that T2T2 termination case could show DP at Γ point with Rashba spin texture which is same as the real 3D TI system; *e.g.* Bi₂Se₃. Thickness effect was also investigated in so as to see the effect of QTE on the surface state. Meanwhile, the analytical calculation based on an effective Hamiltonian was also carried out for both band structure and spin texture to support the numerical calculation on this model.

Section 5.2 examined the effect of non-magnetic disorder on the electronic structure of this model through adding localised potential onto surface termination and it pointed that such kind of disorder could not destroy the surface DP but only cause the translational shift of the surface state, which was doped with disorder, and the relation between spin and momentum remained same as *Rashba* type texture.

Section 5.3 investigated in the effect of magnetic impurity on this model with different doping percentage. The magnetic impurity was first doped on the surface to FKM model and it was found that impurity with out-of-plane magnetization could cause the surface gap opening and the gap value increased with both magnetization strength and doping percentage; while, the in-plane magnetization did not destroy the surface DP but moved the it away from DP. Besides the surface doping, impurity was also doped into the bulk of the model and it was found that as the doping position moved away from the surface, the effect brought onto surface state diminished gradually. To support the numerical calculation, analytical calculation based on an effective Hamiltonian for 3D TI was also carried out and the analytical formula for the surface gap was provided. On the other hand, the surface spin texture was also examined through both numerical and analytical calculations and they both pointed out that out-of-plane magnetization on the surface could cause the spin tilt to the z axis and as the tile angle

increases with magnetization strength. Furthermore, it was found that the ratio of in-plane and out-of-plane spin component vary with k point which is that out-of-plane spin dominate the spin at k point close to Γ and decreases as the k point moved away from Γ and finally, the ratio between in-plane and out-of-plane spin component reached 0.5.

All these theoretical works on the impurity doping scheme could provide a general guidance to the experimentalist on the electronic structure changes with the defects. Particularly, the out-of-plane magnetization induced by magnetic impurity on TI surface could bring spin anisotropy, which could be used as the potential way to modify the spin current in the laboratory.

References:

- [1] Fu, Liang; Kane, C. L. and Mele, E. J. *Phys. Rev. Lett.* (2007) 98, 106803
- [2] Burkov, A. A. *Nature Materials* (2016) 15, 1145-1148
- [3] Soriano, David; Ortmann, Frank and Roche Stephan *Phys. Rev. Lett.* (2012) 109, 266805
- [4] Yu, Rui; Zhang, Wei; Zhang, Hai-Jun; Zhang, Shou-Cheng; Dai, Xi and Fang, Zhong *Science* (2010) 329, 61-64
- [5] Bianchi, Marco; Hatch, Richard C.; Mi, Jianli; Iversen, Bo Brummerstedt and Hofmann, Philip *Phys. Rev. Lett.* (2011) 107, 086802
- [6] Forster, Tobias; Kruger, Peter and Rohlfing, Michael *Phys. Rev. B* (2015) 91, 035313
- [7] Benia, Hadj M.; Lin, Chengtian; Kern, Klaus and Ast, Christian R. *Phys. Rev. Lett.* (2011) 107, 177602
- [8] Jakobs, Sebastian; Narayan, Awadhesh; Stadtmuller, Benjamin; Droghetti, Andrea; Rungger, Ivan; Hor, Yew S.; Klyatskaya, Svetlana; Jungkenn, Dominik; Stockl, Johannes; Laux, Martin; Monti, Oliver L. A.; Aeschlimann, Martin; Cava, Robert J.; Ruben, Mario; Mathias, Stefan; Sanvito, Stefano and Cinchetti, Mirko *Nano Lett.* (2015) 15, 6022-6029
- [9] Hao, G. L.; Qi, X.; Yang, L. W.; Huang, Z. Y.; Cai, C. Y.; Xue, L.; Yu, S. X. and Zhong, J. X. *Solid State Communications* (2012) 152, 22, 2027-2030
- [10] Roy, Sumalay and Meyerheim, H. L. *Phys. Rev. B* (2014) 113, 116802
- [11] Wei, Peng; Wang, Zhiyong; Liu, Xinfei; Aji, Vivek and Shi, Jing *Phys. Rev. B* (2012) 85, 201402(R)
- [12] Kuroda, K.; Arita, M.; Miyamoto, K.; Ye, M.; Jiang, J.; Kimura, A.; Krasovskii, E. E.; Chulkov, E. V.; Iwasawa, H.; Okuda, T.; Shimada, K.; Ueda, Y.; Namatame, H. and Taniguchi, M. *Phys. Rev. Lett.* (2010) 105, 076802
- [13] Hor, Y. S.; Richardella A.; Roushan, P.; Xia, Y.; Checkelsky, J. G.; Yazdani, A.; Hasan, M. Z.; Ong, N. P. and Cava, R. J. *Phys. Rev. B* (2009) 79, 195208
- [14] Koleini, Mohammad; Frauenheim, Thomas and Yan, Binghai *Phys. Rev. Lett.* (2013) 110, 016403
- [15] Wang, Yong; Xiu, Faxian; Cheng, Lina; He, Liang; Lang, Murong; Tang, Jianshi; Kou, Xufeng; Yu, Xinxin; Jiang, Xiaowei; Chen, Zhigang; Zou, Jin and Wang, Kang L. *Nano Lett.* (2012) 12, 1170-1175
- [16] Maurya, Shruti V. K.; Neha, P.; Srivastava, P. and Patnaik, S. *Phys. Rev. B* (2015) 92, 020506(R)

- [17] Koski, Kristie J.; Wessells, Colin D.; Reed, Bryan W.; Cha, Judy J.; Kong, Desheng and Cui, Yi *J. Am. Chem. Soc.* (2012) 134(33), 13773–13779
- [18] Zhang, Yan-Yang; Chu, Rui-Lin; Zhang, Fu-Chun and Shen, Shun-Qing *Phys. Rev. B* (2012) 85, 035107
- [19] Orth, Christoph P.; Sekera, Tibor; Bruder, Christoph and Schmidt, Thomas L. *Scientific Reports* (2016) 6, 24007
- [20] Nagaosa, Naoto; Sinova, Jairo; Onoda, Shigeki; MacDonald, A. H. and Ong, N. P. *Rev. Mod. Phys.* (2010) 82, 1539-1592
- [21] Yu, Rui; Zhang, Wei; Zhang, Hai-Jun; Zhang, Shou-Cheng; Dai, Xi and Fang, Zhong *Science* (2010) 329, 61-64
- [22] He, Ke; Wang, Yayu and Xue, Qi-Kun *National Science Review*, (2014) 1, 39-49
- [23] Chang, Cui-Zu; Zhang, Jinsong; Feng, Xiao; Shen, Jie; Zhang, Zuocheng; Guo, Minghua; Li, Kang; Ou, Yunbo; Wei, Pang; Wang, Li-Li; Ji, Zhong-Qing; Feng, Yang; Ji, Shuaihua; Chen, Xi; Jia, Jinfeng; Dai, Xi; Fang, Zhong; Zhang, Shou-Cheng; He, Ke; Wang, Yayu; Lu, Li; Ma, Xu-Cun and Xue, Qi-Kun *Science* (2013) 340, 6129, 167-170
- [24] Jalil, Mansoor B. A.; Tan, S. G. and Siu, Z. B. *Applied Physics* (2015) 117, 17, C739
- [25] Eelbo1, T.; Sikora, M.; Bihlmayer, G.; Dobrzański, M.; Kozłowski, A.; Miotkowski, I. and Wiesendanger, R. *New Journal of Physics* (2013) 15, 113026
- [26] Valla, T; Pan, ZH; Gardner, D; Lee, YS and Chu, S. *Phys. Rev. Lett.* (2012) 108, 117601
- [27] Wray, L. Andrew; Xu, Su-Yang; Xia, Yuqi; Hsieh, David; Fedorov, Alexei V.; Hor, Yew San; Cava, Robert J.; Bansil, Arun; Lin, Hsin and Hasan, M. Zahid *Nature Physics* (2011) 7, 32-37
- [28] Zhang, Jian-Min; Zhu, Wenguang; Zhang, Ying; Xiao, Di and Yao, Yugui *Phys. Rev. Lett.* (2012) 109, 266405
- [29] Haazen, P. P. J.; Lalo, J.-B.; Nummy, T. J.; Swagten, H. J. M.; Jarillo-Herrero, P.; Heiman, D. and Moodera, J. S. *Appl. Phys. Lett.* (2012) 100, 082404
- [30] Liu, Minhao; Zhang, Jinsong; Chang, Cui-Zu; Zhang, Zuocheng; Feng, Xiao; Li, Kang; He, Ke; Wang, Li-li; Chen, Xi; Dai, Xi; Fang, Zhong; Xue, Qi-Kun; Ma, Xucun and Wang, Yayu *Phys. Rev. Lett.* (2012) 108, 036805
- [31] Chotorlishvili, L.; Ernst, A.; Dugaev, V. K.; Komnik, A.; Vergniory, M. G.; Chulkov, E. V. and Berakdar, J. *Phys. Rev. B* (2014) 89, 075103
- [32] Niu, Chengwang; Dai, Ying; Guo, Meng; Wei, Wei; Ma, Yandong and Huang, Baibiao *Appl. Phys. Lett.* (2011) 98, 252502
- [33] Zhang, Duming; Richardella, Anthony; Rench, David W.; Xu, Su-Yang; Kandala, Abhinav; Flanagan, Thomas C.; Beidenkopf, Haim; Yeats, Andrew L.; Buckley, Bob B.; Klimov, Paul V.; Awschalom, David D.; Yazdani, Ali; Schiffer, Peter; Hasan, M. Zahid and Samarth, Nitin *Phys. Rev. B* (2012) 86, 205127
- [34] Liu, Qin; Liu, Chao-Xing; Xu, Cenke; Qi, Xiao-Liang and Zhang, Shou-Cheng *Phys. Rev. Lett.* (2009) 102, 156603
- [35] Klitzing, Klaus von; Dorda, G. and Pepper, M. *Phys. Rev. Lett.* (1980) 45, 494
- [36] Tsui, D. C.; Stormer, H. L. and Gossard, A. C. *Phys. Rev. Lett.* (1982) 48, 1559
- [37] Kane C. L. and Mele E. J. *Phys. Rev. Lett.* (2005) 95, 22, 226081
- [38] Ye, M.; Eremeev, S. V.; Kuroda, K.; Krasovskii, E. E.; Chulkov, E. V.; Takeda, Y.; Saitoh, Y.; Okamoto, K.; Zhu, S. Y.; Miyamoto, K.; Arita, M.; Nakatake, M.; Okuda, T.; Ueda, Y.; Shimada, K.; Namatame, H.; Taniguchi, M. and Kimura, A. *Phys. Rev. B* (2012) 85, 205317
- [39] Schmidt, Tome M.; Miwa, R. H. and Fazzio, A. *Phys. Rev. B* (2011) 84, 245418
- [40] Honolka, J.; Khajetoorians, A. A.; Sessi, V.; Wehling, T. O.; Stepanow, S.; Mi, J.-L.; Iversen, B. B.; Schlenk, T.; Wiebe, J.; Brookes, N. B.; Lichtenstein, A. I.; Hofmann, Ph.; Kern, K. and Wiesendanger, R. *Phys. Rev. Lett.* (2012) 108, 256811

- [41] Jin, Hosub; Im, Jino and Freeman, Arthur J. *Phys. Rev. B* (2011) 84, 134408
- [42] Schlenk, T.; Bianchi, M.; Koleini, M.; Eich, A.; Pietzsch, O.; Wehling, T. O.; Frauenheim, T.; Balatsky, A.; Mi, J.-L.; Iversen, B. B.; Wiebe, J.; Khajetoorians, A. A.; Hofmann, Ph. and Wiesendanger, R. *Phys. Rev. Lett.* (2013) 110, 126804
- [43] Eelbo, T.; Wasniowska, M.; Sikora, M.; Dobrzański, M.; Kozłowski, A.; Pulkin, A.; Autes, G.; Miotkowski, I.; Yazyev, O. V. and Wiesendanger, R. *Phys. Rev. B* (2014) 89, 104424
- [44] Yu, Rui; Zhang, Wei; Zhang, Hai-Jun; Zhang, Shou-Cheng; Dai, Xi and Fang, Zhong *Science* (2010) 329, 61-64
- [45] Rosenberg, G. and Franz, M. *Phys. Rev. B* (2012) 85, 195119
- [46] Yilmaz, Turgut; Hines, William; Sun, Fu-Chang; Pletikoscic, Ivo; Budnick, Joseph; Valla, Tonica; Sinkovic, Boris *Applied Surface Science* (2017) 407, 371-378
- [47] Saha, Kush and Garate, Ion *Phys. Rev. B* (2014) 90, 245418
- [48] Zhang, Jia; Velez, Julina P.; Dang, Xiaoqian and Tsymbal, Evgeny Y. *Phys. Rev. B* (2016) 94, 014435
- [49] Žutić, Igor; Fabian, Jaroslav and Sarma, S. Das *Rev. Mod. Phys.* (2004) 76, 323-410
- [50] Song, Kenan; Soriano, David; Cummings, Aron W.; Robles, Roberto; Ordejón, Pablo and Roche, Stephan *Nano Lett.* (2018) 18, 2033-2039

Chapter Six: Conclusions

Conclusions

Here 3D Bi₂Se₃-family topological insulator and its related systems were studied based on DFT, TB and analytical calculations. Some interesting phenomena were found and could be interesting for further experimental work.

First, different defects were introduced into TI system with ultrathin thickness (< 5 nm) and it was found that rotation mismatches between different TI quintuple structures could result in enlargement of the surface gap while preserving the typical *Rashba* type spin textures. Then, the hydrogenation scheme on TI surface was examined and it was found that QTE on thin TI was avoided so that gapless surface states were preserved. The hydrogenated surface DP was shifted above the Fermi level; while, the clean surface DP was preserved below the Fermi level. Furthermore, the spin texture was also modified by this scheme and a Dresselhaus-type of texture was found with a new DP showing up at M point on the hydrogenated surface.

Then, the proximity effect of TI was investigated in the heterostructure of graphene interfaced with the Bi₂Se₃ family TI and it was found that the geometry of such structure is fundamental to understand the resulting electronic properties imprinted onto graphene. For an interface symmetry named as hollow position configuration, graphene bands became gapped while electronic states will exhibit some atypical *Rashba* type spin texture, where the spin texture changes with momentum, and a strong spin anisotropy is driven by an emerging out-of-plane component was found. More specifically, such out-of-plane component dominates the spin as the k point moved close to Γ point in Brillouin zone and decreases as the k point

moves away from Γ point where finally, the ratio between in-plane and out-of-plane spin anisotropy reaches 0.5 (conventional for purely Rashba SOC systems). A TB model was built up to explain such peculiar properties and it was found that carbon bonding distortion, known as the *Kekulé* distortion, plays an important role in the gap opening and that both in-plane and out-of-plane *Rashba* SOC terms are controlling the resulting atypical spin textures. On the other hand, other configurations (bridge and top positions) were also examined and the band structures were found to have large band splitting in the lateral direction, which could result in the Edelstein effect, while the spin anisotropy is found to disappear as the ratio of in-plane and out-of-plane spin components are similar.

Based on the FKM model, the effect of impurities with and without magnetization was theoretically studied. Nonmagnetic disorder was found to add a potential to the TI surface state and shift the DP above that of the clean TI surface but the spin texture was unaffected. Regarding the magnetic impurity, a surface gap was opened up due to the magnetization along out-of-plane direction and the spin tilted towards the z axis. Meanwhile, the spin anisotropy, which is similar to that in graphene/TI system, was also found when the out-of-plane spin component increased as k point moves close to Γ and diminish gradually as k point moves away from Γ .

All these works could provide guidance to experimentalists for the measurement of the spin signal of on TI system with defects or the heterostructure device based on graphene with TI; particularly, in the direction of spin anisotropy.